Oxidative Medicine and Cellular Longevity

Inflammation and Oxidative Stress in Age-Related Metabolic Disorders

Lead Guest Editor: Jianbo Wu
Guest Editors: En Yin Lai, Michael A. Hill, and Pei Luo

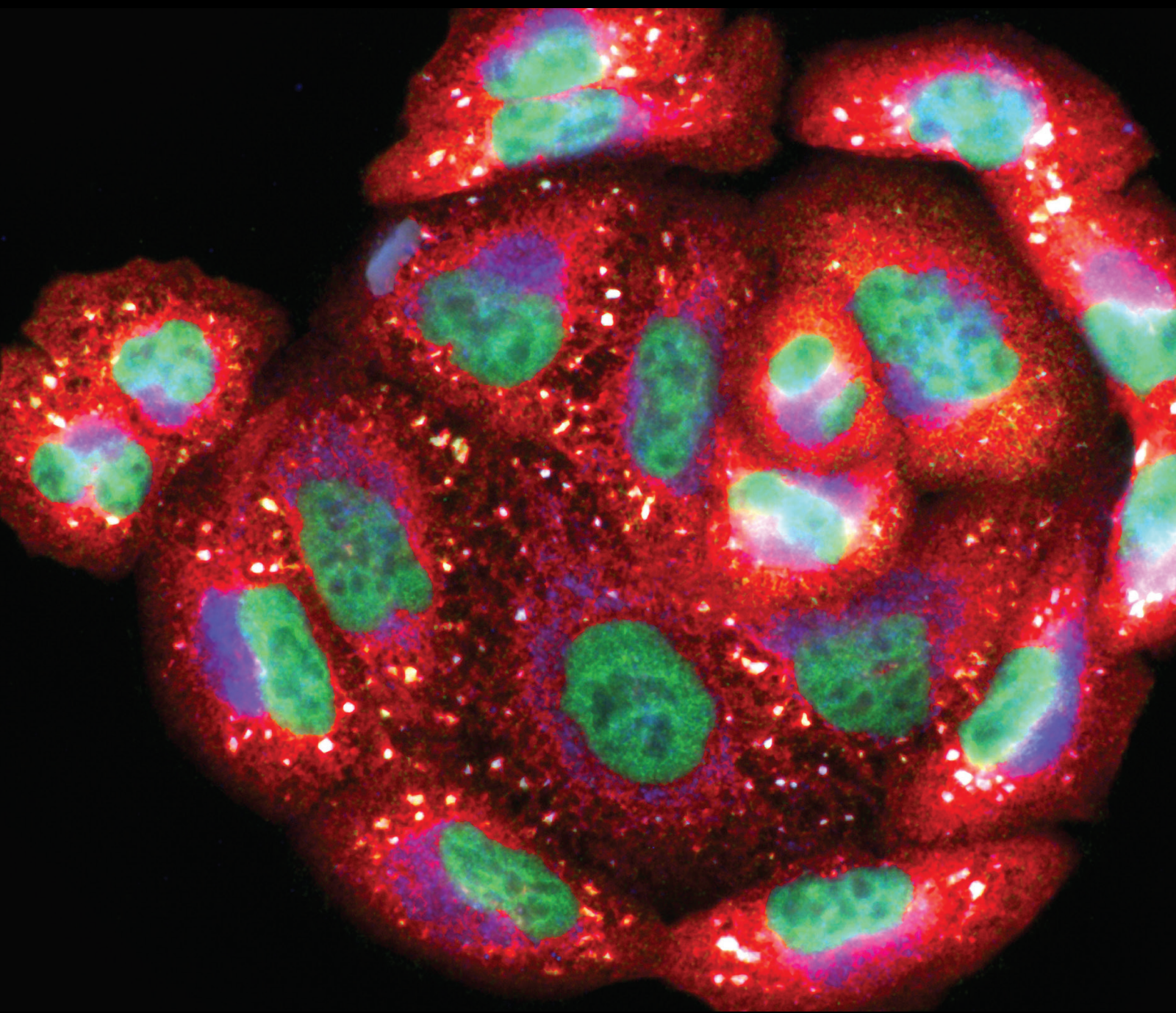

Inflammation and Oxidative Stress in Age-Related Metabolic Disorders

Oxidative Medicine and Cellular Longevity

Inflammation and Oxidative Stress in Age-Related Metabolic Disorders

Lead Guest Editor: Jianbo Wu
Guest Editors: En Yin Lai, Michael A. Hill, and Pei Luo

Contents

Rosin Derivative IDOAMP Inhibits Prostate Cancer Growth via Activating RIPK1/RIPK3/MLKL Signaling Pathway

Hong Xu, Xingkai Zeng, Xuecheng Wei, Zhongfeng Xue, Naiwen Chen, Wei Zhu, Wenhua Xie, and Yi He

Research Article (11 pages), Article ID 9325973, Volume 2022 (2022)

Hindawi
Oxidative Medicine and Cellular Longevity
Volume 2023, Article ID 4365895, 12 pages
https://doi.org/10.1155/2023/4365895

Research Article

Diabetes-Induced Autophagy Dysregulation Engenders Testicular Impairment via Oxidative Stress

Renfeng Xu,[1] Fan Wang,[2] Zhenghong Zhang,[1] Yan Zhang,[1] Yedong Tang,[1,3] Jingjing Bi,[3] Congjian Shi,[1] Defan Wang,[3] Hongqin Yang,[1] Zhengchao Wang,[1] and Zonghao Tang[4,5]

[1]*Key Laboratory of Optoelectronic Science and Technology for Medicine of Ministry of Education, Provincial Key Laboratory for Developmental Biology and Neurosciences, College of Life Sciences, Fujian Normal University, Fuzhou 350007, China*
[2]*Provincial University Key Laboratory of Sport and Health Science, School of Physical Education and Sport Sciences, Fujian Normal University, Fuzhou 350007, China*
[3]*Fujian Provincial Key Laboratory of Reproductive Health Research, School of Medicine, Xiamen University, Xiamen 361102, China*
[4]*Drug Discovery Research Center, Key Laboratory of Medical Electrophysiology, Ministry of Education, Department of Pharmacology, School of Pharmacy, Southwest Medical University, Luzhou 646000, China*
[5]*Cedars-Sinai Medical Center, Los Angeles 90048, USA*

Correspondence should be addressed to Zhengchao Wang; zcwang@fjnu.edu.cn and Zonghao Tang; tangzonghao@163.com

Received 24 May 2022; Revised 1 November 2022; Accepted 24 November 2022; Published 3 February 2023

Academic Editor: Chen-he Zhou

Testes produce sperms, and gamete generation relies on a proper niche environment. The disruption of hierarchical regulatory homeostasis in Leydig or Sertoli cells may evoke a sterile phenotype in humans. In this study, we recapitulated type 2 diabetes mellitus by using a high-fat diet- (HFD-) fed mouse model to identify the phenotype and potential mechanism of diabetes-induced testicular impairment. At the end of the study, blood glucose levels, testosterone structure, testicular antioxidant capacity, and testosterone level and the expression of hypoxia-inducible factor- (HIF-) 1α, apoptosis-related protein cleaved-caspase3, and autophagy-related proteins such as LC3I/II, p62, and Beclin1 were evaluated. We found that long-term HFD treatment causes the development of diabetes mellitus, implicating increased serum glucose level, cell apoptosis, and testicular atrophy ($P < 0.05$ vs. Ctrl). Mechanistically, the results showed enhanced expression of HIF-1α in both Sertoli and Leydig cells ($P < 0.05$ vs. Ctrl). Advanced glycation end products (AGEs) were demonstrated to be a potential factor leading to HIF-1α upregulation in both cell types. In Sertoli cells, high glucose treatment had minor effects on Sertoli cell autophagy. However, AGE treatment stagnated the autophagy flux and escalated cell apoptosis ($P < 0.05$ vs. Ctrl+Ctrl). In Leydig cells, high glucose treatment was adequate to encumber autophagy induction and enhance oxidative stress. Similarly, AGE treatment facilitated HIF-1α expression and hampered testosterone production ($P < 0.05$ vs. Ctrl+Ctrl). Overall, these findings highlight the dual effects of diabetes on autophagy regulation in Sertoli and Leydig cells while imposing oxidative stress in both cell types. Furthermore, the upregulation of HIF-1α, which could be triggered by AGE treatment, may negatively affect both cell types. Together, these findings will help us further understand the molecular mechanism of diabetes-induced autophagy dysregulation and testicular impairment, enriching the content of male reproductive biology in diabetic patients.

1. Introduction

The rising incidence of male infertility has become a global issue in recent decades. Like the increase in many cancer cases, the causes of this outcome are multifactorial, including workplace exposure [1], environmental change [2], drug intake [3], and lifestyle factors [4]. Among these, it has been accepted that the loss of dietary control and its derivate fat and type 2 diabetes mellitus (T2DM) are major factors that engender male infertility [5]. Even several studies have linked the association between T2DM and male infertility, but the underlying mechanisms remain unclear.

Testes are the sites where sperms are produced. The spermatogenic process requires the Sertoli cells, which

nourish spermatocytes [6], and Leydig cells, which regulate the Sertoli cell function by producing testosterone [7]. Several studies have demonstrated that the disorder of metabolism in Sertoli cells and the increased apoptosis in Leydig cells contribute to the testicular structure alteration in diabetics [8, 9]. Oxidative stress contributes to the development of diabetic complications [10]. Simultaneously, oxidative stress is one of the leading causes of male infertility [11]. Numerous studies have shown that oxidative stress can induce blood-testis barrier (BTB) damage by mediating a series of intracellular signaling pathways, such as activating the p38/MAPK pathway [12, 13]. In addition, sperm are particularly susceptible to oxidative stress, with low levels of reactive oxygen species (ROS) playing an essential role in spermatogenesis. However, excess ROS can lead to oxidative damage to sperm, including reduced sperm concentration and motility and reduced fertilization [14]. Mammalian cells have developed several strategies to counteract ROS. On the one hand, ROS could be enzymatically quenched by superoxide dismutase (SOD), catalase (CAT), and glutathione peroxidase (GPX). On the other hand, ROS can be balanced by removing ROS origins, including impaired mitochondria and redundant protein aggregations, by autophagy [15, 16]. In the testes, autophagy plays an essential role in the Sertoli cell function, especially in the assembly of ectoplasmic specialization [17]. Similarly, autophagy is involved in testosterone production by facilitating cholesterol uptake [18]. It is noteworthy that abnormal regulation of autophagy is also a contributor to impaired testicular functions, and this phenomenon has been detected in several diabetic animal models [19–21], highlighting the potential role of autophagy in diabetes-induced testicular pathogenesis. However, many of these studies evaluated the change of autophagy levels at the whole testicular level and did not discriminate between different cell types in the testes, which may cause the unspecificity or inaccuracy of conclusions.

Autophagy, an evolutionarily conserved self-degradation mechanism, affects cellular metabolism and may help balance stress-induced functional disorders [22–24]. Autophagy levels vary in different statuses and could be regulated by many stresses or metabolism-related signaling pathways. For example, autophagy could be induced under serum disruption via Akt/mTOR pathway and hypoxia in a HIF-1α-dependent manner [25, 26]. Previous investigations have established that diabetic context can exacerbate the homeostasis of HIF-1α content in several organs of diabetic patients, which enables the progression of diabetic complications. In the male testes, an increase of HIF-1α is linked to the pathogenesis of varicocele [27]. HIF-1α is also necessarily required for the process of spermatogenesis [28]. Based on our knowledge, no studies have evaluated the role of HIF-1α in diabetes-induced testicular dysfunction. Furthermore, it is known that advanced glycation end products (AGEs) exert a regulatory role on HIF-1α expression in Leydig cells [29], but its pathological effects remain poorly understood.

In the present study, we constructed a high-fat diet-fed mouse model to understand the influences of diabetes on testicular morphology and implicated mechanisms, since previous studies have shown that diabetes can cause testicular damage, even infertility, but the underlying mechanism is not clear. The data showed that diabetes could drive the alteration of normal testicular morphology and disrupt the balance of cellular oxidative status. We also showed that the dimorphic manipulation of autophagic status in Sertoli and Leydig cells may drive the progression of testicular pathogenesis in diabetic mice. Collectively, these findings will contribute to our further understanding of the molecular mechanisms of diabetes-induced autophagy dysregulation and oxidative stress leading to testicular damage and further enrich the content of male reproductive biology in diabetic patients, providing a theoretical basis for subsequent studies.

2. Materials and Methods

2.1. Animals. All male C57/BL6J mice (4 weeks) were purchased from Wushi Experimental Animal Supply Co. Ltd. (Fuzhou, China). The animals were maintained under a 14 h and 10 h light-dark schedule with a continuous supply of chow and water. The high-fat diet (HFD) contained 58% lard oil, 25.6% carbohydrate, and 16.4% protein, while the normal control diet (NCD) contained 11.4% fat, 62.8% carbohydrate, and 25.8% protein [30]. The mice were randomly divided into two groups ($n = 10$/group) and were fed with either NCD or HFD for 8 weeks. The testes were then excised for further analysis. The Institutional Animal Care and Use Committee and the Ethics Committee on Animal Experimentation at Fujian Normal University approved the experimental protocol. All efforts were made to minimize animal discomfort and to reduce the number of animals used.

2.2. Immunofluorescent Staining. The testes were fixed in 10% neutral formalin for 48 h at 23 ∘ C ± 2 ∘ C. After fixation, these testes were embedded in paraffin, and 5 μM sections were cut and mounted on slides. For immunofluorescent (IF) staining, the sections were dried, dewaxed, and rehydrated, followed by antigen retrieval with citrate buffer solution (pH 6.0). The sections were then incubated with anti-LC3 antibody (1 : 200 dilution) and anti-p62 antibody (1 : 200 dilution) overnight at 4°C. Goat serum (Boster Biological Technology, Wuhan) was used as negative control instead of a primary antibody. After washing with PBS, sections were incubated with secondary antibody (A20204 or A20206, Invitrogen, Carlsbad, CA) at RT for 1 h. Finally, the sections were counterstained with 4′,6-diamidino-2-phenylindole (DAPI) and mounted with coverslips.

2.3. Western Blotting. The testes were removed from mice with great care, followed by subcomponent isolation. Briefly, Leydig cells were isolated using a 70 μM cell strainer after the disruption of the tunica albuginea. Seminiferous tubules were collected and minced and then subjected to EDTA (pH 7.4) treatment to remove peritubular cells to purify Sertoli cells. The tubular pellet was digested with collagenase for 10 min at 37°C to remove the germinal cells. The Sertoli cell suspension was collected by centrifugation at 300 × g for 5 min. The Leydig and Sertoli cells were lysed using ice-

cold RIPA buffer supplemented with protease inhibitors (protease inhibitor cocktail, Beyotime Institute of Biotechnology, Haimen, SU) for protein extraction. Protein concentrations were determined using the BCA Kit (Beyotime Institute of Biotechnology, Haimen, SU) with bovine serum albumin standards. Subsequently, 40 μg protein samples were loaded onto SDS-PAGE gel and separated by electrophoresis. The membranes were blocked by 5% skimmed milk, followed by primary antibody incubation at 4°C overnight (Supplementary Table 1). After washing, the membranes were incubated with horseradish peroxidase-conjugated goat antirabbit or mouse IgG (1 : 1000 dilution, Beyotime Institute of Biotechnology, Haimen, SU) for 1 h at RT. Eventually, the bands were visualized by enhanced chemiluminescence star (ECL, Beyotime Institute of Biotechnology, Haimen, SU). The bands were quantified using the ImageJ 1.49 software (National Institutes of Health, Bethesda, MD).

2.4. ROS Detection. For tissular detection, the testes were removed and dissociated according to the protocol in a previous study [31]. After centrifugation, the cells were homogenized in lysis buffer (250 mM sucrose, 20 mM HEPES-NaOH, pH 7.5, 10 mM KCl, 1.5 mM MgCl2, 1 mM EDTA, 1 mM EGTA, and protease cocktail inhibitor) [32], and the supernatants were collected by centrifugation at 10,000 × g, 4°C for 5 min. The mixes were suspended in HBSS containing dichlorodihydrofluorescein diacetate (DCFH-DA) (Jiancheng Biotech Institute, Nanjing, SU). Then, the mixes were incubated at 37°C for 30 min in the dark. The fluorescence of DCF was measured using a microplate reader at an excitation wavelength of 488 nM and an emission wavelength of 535 nM. The intracellular ROS level was measured using a commercial kit (Beyotime Institute of Biotechnology, Haimen, SU). Briefly, cells were washed with cold PBS and then incubated with DCFH-DA at 37°C for 20 min. Subsequently, cells were washed with PBS before measurement, and a microplate reader was used to determine the DCF fluorescence of 20,000 cells at an excitation wavelength of 488 nM and an emission wavelength of 535 nM.

2.5. Detection of Oxidative Stress Markers. SOD, GPX, and CAT were detected in testicular tissues using commercial kits (Jiancheng Bioengineering Institute, Nanjing, SU) according to the manufacturer's instructions.

2.6. Immature Sertoli Cell Culture. According to a previous study, three-week-old mice were used for Sertoli cell extraction [31]. Briefly, the testes were removed and decapsulated before Sertoli cell isolation. Then, the testes were digested with 0.1% collagenase (SCR103, Sigma) in HBSS (14025092, Gibco) for 10 min in a 37°C incubator. During digestion, the tube was gently shaken to promote tissue dispersing. The suspension was then filtered through a 70 μM filter. Seminiferous tubules were collected and minced, followed by EDTA (pH 7.4) treatment to remove the peritubular cells. Afterward, the germinal cells were removed by digesting the tubular pellet with collagenase for 10 min at 37°C. The suspension of Sertoli cells was collected by sedimentation and then resuspended in a Sertoli cell culture medium (4521, ScienCell).

2.7. Mitochondria Isolation. The mitochondria were isolated using a commercial kit (C3601, Beyotime Institute of Biotechnology, Haimen, SU) to detect the level of cytosolic cytochrome C. Briefly, after the isolation, cells were washed with chilled PBS and then centrifuged at 600 × g to obtain the pellet. The pellet was resuspended in the isolation reagent with PMSF, followed by pipetting up and down several times and incubation on ice for 15 min. It was then centrifuged at 600 × g, 4°C for 10 min. Subsequently, the resulting pellet was transferred into a new tube and centrifuged at 10,000 × g, 4°C for 10 min. Finally, the supernatant was collected for Western blotting analysis.

2.8. Statistical Analysis. All data are presented as means ± SD . The significant differences within or between groups were evaluated by a one-way analysis of variance, followed by Tukey's multiple range test. Statistical analysis was conducted using SPSS version 20 software, and $P < 0.05$ was recognized as a statistically significant difference.

3. Results

3.1. Diabetes Induces Testicular Apoptosis and Structural Atrophy. To model T2DM, the mice were fed HFD for 8 weeks. Expectedly, HFD-treated mice showed T2DM phenotypes, including the fortified gain of body weight (Figure 1(a)) and escalated serum glucose (Figure 1(b)). In addition, the testes from HFD-treated mice exhibited diminished size and weight compared to those of the control, suggesting the atrophy of the testes (Figure 1(c)). Morphologically, the diabetic testes showed chaotic structural organization and curtailed size of seminiferous tubule (Figure 1(d)). We, therefore, wondered if diabetes drives testicular apoptosis and thus detected the expression of apoptotic marker cleaved caspase-3, which showed a palpable enhancement in diabetic mice (Figure 2(a)). This result was further validated by Western blotting (Figure 2(b)). These results suggested that HFD enabled the development of T2DM phenotype, accompanied by increased cellular apoptosis and atrophy of testicular structure.

3.2. Diabetes Has Dual Effects on Autophagy Regulation in Sertoli and Leydig Cells. As autophagy is a mechanism for ectoplasmic specialization in Sertoli cells [17] and steroidogenesis in Leydig cells [18], we next detected the autophagy-related markers LC-3I/II, p62, and Beclin1 by IF staining. Interestingly, the expression changes of LC-3I/II, p62, and Beclin1 exhibited divergent trends in Sertoli cells and Leydig cells. Briefly, the level of LC-3I/II and Beclin1 was increased in Sertoli cells while it decreased in Leydig cells (Figure 3(a)). Meanwhile, we noticed the concomitant increase of p62 in diabetic mice (Figure 3(a)), suggesting the disordered autophagy regulation in both cell types. The results of AO staining also confirmed this conclusion (Supplementary Figure 2). To further verify this result, we isolated Sertoli and Leydig cells and proved that our separation was successful by identifying the respective

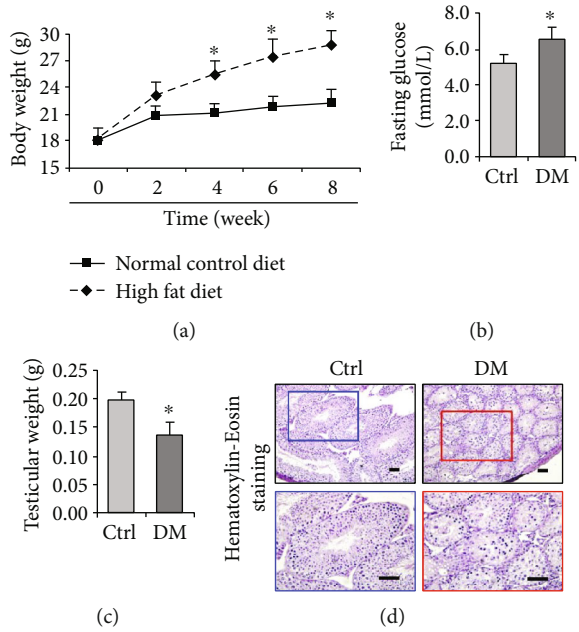

FIGURE 1: Changes of testicular weight and histology in diabetic mice induced by high-fat diet. (a) The growth curve of mice fed with normal control diet or high-fat diet. (b) Effect of diabetes on fasting glucose. (c) Effect of diabetes on testicular weight. (d) Effect of diabetes on testicular histology. The testicular morphology of diabetic mice was impaired, with disordered arrangement of spermatocytes observed by H&E staining. DM: diabetes mellitus. $P < 0.05$ was considered to indicate a statistically significant difference. Bar = 100 μm. $^*P < 0.05$ vs. Ctrl.

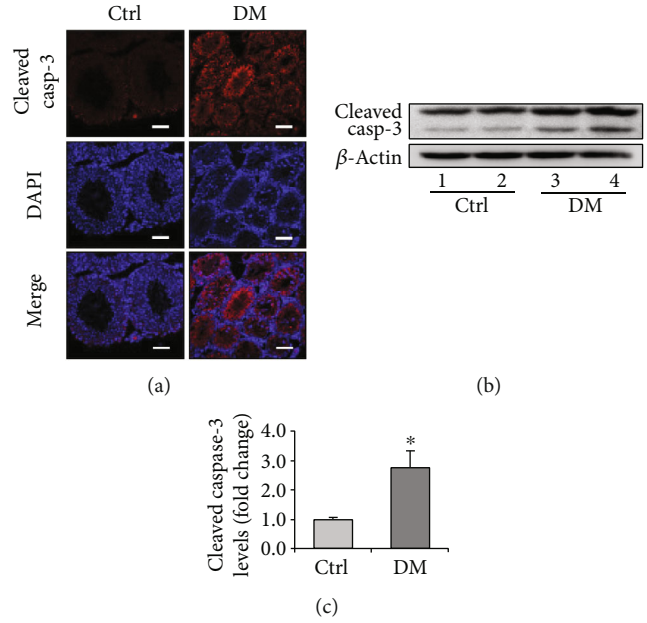

FIGURE 2: Expression of cell apoptosis marker, cleaved caspase-3, in the testis of diabetic mice. (a) The immunofluorescent staining of cleaved caspase-3 in the mouse testis. (b) Representative immunoblotting of cleaved caspase-3. (c) Densitometric qualification of cleaved caspase-3. DM: diabetes mellitus. $P < 0.05$ was considered to indicate a statistically significant difference. Bar = 100 μm. $^*P < 0.05$ vs. Ctrl.

specific markers of Sertoli and Leydig cells (Supplementary Figure 1) and then detected the contents of LC-3I/II, p62, and Beclin1 by Western blotting. Consistently, we observed the augmentation of LC-3I/II, p62, and Beclin1 expression levels in Sertoli cells (Figures 3(b) and 3(c)) while decreased levels of LC-3II and Beclin1 in Leydig cells (Figures 3(d) and 3(e)). These findings indicated that diabetes exerts dimorphic roles during autophagy regulation in Sertoli and Leydig cells.

3.3. Induction of Autophagy Attenuates High Glucose-Induced Oxidative Stress in Leydig Cells. Considering the significant

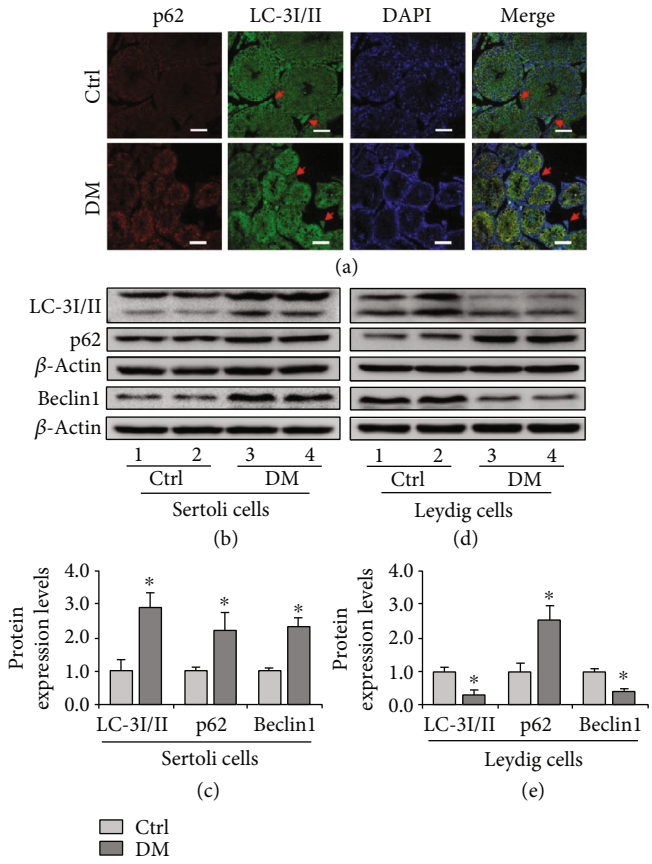

Figure 3: Expression of LC-3I/II, p62, and Beclin1 in the testicular cells *in vivo* and *in vitro*. (a) The immunofluorescent staining of p62 and LC-3I/II in the testis of diabetic mice. Red arrow indicates Leydig cells. (b) Representative immunoblotting of LC-3I/II, p62, and Beclin1 in Sertoli cells. (c) Densitometric qualification of LC-3II, p62, and Beclin1 in Sertoli cells. (d) Representative immunoblotting of LC-3I/II, p62, and Beclin1 in Leydig cells. (e) Densitometric quantification of LC-3II, p62, and Beclin1 in Leydig cells. Diabetes exerts dual effects on autophagy regulation in Sertoli and Leydig cells. DM: diabetes mellitus. $P < 0.05$ was considered to indicate a statistically significant difference. Bar = 100 μm. $^*P < 0.05$ vs. Ctrl.

apoptosis and autophagy observed in Leydig cells of the diabetic testes, we wondered how autophagy plays a role in Leydig cells' survival. Because autophagy is tightly associated with mitochondrial homeostasis and oxidative stress, we detected the level of cytochrome C in the cytoplasm (Cyto-cyc) of Leydig cells. When compared with that of the control, an increase in Cyto-cyc content was observed in diabetic mice (Figures 4(a) and 4(b)), accompanied by the increase of ROS (Figure 4(c)) and the mitigation of GPX and CAT (Figures 4(e) and 4(f)). However, we did not observe the palpable change of SOD in Leydig cells (Figure 4(d)). *In vitro*, we found that high glucose (HG) can induce the upregulation of Cyto-cyc (Figures 5(a) and 5(b)) and ameliorate LC-3II (Figures 5(a) and 5(c)). Nevertheless, rapamycin, an autophagy inducer, partially deregulated the effect of HG on Leydig cells (Figures 5(a) and 5(c)). Furthermore, we found that HG decreased cell viability, whereas rapamycin partially protected the cells (Supplementary Figure 3A). Meanwhile, the induction of autophagy attenuated the increase of ROS induced by HG (Figures 5(a) and 5(d)). These findings suggested that HG is implicated in the oxidative stress of Leydig cells via inhibition of autophagy, and induction of autophagy can partially rescue this phenotype.

3.4. HIF-1α /BNIP3 Pathway May Be Involved in the Autophagy Regulation in Sertoli Cells. Considering the divergent phenotypes in terms of autophagy regulation in Leydig and Sertoli cells, we explored the potential regulation of autophagy induction in Sertoli cells. Therefore, the levels of the predominant autophagy regulator p-Akt and its downstream effector p-P70S6K were detected in Sertoli cells. The results indicated the concomitant upregulation of both proteins (Figures 6(a)–6(d)), suggesting that the Akt pathway may be involved in autophagy regulation in Sertoli cells. HIF-1α is essential in autophagy regulation, especially under hypoxic or oxidative contexts. We showed that, similar to many other diabetic organs, diabetes increased the expression of HIF-1α in Sertoli cells (Figures 6(c) and 6(d)). Interestingly, even though diabetic mice exhibited significant formation of BNIP3 homodimer (Figures 6(e) and 6(f)), we did not observe the concomitant upregulation of BNIP3 monomer (Figures 6(e) and 6(f)). Because BNIP3 homodimerization is an important step for mitophagy initiation, we separated the mitochondrial component and detected the expression changes of both dimer and monomer forms of BNIP3 (Figure 6(g)). Both cytoplasmic and mitochondrial components consistently showed increased homo-BNIP3 (Figures 5(g) and 5(h)), while mono-BNIP3

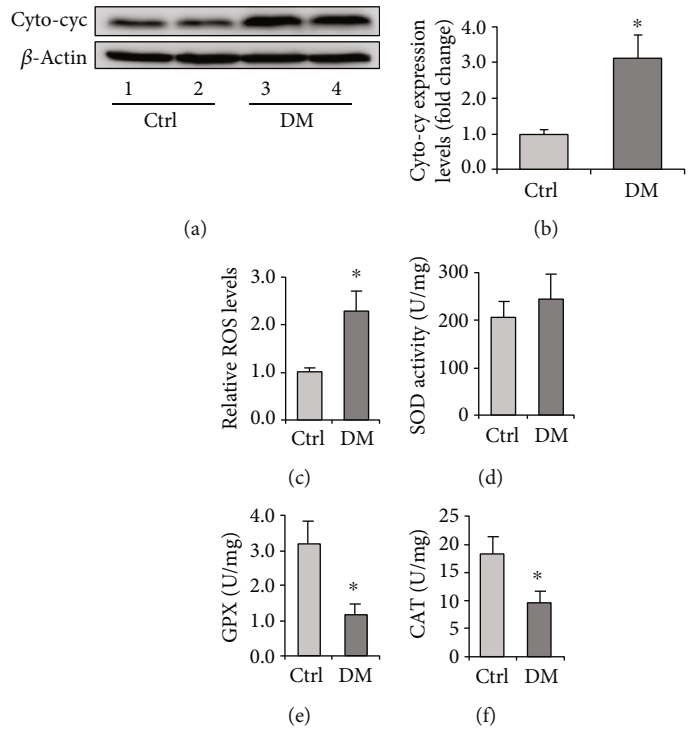

Figure 4: Expression of oxidative stress-related marker proteins in the diabetic testis and Leydig cells. (a) Representative immunoblotting of Cyto-cyc in the testis of diabetic mice. (b) Densitometric qualification of Cyto-cyc in the testis of diabetic mice. (c) Relative ROS levels in the testis of diabetic mice. (d) SOD activity in the testis of diabetic mice. (e) GPX content in the testis of diabetic mice. (f) CAT content in the testis of diabetic mice. DM: diabetes mellitus; Rap: rapamycin; HG: high glucose. $P < 0.05$ was considered to indicate a statistically significant difference. $^{*}P < 0.05$ vs. Ctrl.

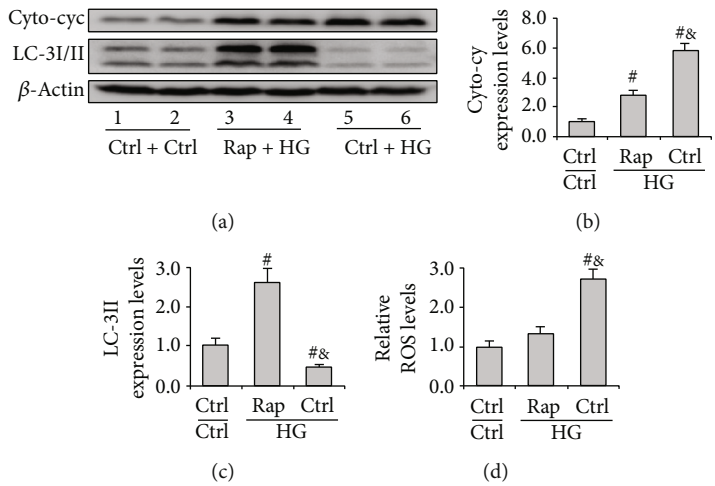

Figure 5: Expression of Cyto-cyc and LC-3 proteins in the diabetic testis and Leydig cells. (a) Representative immunoblotting of Cyto-cyc and LC-3I/II in Leydig cells treated with Rap and HG. (b) Densitometric qualification of Cyto-cyc in Leydig cells treated with Rap and HG. (c) Densitometric qualification of LC-3II in Leydig cells treated with Rap and HG. (d) Relative ROS levels in Leydig cells treated with Rap and HG. DM: diabetes mellitus; Rap: rapamycin; HG: high glucose. $P < 0.05$ was considered to indicate a statistically significant difference. $^{\#}P < 0.05$ vs. Ctrl+Ctrl. $^{\&}P < 0.05$ vs. Rap+HG.

remained unchanged in the cytoplasm (Figure 5(g)). These findings suggested that HIF-1α may be involved in mitophagy regulation by promoting the formation of BNIP3 homodimerization.

3.5. AGEs Promote Oxidative Stress in Sertoli Cells by Enhancing HIF-1α-Mediated Autophagy. To explore the causative factors for autophagy induction, we treated Sertoli cells with HG and AGEs, a nonenzymatic product of glucose

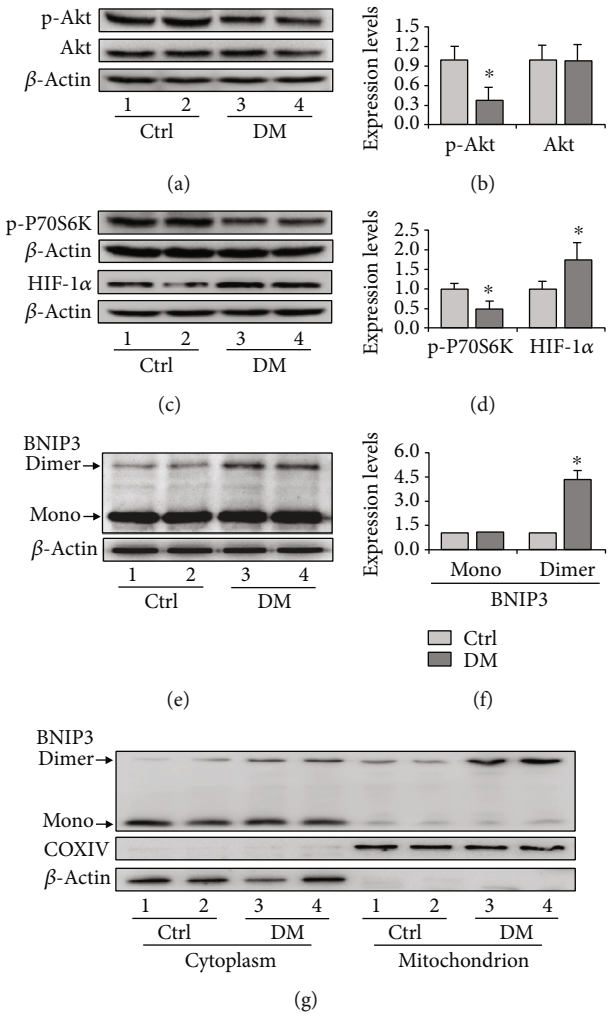

Figure 6: Activation of HIF-1α pathway in Sertoli cells of diabetic mice. (a) Representative immunoblotting of Akt and p-Akt in the testis of diabetic mice. (b) Densitometric qualification of Akt and p-Akt in the testis of diabetic mice. (c) Representative immunoblotting of p-P70S6K and HIF-1α in the testis of diabetic mice. (d) Densitometric qualification of p-P70S6K and HIF-1α in the testis of diabetic mice. (e) Representative immunoblotting of dimer and monomer BNIP3 in the testis of diabetic mice. (f) Densitometric qualification of dimer and monomer BNIP3 in the testis of diabetic mice. (g) Representative immunoblotting of dimer and monomer BNIP3 in the cytoplasm and mitochondrion. DM: diabetes mellitus. $P < 0.05$ was considered to indicate a statistically significant difference. $^*P < 0.05$ vs. Ctrl.

and proteins. The results indicated that the effects of HG on HIF-1α, LC-3II, and p62 expression were not apparent (Figures 7(a)–7(c)). However, AGEs significantly intensified the expression of HIF-1α, LC-3II, p62, and Beclin1 (Figures 7(a)–7(c)), suggesting a positive role of AGEs in autophagy regulation. The increase of p62 indicated a decrease in autophagy flux in Sertoli cells. Furthermore, Chloroquine, an autophagy inhibitor, partially abolished the effect of AGEs on Sertoli cells, and the expression of HIF-1α was also relatively reduced (Supplementary Figure 4). Moreover, we found that AGEs decreased cell viability while chloroquine partially protected cells (Supplementary Figure 3B). To further confirm the role of HIF-1α in AGE-induced autophagy, we treated the cells with Px478 to inhibit HIF-1α expression and observed the concomitant decrease of LC-3II (Figures 8(a) and 8(b)), suggesting a positive role for HIF-1α in autophagy regulation.

We also detected the effects of HG and AGEs on the apoptosis of Sertoli cells (Figures 7(a) and 7(c)). Comparatively, AGEs led to an apparent increase of cleaved caspase-3 expression (Figures 7(a) and 7(c)), while this effect could be partially reversed by HIF-1α inhibition (Figures 8(a), 8(c), and 8(d)). When measuring the level of ROS, we observed concomitant mitigation after Px478 treatment (Figure 8(e)). These results suggested that AGEs significantly contribute to enhanced autophagy levels and aggravate oxidative stress in Sertoli cells.

3.6. Upregulation of HIF-1α Ameliorates Testosterone Production in Leydig Cells. A previous study demonstrated the stable expression of HIF-1α in Leydig cells and its function as a crucial regulator of steroidogenesis [33]. However, how HIF-1α is regulated and its role in testosterone production remains unknown. In the present study, an improvement of HIF-1α content was detected in Leydig cells of

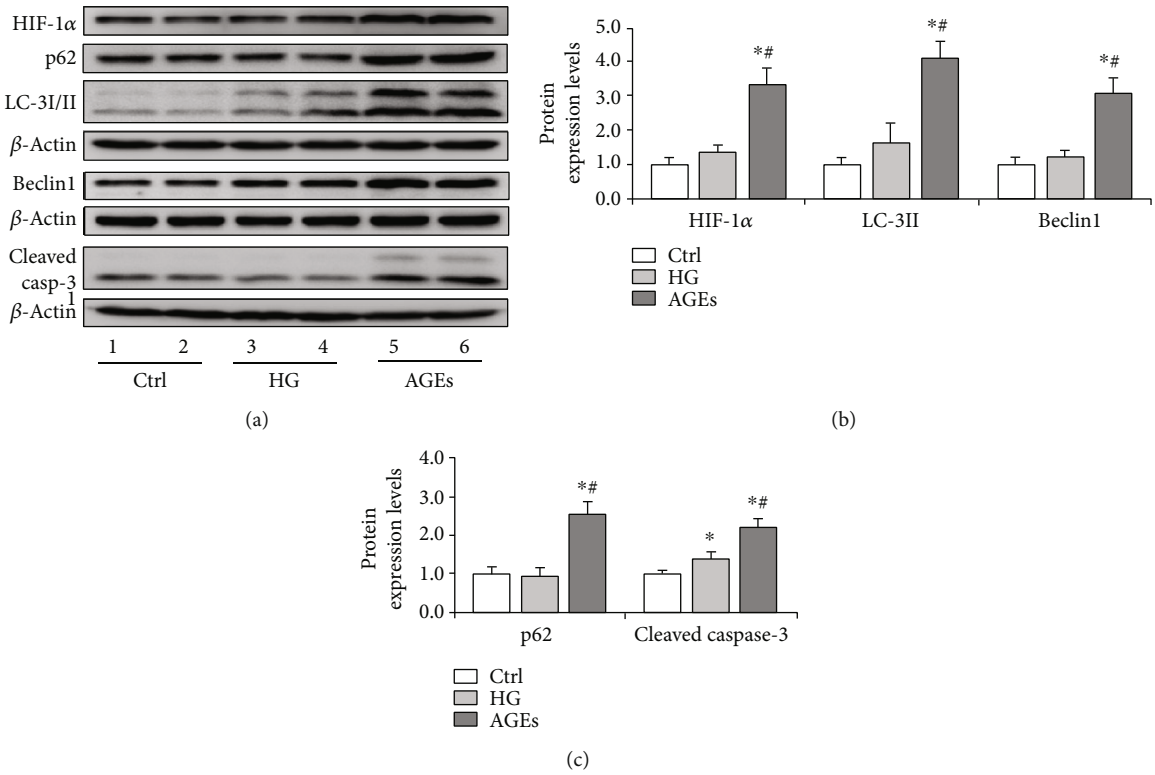

Figure 7: Expression of HIF-1α, LC-3I/II, p62, and cleaved caspase-3 during AGE-induced oxidative stress in Sertoli cells. Sertoli cells were treated with HG (20 mM) or AGEs (100 μg/ml) for 72 h. AGEs aggravated HIF-1α expression and induced autophagy dysregulation. (a) Representative immunoblotting of HIF-1α, LC-3I/II, p62, Beclin1, and cleaved caspase-3 in Sertoli cells treated with HG and AGEs. (b) Densitometric qualification of HIF-1α, LC-3II, and Beclin1 in Sertoli cells treated with HG and AGEs. (c) Densitometric qualification of p62 and cleaved caspase-3 in Sertoli cells treated with HG and AGEs. $P < 0.05$ was considered to indicate a statistically significant difference. $^{*}P < 0.05$ vs. Ctrl. $^{\#}P < 0.05$ vs. HG.

diabetic mice (Figures 9(a) and 9(b)). Additionally, AGEs enabled the upregulation of HIF-1α, indicating a potential regulatory effect on HIF-1α expression (Figures 9(d) and 9(e)). Consistent with preceding results, diabetic mice exhibited downregulation of serum testosterone content (Figure 9(c)), and this effect could be recapitulated by AGEs treatment *in vitro* (Figure 9(f)). However, inhibition of HIF-1α attenuated the decrease in testosterone production (Figure 9(f)). These findings suggested that AGEs can induce HIF-1α expression, and this enhanced HIF-1α expression is associated with lowered testosterone levels.

4. Discussion

In this study, we investigated the role of autophagy in diabetes-induced testicular impairment and demonstrated that diabetes disrupted testicular structure and exerted dual effects on autophagy regulation in Sertoli and Leydig cells. Nevertheless, the autophagy dysregulation in both cell types contributed to skewed-oxidative homeostasis. Our results also suggested that enhanced HIF-1α expression is a driving force for autophagy in Sertoli cells and promotes oxidative stress in Leydig cells in an autophagy-independent manner.

Diabetes is an important causative factor for hormonal dysregulation, testicular impairment, and male infertility. Sertoli and Leydig cells are the major components of the testis, and they are, respectively, involved in sperm maturation and testosterone production. Sertoli cells are also required to form BTB to prevent the invasion of extracellular material into the intratubular fluid. Previous investigations have demonstrated the deleterious effect of diabetes on the integrity of BTB [34]. Similarly, the diabetic context can drive the change of the ultrastructure of Leydig cells and facilitate cell apoptosis [35]. However, most of these studies adopted a streptozotocin-induced mouse model, which is different from the pathological process. In the present study, we constructed a diabetic model by HFD feeding of rats and observed the increase of cell apoptosis, the loss of testicular architecture, and the atrophy of the testes. These findings are consistent with those from streptozotocin-induced diabetic mice, which validated the role of diabetes in male infertility.

Although several lines of evidence have confirmed the effect of diabetes on testicular damage, the mechanism remains elusive. It has been reported that the disruption of the microvascular system induced by Akt downregulation is one of the impactors of testicular impairment, and this effect could be recapitulated by HG treatment [36].

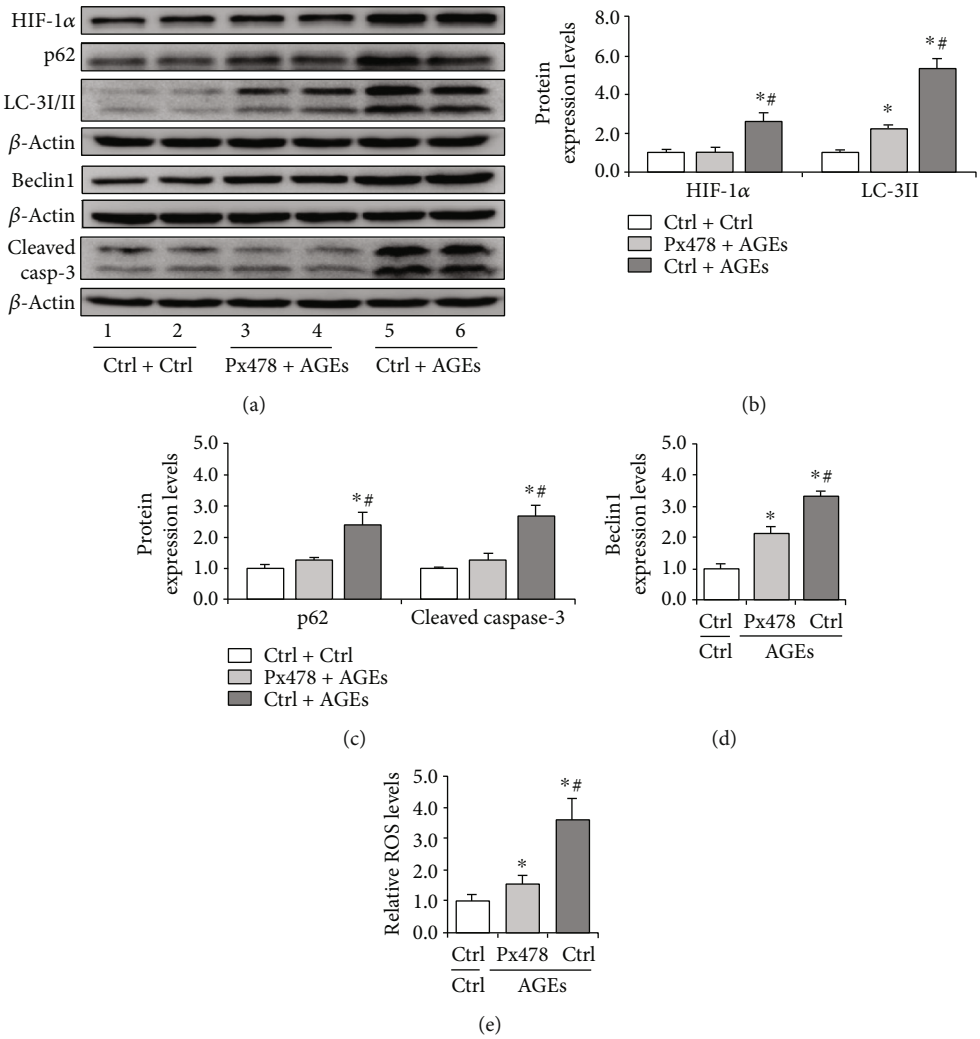

Figure 8: Effect of Px478 on HIF-1α, LC-3I/II, p62, and cleaved caspase-3 expression during AGE-induced oxidative stress in Sertoli cells. The cells were treated with AGEs (100 μg/ml) for 72 h, and Px478 (20 μM) was added 16 h before harvesting. (a) Representative immunoblotting of HIF-1α, LC-3I/II, p62, Beclin1, and cleaved caspase-3 in Sertoli cells treated with Px478 and AGEs. (b) Densitometric qualification of HIF-1α, LC-3II, and Beclin1 in Sertoli cells treated with Px478 and AGEs. (c) Densitometric qualification of p62 and cleaved caspase-3 in Sertoli cells treated with Px478 and AGEs. (d) Relative ROS levels in Sertoli cells treated with Px478 and AGEs. $P < 0.05$ was considered to indicate a statistically significant difference. $^{*}P < 0.05$, vs. Ctrl+Ctrl. $^{\#}P < 0.05$, vs. Px478+AGEs.

Autophagy is a stress-driven, self-degradation mechanism that is initiated under unfavorable conditions. The dysregulation of autophagy is a hallmark of many human diseases, especially cancer [37] and degradative diseases, including Alzheimer's disease [38]. Predominantly, the essential contribution of autophagy in testicular function has also been evaluated in several publications. However, the pathological function of autophagy under diabetic conditions has not been investigated yet. In our study, through IF staining and Western blot of autophagy-related proteins and AO staining, we found that diabetes plays dimorphic roles in autophagy regulation, promoting autophagy in Sertoli cells while inhibiting autophagy in Leydig cells. Nevertheless, both effects undermine cell functions.

Extensive research data suggest that ROS contribute to glucolipotoxicity in diabetes, leading to cellular and tissue dysfunction and damage [39]. Indeed, high ROS production, low ATP levels, and mitochondrial dysfunction are hallmarks of type 2 diabetes [40]. The increased oxidative stress has been confirmed in many diabetic tissues and detected in the testes [41, 42]. So far, compelling evidence has verified the decrease of testosterone in diabetic patients [43], and oxidative stress is detrimental to Leydig cell functions [44]. However, how diabetes drives oxidative stress and its phenotype has not been uncovered. Studies have shown that the overproduction of ROS caused by T1DM activates apoptotic signaling pathways in supporting cells, ultimately affecting the survival of these cells [45]. We mainly studied the effect of ROS excess caused by T2DM on Sertoli and Leydig cells. Our results indicated that diabetes induced an appreciable release of Cyto-cyc in Leydig cells, which was consistent with the increase of ROS and the downregulation of GPX and

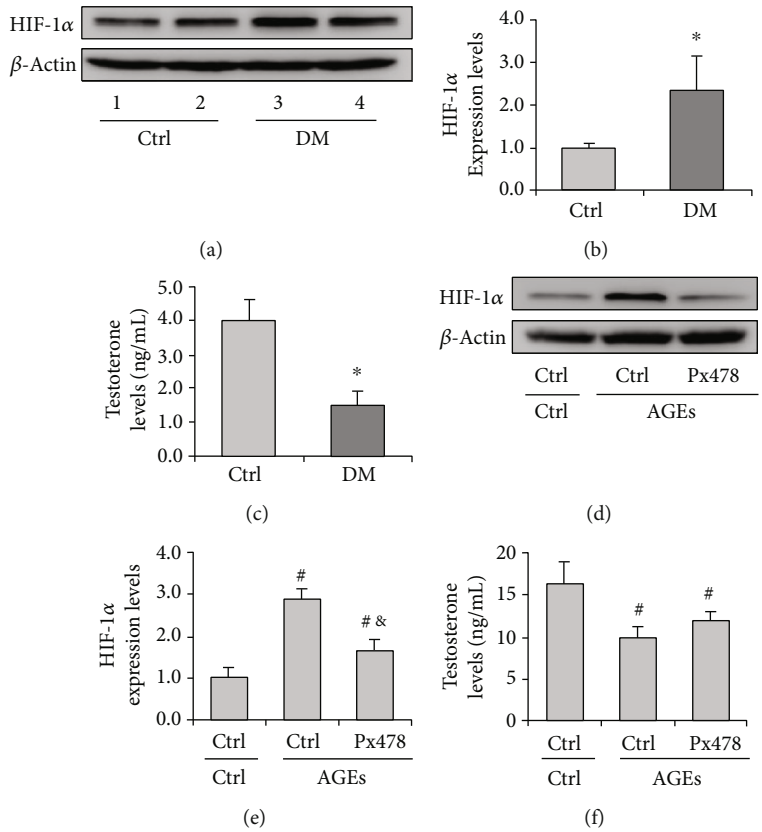

Figure 9: Expression of HIF-1α in the diabetic testis and Leydig cells. Leydig cells were treated with AGEs (100 μg/ml) for 72 h, and Px478 was added 16 h before harvesting. (a) Representative immunoblotting of HIF-1α in the testis of diabetic mice. (b) Densitometric qualification of HIF-1α in the testis of diabetic mice. (c) Serum testosterone level in diabetic mice. (d) Representative immunoblotting of HIF-1α in Leydig cells treated with Px478 and AGEs. (e) Densitometric qualification of HIF-1α in Leydig cells treated with Px478 and AGEs. (f) Testosterone level in supernatant of Leydig cells treated with Px478 and AGEs. $P < 0.05$ was considered to indicate a statistically significant difference. $^{*}P < 0.05$ vs. Ctrl. $^{\#}P < 0.05$ vs. Ctrl+Ctrl. $^{\&}P < 0.05$, vs. Px478+AGEs.

CAT, indicating mitochondrial balance and oxidative stress. The results also showed that HG is a causative factor for attenuated autophagy, and autophagy induction can attenuate the cytochrome C level in the cytoplasm, suggesting a protective role for autophagy in Leydig cell function under diabetic context.

The regulation of autophagy involves a spectrum of signaling pathways. Among these, Akt/mTOR mainly regulates autophagy under serum or glucose starvation. HIF-1α signaling is another pathway that could be activated under hypoxia or oxidative stress condition [46]. In the present study, we observed the amelioration of p-Akt expression and its downstream p-p70s6k in Sertoli cells. Conversely, we found that the level of HIF-1α was upregulated compared with that in the control. BNIP3 is a primary target of HIF-1α to regulate mitophagy in eukaryotes [47], which forms a homodimer to localize on mitochondria and label it for degradation. We found that the diabetic condition drives the formation of dimer-BNIP3 in the mitochondria of Sertoli cells, indicating a positive role for HIF-1α/BNIP3 pathway in autophagy regulation. Nonetheless, when treating Sertoli cells with HG, we did not observe a significant increase in autophagy level, while AGE treatment increased both HIF-1α and LC-3II expression. We also compared the effects of HG and AGEs on the apoptosis of Sertoli cells and found that AGEs can exacerbate caspase-3 cleavage compared to HG. This effect could be partially rescued by HIF-1α inhibition, suggesting that AGEs may regulate autophagy in Sertoli cells by promoting HIF-1α expression. We also showed that AGEs could induce HIF-1α expression in Leydig cells, which is related to attenuated testosterone levels.

5. Conclusion

Our present study showed a dual effect of diabetes on autophagy in Sertoli and Leydig cells, which drives the formation of oxidative stress in both cell types. HIF-1α plays a consistent role in exacerbating oxidative homeostasis in an autophagy-dependent or independent manner. Furthermore, the HFD-fed diabetic mouse model used in the present experiment was more in line with the pathological process of type 2 diabetes and is more helpful for studying type 2 diabetes. Our findings also draw attention to testicular damage in diabetic patients and indicate that HIF-1α inhibitors may become a new direction for research and treatment of diabetes. Although we have confirmed that the HIF-1α signaling plays a role in testicular injury in diabetic mice, further studies are still needed to identify possible HIF-1α

upstream-regulated genes and their downstream target genes to explore whether it regulates or coregulates diabetes-induced autophagy leading to testicular damage.

Data Availability

The original contributions presented in the study are included in the article, and further inquiries can be directed to the corresponding authors.

Conflicts of Interest

The authors declare that they have no competing interests.

Authors' Contributions

The work was conceived by RX, FW, ZZ, ZT, and ZW; the experiments were performed by RX, FW, ZZ, YZ, YT, JB, CS, DW, and HY; the data was analyzed by RX, FW, ZZ, YZ, YT, JB, CS, DW, HY, ZT, and ZW; the draft was written by RX, FW, and ZZ; and the manuscript was revised by ZT and ZW. All authors have reviewed and approved the final version of the manuscript for publication. Renfeng Xu, Fan Wang, and Zhenghong Zhang contributed equally to this work.

Acknowledgments

This work was supported by the Key Projects of Scientific and Technological Innovation in Fujian Province (2021G02021 and 2021G02028), the Special Funds of the Central Government Guilding Local Science and Technology Development (2020 L3008), the Luzhou Science and Technology Bureau (2020-JYJ-37), the Natural Science Foundation of Fujian Province (2020 J01176, 2021 J02028, and 2022 J01172), and the Innovation and Entrepreneurship Project of Fujian Normal University (I202003009 and I202102008).

Supplementary Materials

Figure S1: identification of Sertoli and Leydig cells by cell-specific marker expression. Figure S2: evaluation of changes of autophagy in the testis of diabetic mice by acridine orange staining. Figure S3: effects of autophagy on the cell viability of Sertoli and Leydig cells. Figure S4: effects of chloroquine on the expressions of HIF-1α, LC-3I/II, p62, and cleaved caspase-3 in Sertoli cells. Table S1: antibody information for Western blotting. *(Supplementary Materials)*

References

[1] P. Claman, "Men at risk: occupation and male infertility," *Fertility and Sterility*, vol. 81, pp. 19–26, 2004.

[2] R. M. Sharpe and S. Franks, "Environment, lifestyle and infertility – an inter-generational issue," *Nature Medicine*, vol. 8, no. S10, pp. S33–S40, 2002.

[3] M. Semet, M. Paci, J. Saïas-Magnan et al., "The impact of drugs on male fertility: a review," *Andrology*, vol. 5, no. 4, pp. 640–663, 2017.

[4] G. Homan, M. Davies, and R. Norman, "The impact of lifestyle factors on reproductive performance in the general population and those undergoing infertility treatment: a review," *Human Reproduction Update*, vol. 13, no. 3, pp. 209–223, 2007.

[5] R. P. Hayden, R. Flannigan, and P. N. Schlegel, "The role of lifestyle in male infertility: diet, physical activity, and body habitus," *Current Urology Reports*, vol. 19, no. 7, p. 56, 2018.

[6] L. Zhao, C. Yao, X. Xing et al., "Single-cell analysis of developing and azoospermia human testicles reveals central role of Sertoli cells," *Nature Communications*, vol. 11, p. 5683, 2020.

[7] P. Chen, B. R. Zirkin, and H. Chen, "Stem Leydig cells in the adult testis: characterization, regulation and potential applications," *Endocrine Reviews*, vol. 41, no. 1, pp. 22–32, 2020.

[8] D. Kianifard, R. A. Sadrkhanlou, and S. Hasanzadeh, "The ultrastructural changes of the Sertoli and Leydig cells following streptozotocin induced diabetes," *Iranian Journal of Basic Medical Sciences*, vol. 15, no. 1, p. 623, 2012.

[9] L. Rato, M. G. Alves, A. I. Duarte et al., "Testosterone deficiency induced by progressive stages of diabetes mellitus impairs glucose metabolism and favors glycogenesis in mature rat Sertoli cells," *The International Journal of Biochemistry & Cell Biology*, vol. 66, pp. 1–10, 2015.

[10] O. M. Ighodaro, "Molecular pathways associated with oxidative stress in diabetes mellitus," *Biomedicine & Pharmacotherapy*, vol. 108, pp. 656–662, 2018.

[11] R. J. Aitken and M. A. Baker, "Oxidative stress and male reproductive biology," *Reproduction, Fertility, and Development*, vol. 16, no. 5, pp. 581–588, 2004.

[12] N. Chen, P. Su, M. Wang, and Y. M. Li, "Ascorbic acid inhibits cadmium-induced disruption of the blood-testis barrier by regulating oxidative stress-mediated p38 MAPK pathways," *Environmental Science and Pollution Research International*, vol. 25, no. 22, pp. 21713–21720, 2018.

[13] J. Li, Y. You, P. Zhang et al., "Qiangjing tablets repair of blood-testis barrier dysfunction in rats via regulating oxidative stress and p38 MAPK pathway," *BMC complementary medicine and therapies*, vol. 22, 2022.

[14] S. S. Du Plessis, A. Agarwal, and J. E. Halabi, "Contemporary evidence on the physiological role of reactive oxygen species in human sperm function," *Journal of Assisted Reproduction and Genetics*, vol. 32, no. 4, pp. 509–520, 2015.

[15] R. Kiffin, U. Bandyopadhyay, and A. M. Cuervo, "Oxidative stress and autophagy," *Antioxidants & Redox Signaling*, vol. 8, no. 1-2, pp. 152–162, 2006.

[16] G. Filomeni, D. De Zio, and F. Cecconi, "Oxidative stress and autophagy: the clash between damage and metabolic needs," *Cell Death & Differentiation*, vol. 22, no. 3, pp. 377–388, 2015.

[17] C. Liu, H. Wang, Y. Shang et al., "Autophagy is required for ectoplasmic specialization assembly in Sertoli cells," *Autophagy*, vol. 12, no. 5, pp. 814–832, 2016.

[18] F. Gao, G. Li, C. Liu et al., "Autophagy regulates testosterone synthesis by facilitating cholesterol uptake in Leydig cells," *The Journal of Cell Biology*, vol. 217, no. 6, pp. 2103–2119, 2018.

[19] G.-J. Shi, J. Zheng, X.-X. Han et al., "Lycium barbarum polysaccharide attenuates diabetic testicular dysfunction via inhibition of the PI3K/Akt pathway-mediated abnormal

autophagy in male mice," *Cell and Tissue Research*, vol. 374, no. 3, pp. 653–666, 2018.

[20] Y. Tian, W. Song, D. Xu, X. Chen, X. Li, and Y. Zhao, "Autophagy induced by ROS aggravates testis oxidative damage in diabetes via breaking the feedforward loop linking p62 and Nrf2," *Oxidative Medicine and Cellular Longevity*, vol. 2020, Article ID 7156579, 9 pages, 2020.

[21] Y. Zhao, W. Song, Z. Wang et al., "Resveratrol attenuates testicular apoptosis in type 1 diabetic mice: role of Akt-mediated Nrf2 activation and p62-dependent Keap1 degradation," *Redox Biology*, vol. 14, pp. 609–617, 2018.

[22] Z. Tang, J. Chen, Z. Zhang et al., "HIF-1 _α_ activation promotes luteolysis by enhancing ROS levels in the corpus luteum of pseudopregnant rats," *Oxidative medicine and cellular longevity*, vol. 2021, Article ID 1764929, 11 pages, 2021.

[23] Z. Tang, R. Xu, Z. Zhang et al., "HIF-1α protects granulosa cells from hypoxia-induced apoptosis during follicular development by inducing autophagy," *Frontiers in cell and developmental biology*, vol. 9, p. 32, 2021.

[24] V. Roca-Agujetas, C. de Dios, L. Lestón, M. Marí, A. Morales, and A. Colell, "Recent insights into the mitochondrial role in autophagy and its regulation by oxidative stress," *Oxidative medicine and cellular longevity*, vol. 2019, Article ID 3809308, 16 pages, 2019.

[25] Z. Tang, Z. Zhang, Q. Lin et al., "HIF-1α/BNIP3-mediated autophagy contributes to the luteinization of granulosa cells during the formation of corpus luteum," *Frontiers in cell and developmental biology*, vol. 8, p. 1815, 2020.

[26] M. B. Azad, Y. Chen, E. S. Henson et al., "Hypoxia induces autophagic cell death in apoptosis-competent cells through a mechanism involving BNIP3," *Autophagy*, vol. 4, no. 2, pp. 195–204, 2008.

[27] W. Hu, P. H. Zhou, X. B. Zhang, C. G. Xu, and W. Wang, "Roles of adrenomedullin and hypoxia-inducible factor 1 alpha in patients with varicocele," *Andrologia*, vol. 47, no. 8, pp. 951–957, 2014.

[28] L. J. Velickovic and V. Stefanovic, "Hypoxia and spermatogenesis," *International Urology and Nephrology*, vol. 46, no. 5, pp. 887–894, 2014.

[29] Y. Chen, Y. Zhang, H. Ji et al., "Involvement of hypoxia-inducible factor-1α in the oxidative stress induced by advanced glycation end products in murine Leydig cells," *Toxicology In Vitro*, vol. 32, pp. 146–153, 2016.

[30] M. S. Winzell and B. Ahrén, "The high-fat diet-fed mouse," *Diabetes*, vol. 53, Supplement_3, pp. S215–S219, 2004.

[31] M. D. Anway, J. Folmer, W. W. Wright, and B. R. Zirkin, "Isolation of Sertoli cells from adult rat testes: an approach to ex vivo studies of Sertoli cell function1," *Biology of Reproduction*, vol. 68, no. 3, pp. 996–1002, 2003.

[32] J. Kim, C.-H. Chen, J. Yang, and D. Mochly-Rosen, "Aldehyde dehydrogenase 2* 2 knock-in mice show increased reactive oxygen species production in response to cisplatin treatment," *Journal of Biomedical Science*, vol. 24, no. 1, pp. 33–38, 2017.

[33] X. Wang, Z. Zou, Z. Yang et al., "HIF 1 inhibits StAR transcription and testosterone synthesis in murine Leydig cells," *Journal of Molecular Endocrinology*, vol. 62, 2018.

[34] M. G. Alves, A. D. Martins, J. E. Cavaco, S. Socorro, and P. F. Oliveira, "Diabetes, insulin-mediated glucose metabolism and Sertoli/blood-testis barrier function," *Tissue barriers*, vol. 1, no. 2, article e23992, 2013.

[35] Z. Du, S. Xu, S. Hu et al., "Melatonin attenuates detrimental effects of diabetes on the niche of mouse spermatogonial stem cells by maintaining Leydig cells," *Cell Death & Disease*, vol. 9, no. 10, p. 968, 2018.

[36] L. Long, H. Qiu, B. Cai et al., "Hyperglycemia induced testicular damage in type 2 diabetes mellitus rats exhibiting microcirculation impairments associated with vascular endothelial growth factor decreased via PI3K/Akt pathway," *Oncotarget*, vol. 9, no. 4, pp. 5321–5336, 2018.

[37] X. Li, S. He, and B. Ma, "Autophagy and autophagy-related proteins in cancer," *Molecular Cancer*, vol. 19, no. 1, pp. 12–16, 2020.

[38] B. L. Heckmann, B. J. Teubner, E. Boada-Romero et al., "Non-canonical function of an autophagy protein prevents spontaneous Alzheimer's disease," *Science Advances*, vol. 6, no. 33, p. eabb9036, 2020.

[39] P. Newsholme, E. P. Haber, S. M. Hirabara et al., "Diabetes associated cell stress and dysfunction: role of mitochondrial and non-mitochondrial ROS production and activity," *The Journal of Physiology*, vol. 583, no. 1, pp. 9–24, 2007.

[40] S. Rovira-Llopis, C. Banuls, N. Diaz-Morales, A. Hernandez-Mijares, M. Rocha, and V. M. Victor, "Mitochondrial dynamics in type 2 diabetes: pathophysiological implications," *Redox Biology*, vol. 11, pp. 637–645, 2017.

[41] W. Shi, Z. Guo, Y. Ji, and J. Feng, "The protective effect of recombinant globular adiponectin on testis by modulating autophagy, endoplasmic reticulum stress and oxidative stress in streptozotocin-induced diabetic mice," *European Journal of Pharmacology*, vol. 879, article 173132, 2020.

[42] V. U. Nna, A. B. A. Bakar, A. Ahmad, and M. Mohamed, "Diabetes-induced testicular oxidative stress, inflammation, and caspase-dependent apoptosis: the protective role of metformin," *Archives of Physiology and Biochemistry*, vol. 126, no. 5, pp. 377–388, 2020.

[43] E. Gianatti and M. Grossmann, "Testosterone deficiency in men with type 2 diabetes: pathophysiology and treatment," *Diabetic Medicine*, vol. 37, no. 2, pp. 174–186, 2020.

[44] S. Chen, S. Yang, M. Wang et al., "Curcumin inhibits zearalenone-induced apoptosis and oxidative stress in Leydig cells via modulation of the PTEN/Nrf2/Bip signaling pathway," *Food and Chemical Toxicology*, vol. 141, article 111385, 2020.

[45] H. Shoorei, A. Khaki, M. Shokoohi et al., "Evaluation of carvacrol on pituitary and sexual hormones and their receptors in the testicle of male diabetic rats," *Human & Experimental Toxicology*, vol. 39, no. 8, pp. 1019–1030, 2020.

[46] L. L. Li, J. Tan, Y. Y. Miao, P. Lei, and Q. Zhang, "ROS and autophagy: interactions and molecular regulatory mechanisms," *Cellular and Molecular Neurobiology*, vol. 35, no. 5, pp. 615–621, 2015.

[47] S. Rikka, M. N. Quinsay, R. L. Thomas et al., "Bnip3 impairs mitochondrial bioenergetics and stimulates mitochondrial turnover," *Cell Death and Differentiation*, vol. 18, no. 4, pp. 721–731, 2011.

Hindawi
Oxidative Medicine and Cellular Longevity
Volume 2023, Article ID 2713864, 14 pages
https://doi.org/10.1155/2023/2713864

Research Article

High Glucose-Induced Kidney Injury via Activation of Necroptosis in Diabetic Kidney Disease

Man Guo,[1,2] **Qing Chen**,[1,2] **Yongli Huang**,[3] **Qi Wu**,[4] **Yan Zeng**,[1,2,5] **Xiaozhen Tan**,[1,2] **Fangyuan Teng**,[1,2] **Xiumei Ma**,[1,2,5] **Yueli Pu**,[1,2] **Wei Huang**,[1,2] **Junling Gu**,[6] **Chunxiang Zhang**,[7] **Yang Long**,[2,8] **and Yong Xu**[1,2,5]

[1]*Department of Endocrinology and Metabolism, The Affiliated Hospital of Southwest Medical University, Luzhou 646000, China*
[2]*Metabolic Vascular Disease Key Laboratory of Sichuan Province, The Affiliated Hospital of Southwest Medical University, Luzhou 646000, China*
[3]*Department of Outpatient, The Affiliated Hospital of Southwest Medical University, Luzhou 646000, China*
[4]*Department of Pathology, and Academician Workstation of Sichuan Province, The Affiliated Hospital of Southwest Medical University, Luzhou 646000, China*
[5]*Faculty of Chinese Medicine, Macau University of Science and Technology, Avenida Wai Long, Macau, China*
[6]*Department of Endocrinology, Yibin Second People's Hospital, Yibin 644000, China*
[7]*Institute of Cardiovascular Research, Southwest Medical University, Luzhou 646000, China*
[8]*Experimental Medicine Center, The Affiliated Hospital of Southwest Medical University, Luzhou 646000, China*

Correspondence should be addressed to Chunxiang Zhang; zhangchx999@163.com, Yang Long; longyang0217@swmu.edu.cn, and Yong Xu; xywyll@aliyun.com

Received 22 May 2022; Revised 29 September 2022; Accepted 30 September 2022; Published 30 January 2023

Academic Editor: En Yin Lai

Diabetic kidney disease (DKD) is a major microvascular complication of diabetes mellitus (DM) and is closely associated to programmed cell death. However, the complex mechanisms of necroptosis, an alternative cell death pathway, in DKD pathogenesis are yet to be elucidated. This study indicates that necroptosis is involved in DKD induced by high glucose (HG) both in vivo and in vitro. HG intervention led to the activation of RIPK1/RIPK3/MLKL signaling, resulting in renal tissue necroptosis and proinflammatory activation in streptozotocin/high-fat diet- (STZ/HFD-) induced diabetic mice and HG-induced normal rat kidney tubular cells (NRK-52E). We further found that in HG-induced NRK-52E cell, necroptosis might, at least partly, depend on the levels of reactive oxygen species (ROS). Meanwhile, ROS participated in necroptosis via a positive feedback loop involving the RIPK1/RIPK3 pathway. In addition, blocking RIPK1/RIPK3/MLKL signaling by necrostatin-1 (Nec-1), a key inhibitor of RIPK1 in the necroptosis pathway, or antioxidant N-acetylcysteine (NAC), an inhibitor of ROS generation, could effectively protect the kidney against HG-induced damage, decrease the release of proinflammatory cytokines, and rescue renal function in STZ/HFD-induced diabetic mice. Inhibition of RIPK1 effectively decreased the activation of RIPK1-kinase-/NF-κB-dependent inflammation. Collectively, we demonstrated that high glucose induced DKD via renal tubular epithelium necroptosis, and Nec-1 or NAC treatment downregulated the RIPK1/RIPK3/MLKL pathway and finally reduced necroptosis, oxidative stress, and inflammation. Thus, RIPK1 may be a therapeutic target for DKD.

1. Introduction

Type 2 diabetic kidney disease (DKD) is a major microvascular complication of diabetes mellitus (DM), which is the leading cause of chronic renal disease (CKD) and end-stage renal disease (ESRD) worldwide [1, 2]. The mechanisms leading to the initiation and progression of renal dysfunction in DKD are yet to be elucidated. Confounding factors have been reported that mainly relate to metabolic disorders, inflammatory responses, oxidative stress [3], and DNA methylation profiles [4]. Cell depletion, loss or necrosis in the form of apoptosis, and other programmed cell

death pathways may also play important roles and are recognized as considerable drivers of progressive decline in renal function [5, 6]. Both apoptosis and necrosis can cause tubular injury. Renal cell loss which is partly a consequence of apoptosis is the predominant mechanism mediating renal tubular epithelial cell loss and is central to the pathophysiology of renal damage [7–9].

Necroptosis shares several upstream signaling pathways with apoptosis; cell death can switch into a specific form of necrosis when aspartate-specific cysteine protease-8 (caspase-8) is defective, resulting in necroptosis [10, 11]. Necroptosis, a recently recognized form of nonapoptotic, regulated necrotic cell death, has a typical necrotic morphology. It can be activated by death receptors such as tumor necrosis factor receptor 1 (TNFR1) and a factor associated with suicide (FASL) [12, 13]. Among the various triggers, TNF-α/TNFR signaling has been the most typical and intensively investigated [14]. The binding of TNF to TNFR1 leads to the activation of receptor-interacting protein kinase 1 (RIPK1) and receptor-interacting protein kinase 3 (RIPK3), resulting in the recruitment a RIPK1-RIPK3-mixed lineage kinase domain-like protein (MLKL) complex that is localized on the cell membrane via phosphorylation of MLKL by RIPK3. This leads ultimately to the disruption of the plasma membrane and causes cell lysis [15, 16]. Reactive oxygen species (ROS), DNA methylation profiles, mitochondrial bioenergetic disorders, and advanced glycation end products (AGEs) have been implicated as necrotic effectors [17]. RIPK1, a crucial regulator of cell fate [18], functions as a start switch for caspase-8-dependent apoptotic or RIPK3/MLKL-mediated necroptosis, as well as for the activation of the nuclear factor-κB (NF-κB) pathway that is involved in promoting cell survival and inflammation [19]. RIPK1 can be regulated and pharmacologically inhibited by necrostatin-1 (Nec-1). Nec-1 is a cellular protector that has been widely used in various cellular and animal models of human diseases and is especially sensitive to TNF-induced necroptosis [20–22].

Accumulating evidence has shown that necroptosis plays an important role in various pathological conditions in humans, including neurodegenerative and cerebrovascular diseases [23–25], liver and retinal injuries [21, 26], and osteoporosis [27, 28]. Few studies have reported the role of necroptosis in the pathogenesis of renal diseases. Although necrosis nephron segment injury is the main mediator of acute kidney injury (AKI), necroptosis is another alternative cell death pathway that operates alongside [29]. Necroptosis is the primary mechanism mediating renal tubular epithelial cell loss in early and intermediate chronic renal disorders that result from necrosis preceding regeneration and/or fibrotic tissue remodeling [30]. Diabetes-related risk factors such as high glucose, AGEs, and lipopolysaccharide (LPS) can induce necroptosis in cardiomyocytes [31, 32], podocytes [33], glomerular endothelial cells, and umbilical vein endothelial cells [34]. It was speculated that high glucose-induced necroptosis mediated by TNF might be further regulated by ubiquitin carboxy-terminal hydrolase L1 (UCHL1) via the RIPK1/RIPK3 pathway, leading to enhanced progression of diabetic nephropathy and increased podocyte injury and loss [33]. Nec-1 effectively protects against renal ischemia and reperfusion (I/R) injury by inhibiting necroptosis and oxidative stress [35]. However, whether RIPK1 mediates damage by high glucose stimulation via activation of necroptosis in DKD patients and animal models remains unknown. Moreover, it has not yet been investigated whether necrostatin-1 effetely repairs the injury and ameliorates loss of renal tubular epithelial cells and if the antioxidants of N-acetylcysteine (NAC) decrease the release of inflammatory cytokines by inhibiting the RIPK1/RIPK3 pathway.

To validate this hypothesis, we created an in vitro cell model of HG intervention using normal rat kidney tubular cells (NRK-52E) and an in vivo mouse model of DKD along with an investigation of human kidney tissue samples collected postsurgery. Our research revealed that HG treatment increased renal tubular epithelial cell necroptosis and accelerated renal injury and fibrosis and that ROS are a driving force for necroptosis to an extent. Furthermore, Nec-1 and NAC were found to ameliorate renal function via inhibition of the RIPK1/RIPK3/MLKL signaling pathway. Our findings indicate that RIPK1 and targeted antioxidants may be potential therapeutic targets for DKD.

2. Materials and Methods

2.1. Kidney Sample Collection from Patients. Three patients with DKD (aged 56–65 years, two males and one female) in the Department of Pathology and three nondiabetic patients in the Department of Urology, Affiliated Hospital of Southwest Medical University, China, were recruited for histological and immunohistochemical studies. DKD was diagnosed by the urinary microalbumin/creatinine ratio (UACR, >30 mg/g) and typical pathological manifestations of the kidney, in accordance with the policies of the Clinical Trial Ethics Committee of the Affiliated Hospital of Southwest Medical University (KY2021086).

2.2. Animal Experiments. The animal experimental protocols were approved by the Animal Research Center of Southwest Medical University (20210928-007) and were performed in compliance with the policies of the Chinese Animal Research Committees. Six-week-old male C57BL/6J mice were purchased from Chengdu Dossy Experimental Animal Co., Ltd. (China) and randomly assigned to four groups: control vehicle-treated (NC), necrostatin-1 drug control (Nec-1), diabetic kidney disease (DKD), and type 2 diabetes mellitus (T2DM) injected with necrostatin-1 (DKD+Nec-1) ($n = 15$/group). After feeding the mice a high-fat diet for 8 weeks and followed by the occurrence of insulin resistance, 50 mg/kg streptozotocin (STZ, Sigma-Aldrich, Louis, USA) was continuously injected intraperitoneally (ip) for 4 days. When the fasting blood glucose level was higher than 16.7 mM, 1.65 mg/kg/d of necrostatin-1 (Sigma-Aldrich, Louis, USA) was injected intraperitoneally, and the control received 1000 μL/kg/d of 1‰ DMSO solution (Sigma-Aldrich, Louis, USA) in the same volume for 16 weeks.

Mice were anesthetized with 1% pentobarbital sodium (50 mg/kg body weight, ip, Sigma-Aldrich, Louis, USA), and blood was collected for the detection of the blood urea

nitrogen (BUN) levels and urine albumin-to-creatinine ratio (ACR) and urine for microalbuminuria. Microalbuminuria was measured by ELISA, ACR by picric acid colorimetry, and BUN by urease. The kidneys were cut along the coronal plane, and the right was used for pathological assessments and the left for western blotting and real-time PCR assays.

2.3. Cell Culture. The NRK-52E cells were purchased from American Type Culture Collection (ATCC, USA) and cultured in Dulbecco's modified Eagle's medium (DMEM; Gibco, Grand Island, NY, USA) containing 5.6 mM glucose and supplemented with 10% fetal bovine serum (FBS; Gibco, Grand Island, NY, USA), 100 U/mL penicillin, and 100 μg/mL streptomycin (Invitrogen, Grand Island, NY, USA). The incubated cells were grown at 37°C with 5% CO_2 and were starved for 6 h and treated with different concentrations of glucose (5.6 mM for control group and 30 mM for high glucose intervention) and then pretreated with 50 μM Nec-1 and 2 mM NAC for 24, 48, and 72 h. Following induction for 48 h, the total protein and mRNA were extracted from the cells for further study.

2.4. Cell Viability Assay. Cell growth and viability were measured using 3-(4,5-dimethylthiazol-2-yl)-2,5-diphenyltetrazolium bromide (MTT; Beyotime Institute of Biotechnology, Shanghai, China) assay. NRK-52E cells (1×10^5 cells/well) were seeded in 96-well plates in growth medium and pretreated with different concentrations of glucose; 10 μL of MTT (1 mg/mL) was added to each well, with 5 replicate wells, to allow the formation of MTT formazan crystals at 37°C for 4 h, which were solubilized in 100 μL of DMSO. Cell proliferation was recorded at 570 nm (Thermo Fisher Scientific, MA, USA) according to the manufacturer's instructions, and the appropriate time and concentration of glucose intervention were determined. The same method was used for Nec-1 and NAC.

2.5. Histopathological Analysis. Human and mouse kidneys were fixed in 4% PFA for 24 h and embedded in paraffin. The sections were deparaffinized, dehydrated, and stained with hematoxylin and eosin (H&E) and subjected to Masson's staining for histomorphometric analysis (Leica, Germany). Other sections subjected to immunofluorescence and immunohistochemical (IHC) analysis were incubated with rabbit phosphor-RIPK1 (p-RIPK1; 1 : 100; Cell Signaling Technology, USA), mouse phosphor-RIPK3 (p-RIPK3; 1 : 100; Abcam, Cambridge, UK), phospho-MLKL (p-MLKL; 1 : 100; Abcam, Cambridge, UK) antibodies, and anti-active caspase-3 (1 : 100; Abcam, Cambridge, UK), treated with goat anti-rabbit IgG (1 : 100), and incubated with streptavidin-horseradish peroxidase complex (HRP, 1 : 100, Biosynthesis Biotech, China). To visualize the signals, the sections were treated with the peroxidase substrate DAB (3,3-diaminobenzidine) and counterstained with hematoxylin. The renal tissue structure was observed, and the percentage of p-RIPK1-, p-RIPK3-, and p-MLKL-positive cells was calculated using Image-Pro Plus software.

2.6. Western Blotting Analysis. Total protein was extracted from kidney and mouse NRK-52E cells using the RIPA cell lysis buffer system (Cell Signaling Technology, USA), supplemented with phosphatase inhibitors, and was quantified by BCA-protein assay kit (Beyotime Institute of Biotechnology, Shanghai, China). An aliquot (20 μg) of the proteins was separated by 10% SDS-PAGE for protein electrophoresis and transferred to a polyvinylidene fluoride (PVDF) membrane (Millipore). Following blocking in 5% nonfat dry milk for 1 h at room temperature, the membrane was incubated at 4°C overnight with primary antibodies. The following antibodies were used: mouse RIPK1, p-RIPK3/RIPK3, p-MLKL/MLKL, IL-1β, anti-active caspase-3, phosphor-inhibitor κB α (p-IκBα), phosphor-inhibitor of kappa B kinase α/β (p-IKKα/β), GAPDH (all antibodies dilution ratios are 1 : 1000; Abcam, Cambridge, UK), and rabbit p-RIPK1. After washing three times with phosphate-buffered saline with Tween-20 (PBST), the membrane was incubated with HRP-conjugated secondary antibody (1 : 2000, Abcam, Cambridge, UK) at room temperature for 1 h. Bands were quantified using ImageJ software and normalized to GAPDH.

2.7. Quantitative Real-Time PCR (qRT-PCR) Analysis. Total RNA was isolated from mouse kidney tissue and NRK-52E cells using TRIzol reagent (Qiagen, Valencia, CA, USA), and the concentration and purity were assessed using a spectrophotometer. The isolated RNA was subjected to reverse transcription using a ReverTra Ace® qPCR RT Kit (Toyobo, Japan), and the synthesized cDNA was used as a template for quantitative PCR analysis. The primer sequence of monocyte chemoattractant protein- (MCP-) 1 was determined using Primer Premier 5.0 software, which confirmed the definition of primers in the NCBI website via Primer-BLAST, and synthesized by Shanghai Biotechnology Co., Ltd. Quantitative PCR reactions were performed in triplicate to remove any outliers. Finally, the CT values were analyzed in relation to GAPDH CT values ($RQ = -\Delta\Delta Ct$).

2.8. Intracellular ROS Assay, ELISA Assay, and TUNEL Assay. The intracellular production of ROS was measured using a ROS detection kit (Beyotime Institute of Biotechnology, Shanghai, China). The fluorescence of 2′-7′-dihydrodichlorofluorescein diacetate (DCFH-DA) was determined using a spectrofluorophotometer (BMG LABTECH, Germany) and measured in a plate reader with excitation at 488 nm and emission at 525 nm according to the manufacturer's instructions. Urine microalbuminuria levels were measured using a mouse microalbuminuria ELISA kit (Beijing Cheng Lin Biological Technology Co. Ltd., China) according to the manufacturer's protocols in 96 wells. The same method was applied to examine urine creatinine, BUN, and ACR in mouse serum. Apoptosis was detected using a TUNEL assay. Sections were incubated with 50 μL TUNEL reaction mixture in a wet box for 60 min at 37°C in the dark. Apoptotic cell death was quantified using a fluorescence microscope in the wavelength range of 570-620 nm (Roche).

2.9. Data Analysis. All data are expressed as mean ± standard deviation (SD) from at least three independent

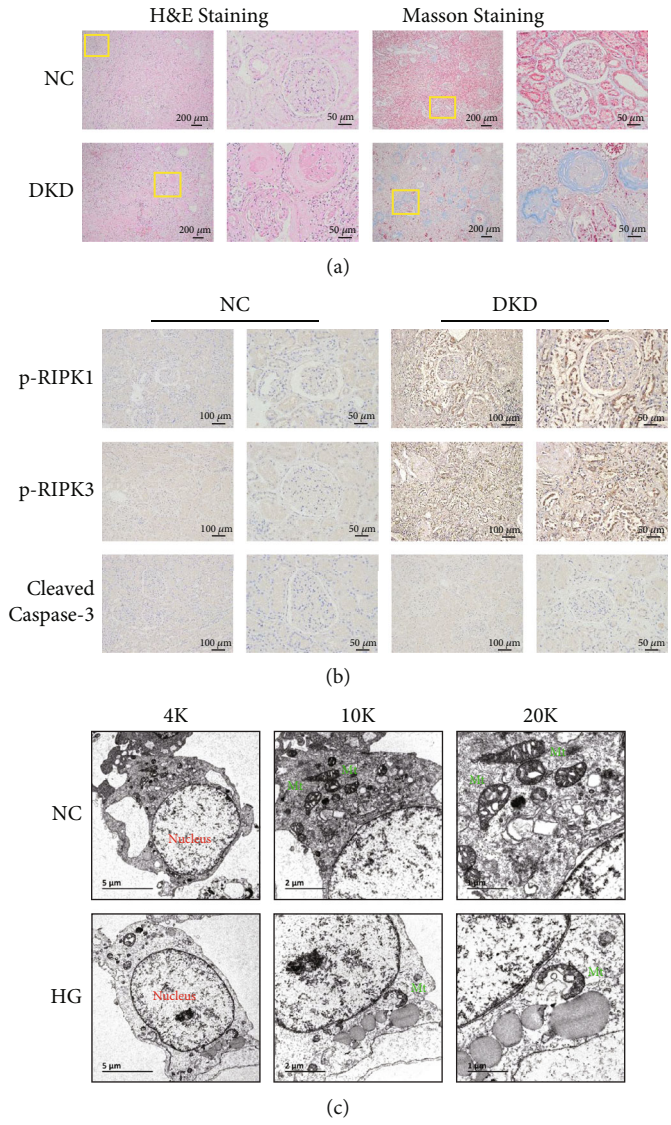

Figure 1: Necroptosis found in the kidney of DKD patients. (a) H&E and Masson's staining showing the pathological renal structure and deposited collagenous matrix in DKD patients. Scale bar: 200 μm and 50 μm, respectively. (b) IHC staining showing the difference in the expression of p-RIPK1 and p-RIPK3, and not of anti-active caspase-3, and the positive expression on renal tubules in DKD. Scale bar: 100 μm. (c) TEM analysis reveals that NRK-52E cells exhibit normal nuclear and cytoplasmic morphology in the control group and display typical necrotic ultrastructural changes including a disrupted plasma membrane, fragmented and vacuolated mitochondrial membranes (green mark), and expanded endoplasmic reticulum after exposure to 30 mM HG for 48 h. Scale bar: 5 μm and 1 μm, respectively. p-RIPK1: phosphor receptor-interacting serine/threonine kinases 1; p-RIPK3: phosphor receptor-interacting serine/threonine kinases 3; TEM: transmission electron microscopy; Mt: mitochondrion.

experiments, and comparisons between multiple groups were analyzed using one-way analysis of variance (ANOVA) with SPSS 22.0 software (SPNN Inc., Chicago, IL, USA). Statistical significance was set at $p < 0.05$.

3. Results

3.1. Protein Signaling Necroptosis Increased in Human DKD. To explore cell lysis by necroptosis in DKD, we performed IHC analysis for the necroptosis markers p-RIPK1 and p-RIPK3 in kidney biopsy specimens from three nondiabetic patients (control, NC) and three patients with DKD. Histomorphometric analysis performed on H&E-stained sections revealed that glomerular volume decreased and glomerular basement membrane (GBM) thickness increased in diabetic patients. It also indicated glomerulosclerosis and mesangial thickening in these patients. Masson's staining showed collagenous matrix deposition in glomeruli and tubules (indicated by more collagen deposition, blue staining in Figure 1(a)) and tubulointerstitial fibrosis. These are the typical renal pathological manifestations of DKD. Notably, IHC staining indicated an increase in the expression of p-RIPK1 and p-RIPK3 in glomeruli, especially in renal tubules, whereas the cleaved caspase-3 levels were not significantly different between the NC and DKD groups (Figure 1(b)). Therefore, we focused on the necroptosis of renal tubules

for the remaining study. Next, NRK-52E cells were cultured and stimulated by high glucose (30 mM) for 48 h. Transmission electron microscopy (TEM) analysis revealed that the plasma membrane was disrupted, mitochondrial membranes fragmented and vacuolated, and the endoplasmic reticulum expanded (Figure 1(c)), which are the typical characteristics of necroptosis. We concluded that the renal tubules developed necroptosis in patients with DKD.

3.2. HG-Induced Necroptosis of Renal Tubular Epithelial Cells by the Activation of RIPK1/RIPK3/MLKL Signaling. To investigate the effects of HG-induced necrocytosis in the mouse model of streptozotocin/high-fat diet- (STZ/HFD-) induced DKD, we detected necroptosis signaling. Interestingly, TUNEL staining indicated that the number of necrotic cells increased in the DKD kidneys (Figures 2(a) and 2(b)). The apoptosis marker, anti-active caspase-3, showed no significant change in the kidneys of mice with HG-induced DKD (Figures 2(c) and 2(d)). HG markedly elevated necroptosis in renal tissue, as indicated by the increased number of p-RIPK1- and p-MLKL-positive cells (Figures 2(e) and 2(f)) observed by IHC staining. Further, to investigate the molecular signaling pathways underlying cell death, we cultured NRK-52E cells, starved them for 6 h, and stimulated them with 30 mM glucose, followed by a 50 μM Nec-1 treatment for 48 h each. The protein expression levels of p-RIPK1, p-RIPK3, and p-MLKL increased correspondingly, and Nec-1 treatment lowered these elevated levels both in vivo (Figures 2(g) and 2(h)) and in vitro (Figures 2(i) and 2(j)). Therefore, we concluded that high glucose-induced cell death could mainly be attributed to necroptosis rather than apoptosis of renal tissue and NRK-52E cells and depends on the activation of RIPK1/RIPK3/MLKL signaling.

3.3. Nec-1 Treatment Ameliorated Renal Dysfunction and Pathophysiology in DKD Mice. Necroptosis occurs in the renal tissues of STZ/HFD-induced diabetic mice, and RIPK1 plays an important role in the occurrence and development of DKD. To examine whether necrostatin-1 treatment ameliorated renal dysfunction, we treated mice with 1.65 mg/kg/d Nec-1 for 16 weeks and observed renal function, morphological changes, and fibrosis. We found that Nec-1 treatment substantially reduced the increased urine microalbuminuria, BUN, and ACR, as assayed by ELISA (Figures 3(a)–3(d)). Furthermore, H&E staining revealed that Nec-1 treatment significantly improved pathological changes in the kidney and inhibited mesangial cell proliferation and decreased matrix increase, basement membrane thickening, and interstitial inflammatory cell infiltration (Figure 3(e)). Masson's staining showed that the renal fibrosis in DKD mice was significantly ameliorated following Nec-1 treatment (Figures 3(e) and 3(f)). Collectively, these data suggest that Nec-1 significantly improves renal function, renal remodeling, and fibrosis in DKD mice.

3.4. Nec-1 Treatment Reduced Kidney Inflammation Induced by HG. Immune-mediated chronic low-grade inflammation is closely associated with the pathogenesis of diabetes mellitus and microvascular complications. Inflammatory cytokines are involved in the progression of diabetic nephropathy [36]. The protein expression levels of p-IκBα and p-IKKα/β correspondingly increased, and Nec-1 effectively suppressed this increase (Figures 4(a) and 4(b)). IL-1β expression was upregulated after HG intervention, both in vivo (Figures 4(c) and 4(e)) and in vitro (Figures 4(d) and 4(f)). The expression of MCP-1 mRNA was significantly increased in DKD mice (Figure 4(g)) and cells in the high glucose group (Figure 4(h)), and Nec-1 treatment significantly reversed this phenotype. Therefore, we believe that Nec-1 intervention can reduce proinflammatory cytokine levels in the kidneys of DKD mice.

3.5. NAC Treatment Decreased Necroptosis and Inflammation by Inhibiting the RIPK1/RIPK3 Signaling. Previous studies have found that the overproduction of ROS plays an important role in programmed cell death, such as apoptosis [37], pyroptosis [38, 39], and necroptosis [40]. Among the various stimuli that trigger necroptosis, ROS are essential factor [41]. However, whether ROS increase kidney necroptosis in DKD remains unclear. Our results supported that HG intervention increased the intracellular ROS levels compared with the control group. Moreover, Nec-1 directly inhibited the elevated ROS, and the effect was equivalent to the treatment with NAC, an inhibitor of ROS (Figures 5(a) and 5(b)). We further explored whether ROS are crucial for HG-induced necroptosis in NRK-52E cells using the antioxidant NAC to inhibit ROS production. Addition of NAC effectively reduced HG-induced necroptosis in NRK-52E cells, as NAC attenuated the upregulation of the RIPK1 signaling pathway, including p-RIPK1, p-RIPK3, and p-MLKL, compared to that in the control group (Figures 5(d) and 5(e)). Meanwhile, NAC treatment significantly lowered the elevated levels of MCP-1 (Figure 5(c)) and significantly downregulated the production of proinflammatory cytokines (IL-1β) in vitro (Figures 5(f) and 5(g)). Together, these results highlight the role of ROS in the regulation of HG-induced NRK-52E cell necroptosis via a positive feedback loop involving RIPK1/RIPK3 and confirm that NRK-52E cell necroptosis, at least in part, promotes the generation of ROS.

4. Discussion

The mechanisms underlying DKD have not been fully elucidated. At present, studies have found that high glucose [31, 42, 43] and LPS [44] could induce necroptosis and participate in the development of diabetes and related complications. High glucose [32] and AGE [45] levels induce necroptosis in cardiomyocytes, thus contributing to the occurrence and development of diabetic myocardial fibrosis. Hyperglycemia-induced necroptosis of endothelial cells may accelerate the formation of atherosclerotic plaques in diabetes patients [34], and the apoptosis or necroptosis of podocytes [43] and glomerular endothelial cells [42] results in diabetic glomerulopathy and fibrosis. Herein, we found that the expression levels of p-RIPK1/RIPK1, p-RIPK3/RIPK3, and p-MLKL/MLKL in the kidney tissues of DKD mice were

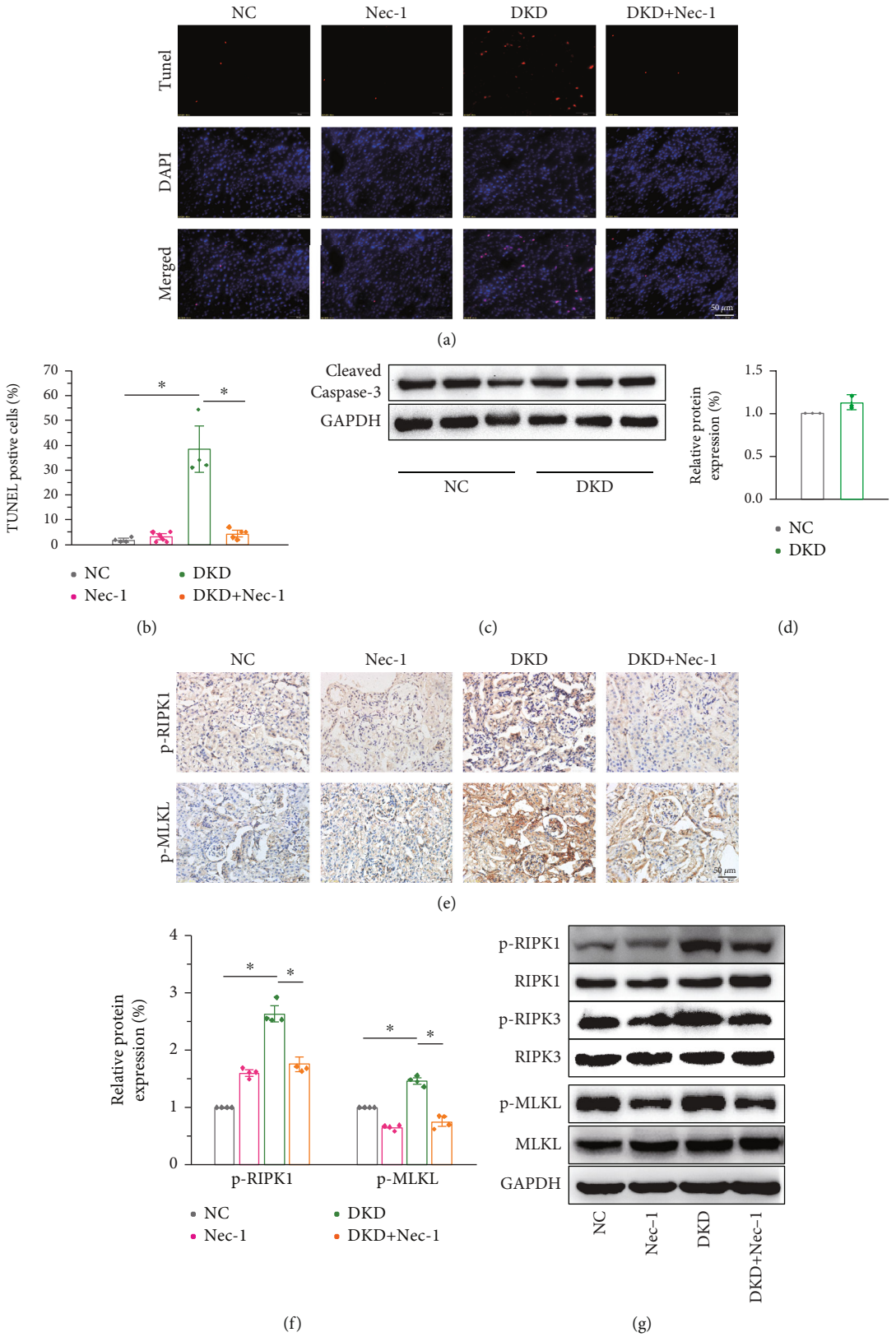

Figure 2: Continued.

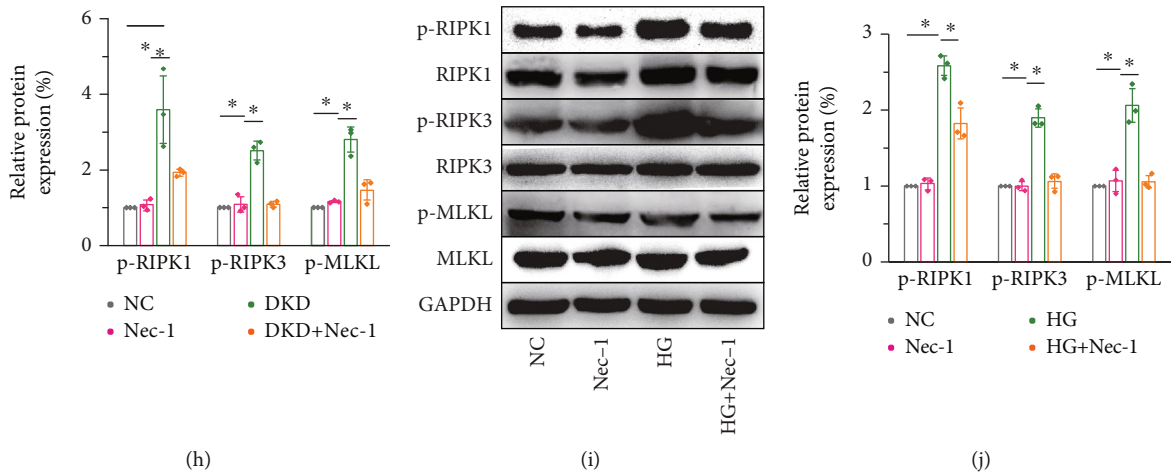

Figure 2: HG-induced necroptosis in kidney by activation of the RIPK1/RIPK3/MLKL signaling in diabetic mice. (a, b) TUNEL staining indicating the increase in necrotic cells in STZ/HFD-induced diabetic mice. Scale bar: 50 μm. (c, d) No significant difference is seen in the protein levels of cleaved caspase-3 between the NC and DKD groups. (e, f) IHC analysis revealing that the key markers of necroptosis (p-RIPK1 and p-MLKL) are significantly elevated in diabetic mice. Scale bar: 50 μm. Western blot confirming the upregulation of p-RIPK1 and p-RIPK3 and the downstream effector, p-MLKL, in vivo (g, h) and in vitro (i, j). Nec-1 treatment of 1.65 mg/kg/d for 16 weeks in mice and 50 μM for 48 h in cells, respectively. All experimental data were verified in at least three independent experiments. Error bars represent the SD from the mean values. $^*p < 0.05$. p-MLKL: phosphorylated mixed lineage kinase domain-like protein; Nec-1: necrostatin-1.

significantly increased, suggesting that necroptosis may be involved in the development of DKD. Furthermore, we found that treatment with RIPK1 inhibitor, Nec-1 significantly inhibited the activation of the RIPK1/RIPK3/MLKL signaling pathway, ameliorated renal dysfunction, and reduced kidney inflammation and renal fibrosis. These conclusions indicate the involvement of necroptosis-associated mechanisms in HG-treated kidneys.

Necroptosis is triggered by the ligation of death receptors or initiators, leading to the phosphorylation of RIPK1. This initiates the phosphorylation of a pseudokinase substrate MLKL, which recruits p-RIPK3 to form a necrosome and translocates to the cell membrane, finally leading to necroptosis. Previous studies have revealed important functions and regulatory mechanisms of RIPK1 in inflammation and have indicated that RIPK1 may be a therapeutic target for multiple human diseases [46]. However, our study is the first to show that blocking RIPK1 by Nec-1 ameliorates renal dysfunction and reduces kidney inflammation in DKD. Our findings suggested that Nec-1 significantly reduced necrosis of kidney tissue, decreased the expression of necroptosis markers, and blocked/reduced inflammation. Meanwhile, the activation of RIPK1 and RIPK3 was suggested to play a key role in the process of regulated necrotic cell death [18, 41]. Tumor necrosis factor receptor type 1-related death domain protein (TRADD) acts as an interaction partner of RIPK3 to mediate RIPK1-independent necroptosis [47]. RIPK3-dependent calcium/calmodulin-dependent kinase (CaMKII) activation plays a key role in necroptosis in cardiac ischemia-reperfusion injury models [48]. Thus, the molecular mechanisms underlying necroptosis are complex and diverse. While our research focused on the mechanisms involving RIPK1, further research is required to investigate whether necroptosis induced by high glucose is dependent on the activation of RIPK3 and to validate its role in necroptosis in DKD though knockdown experiments or by the use of specific inhibitors.

Chronic persistent inflammation plays an important role in the progression of DKD. The activation of necroptosis can strongly promote inflammation by regulating the production of inflammatory cytokines and the release of DAMP-related molecular patterns (DAMPs) from damaged cell membranes after lysis [15]. Studies have revealed that RIPK1 was involved in regulating the production and activation of proinflammatory factors such as TNF, IL-6, NLRP3 inflammasome, and NF-κB [49]. RIPK1 plays an important role in the signaling pathways triggered by death receptors through its regulation of caspase-dependent apoptosis and RIPK3/MLKL-mediated necroptosis. It is also involved in promoting cell survival and inflammation by activating the NF-κB pathway [19, 50]. Deubiquitination of RIPK1 promotes the formation of complex IIa with caspase-8 and FADD to induce apoptosis, or complex IIb with RIPK1 and RIPK3 to induce necroptosis [51, 52]. When RIPK1 is modified by ubiquitination, it forms a scaffold for stabilization of IKKα/β, degradation of IκBα, release of NF-κB, and activation of inflammation and prosurvival genes [53]. Given this, we found that the expression of p-IκBα and p-IKKα/β, phosphorylation of S321 RIPK1, and proinflammatory cytokines IL-1β and MCP-1 increased. Moreover, inhibition of RIPK1 with Nec-1 effectively lowered the elevated levels in vivo and in vitro. Since the phosphorylation of S321 RIPK1 and IKKα/β is both mediated by TNF-mediated signaling [54–56], these results suggest that high glucose levels increase the activation of RIPK1-kinase-/NF-κB-dependent inflammation upon stimulation by TNF-α. Thus, RIPK1 is

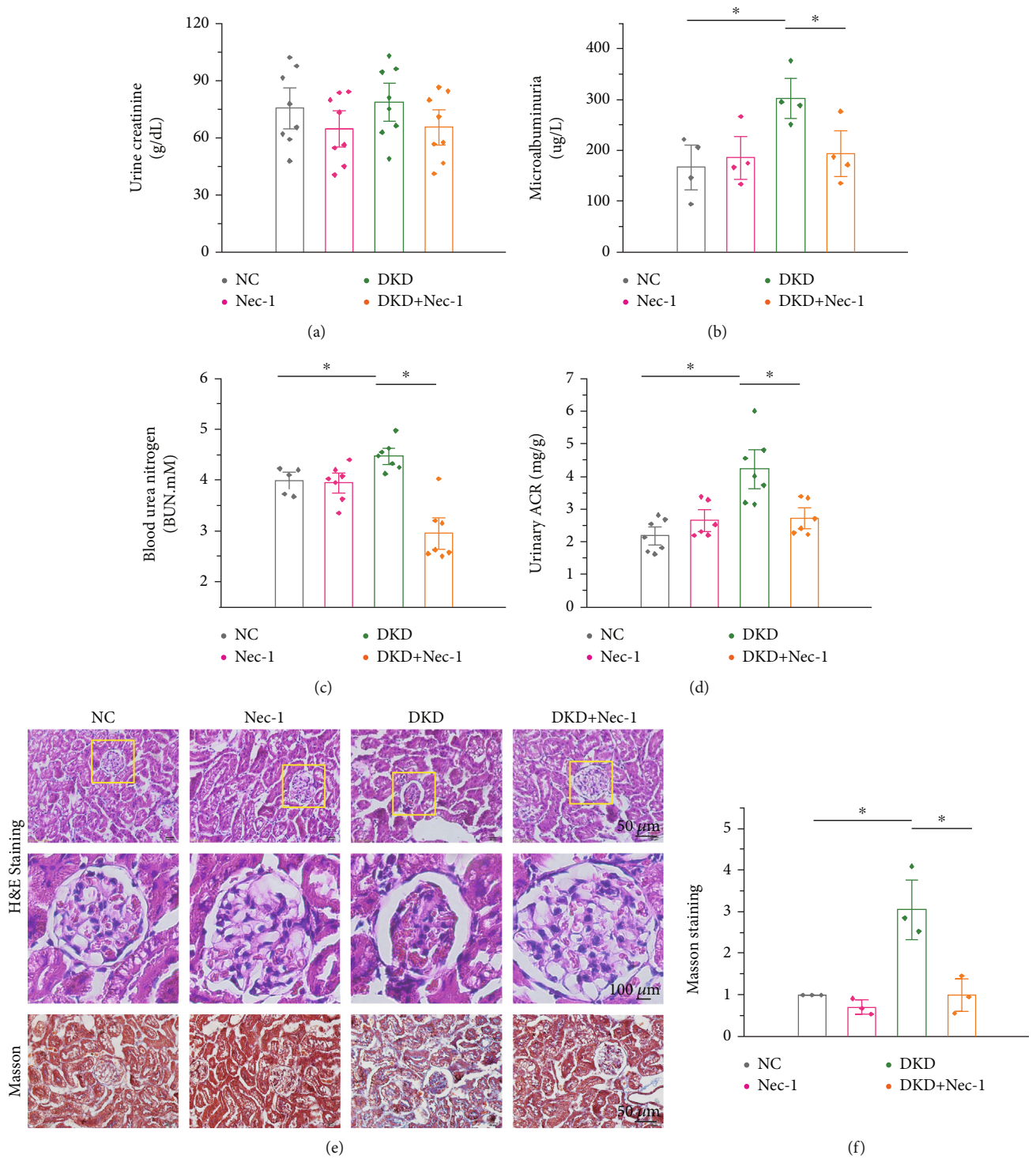

FIGURE 3: Nec-1 treatment ameliorates renal dysfunction in DKD mice. (a–d) Nec-1 (1.65 mg/kg/d for 16 weeks) treatment substantially reduces the increased urine microalbuminuria, blood urea nitrogen (BUN), and urine albumin-to-creatinine ratio (ACR) in mice serum as detected by ELISA. (e) H&E-stained sections revealing that Nec-1 treatment significantly improves the pathological changes in DKD, such as mesangial cell proliferation, matrix increase, basement membrane thickening, and increase in interstitial inflammatory cells. Scale bar: 50 μm and 100 μm. (f) Masson's staining showing the renal fibrosis in mice with DKD improved significantly after treatment with Nec-1. Scale bar: 50 μm.

the key checkpoint that determines cell survival based on the activation of NF-κB prosurvival signaling or induction of necroptosis.

ROS are mainly derived from the electron transfer process during mitochondrial oxidative respiration. At the physiological level, ROS are involved in a variety of

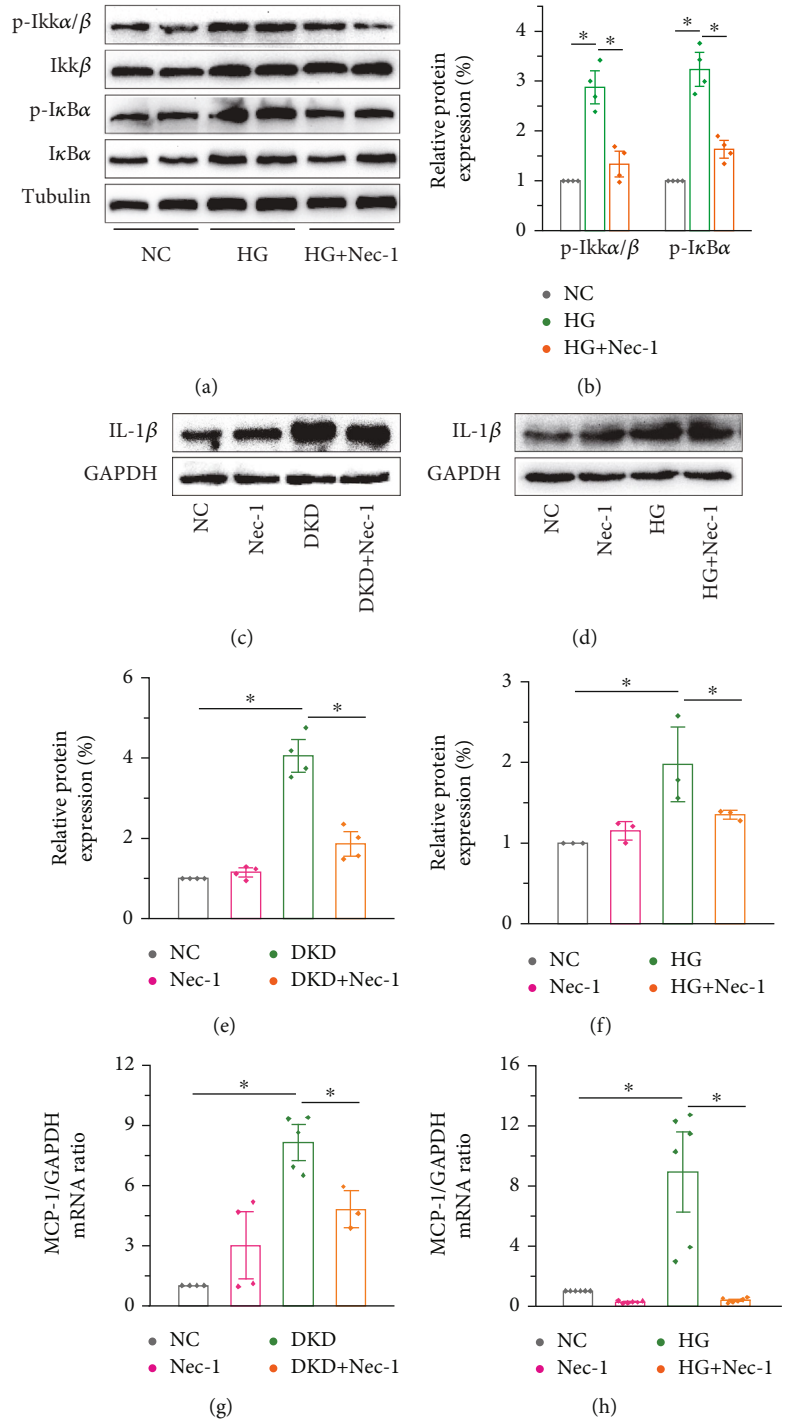

Figure 4: Nec-1 treatment reduces kidney inflammation induced by HG. (a, b) The protein expression levels of p-IκBα and p-IKKα/β increased correspondingly, and Nec-1 effectively lowered the elevated levels. The expression levels of IL-1β were upregulated after HG intervention; however, Nec-1 treatment (1.65 mg/kg/d for 16 weeks in mice and 50 μM for 48 h in cells, respectively) downregulated the expression levels both in vivo (c, e) and in vitro (d, f). qRT-PCR showing the significant increase in the expression of MCP-1 in DKD mice (g) and cells in the high glucose group (h), and a clear decrease following the use of RIPK1 inhibitor Nec-1. MCP-1: monocyte chemotactic protein-1.

intracellular signal transduction pathways and play an important role in the regulation of cell proliferation, differentiation, and other physiological processes [57]. Excessive intracellular ROS production leads to an imbalance in oxidative and reductive capacity, and oxidative stress damage occurs in the development of numerous diseases, including cardiovascular system diseases such as coronary heart disease, chronic lung diseases, pulmonary fibrosis [58], neurodegenerative diseases [59], and chronic kidney diseases such as diabetic nephropathy [60]. ROS overproduction

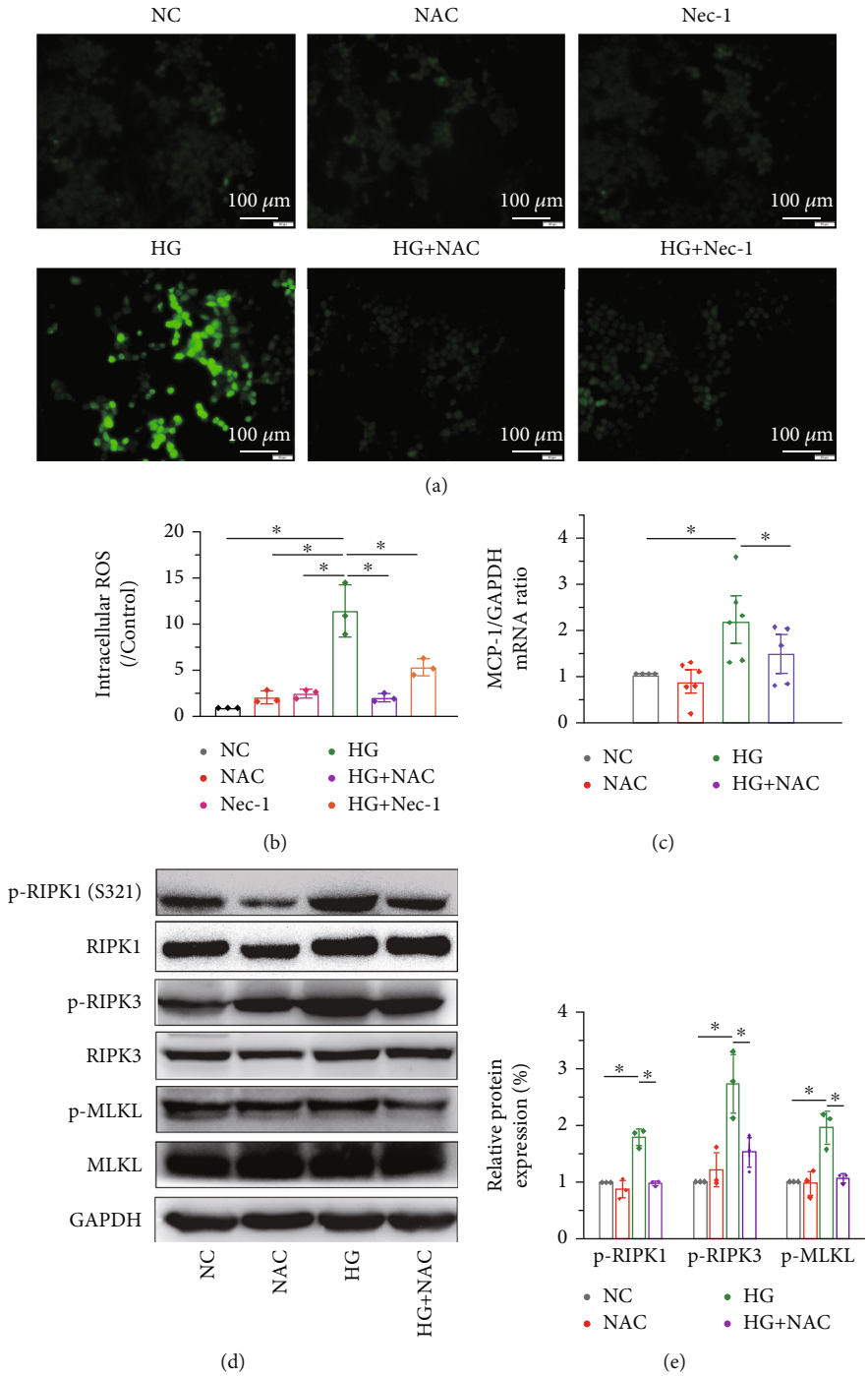

Figure 5: Continued.

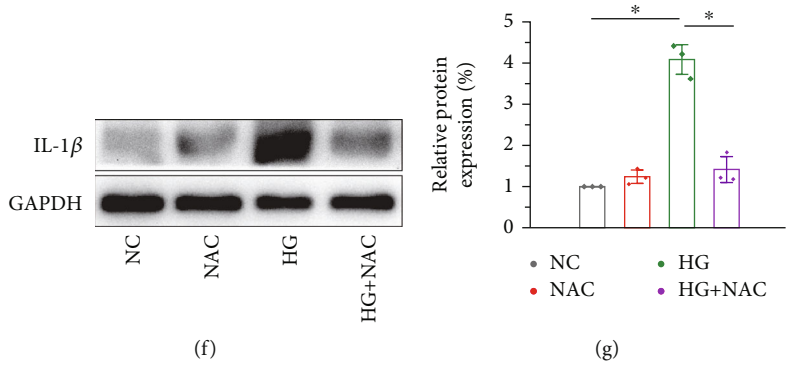

Figure 5: NAC treatment decreases necroptosis and inflammation by inhibiting RIPK1/RIPK3 signaling. (a, b) ROS levels increase significantly upon HG intervention and are effectively downregulated by NAC (2 mM for 48 h) and Nec-1 (50 μM for 48 h). Scale bar: 100 μm. Western blot analysis showing that HG activates the expression levels of the RIPK1 signaling pathway, including p-RIPK1, p-RIPK3, and p-MLKL compared to the control group. The addition of NAC effectively reduces necroptosis of the NRK-52E cells as NAC attenuates the upregulation of p-RIPK1 and p-RIPK3 (d, e). NAC treatment reduces the elevated mRNA level of MCP-1 induced by HG (c) and significantly decreases the level of proinflammatory cytokines (IL-1β) in vitro (f, g).

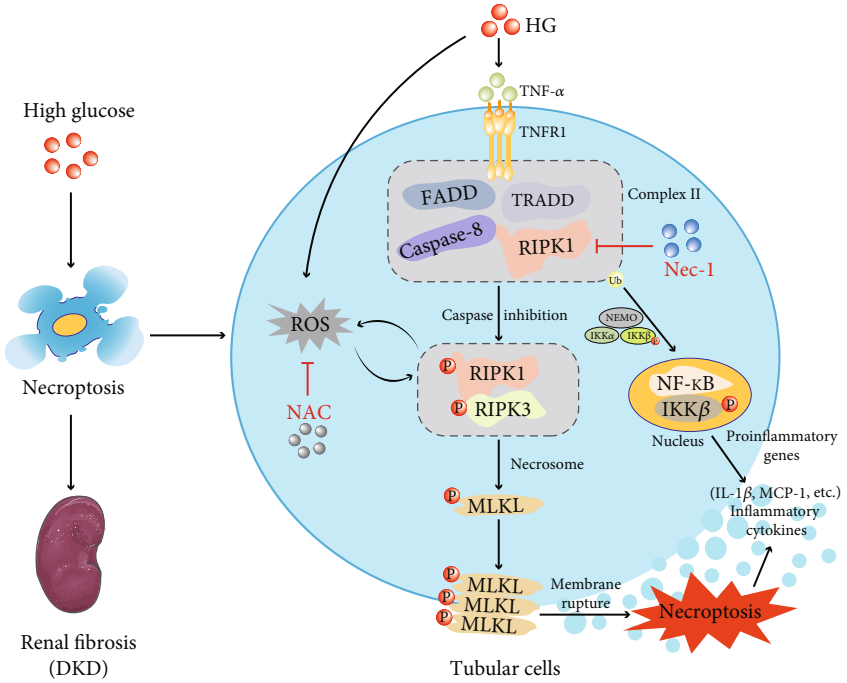

Figure 6: HG intervention drives the progression of DKD by increasing tubular cell necroptosis and inflammasome activation. Stimulated by HG, FADD and TRADD recruit RIPK1 and form complex II when caspase-8 is inhibited. ROS leads to the activation and phosphorylation of RIPK1 to an extent, recruits the RIPK1-RIPK3-MLKL complex, and localizes on the cell membrane via MLKL phosphorylation, ultimately disrupting the plasma membrane and causing cell lysis. When RIPK1 is modified by ubiquitination, it forms a scaffold for the stabilization of IKKα/β, leading to the release of NF-κB and activation of inflammation and prosurvival genes. Ultimately, occurrence of tubular cell necroptosis, inflammation, renal fibrosis, and renal dysfunction contribute to DKD. HG: high glucose; TNFR1: tumor necrosis factor receptor 1; FADD: Fas-associated protein with death domain; TRADD: TNFR1-associated death domain; NEMO: nuclear factor kappa B essential modulator; IKKα/β: inhibitor kappa B kinase α/β; NF-κB: nuclear factor-κB; Ub: ubiquitination; ROS: reactive oxygen species; Nec-1: necrostatin-1; NAC: antioxidant N-acetylcysteine.

leads to oxidative stress injury and cell death in renal tissues, which is one of the key mechanisms underlying the occurrence and development of DKD. In addition, ROS overproduction is involved in mediating programmed necrosis induced by inflammatory factors such as TNF-α [61], ischemia-reperfusion injury [48], and respiratory syncytial viral infection [62]. ROS have been considered as a driving force for necroptosis [63], and their major function is the regulation of RIPK1 kinase activity. Three crucial cysteines (cysteines 257, 268, and 586) sense ROS levels and promote

RIPK1 autophosphorylation on serine residue 161 (S161) and form a functional necrosome [64]. TNF induced ROS activation in a positive feedback to enhance necrosome formation and induced NRK-52E necroptosis; ROS production decreases upon knockdown of RIPK1 or RIPK3 [65]. However, most of the research on ROS and disease, especially high glucose-stimulated ROS production, did not clearly distinguish the specific type of ROS. Unfortunately, we did not perform a direct analysis to distinguish between various ROS or precisely the specific type of ROS in our study. In our study, we found that HG treatment increased the production of intracellular ROS and the necrosome complex. Furthermore, NAC markedly suppressed necroptosis and proinflammatory cytokine production in NRK-52E, and Nec-1 treatment effectively reduced the elevated ROS levels. Altogether, hyperglycemic necroptosis partly depends on ROS generation, and high glucose can induce necroptosis by promoting ROS overproduction (Figure 6).

5. Conclusion

In conclusion, our findings provide the first evidence that Nec-1 inhibits RIPK1/RIPK3/MLKL-dependent signaling by targeting RIPK1 and that NAC partly decreases the activation of necroptosis by preventing the production of ROS, ultimately regulating renal necroptosis, oxidative stress, and inflammation. Consequently, we postulated that the efficacy of Nec-1 or NAC treatment against DKD may be driven by the inhibition of necroptosis signaling. Our data highlights the role of RIPK1 as a key determinant of whether the cell activates the NF-κB prosurvival signaling or undergoes death by necroptosis. Thus, our study underscores RIPK1 as a potential therapeutic target for DKD.

Data Availability

The data that support the findings of this study are available from the corresponding authors upon reasonable request.

Conflicts of Interest

The authors declare that they have no conflicts of interest.

Authors' Contributions

M. G., Q. C., Y. H., and Y. X. participated in the study conception and design. M. G. and Y. Z. performed cell culture, qPCR, and signaling studies. Q. C., X. M., Y. P., and S. W. designed and performed animal experiments. M. G. and Q. W. conducted histopathological analysis. X. T., F. T., and J. G. prepared the figures and performed data analysis. M. G., C. Z., Y. L., and Y. X. prepared and revised the manuscript. Man Guo, Qing Chen, and Yongli Huang contributed equally to this work.

Acknowledgments

This study was supported by the Natural Science Foundation of China (Nos. 81970676, 81800741, and 82170834) and the Suining First People's Hospital-Southwest Medical University Cooperation Project (No. 2021SNXNYD01).

References

[1] R. Z. Alicic, M. T. Rooney, and K. R. Tuttle, "Diabetic kidney disease: challenges, progress, and possibilities," *Clinical Journal of the American Society of Nephrology*, vol. 12, no. 12, pp. 2032–2045, 2017.

[2] W. M. Valencia and H. Florez, "How to prevent the microvascular complications of type 2 diabetes beyond glucose control," *BMJ*, vol. 356, article i6505, 2017.

[3] A. S. De Vriese, M. S. Stoenoiu, M. Elger et al., "Diabetes-induced microvascular dysfunction in the hydronephrotic kidney: role of nitric oxide," *Kidney International*, vol. 60, no. 1, pp. 202–210, 2001.

[4] A. Lecamwasam, ,A. Sexton-Oates, J. Carmody, E. I. Ekinci, K. M. Dwyer, and R. Saffery, "DNA methylation profiling of genomic DNA isolated from urine in diabetic chronic kidney disease: a pilot study," *PLoS One*, vol. 13, no. 2, article e0190280, 2018.

[5] A. A. Eid, Y. Gorin, B. M. Fagg et al., "Mechanisms of podocyte injury in diabetes: role of cytochrome P450 and NADPH oxidases," *Diabetes*, vol. 58, no. 5, pp. 1201–1211, 2009.

[6] K. Turkmen, "Inflammation, oxidative stress, apoptosis, and autophagy in diabetes mellitus and diabetic kidney disease: the four horsemen of the apocalypse," *International Urology and Nephrology*, vol. 49, no. 5, pp. 837–844, 2017.

[7] Y. J. Choi, E. Baranowska-Daca, V. Nguyen et al., "Mechanism of chronic obstructive uropathy: increased expression of apoptosis- promoting molecules," *Kidney International*, vol. 58, no. 4, pp. 1481–1491, 2000.

[8] J. R. Schelling, N. Nkemere, J. B. Kopp, and R. P. Cleveland, "Fas-dependent fratricidal apoptosis is a mechanism of tubular epithelial cell deletion in chronic renal failure," *Laboratory Investigation*, vol. 78, no. 7, pp. 813–824, 1998.

[9] Y. Zhu, H. Cui, Y. Xia, and H. Gan, "RIPK3-mediated necroptosis and apoptosis contributes to renal tubular cell progressive loss and chronic kidney disease progression in rats," *PLoS One*, vol. 11, no. 6, article e0156729, 2016.

[10] C. Günther, E. Martini, N. Wittkopf et al., "Caspase-8 regulates TNF-α-induced epithelial necroptosis and terminal ileitis," *Nature*, vol. 477, no. 7364, pp. 335–339, 2011.

[11] M. Fritsch, S. D. Günther, R. Schwarzer et al., "Caspase-8 is the molecular switch for apoptosis, necroptosis and pyroptosis," *Nature*, vol. 575, no. 7784, pp. 683–687, 2019.

[12] S. Jouan-Lanhouet, M. I. Arshad, C. Piquet-Pellorce et al., "TRAIL induces necroptosis involving RIPK1/RIPK3-dependent PARP-1 activation," *Cell Death and Differentiation*, vol. 19, no. 12, pp. 2003–2014, 2012.

[13] S. Saveljeva, S. L. Mc Laughlin, P. Vandenabeele, A. Samali, and M. J. Bertrand, "Endoplasmic reticulum stress induces ligand-independent TNFR1-mediated necroptosis in L929 cells," *Cell Death & Disease*, vol. 6, no. 1, article e1587, 2015.

[14] S. Fulda, "The mechanism of necroptosis in normal and cancer cells," *Cancer Biology & Therapy*, vol. 14, no. 11, pp. 999–1004, 2013.

[15] B. Shan, H. Pan, A. Najafov, and J. Yuan, "Necroptosis in development and diseases," *Genes & Development*, vol. 32, no. 5-6, pp. 327–340, 2018.

[16] L. Galluzzi, O. Kepp, F. K. Chan, and G. Kroemer, "Necroptosis: mechanisms and relevance to disease," *Annual Review of Pathology*, vol. 12, no. 1, pp. 103–130, 2017.

[17] C. Xue, X. Gu, G. Li, Z. Bao, and L. Li, "Mitochondrial mechanisms of necroptosis in liver diseases," *International Journal of Molecular Sciences*, vol. 22, 2021.

[18] J. Li, T. McQuade, A. B. Siemer et al., "The RIP1/RIP3 necrosome forms a functional amyloid signaling complex required for programmed necrosis," *Cell*, vol. 150, no. 2, pp. 339–350, 2012.

[19] J. Silke, J. A. Rickard, and M. Gerlic, "The diverse role of RIP kinases in necroptosis and inflammation," *Nature Immunology*, vol. 16, no. 7, pp. 689–697, 2015.

[20] C. C. Smith, S. M. Davidson, S. Y. Lim, J. C. Simpkin, J. S. Hothersall, and D. M. Yellon, "Necrostatin: a potentially novel cardioprotective agent?," *Cardiovascular Drugs and Therapy*, vol. 21, no. 4, pp. 227–233, 2007.

[21] L. Duprez, N. Takahashi, F. van Hauwermeiren et al., "RIP kinase-dependent necrosis drives lethal systemic inflammatory response syndrome," *Immunity*, vol. 35, no. 6, pp. 908–918, 2011.

[22] Y. Gong, Z. Fan, G. Luo et al., "The role of necroptosis in cancer biology and therapy," *Molecular Cancer*, vol. 18, no. 1, p. 100, 2019.

[23] X. X. Deng, S. S. Li, and F. Y. Sun, "Necrostatin-1 prevents necroptosis in brains after ischemic stroke via inhibition of RIPK1-mediated RIPK3/MLKL signaling," *Aging and Disease*, vol. 10, no. 4, pp. 807–817, 2019.

[24] A. Iannielli, S. Bido, L. Folladori et al., "Pharmacological inhibition of necroptosis protects from dopaminergic neuronal cell death in Parkinson's disease models," *Cell Reports*, vol. 22, no. 8, pp. 2066–2079, 2018.

[25] H. H. Chan, R. Y. Koh, C. L. Lim, and C. O. Leong, "Receptor-interacting protein kinase 1 (RIPK1) as a potential therapeutic target: an overview of its possible role in the pathogenesis of Alzheimer's disease," *Current Alzheimer Research*, vol. 16, no. 10, pp. 907–918, 2019.

[26] A. Linkermann, J. H. Bräsen, N. Himmerkus et al., "Rip1 (receptor-interacting protein kinase 1) mediates necroptosis and contributes to renal ischemia/reperfusion injury," *Kidney International*, vol. 81, no. 8, pp. 751–761, 2012.

[27] H. Cui, Y. Zhu, Q. Yang et al., "Necrostatin-1 treatment inhibits osteocyte necroptosis and trabecular deterioration in ovariectomized rats," *Scientific Reports*, vol. 6, no. 1, article 33803, 2016.

[28] M. Guo, Y. L. Huang, Q. Wu et al., "Chronic ethanol consumption induces osteopenia via activation of osteoblast necroptosis," *Oxidative Medicine and Cellular Longevity*, vol. 2021, Article ID 3027954, 24 pages, 2021.

[29] T. Müller, C. Dewitz, J. Schmitz et al., "Necroptosis and ferroptosis are alternative cell death pathways that operate in acute kidney failure," *Cellular and Molecular Life Sciences*, vol. 74, no. 19, pp. 3631–3645, 2017.

[30] A. Belavgeni, C. Meyer, J. Stumpf, C. Hugo, and A. Linkermann, "Ferroptosis and necroptosis in the kidney," *Cell Chemical Biology*, vol. 27, no. 4, pp. 448–462, 2020.

[31] L. Ou, ,T. Sun, Y. Cheng et al., "MicroRNA-214 contributes to regulation of necroptosis via targeting ATF4 in diabetes-associated periodontitis," *Journal of Cellular Biochemistry*, vol. 120, no. 9, pp. 14791–14803, 2019.

[32] P. Kang, J. Wang, D. Fang et al., "Activation of ALDH2 attenuates high glucose induced rat cardiomyocyte fibrosis and necroptosis," *Free Radical Biology & Medicine*, vol. 146, pp. 198–210, 2020.

[33] J. Sosna, S. Voigt, S. Mathieu et al., "The proteases HtrA2/Omi and UCH-L1 regulate TNF-induced necroptosis," *Cell Communication and Signaling: CCS*, vol. 11, no. 1, p. 76, 2013.

[34] J. Lin, M. Chen, D. Liu et al., "Exogenous hydrogen sulfide protects human umbilical vein endothelial cells against high glucose-induced injury by inhibiting the necroptosis pathway," *International Journal of Molecular Medicine*, vol. 41, no. 3, pp. 1477–1486, 2018.

[35] B. Shen, M. Mei, Y. Pu et al., "Necrostatin-1 attenuates renal ischemia and reperfusion injury via meditation of HIF-1α/mir-26a/TRPC6/PARP1 signaling," *Molecular Therapy - Nucleic Acids*, vol. 17, pp. 701–713, 2019.

[36] J. F. Navarro-González and C. Mora-Fernández, "The role of inflammatory cytokines in diabetic nephropathy," *Journal of the American Society of Nephrology*, vol. 19, no. 3, pp. 433–442, 2008.

[37] S. Wang, M. Zeng, B. Li et al., "Raw and salt-processed *Achyranthes bidentata* attenuate LPS-induced acute kidney injury by inhibiting ROS and apoptosis via an estrogen-like pathway," *Biomedicine & Pharmacotherapy*, vol. 129, article 110403, 2020.

[38] Y. S. Tang, Y. H. Zhao, Y. Zhong et al., "Neferine inhibits LPS-ATP-induced endothelial cell pyroptosis via regulation of ROS/NLRP3/Caspase-1 signaling pathway," *Inflammation Research*, vol. 68, no. 9, pp. 727–738, 2019.

[39] C. Zhang, T. Lin, G. Nie et al., "Cadmium and molybdenum co-induce pyroptosis via ROS/PTEN/PI3K/AKT axis in duck renal tubular epithelial cells," *Environmental Pollution*, vol. 272, article 116403, 2021.

[40] Y. Jia, F. Wang, Q. Guo et al., "Curcumol induces RIPK1/RIPK3 complex-dependent necroptosis via JNK1/2-ROS signaling in hepatic stellate cells," *Redox Biology*, vol. 19, pp. 375–387, 2018.

[41] M. Pasparakis and P. Vandenabeele, "Necroptosis and its role in inflammation," *Nature*, vol. 517, no. 7534, pp. 311–320, 2015.

[42] W. Yi and Q. OuYang, "Adiponectin improves diabetic nephropathy by inhibiting necrotic apoptosis," *Archives of Medical Science*, vol. 15, no. 5, pp. 1321–1328, 2019.

[43] Y. Xu, H. Gao, Y. Hu et al., "High glucose-induced apoptosis and necroptosis in podocytes is regulated by UCHL1 via RIPK1/RIPK3 pathway," *Experimental Cell Research*, vol. 382, no. 2, article 111463, 2019.

[44] Y. Zhang, ,X. Qi, X. Chen, J. Zhang, W. Zhang, and H. Lin, "Dietary selenomethionine ameliorates lipopolysaccharide-induced renal inflammatory injury in broilers via regulating the PI3K/AKT pathway to inhibit necroptosis," *Food & Function*, vol. 12, no. 10, pp. 4392–4401, 2021.

[45] J. Yang, F. Zhang, H. Shi et al., "Neutrophil-derived advanced glycation end products-Nε-(carboxymethyl) lysine promotes RIP3-mediated myocardial necroptosis via RAGE and exacerbates myocardial ischemia/reperfusion injury," *The FASEB Journal*, vol. 33, no. 12, pp. 14410–14422, 2019.

[46] R. Weinlich, A. Oberst, H. M. Beere, and D. R. Green, "Necroptosis in development, inflammation and disease," *Nature Reviews. Molecular Cell Biology*, vol. 18, no. 2, pp. 127–136, 2017.

[47] L. Wang, X. Chang, J. Feng, J. Yu, and G. Chen, "TRADD mediates RIPK1-independent necroptosis induced by tumor necrosis factor," *Frontiers in Cell and Development Biology*, vol. 7, p. 393, 2019.

[48] T. Zhang, Y. Zhang, M. Cui et al., "CaMKII is a RIP3 substrate mediating ischemia- and oxidative stress-induced myocardial necroptosis," *Nature Medicine*, vol. 22, no. 2, pp. 175–182, 2016.

[49] D. Saleh, M. Najjar, M. Zelic et al., "Kinase activities of RIPK1 and RIPK3 can direct IFN-β synthesis induced by lipopolysaccharide," *Journal of Immunology*, vol. 198, no. 11, pp. 4435–4447, 2017.

[50] R. Weinlich and D. R. Green, "The two faces of receptor interacting protein kinase-1," *Molecular Cell*, vol. 56, no. 4, pp. 469–480, 2014.

[51] D. M. Moquin, T. McQuade, and F. K. Chan, "CYLD deubiquitinates RIP1 in the TNFα-induced necrosome to facilitate kinase activation and programmed necrosis," *PLoS One*, vol. 8, no. 10, article e76841, 2013.

[52] D. E. Christofferson, Y. Li, and J. Yuan, "Control of life-or-death decisions by RIP1 kinase," *Annual Review of Physiology*, vol. 76, no. 1, pp. 129–150, 2014.

[53] Y. Dondelinger, M. Darding, M. J. Bertrand, and H. Walczak, "Poly-ubiquitination in TNFR1-mediated necroptosis," *Cellular and Molecular Life Sciences*, vol. 73, no. 11-12, pp. 2165–2176, 2016.

[54] J. Geng, Y. Ito, L. Shi et al., "Regulation of RIPK1 activation by TAK1-mediated phosphorylation dictates apoptosis and necroptosis," *Nature Communications*, vol. 8, no. 1, p. 359, 2017.

[55] M. A. Kelliher, S. Grimm, Y. Ishida, F. Kuo, B. Z. Stanger, and P. Leder, "The death domain kinase RIP mediates the TNF-induced NF-κB signal," *Immunity*, vol. 8, no. 3, pp. 297–303, 1998.

[56] F. K. Chan, N. F. Luz, and K. Moriwaki, "Programmed necrosis in the cross talk of cell death and inflammation," *Annual Review of Immunology*, vol. 33, no. 1, pp. 79–106, 2015.

[57] C. R. Reczek and N. S. Chandel, "ROS-dependent signal transduction," *Current Opinion in Cell Biology*, vol. 33, pp. 8–13, 2015.

[58] A. van der Vliet, Y. M. W. Janssen-Heininger, and V. Anathy, "Oxidative stress in chronic lung disease: from mitochondrial dysfunction to dysregulated redox signaling," *Molecular Aspects of Medicine*, vol. 63, pp. 59–69, 2018.

[59] B. G. Trist, D. J. Hare, and K. L. Double, "Oxidative stress in the aging substantia nigra and the etiology of Parkinson's disease," *Aging Cell*, vol. 18, no. 6, article e13031, 2019.

[60] T. Nakanishi, T. Kuragano, M. Nanami, Y. Nagasawa, and Y. Hasuike, "Misdistribution of iron and oxidative stress in chronic kidney disease," *Free Radical Biology & Medicine*, vol. 133, pp. 248–253, 2019.

[61] Y. C. Ye, H. J. Wang, L. Yu, S. I. Tashiro, S. Onodera, and T. Ikejima, "RIP1-mediated mitochondrial dysfunction and ROS production contributed to tumor necrosis factor alpha-induced L929 cell necroptosis and autophagy," *International Immunopharmacology*, vol. 14, no. 4, pp. 674–682, 2012.

[62] S. P. Muraro, G. F. de Souza, S. W. Gallo et al., "Respiratory syncytial virus induces the classical ROS-dependent NETosis through PAD-4 and necroptosis pathways activation," *Scientific Reports*, vol. 8, no. 1, article 14166, 2018.

[63] Y. S. Kim, M. J. Morgan, S. Choksi, and Z. G. Liu, "TNF-induced activation of the Nox1 NADPH oxidase and its role in the induction of necrotic cell death," *Molecular Cell*, vol. 26, no. 5, pp. 675–687, 2007.

[64] Y. Zhang, S. S. Su, S. Zhao et al., "RIP1 autophosphorylation is promoted by mitochondrial ROS and is essential for RIP3 recruitment into necrosome," *Nature Communications*, vol. 8, no. 1, article 14329, 2017.

[65] B. Schenk and S. Fulda, "Reactive oxygen species regulate Smac mimetic/TNFα-induced necroptotic signaling and cell death," *Oncogene*, vol. 34, no. 47, pp. 5796–5806, 2015.

Hindawi
Oxidative Medicine and Cellular Longevity
Volume 2023, Article ID 5964723, 17 pages
https://doi.org/10.1155/2023/5964723

Research Article

Cysteine Pathogenic Variants of PMM2 Are Sensitive to Environmental Stress with Loss of Structural Stability

Fan Yu,[1] Li Lin,[1] Jingmiao Sun,[1] Jicheng Pan,[2] Yixin Liao,[3] Yunfan Pan,[4] Guannan Bai,[1] Liangjian Ma,[1,5] Jianhua Mao,[6] and Lidan Hu[1]

[1]*The Children's Hospital, Zhejiang University School of Medicine, National Clinical Research Center for Child Health, Hangzhou 310052, China*
[2]*Hubei Normal University, Huangshi, 435002 Hubei, China*
[3]*Department of Obstetrics and Gynecology, Nanfang Hospital, Southern Medical University, Guangzhou 510515, China*
[4]*Beijing Advanced Innovation Center for Structural Biology, Tsinghua-Peking Center for Life Sciences, School of Life Sciences, Tsinghua University, Beijing 100084, China*
[5]*The First Clinical Medical College of Lanzhou University, Lanzhou 730000, China*
[6]*Department of Nephrology, The Children's Hospital, Zhejiang University School of Medicine, National Clinical Research Center for Child Health, National Children's Regional Medical Center, Hangzhou, China*

Correspondence should be addressed to Jianhua Mao; maojh88@zju.edu.cn and Lidan Hu; right6852940@sina.com

Received 2 June 2022; Revised 27 August 2022; Accepted 10 September 2022; Published 25 January 2023

Academic Editor: Jianbo Wu

Congenital disorders of glycosylation (CDG) are severe metabolic disorders caused by an imbalance in the glycosylation pathway. Phosphomannomutase2 (PMM2-CDG), the most prevalent CDG, is mainly due to the disorder of PMM2. Pathogenic variants in cysteine have been found in various diseases, and cysteine residues have a potential as therapeutic targets. PMM2 harbor six cysteines; the variants Cys9Tyr (C9Y) and Cys241Ser (C241S) of PMM2 have been identified to associate with CDG, but the underlying molecular mechanisms remain uncharacterized. Here, we purified PMM2 wild type (WT), C9Y, and C241S to investigate their structural characteristics and biophysical properties by spectroscopic experiments under physiological temperature and environmental stress. Notably, the variants led to drastic changes in the protein properties and were prone to aggregate at physiological temperature. Meanwhile, PMM2 was sensitive to oxidative stress, and the cysteine pathogenic variants led to obvious aggregate formation and a higher cellular apoptosis ratio under oxidative stress. Molecular dynamic simulations indicated that the pathogenic variants changed the core domain of homomeric PMM2 and subunit binding free energy. Moreover, we tested the potential drug targeting PMM2-celastrol in cell level and explained the result by molecular docking simulation. In this study, we delineated the pathological mechanism of the cysteine substitution in PMM2, which addressed the vital role of cysteine in PMM2 and provided novel insights into prevention and treatment strategies for PMM2-CDG.

1. Introduction

Congenital disorders of glycosylation (CDG) 2 are genetic disorders resulting from abnormal glycosylation. PMM2-CDG, due to the impairment of enzyme phosphomannomutase2 (PMM2), is the most prevalent CDG with an incidence rate of 1 in 20,000 individuals [1–3]. The clinical symptoms of PMM2-CDG involve multisystem disorders, such as hypotonia, stroke-like episodes, and peripheral neuropathy [4]. There is a substantial childhood mortality rate of approximately 15–30%, and surviving patients develop permanent neurological disabilities [5]. PMM2-CDG, considered a misfolding proteins disease, ongoing efforts are made to develop drugs, including glucose-1,6-bisphosphate, D-mannose, epalrestat, or proteostasis regulators [6–9]. Increasing efforts towards the treatment of misfolding proteins disease, such as identification some chaperones: small-molecule modulators or structural-correctors for conformationally

destabilized proteins; PROTACs and autophagosome-tethering compound (ATTEC) to degrade misfolded proteins, DAXX to prevent aggregation, *etc* [10–13]. However, to date there is no specific curative treatment is available [14–16]. Therefore, elucidating the pathogenesis of PMM2-CDG is warranted and might provide new insights into its treatment.

PMM2 is highly conserved among species and essential for early development, and deficiency of PMM2 led to lethality in a mouse and zebrafish model [17, 18]. PMM2 catalyzes mannose-6-phosphate to the mannose-1-phosphate precursor of the GDP-mannose [1]. Very recently, the complete crystal structure of hPMM2 was resolved, including the cap domain (87-184 aa) and the core domain (1-83 and 189-246 aa), folding 9 α-helix, 11 β-sheet and two flexible linker regions (84-86 and 185-188 aa) [19]. Over 135-point pathogenic variants have been reported in *PMM2*, and approximately 85% of these pathogenic variants are missense (http://www.hgmdl.cf.ac.uk). When we examined the specific mutation sites of PMM2 in the clinical report, cysteine (Cys) pathogenic variants have attracted our attention. The primary structure of PMM2 comprises six Cys residues (C9, C83, C103, C136, C192, and C241), and four (C9Y, C103F, C192G, and C241S) of these sites are linked to PMM2-CDG [20–22].

The Cys residues, as one of the least abundant amino acids, have unique attributes to the structure and function of proteins, especially for the catalytic activity and protein folding [23–25]. As the Cys residues likely have higher reactivity properties than other amino acids, replacement of even one such 'critical' residue may lead to drastic changes in the protein's properties [26, 27]. Sulfur-containing amino acid residues, such as the Cys residues in proteins, are particularly sensitive to oxidative damage [28, 29]. However, in this case, the opposite is observed. The Cys residues are mutated to other amino acids that cause the disease. Thus, it is significantly important to delineate the uncommon role of Cys in PMM2.

Previous studies focused on detecting the enzymatic differences between WT and disease-associated variants [14, 15, 30]. There was no study focused on the effects of Cys variants on the structure of the PMM2 protein and cellular function. In this study, we selected two Cys variants that may form disulfide bonds to identify the role of the Cys residue in the protein structure and function in cells.

Our results showed that the C9Y and C241S destabilized the secondary and tertiary structures of PMM2, increased the susceptivity to oxidase stress and temperature, and promoted PMM2 protein aggregation and degradation, which eventually induced cell death. Findings from this study will help elucidate the molecular mechanism underlying the loss-of-function of the Cys pathogenic variants in PMM2 and facilitate the development of personalized PMM2-CDG treatment strategies.

2. Materials and Methods

2.1. Materials. DNA polymerase, restriction endonucleases, and DNA ligase were purchased from Takata. Dimethyl sulfoxide (DMSO), paraformaldehyde (PFA), Triton X-100, Nonidet P40 (NP-40), phenylmethanesulfonyl fluoride (PMSF), heparin, protease inhibitor cocktail, KCl, $MgCl_2$, DTT, EDTA, Imidazole, cisplatin, H_2O_2, isopropyl-1-thio-β-D-glucopyranoside (IPTG), and 1-anilinonaphthalene-8-sulfonate (ANS) were Sigma products. *Escherichia coli*. (*E. coli*) DH5α and BL21 (DE3) strains were obtained from Biomed (Beijing, China). Dulbecco's modified Eagle's medium (DMEM), fetal bovine serum (FBS), lipofectamine 2000, and DAPI were purchased from Invitrogen. The antibody against PMM2 and p62 were obtained from Abcam, while the antibodies against GFP and GAPDH were from Yeasen Biotechnology. Donkey anti-rabbit Alexa Fluor 549, HRP-conjugated affinipure goat anti-rabbit IgG (H+L) were from EarthOx. BSA and skim milk powder were from BD Biosciences. All other chemicals were local products of analytical grade.

2.2. Plasmid and Site-Directed Mutagenesis. The open reading frame of *PMM2 (NM_000303)* was purchased by Youbio Co., Ltd. For the prokaryotic system, the WT PCR primers were as follows: Forward (F): 5′- ATTCGAGCT CCGTCGACATATGGCAGCGCCTGGCCCAGCGCTCT-3′; Reverse (R): 5′- TGCTCGAGTGCGGCCGCTTAGGAG AACAGCAGTTCACAG-3′. The C9Y variant was constructed by PCR-based site-directed mutagenesis: F, 5′- TCAGATCTCGAGCTCAAGCTTATGGCAGC GCCTGG CCCAGCGCTCTAC-3′; R, the same with WT. The C241S variant was constructed by PCR-based site-directed mutagenesis: F, the same with the WT; R, 5′- TGCTCGAGTGC GGCCGCTTAGGAGAACAGCAGTTCACTGATCC-3′. Then, PCR product was inserted into the expression pET28a(+) plasmid containing 6x His-tag. The recombinant plasmids containing the WT or mutation gene was transformed into *E. coli* BL21 (DE3) for the overexpression of the recombinant protein. For the eukaryotic system, the WT PCR primers were as follows: Forward (F): 5′- TCAG ATCTCGAGCTCAAGCTTATGGCAGCGCCTGGCCCA GCGCTCT-3′; Reverse (R): 5′- CGACTGCAGAATTCGA AGCTTGGAGAACAGCAGTTCACAGATCC-3′. The C9Y variant was constructed by PCR-based site-directed mutagenesis: F, 5′- TCAGATCTCGAGCTCAAGCTTATGGCAGC GCCTGGCCCAGCGCTCTA c-3′; R, the same with WT. The C241S variant was constructed by PCR-based site-directed mutagenesis: F, the same with WT; R, 5′-CGACTG CAGAATTCGAAGCTTGGAGAACAGCAGTTCACTGA TCC-3′. The obtained gene was inserted into the pEGFP-C3 vector, and endotoxin-free plasmids for cell transfection were obtained using the Plasmid Maxiprep kit.

2.3. Expression and Purification of Recombinant PMM2. Details about expression and purification were conducted by the same methods as those described previously [14]. The *E. coli* BL21 (DE3) containing the WT or variants' plasmids were amplified in the Luria-Bertani medium. The *E. coli* cells were harvested, lysed, and the soluble fraction were obtained by centrifugation at 12000 g at 4°C for 0.5 hours. After filtration 0.22 μm pore size filter twice,

the recombinant protein was collected using a Ni-NTA affinity column and purified by Hiload 16/600 Superdex 75 preparative column equipped with ÄKTA purifier in buffer containing 20 mM Na_2HPO_4, 150 mM NaCl, and 1 mM EDTA. The protein concentration was determined according to the BCA method.

2.4. Size Exclusion Chromatography (SEC), SDS-PAGE Analysis, and Protein Solubility. The purity of the final protein (>98%) was checked through SDS-PAGE and size exclusion chromatography (SEC) analysis and stored at -80°C. The SEC analysis was performed using ÄKTA purifier in the buffer with an elution rate of 0.6 mL/min. About 100 μL protein solutions were injected into the column. The protein concentration for SEC analysis was 0.2 mg/mL. The SDS-PAGE analysis was performed using the 10% separating gel. About 10 μL protein solutions with a protein concentration of 0.2 mg/mL were used for the SDS-PAGE analysis. Size exclusion chromatography can be used to estimate the molecular weight (MW) [31–33]. The purified protein was concentrated by Millipore Amicon Ultra-15 series and Millipore Amicon Ultra-0.5 series concentrators at 11000xg on 4°C. The protein concentration was determined every 15 min until the maximum concentration was reached. The maximum protein concentration was defined by the unchanged value after three successive replications of centrifugation. All 7solubility experiments are performed at least in triplicate.

2.5. Spectroscopy Experiments. Details about spectroscopic experiments were conducted by the same methods as those described previously [34]. In brief, the fluorescence spectra was determined using the F-4700 fluorescence spectrophotometer (Hitachi Co., Tokyo, Japan). The intrinsic fluorescence was monitored with an excitation wavelength of 280 nm or 295 nm, respectively, and an emission wavelength from 300 to 400 nm. For extrinsic ANS fluorescence measurement, the excitation wavelength was 380 nm and the scanning wavelength ranged from 400 to 700 nm. The Far-UV circular dichroism (CD) experiments were measured using Jasco J-715 spectropolarimeter (Jasco Corp, Tokyo, Japan) at room temperature using 0.2 mg/mL protein concentrations, respectively. Far-UV CD signals were collected using a 1 mm path length cell over a wavelength range of 190–250 nm. The solution turbidity was detected by the absorbance at 400 nm with an Ultraspec 4300 pro UV-Vis spectrophotometer (Amersham Pharmacia Biotech). The parameter A, defined as the ratio of the intensity at 320 nm (I_{320}) to 365 nm (I_{365}), suggested the position and shape change of the Trp fluorescence spectrum [35]. All spectroscopy experiments were repeated at least three times, and the buffer control was subtracted for correction.

2.6. Free Thiol Measurement. The number of free thiol in the proteins was determined by a micrototal mercapto assay kit (Solarbio, product number: BC1375). The thiol groups react with 5,50-dithiobis-(2-nitrobenzoic acid) (DTNB) and form yellow compounds with a maximum absorption peak at 412 nm. Evolution 300 Security UV-Vis Spectrophotometer (Thermo Fisher Scientific, Madison, USA) was used to detect the absorption peak at 412 nm, and then, the number of free thiols was calculated according to the formula given in the assay kit.

2.7. Cell Culture, Cell Transfection, and Immunofluorescence. HEK293T cells were obtained from public cell banks (ATCC, USA). These cells were cultured in DMEM containing 4.5 g/L high glucose, 10% fetal bovine serum, and 1% penicillin/streptomycin (Solarbio Science & Technology). All the cells were incubated in a humidified 37°C incubator and 5% CO_2. All the recombinant plasmids (WT, C9Y, and C241S) were transiently transfected in HEK293T cells by Hieff Trans™ Liposomal Transfection Reagent (Yeason), following the manufacturer's protocol. After 24 h transfection, for the oxidative stress group, the cells were treated with 2 mM H_2O_2 for 2 h. Then, the two groups of cells were washed by PBS buffer three times for 5 min, fixed by 4% PFA for 40 min, treated by 0.4% Triton X-100 for 10 min, and blocked by 10% FBS for 40 min. The fixed cells were stained by P62 antibody. The nuclei were dyed with DAPI. The cells were observed by OLYMPUS IX83-FV3000-OSR confocal microscope. The percentage of cells with aggregates was qualified by calculating the percentages from at least 200 positively transfected cells from 5 random fields.

2.8. Cell Apoptosis Assay. Untreated or treated cells were detached using Trypsin-no EDTA and collected by 300 g for 5 min and washed with cold PBS twice at 4°C. The procedure was followed by the instruction of Annexin V-Alexa Fluor 647/PI Apoptosis Detection Kit. Cell analysis was performed on BD FACS Calibur flow cytometer (BD Biosciences) within 1 h. All experiments were performed in triplicate.

2.9. Cell Viability. The Cell Counting Kit-8 (Solarbio Science & Technology) was performed to detect cell proliferation. The 3^*10^3 cells in 96-well plates were treated with 2 mM H_2O_2 for 2 h. 10 μL CCK8 reagent was added into each well according to the instruction of CCK8. And then, absorbance of samples was detected at 450 nm wavelength using an MD M5 (molecular devices).

2.10. Western Blot. The cells transfected for WB were divided into four groups based on different treatments: normal, 2 mM H_2O_2, 0.5 μM celastrol, and DMSO. The total protein concentration was detected using BCA Protein Quantification Kit (Vazyme). The nonreducing SDS-PAGE was done following the same protocol of the normal SDS-PAGE analysis without β-mercaptoethanol.

2.11. Molecular Dynamic Simulations. This study used the X-ray structure of the human PMM2 dimer template with residues 7–245 at pH 7.0 (PDB ID: 7O0C). The structure of the PMM2-C9Y and C241S dimer were constructed based on WT by PyMOL. Details of molecular dynamic (MD) simulation analysis were the same as those described previously. In brief, all structures were immersed in cubic water box with 10 Å between protein and the box boundary and water box contained 150 mM NaCl and 5 mM $MgCl_2$. Calculations

were simulated by GROMACS in CHARMM36 force field. Water was described with the TIP3P model. Electrostatics were treated using the particle mesh Ewald (PME) method We equilibrated the system for 5 ns under NVT and NPT conditions at 300 K and ran program for 100 ns to generate trajectories. Finally, visual molecular dynamics (VMD) was used to process and analyze the trajectories.

2.12. Protein Disulfide Bond Determination by Mass Spectrometry (MS). Related principles and procedures were referred from Gorman et al. [36]. This study used 50 μL PMM2-WT protein solution with a concentration of 0.2 μg/μL. We added prewashed beads and ethanol and elution the protein sample. Digestion the sample with trypsin+lysC mix (trypsin : protein = 1 : 50 (w/w)), and samples were freeze-dried in vacuum concentrator and redissolved with 0.1% trifluoroacetic acid. The sample was further analyzed by matrix-assisted laser desorption/ionization (MALDI) and electrospray ionization (ESI) in MS platform of Westlake University Institute for advanced study.

2.13. Data Analysis and Visualization. Data were analyzed by GraphPad Prism 8.0 (GraphPad Software Inc., San Diego, CA, USA). A p value of less than 0.05 was considered statistically significant. Results were visualized by GraphPad prism 8.0. All experiments in this work were repeated three times.

3. Results

3.1. Cys Substitution Impaired the Secondary and Tertiary Structures of PMM2 and Decreased Protein Solubility. The C9Y (c. G26A) variant has been identified in at least 7 families from France, Germany, Sweden, and the USA [37, 38]. The C9 was highly conserved and located near the active site Asp12, probably leading to enzymatic inactivation. And the C241S (c. G722C) variant has been identified in at least 6 families from France, Belgium, Spain, and the USA [3, 21, 22]. In terms of the enzyme, the C9Y variant retained approximately 28% of the enzymatic activity of the WT, and the C241S variant retained approximately 32% [30]. The C9Y and C241S substitution were predicted to be "probably damaging" with scores of 0.969 and 0.987, respectively, by Polyphen analysis, which was consistent with the result predicted by PROVEAN (C9Y: -5.493, C241S: -2.986). Combining the structure from the PDB website (PDB ID: 7O0C) and bioinformation, we found that the distance between Cys9 and Cys241 of PMM2 was suitable for disulfide bond formation and MS have confirmed (Figure 1(a) and Table 1).

To elucidate the Cys substitution effect on the PMM2 protein, the recombinant WT, C9Y, and C241S proteins were purified from the *E. coli* expression system and measured by spectroscopic experiments. According to the results of SEC analysis and SDS-PAGE, a single main peak and band indicated that the purified proteins had high homogeneity (Figure 1(b)). The results showed that the C9Y variant had slight shift at elution volume, which suggested that it had a bigger apparent molecular weight, consistent with the SDS-PAGE result. The C241S variant had similar elution positions in the SEC profiles as WT, thereby suggesting that C241S mutation did not affect the overall molecular size, oligomeric state, or hydrodynamic radius of PMM2. According to analysis on the Superdex 75 10/300GL gel column, both the WT and variants had a molecular mass of ~60 kDa in aqueous solution, which is approximately the theoretical homomer molar mass of 55.7 kDa. The catalytically active form of the PMM2 enzyme is a homodimeric protein, and we performed the assay and confirmed that the purified proteins had the enzyme activity (supplement Figure 1), meaning the purified proteins as dimmer form, consistent with a previous study [14, 19]. The effect of the Cys substitution on the microenvironment around Trp was further evaluated by the intrinsic Trp fluorescence. Compared to the WT protein, the Cys pathogenic variants dramatically decreased the Trp fluorescence of PMM2, and the C9Y was accompanied with an about 2 nm redshift of the maximum emission wavelength (E_{max}), suggesting that the structure of Cys variants became loose (Figure 1(c)). The ANS spectra provided clear evidence that the Cys substitution induced a large change in the nonpolarity of the ANS-binding site, and the C9Y variant caused a larger change than the C241S variant did (Figure 1(d)). Far-CD spectra represent the protein secondary structure elements. In the Far-UV regions, the variants CD spectra were generally characterized by distinct peaks at 208 and 222 nm, respectively, which are features of proteins that contain α-helix conformational elements, displayed lighter 208 nm and 222 nm minima than the WT (Figure 1(e)). The ratio of α-helix and β-sheet of C9Y were significantly lower than that in WT after qualification by CDNN software (Figure 1(f)). Moreover, the solubility of the C9Y variant was decreased (WT: $4.12 \pm 0.15\,\mathrm{mg\,mL^{-1}}$, C9Y: $0.75 \pm 0.14\,\mathrm{mg\,mL^{-1}}$, and C241S: $3.21 \pm 0.11\,\mathrm{mg\,mL^{-1}}$) (Figure 1(g)). Taking into account that the Cys substitution may affect the amount of free thiol, C9Y and C241S were monitored by DTNB modification according to Ellman's method. As expected, the C9Y variant contained more number of free thiol than the WT, which provided possible support for the disulfide-bonding network between the C9 and C241 (Figure 1(h)). Meanwhile, we performed mass spectrometry (MS) to detect the formation of disulfide bond. The lower value of score, the higher potential to form disulfide bond. The value below $1E-3$ was considered to form disulfide bond, and the value of C9 and C241 was $5.01E-04$ (Table 1). Taken together, these results support the hypothesis that Cys variants caused the changes in the secondary and tertiary structures of PMM2 that led to the Cys variants becoming more unstable.

3.2. Cys Substitution Impaired the Structural Stability at Physiological Temperature. To assess the effect of Cys substitution on protein stability, the aggregation of the samples was monitored by measuring the turbidity at 400 nm (A_{400}) at a physiological temperature of 37°C at consecutive time points, where the optical density of the protein solution was used as a measurement of the protein aggregation. As the data showed that the A_{400} value of C9Y and C241S reached a plateau at 4 hour (h) and significantly higher than

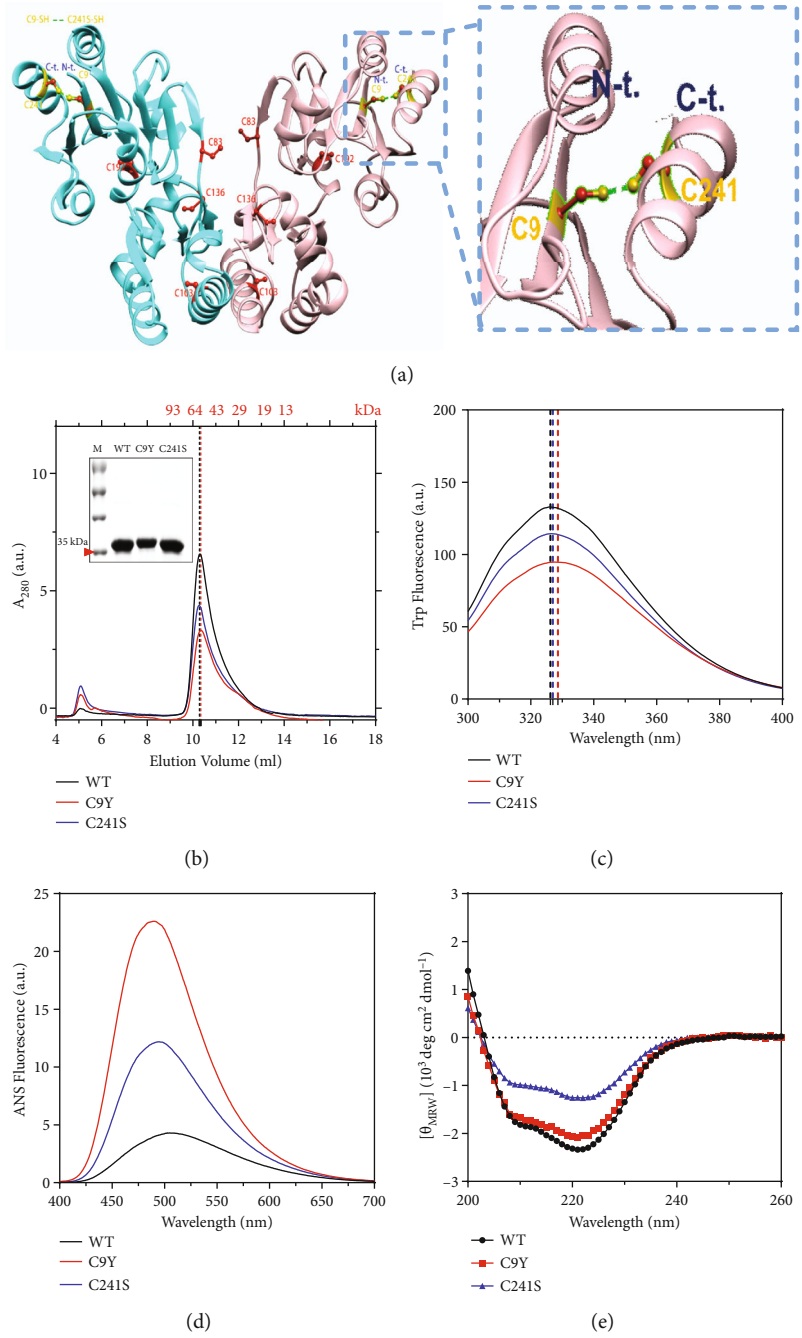

Figure 1: Continued.

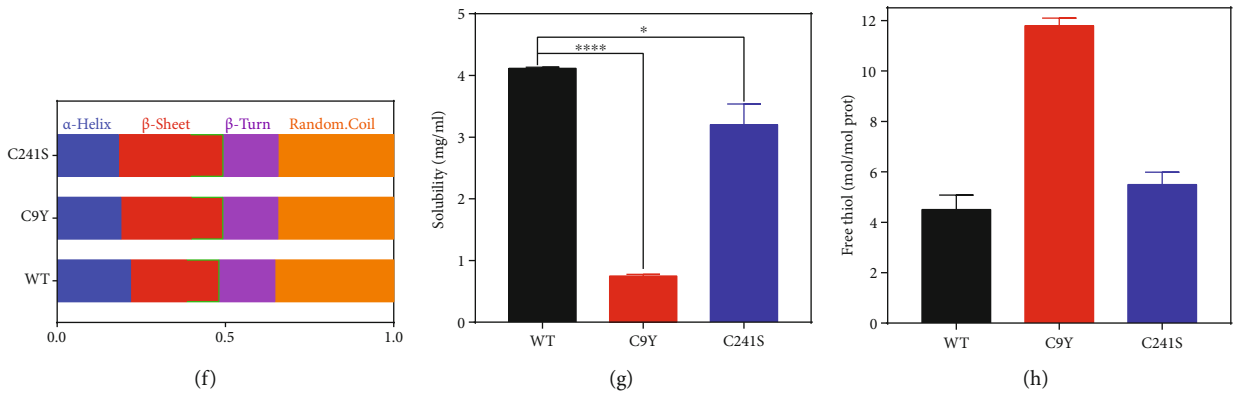

Figure 1: The cysteine variants decreased protein solubility with changing the secondary and tertiary structures of PMM2. (a) Representative cartoon crystal structure of the hPMM2 dimer (PDB ID: 7O0C). All the Cys were marked by stick, C9 and C241 colored by orange and the others colored by red. (b) SEC profiles of 100 μL, 0.2 mg/mL and SDS-PAGE analysis of the purified proteins. The inset shows the SDS-PAGE analysis of the purified proteins. (c) Intrinsic Trp fluorescence spectra of the 10 μM WT, C9Y, and C241S. (d) ANS fluorescence spectra of the 10 μM WT, C9Y, and C241S. (e) Far-UV CD spectra of the 10 μM WT, C9Y, and C241S. (f) Qualification the secondary ratio according to the Far-UV CD spectra by CDNN software. (g) The solubility of WT, C9Y, and C241S at 4°C ($^{*}p < 0.05$). (h) Number of free thiol of WT C9Y and C241S, the DTNB-reactive free –SH groups were calculated using a standard curve determined using L-cysteine. The presented results were calculated from three repetitions ($^{****}p < 0.0001$).

Table 1: Mass spectrometry (MS) detection the formation of disulfide bond.

Peptide	Proteins	Protein_Type	Score (<1.00$E-03$)
AAPGPALCLFDVDGTLTAPR(8)-ICELLFS(2)	PMM2(9)-PMM2(241)/	Intraprotein	5.01$E-04$
AAPGPALCLFDVDGTLTAPR(8)-SCSQEER(2)	PMM2(9)-PMM2(136)/	Intraprotein	5.31$E-05$
QNIQSHLGEALIQDLINYCLSYIAK(19)-ICELLFS(2)	PMM2(103)-PMM2(241)/	Intraprotein	4.55$E-07$
QNIQSHLGEALIQDLINYCLSYIAK(19)-SCSQEERIEFYELDKK(2)	PMM2(103)-PMM2(136)/	Intraprotein	5.31$E-05$
SCSQEER(2)-ICELLFS(2)	PMM2(136)-PMM2(241)/	Intraprotein	6.19$E-06$
SCSQEERIEFYELDKK(2)-SCSQEERIEFYELDKK(2)	PMM2(136)-PMM2(136)/	Interprotein	7.69$E-07$

the WT (Figure 2(a)). Thus, the intrinsic Trp, extrinsic ANS fluorescence, and Far-CD spectra were monitored at the 4 h timepoint. It is intriguing to discover the Cys variants led to drastic structural change loss, characterized by a redshifted peak position and lower intensity (Figure 2(b)). Strikingly, major alterations of protein secondary structures were observed by Far-CD spectra (Figure 2(c)). In addition, the extrinsic ANS fluorescence was higher intensity and a blue-shifted peak position compared to the WT (Figure 2(d)). For a more intuitive and more comprehensive analysis, sedimentation assay was applied, in which samples were centrifuged, and partitioning of PMM2 into the soluble fraction was used as a measurement of the state of PMM2. According to the SDS-PAGE analysis, the C9Y variant remained mainly in the soluble fraction, whereas a vast amount of protein entered the pellet fraction after 4 h under 37°C treatment; for the C241S variant, almost half the protein entered the pellet fraction at 37°C treatment. However, WT remained in the soluble fraction even when all other conditions were the same (Figure 2(e); see Figure 2(f) for quantification). Together, these results demonstrate that the Cys substitution became more unstable and prone to aggregation.

3.3. The Mutation Increased PMM2 Susceptibility to Heat Shock. We aimed to elucidate the thermal stability of the PMM2, for which we applied previously described procedures [34]. CD spectroscopy, A_{400}, and Uncle were applied to obtain further information on the temperature sensitivity of the PMM2 WT and Cys variants. As shown in Figure 3, as expected, the Cys variants showed significantly decreased starting and midpoint temperatures of thermal denaturation (T_m) when measured by the transition curves that were obtained from the changes of E_{222} in Far-UV CD (Figure 3(a)) and A_{400} (Figure 3(b)). In addition, the unfolding profiles were obviously different, and the heat denaturation analysis revealed that the WT began to dramatically lose the CD signal at 54°C, whereas the Cys variants started to significantly lose the CD signal at a temperature as low as 46°C for C9Y and C241S.

The A_{400} data of PMM2 were fit very well to a two-state thermal transition model between the folded and unfolded states and the T_m values were calculated. The T_m values of the WT, C9Y, and C241S proteins were 60.81 ± 0.1°C, 42.02 ± 0.2°C, and 48.72 ± 0.1°C, respectively. The thermal aggregation kinetics were determined by recording the time-course changes in turbidity when heating the protein

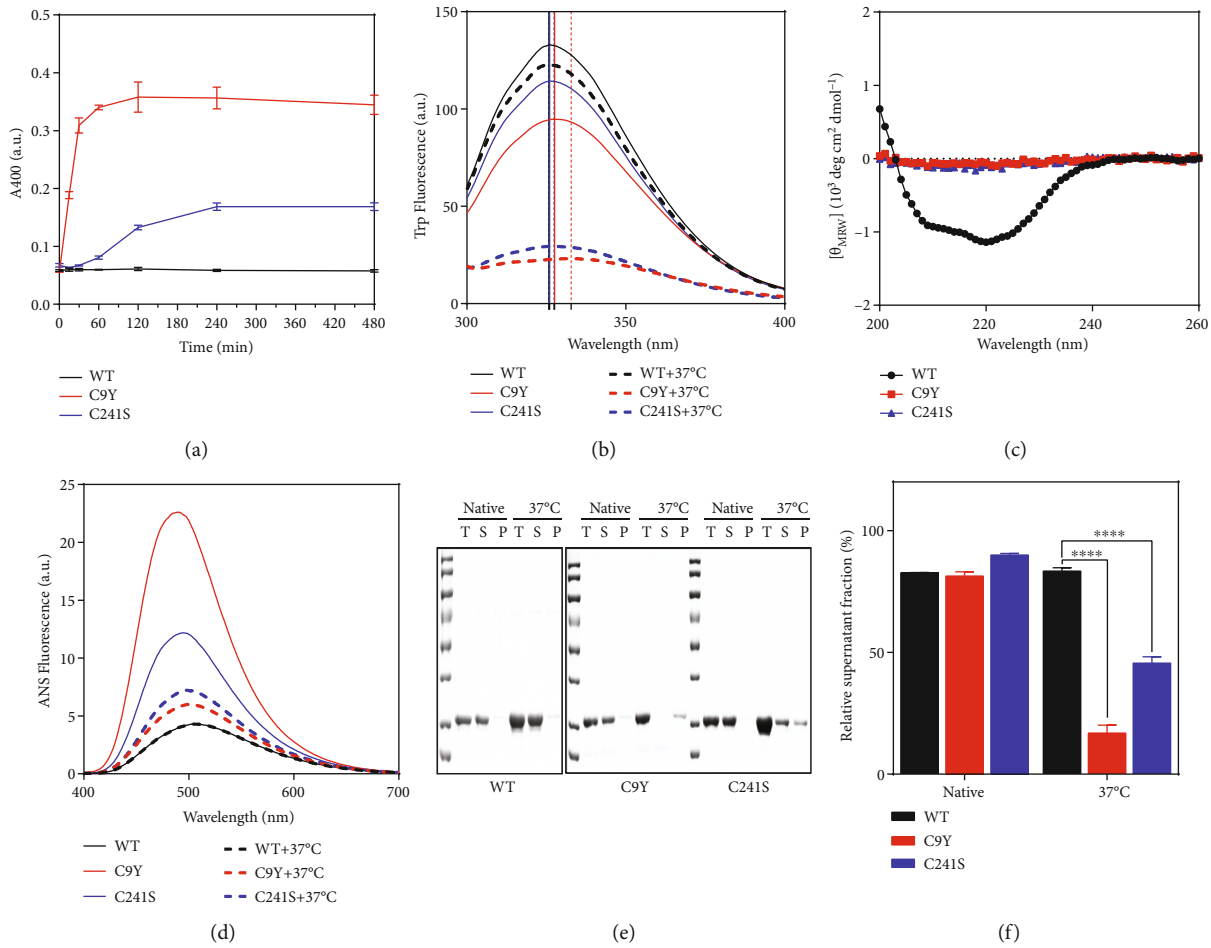

Figure 2: The C9Y and C241S variants lowered the stability of PMM2 under physiological temperature. (a) Turbidity (A_{400}) curve of WT, C9Y, and C241S during under physiological temperature for 15 min, 30 min, 1 h, 2 h, 4 h, and 8 h. (b) Intrinsic Trp fluorescence spectra of the 10 μM WT, C9Y, and C241S under physiological temperature for 4 h. (c) Far-UV CD of the 10 μM WT, C9Y, and C241S under physiological temperature for 4 h. (d) ANS fluorescence spectra of the 10 μM WT, C9Y, and C241S under physiological temperature for 4 h. (e) SDS-PAGE analysis of the soluble and insoluble fractions of protein solutions incubated at 37°C for 4 h. T: total, S: supernatant, P: precipitate. (f) Qualification of the soluble expression of proteins by SDS-PAGE analysis (e) with the supernatant/total (****$p < 0.0001$).

solutions at 50°C (Figure 3(c)). The A_{400} values of Cys variants abruptly increased over time, but that of WT nearly sustained at baseline, implying that the variants aggregated with a shorter lag time and a faster aggregation rate (Figure 3(d)). Simultaneously, the Uncle was applied to monitor the more detail status of thermal unfolding and aggregation of WT and the Cys variants. The results of E_{266} and E_{473} were showed in Figures 3(e) and 3(f). The Cys variants each had a higher peak and lower temperature for the formation of small and large aggregates. Notably, these multifaceted results implied that the Cys pathogenic variants appeared to disrupt a compact domain organization and prone to forming more massive aggregates.

3.4. The Cys Substitution of PMM2 Caused More Aggregates and Higher Cellular Apoptosis under Oxidative Stress. The Cys residues and disulfide bonds were expected to exert reversal thiol oxidation effect upon temporary oxidative stress shock. In our cases, what effects did the Cys substitution and subsequent potential disulfide bond disruption on the protein structure upon temporary oxidative stress shock? We applied hydrogen peroxide (H_2O_2) induced oxidative stress. H_2O_2 played a clear role as signaling second messenger in the cell. The result in Figure 4 indicated that the purified Cys variant proteins had a redshifted peak position, lower intensity in the Trp fluorescence curve (Figure 4(a)), and higher intensity and a blueshifted peak position in extrinsic ANS fluorescence curve (Figure 4(b)). As shown in Figures 4(d)–4(g), the intensity of the Trp fluorescence reduced and the intensity of the ANS fluorescence enhanced along the time course of H_2O_2 treatment. Together, PMM2 proteins were sensitive to oxidative stress. However, the changed structures of Cys variant proteins did not cause aggregate formation showed by A_{400} curve (Figure 4(i)). Further, nonreducing SDS-PAGE results indicated that the changed structure of Cys variant proteins may exist as higher multimeric form (Figure 4(c); see Figure 4(f) for quantification).

To provide deeper insight into the molecular pathogenesis of the Cys variants, we studied the effect at the cellular

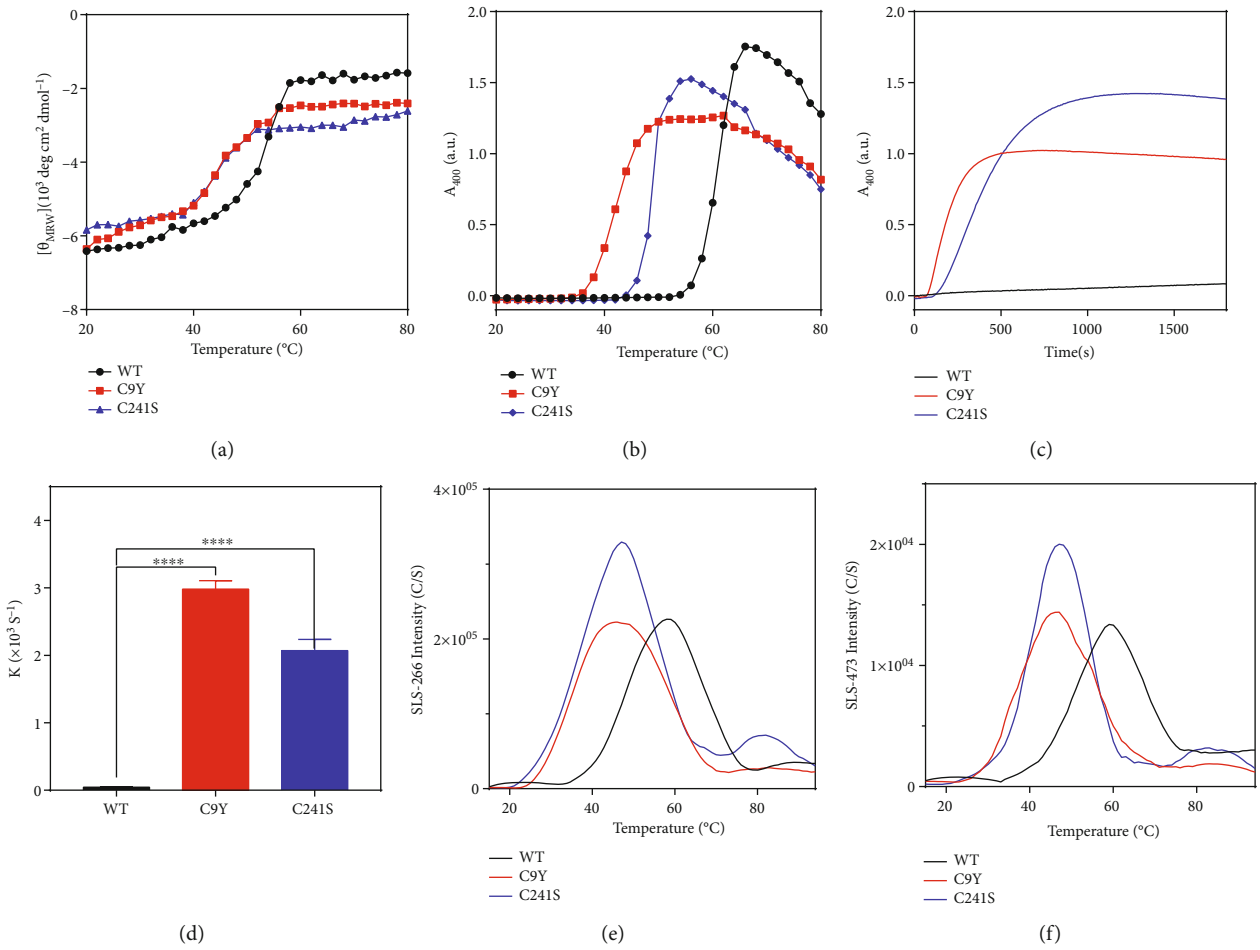

FIGURE 3: The C9Y and C241S variants significantly impairs thermal stability of PMM2. (a) The ellipticity at 222 nm of Far-UV CD upon temperature-gradient changes. (b) Turbidity (A_{400}) curves of WT, C9Y and C241S during temperature-gradient heating experiments. (c) Thermal aggregation kinetics of the proteins obtained by heating the protein solutions at 50°C. (d) The lag time and aggregation rate (k) of thermal aggregation kinetics. (e, f) The Uncle system evaluated the temperature-gradient heating process with different protein concentrations. The emission intensity in 266 (e) and 473 nm (f) wavelength of WT, C9Y, and C241S with 10 μM during the heating process, E266 and E473 with index of small and large aggregates, respectively ($^{****}p < 0.0001$).

level. It was feasible to hypothesize that these proteins were susceptible to be rapidly aggregated in cells. To test our hypothesis, we overexpressed the WT and Cys variants in HEK293T cell lines. Immunofluorescence results indicated that most of the overexpressed WT and Cys variants were distributed in the cytoplasm. However, a few cells were found to form protein aggregates, which were colocalized with P62 (Figure 5(a)). As expected, the aggregates were significantly increased after 2 mM H_2O_2 treatment, thereby suggesting that the Cys variants were more sensitive to oxidative conditions (Figures 5(b) and 5(c)). This result was consistent with that for the purified protein in a tube. To explore the effect of Cys variants on proliferation and apoptosis, we performed CCK-8 and flow cytometry experiments. The cell growth result indicated that the proliferation abilities of the Cys variants were significantly weaker after Cys substitution and that C241S was heavier than C9Y (Figure 5(d)). Furthermore, the proportion of late apoptosis was significantly increased in the C9Y and C241S groups (Figure 5(e)). According to the WB results of reduced SDS-PAGE, after treatment for 2 h in the presence or absence of H_2O_2, the Cys variants did not exhibit changes in protein molecular weight (Figure 5(f)). According to the WB results of nonreduced SDS-PAGE, notably, the protein size of C9Y was larger than that of the WT, while the protein size of C241S was smaller than that of the WT (Figure 5(g)). Taken together, these findings demonstrated that the Cys substitution elevated the PMM2 susceptibility to H_2O_2 treatment at both protein and cellular levels.

Gámez et al. have proposed that PMM2-CDG is a conformational disease and, based on this, suggested that pharmacological chaperones may be an effective treatment [16]. Their latest work indicated that celastrol treatment led to significant increases in variant PMM2 protein concentration and activity [7]. However, in our cases, at the cellular level, during H_2O_2 treatment, the protein levels of Cys variants did not change after celastrol treatment, according to both reduced SDS-PAGE and nonreduced SDS-PAGE (Figures 5(h) and 5(i)). Celastrol may act as a proteostasis regulators by triggering the HSR (i.e., it increased the

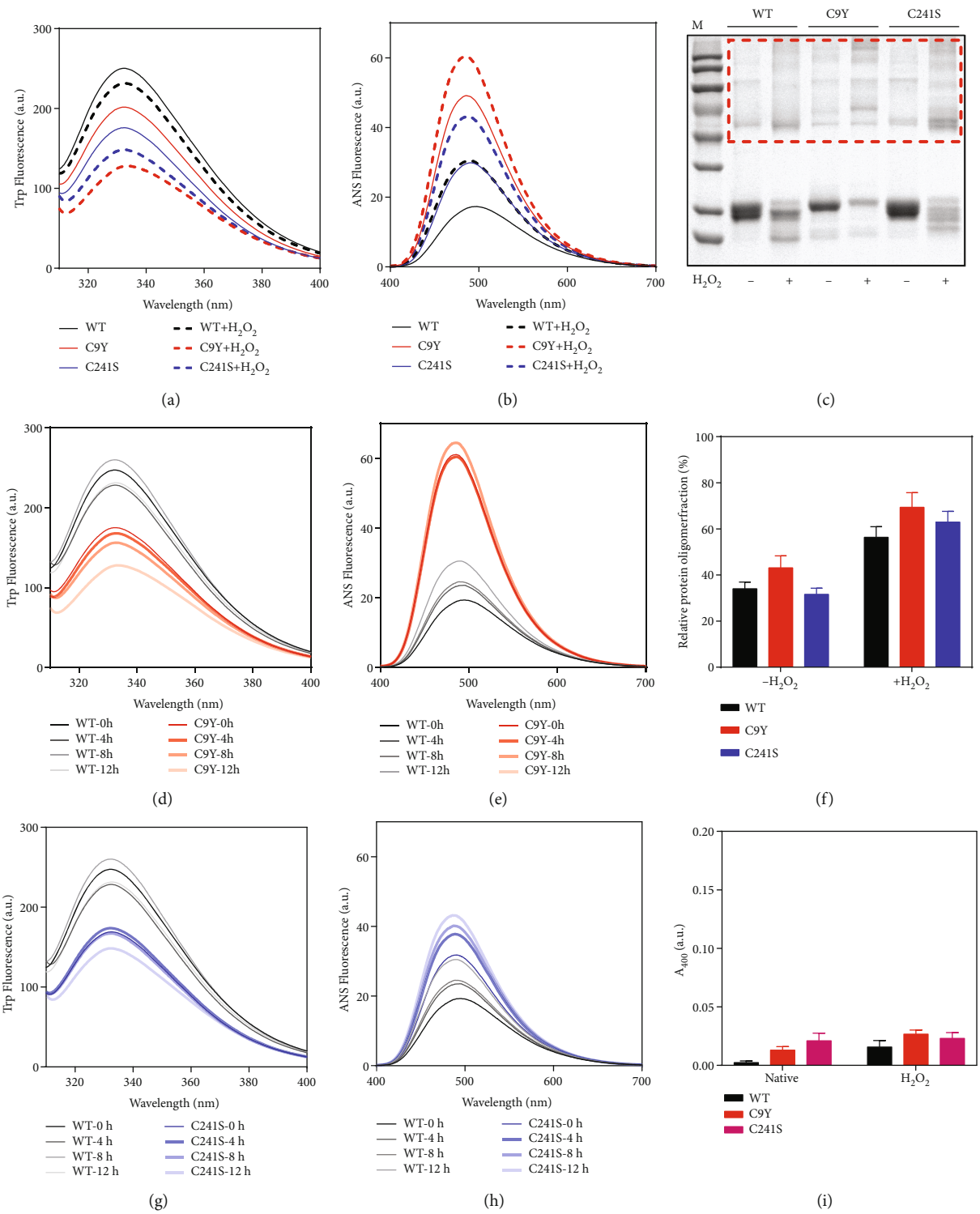

FIGURE 4: The C9Y and C241S variants elevated PMM2 susceptibility to H_2O_2 treatment. (a, b) Intrinsic Trp and ANS fluorescence spectra of the 10 μM WT, C9Y, and C241S after 1 mM H_2O_2 treatment for 12 h at 4°C. (c, f) Nonreducing SDS-PAGE analysis of the protein solutions, the samples were incubated in SEC buffer with or without 1 mM H_2O_2 for 12 h. (d, e) Intrinsic Trp and ANS fluorescence spectra of the 10 μM WT and C9Y after 1 mM H_2O_2 treatment for 4 h, 8 h, and 12 h. (g, h) Intrinsic Trp and ANS fluorescence spectra of the 10 μM WT and C241S after 1 mM H_2O_2 treatment for 4 h, 8 h, and 12 h. (i) Turbidity (A_{400}) curves of the 10 μM WT, C9Y, and C241S after 1 mM H_2O_2 treatment for 12 h at 4°C.

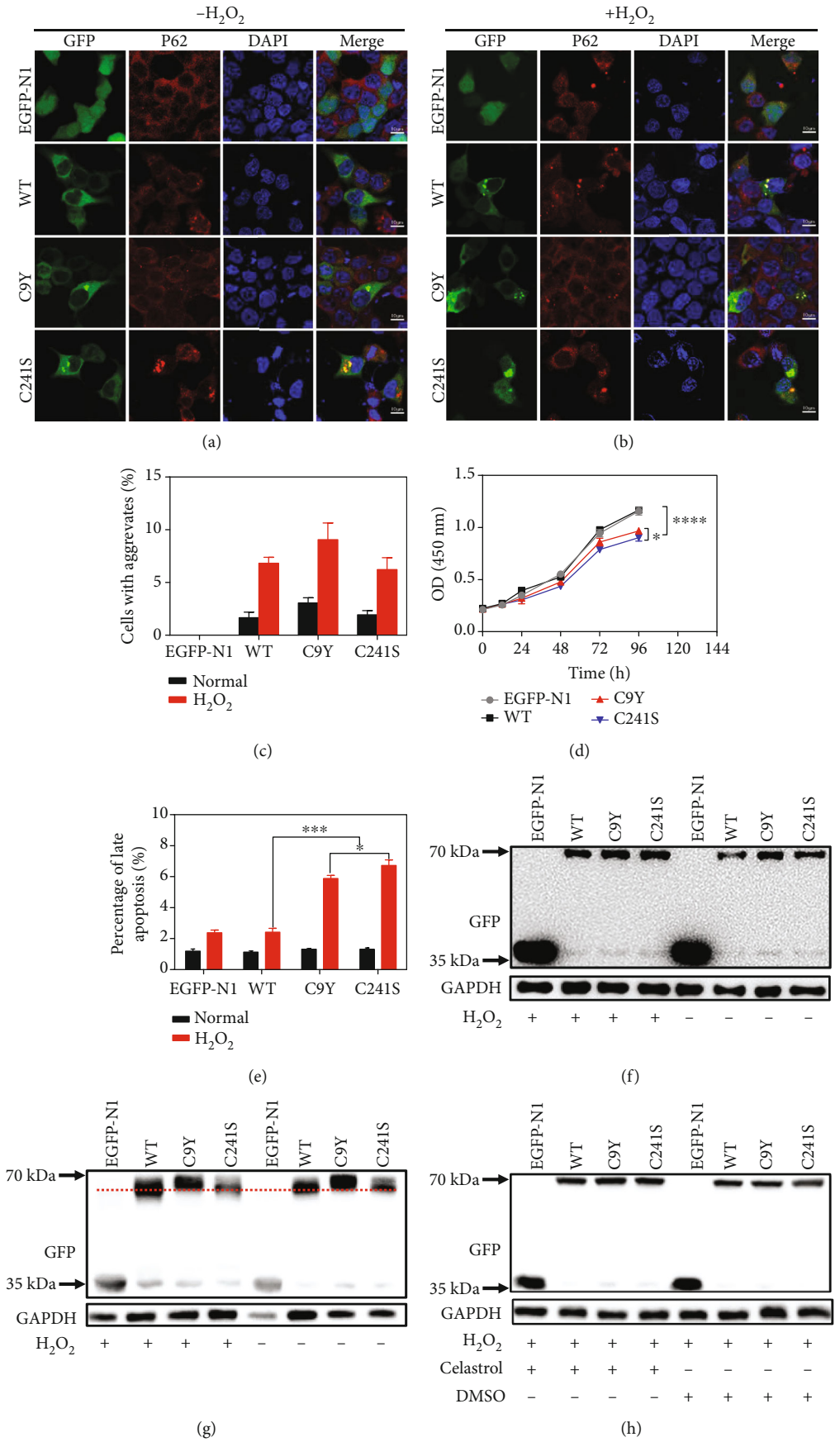

Figure 5: Continued.

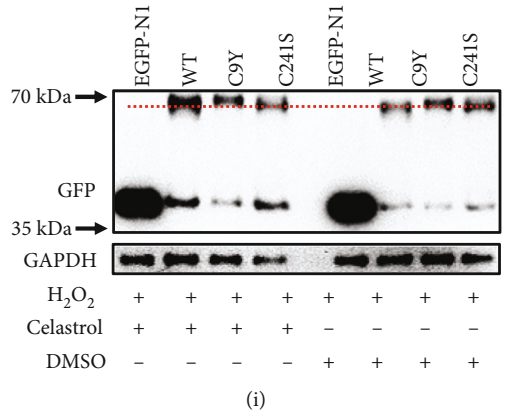

Figure 5: The oxidization and mutation promote protein aggregation and cell apoptosis in cell. (a, b) Representative confocal images of HEK293T cells with exogenous expression of the WT, C9Y, and C241S fused by GFP at the C-terminus without (a) or with (b) 2 mM H_2O_2 treatment. Exogenously expressed PMM2 proteins were visualized by GFP (green), the aggresomes were marked by P62 (red), and nucleus was stained by DAPI (blue) represented nucleus; scale bars, 10 μm. (c) Quantitative analysis of protein aggregation in HEK293T cells. (d) Cell growth assay was performed in 96-well format using the CCK8 cell proliferation kit. Each sample was assayed in triplicates for 4 days consecutively. (e) Quantitative analysis of the percentages of late apoptosis. (f, g) Reduced (f) and nonreducing (g) SDS-PAGE and Western blot analysis of protein solutions without or with 2 mM H_2O_2 for 2 h before cells harvested. $^{*}p < 0.05$. (h, i) Reduced (h) and nonreducing (i) SDS-PAGE and Western blot analysis of protein solutions with 2 mM H_2O_2 and treated with 0.5 μM celastrol ($^{***}p < 0.001$, $^{****}p < 0.0001$).

expression of Hsp27, Hsp40, Hsp70, and Hsp90) and by inhibiting the proteasome system, whereas knockdown the HSR led to different responses of the variants, which suggest different cellular strategies exist for dealing with misfolded proteins. In our cases, C9Y and C241S did not change the protein level compared to WT both at normal and H_2O_2 treatment, and celastrol did not elevate the protein level of these variants. Furthermore, we found celastrol may bind at the interface between the domains of PMM2, which is similar to the binding site of Glc-1,6-P2, the essential activator of PMM2 (supplement Figure 2). Celastrol could not change the states of Cys variants, which was taken for granted.

3.5. The Cysteine Variants Led to More Flexible Structure Identified by MD. The Cys9 and Cys241 were located in the N-terminal first β-sheet and last α-helix, respectively, in the core domain. To monitor the aggregation process caused by Cys variants, molecular dynamic (MD) simulations of the dimer was performed to establish a structural basis for the harmful effects of Cys substitution. Alignment of the dimeric structures accomplished by simulations of PMM2 and Cys variants indicated that the mutation apparently altered the overall folding of PMM2 (Figure 6(a)). A close inspection of the surface electrostatic potentials indicated that the Cys variants modified the distribution of charged/polar residues around the subunit interface, especially within the field of dashed circles (Figure 6(b)). The root mean square deviations (RMSDs) of Cα atoms were calculated (residues 5–244 aa) from the starting structure. As shown in Figure 6(c), the RMSD of the PMM2 WT stayed fairly low, whereas the Cys variants C9Y/C241S displayed changeable values throughout the simulation. The changes were most obvious in the simulation around the C9Y and C241S mutation sites, particularly for the core domain (1-83 and 189-246 aa). The results of the time course of Cα RMSD were similar and that of the WT remained practically steady in the last 100 ns. However, the CαRMSD values of C9Y and C241S varied substantially during the simulation (Figure 6(d)). Similar to the changes in the global dynamics, the Cα root mean square fluctuations (RMSFs) from the initial structures were measured throughout the trajectories. As Figure 6(e) showed, the large changes in RMSF were focused on the local mutation sites. Furthermore, the Cys variants greatly reduced the subunit binding energy arisen from electrostatic interactions (Figures 6(f)–6(h)). Our simulation results were consistent with experimentally observed phenomena and further explained the instability of the Cys variants.

4. Discussion

Glycosylation modifications are ubiquitous in biology and play a pivotal role that includes recognition in the immune system and mediation of diverse responses such as cellular trafficking, and surface receptor signaling dynamics to modulate signal transduction, apoptosis, and tumor metastasis [39]. PMM2-CDG is a rare autosomal recessive disease. Normally, it is an outcome of high-risk pregnancy; the risk of having a child with PMM2-CDG is close to 1/3 instead of the expected 1/4 that was usually estimated by the previous studies [1, 19]. PMM2 is a key enzyme in the initial steps of N-glycosylation, which is essential for the translation of mannose-6-phosphate into mannose-1-phosphate [3]. Its mutation in humans leads to various kinds of diseases, including PMM2-CDG, glaucoma, hyperinsulinemic hypoglycemia, polycystic kidney disease, and premature ovarian insufficiency [40–43]. The clinical presentation and onset of PMM2-CDG vary among affected individuals according to mutation sites and types [44]. However,

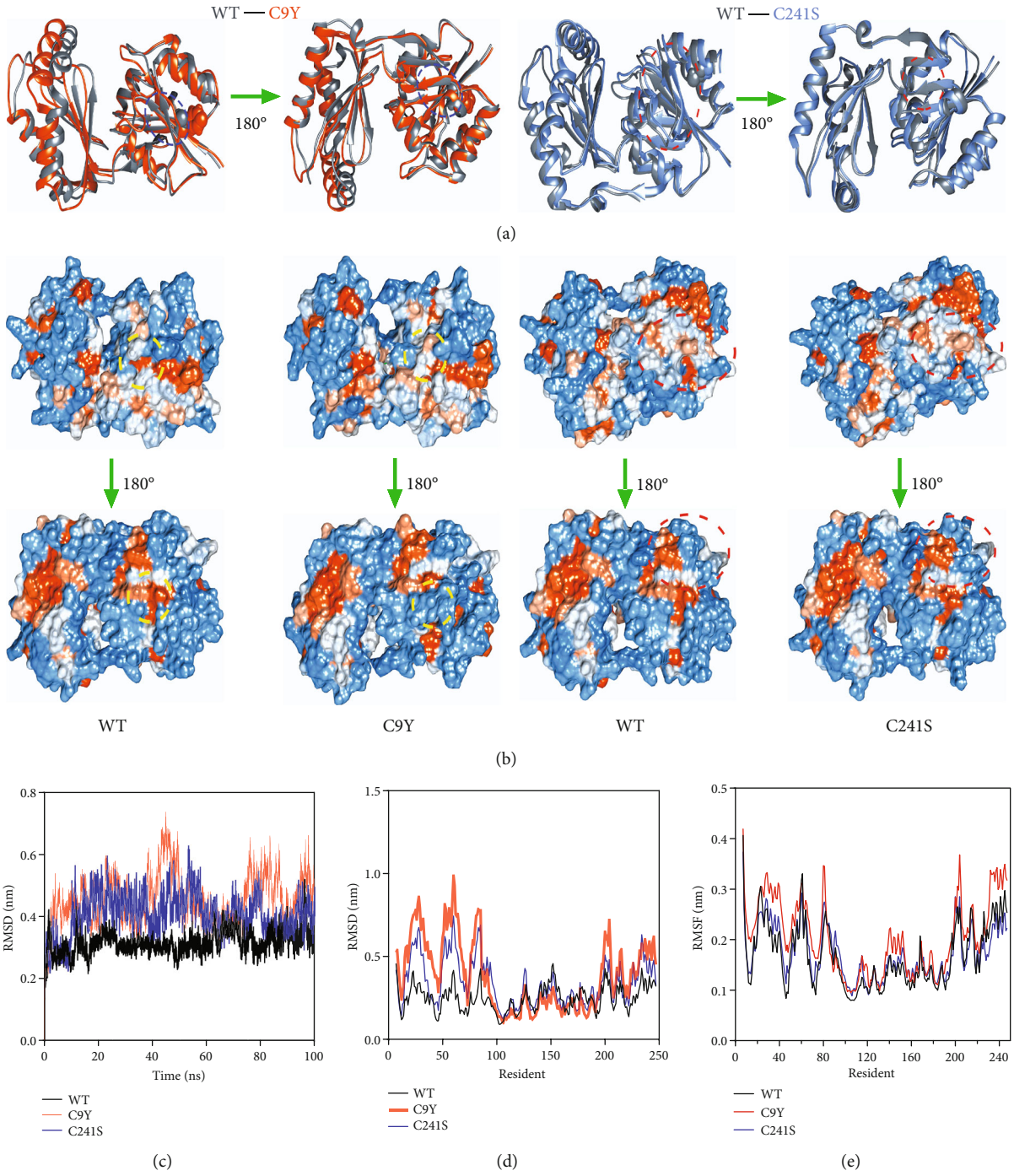

Figure 6: Continued.

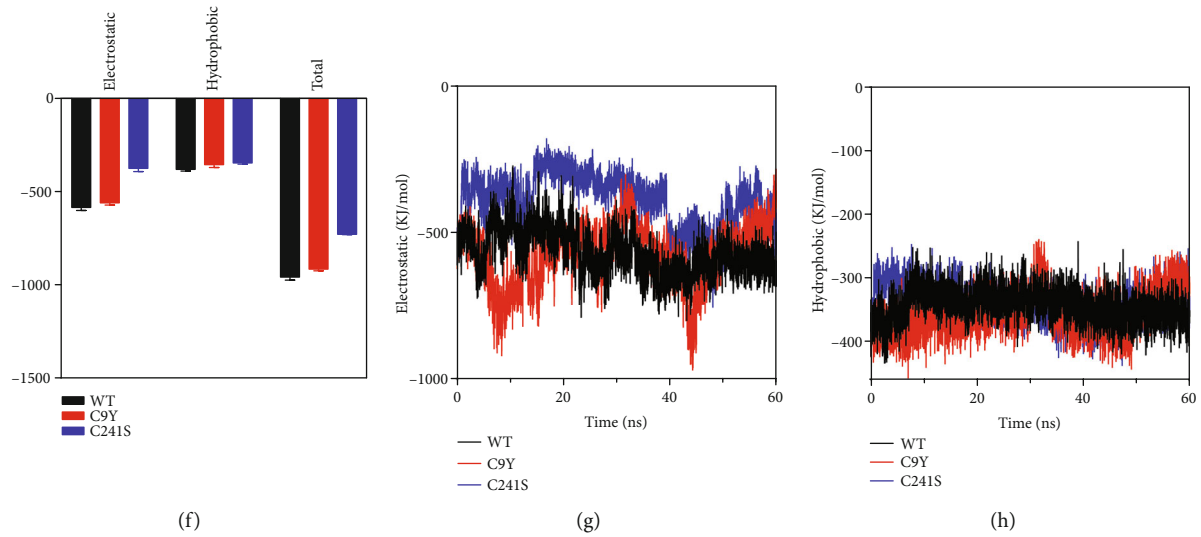

(f) (g) (h)

Figure 6: Overall dynamics of PMM2 calculated from simulations. (a) A comparison of the well-done simulated dimeric structures of the WT, C9Y, and C241S. The Cys variants altered the structure were indicated by dotted circles; blue: C9Y; red: C241S. (b) Surface electrostatic potentials of the dimeric WT and Cys variants. The Cys variants altered the distribution of charged residues, and the representative areas were indicated by dotted circles; yellow: C9Y; red: C241S. (c) Cα root mean square deviation (RMSD) of the dimeric WT and Cys variants from the initial structure of time for all simulations. (d) RMSD of residues for all simulations. (e) Cα root mean square fluctuation (RMSF) of residues for all simulations. (f) Average subunit binding energies calculated from the simulated structures. (g, h) The time-course changes in subunit binding energies of electrostatic (g) and hydrophobic (h).

currently, no suitable treatment is available, only symptomatic therapy. Previous studies that focused on hotspot pathogenic variants R141H and F119L in the native state were limited to the protein level [8, 14]. Rare attention has been given to the unique Cys residue functions under stress conditions in PMM2. However, the Cys residues are active components of catalytic, oxidation-reduction, and signal transduction pathways and have distinct physicochemical properties [24]. Cys could help constrain any structural component of a peptide by creating disulfide bonds that increase the rigidity [45]. Variants in Cys have been found in various diseases, and Cys residues have potential for use as therapeutic targets [46–49]. Therefore, the goal of this article was to elucidate the molecular mechanism underlying the loss-of-function of the Cys pathogenic variants, by evaluating the pathogenicity of the Cys changes and their effects on the stability of the PMM2 protein.

Our experimental results showed that the two examined Cys pathogenic variants changed the secondary and tertiary structures, led to a looser global structure, and reduced the solubility of PMM2, as indicated by spectroscopy experiments using purified recombinant proteins (Figures 1(b)–1(g)). Concomitantly, the MD results suggested that the two Cys variants mainly disrupted the core domain (1-83 and 189-246 aa) (Figures 6(c)–6(e)). Regardless of whether the mutation was of the N-terminus (C9Y) or the C-terminus (C241S), the Cα RMSF values fluctuated similarly, thereby suggesting that there might be a link between C9 and C241. Alignment of well-balanced simulated structures indicated that the Cys variants exhibited a higher ratio of β-sheet and hydrophobic surface and were prone to form aggregates, which was consistent with the Far-UV data (Figures 1(d), 1(e), 6(a), and 6(b)). As for the subunit binding energy, C241Y significantly reduced the subunit binding energy, especially in the electronic part (Figures 6(f)–6(h)). Combined with the structural analysis of the Cys variants by spectroscopy experiments and MD, these experiments provided detailed insights into the mechanism by which the Cys pathogenic variants changed the molecular structure of PMM2.

Cys residues play a vital role in sensing and protecting cells against oxidation, which is one of the major and most studied mechanisms. Oxidative stress has been established as a primary source of various forms of cellular damage, which all might result in protein misfolding and aggregation [50]. Sulfur-containing Cys residues not only manifest potent nucleophilicity but also undergo a facile oxidation reaction to generate disulfide bonds. From the structure obtained by X-ray diffraction, we measured the distance between Cys9 and Cys241, which is suitable for the formation of disulfide bonds. The result of disulfide linkages characterized by MS showed that C9 and C241 had a high potential to form intradisulfide bond (Table 1). Intrachain disulfide bonds are buried between the two layers of antiparallel β-sheet structure [51], and disruption the disulfide bond may explain that the C9Y and C241S destabilized the secondary and tertiary structures of PMM2. The free thiol measurement indicated that C9Y variant contained more number of free thiol than the WT, and the introduced free thiol may have come from the disruption of the disulfide bond (Figures 1(a) and 1(h)). Moreover, as shown in supplement Figure 3, after 100 ns simulation, the C9Y had a visible looser structure than WT and C241S. Meanwhile, for WT, there were two hydrogen bonds of Cys9 and two hydrogen

bonds of Cys241; for C9Y and C241S, there were a total of three hydrogen bonds. The free thiol contents and hydrogen bond of the variants may explain why C9Y had less enzymatic activity than C241S and why C241S presented a milder phenotype [14, 15].

Consistent with previous results, oxidative stresses modified the structure and decreased the stability of the Cys variant proteins [47, 52]. The perturbation of the disulfide-bonding network favored hydrophobic side chain exposure, which was consistent with a previous study [46]. H_2O_2, considered an important redox signaling molecule, could cause oxidation of thiol groups of Cysteines in target proteins [53]. Substitution by Cys has been shown to increase sensitivity to oxidative stress in various diseases [54–56]. In our case, conversely, the Cys residues were replaced with other amino acids. Surprisingly, however, at both the purified protein level and the cellular level, we found the Cys mutation increased the susceptibility to oxidase stress (Figures 4 and 5). After H_2O_2 treatment, the C9Y formed more of the larger oligomers observed in the nonreducing PAGE gels. To the best of our knowledge, this is the first study to demonstrate that PMM2 would form aggregates in cells. The Cys variants could inhibit cell growth and promote cell apoptosis under oxidizing stress. It may provide a new horizon that PMM2 mutation may not only changed the enzymatic activity of PMM2 but also affected the cell viability. Of course, it is possible that decreased cell viability is the indirect result of decreased enzymatic activity.

Previous thermal stability results indicated that PMM2 variants were less stable than the WT [15]. In our work, we obtained a similar conclusion: The A_{400} turbidity curve showed a significant increase over time and plateaued at 4 h (Figure 2(a)). Trp and ANS fluorescence curves indicated that a large hydrophobicity surface was exposed after 37°C treatment (Figures 2(b) and 2(d)). Far-CD spectra result suggested that most of the variants lost their fold structure at physiological temperature, namely, 37°C (Figure 2(c)). Most of the Cys variants were unstable and were present in the precipitated fraction after treatment at 37°C for 4 h (Figures 2(e) and 2(f)). Further thermal aggregation results and Uncle data showed the Cys variants disrupted the compact domain organization and that the variants were prone to forming more massive aggregates (Figure 3). Meanwhile, we tested the protein stability in vivo by cycloheximide and got similar results that the C9Y and C241S mutants showed faster degradation rate than that of EGFP-N1 and WT in HEK293T cells (supplement Figure 4). Combined with the spectroscopic results shown in Figures 1 and 6, it is possible that the Cys mutation destabilized the core domain of PMM2.

Approximately 20% of human proteins are predicted to contain a disulfide bond [57]. Combined with the free thiol assay results and susceptibility to oxidative stresses, the changes that were observed in the stability and folding of the PMM2 protein in response to rupture of the disulfide bond were similar to those of some prion proteins [46]. We hypothesized that the disulfide bond in C9 and C241 stabilized the core structure much like the pincers of a crab. When one of the Cys residues was substituted, the core domain became loose, as indicated by the experimental data. The number of free thiols for C241S did not change, and C241S presented a milder clinical phenotype than C9Y [21]. This may have been due to the occurrence of unwanted intermolecular disulfide bonding as C241 was located at the C-terminus. From the MS data, for C241S variant, we guessed C9 may form disulfide bond with C136. That could explain why C241S had a free thiol content that was similar to that of the WT (Table 1). Furthermore, the potential disulfide bonding could explain why C9Y and C241S were not in accord with the expectation that the Cys residues would become more sensitive to oxidative stresses. In this case, the disulfide bonds were covalent bonds between sulfur atoms of cysteine residues, which could stabilize the structure of PMM2.

Patients with PMM2-CDG have a life-threatening insufficiency; thus, more effective drugs warrant to be developed. However, celastrol, recently proposed as a potential rescuer of PMM2 activity [7], did not change the Cys variants protein level in either nonreducing PAGE gels or reducing PAGE gels (Figure 5). And our results of molecular docking simulation revealed that celastrol did not interact at the mutation sites and no protective effects on the Cys variants. In this project, we have documented for the first time that PMM2 variants form aggresomes, inhibit cell growth, and promote cell apoptosis, especially under environmental stress (thermal and oxidative). Furthermore, we proposed Cys and potential disulfide bond may have a significant effect on the conformation and thermal stability of the PMM2. These results provide proof-of-concept regarding the clinical treatment of PMM2-CDG. Beyond pharmacological chaperones, combinations with antioxidation reagents merit investigation as treatments. Our study contributed to fill in the knowledge gap in terms of PMM2 mechanisms, and accordingly, the early detection of patients at risk and development of prevention and treatment strategies could be conducted by future studies.

Data Availability

The original data used to support the findings of this study are available from the corresponding author upon request.

Conflicts of Interest

The authors declare no competing interests.

Authors' Contributions

Lidan Hu and Jianhua Mao conceived, designed, and supervised the research. Fan Yu, Li Lin, and Jingmiao Sun performed the experiments. Liangjian Ma, Jicheng Pan, Yixin Liao, and Guannan Bai identified pathogenic variants. Lidan Hu, Jianhua Mao, Fan Yu, and Li Lin performed data analyses. Lidan Hu wrote the manuscript. All authors have read and approved the final version of the manuscript. Fan Yu, Li Lin, and Jingmiao Sun contributed equally to this work.

Acknowledgments

I am extremely grateful to all members of the Hu Lab and Mao Lab, past and present, for the interesting discussions and great contributions to the project. We thank Dr. Xiangjun Chen for the helpful suggestions on this manuscript. I thank the National Clinical Research Center for Child Health for the great support. This study was financially supported by the grant of the Natural Science Foundation of Zhejiang Province (No. LQ22C070004) to Lidan Hu and by the grant of the National Natural Science Foundation of China (U20A20351, 81770710) to Jianhua Mao.

Supplementary Materials

Supplement Figure 1: analysis the enzymatic activity of purified WT-PMM2. Supplement Figure 2: the molecular docking simulation of celastrol by AutoDock Vina software. Supplement Figure 3: analysis the structural difference by MD. (A) The last frames of the MD equilibrations were used as structures for further analysis. (B) Analysis the hydrogen bonding of Cys9 (shown with green color) and Cys241 (shown with red color). Supplement Figure 4: the CHX-mediated protein stability assay of EGFP-N1, WT, C9Y, and C241S mutants. (A) Cells were harvested at the indicated times (0, 2, 4, 6, 8, and 12 h) after treatment of 100 μg/mL CHX and analyzed by Western blotting of GFP. GAPDH was used as a loading control. (B) The relative amounts of GFP for the Western blots shown in (A) were determined by densitometry and corrected for loading against GAPDH. The ratio of relative densitometry value at each time to 0 h is presented on the line chart. *(Supplementary Materials)*

References

[1] C. Lam and D. M. Krasnewich, "PMM2-CDG," in *GeneReviews(®), University of Washington, Seattle Copyright © 1993-2021*, M. P. Adam, H. H. Ardinger, R. A. Pagon, S. E. Wallace, L. J. H. Bean, K. W. Gripp, G. M. Mirzaa, and A. Amemiya, Eds., University of Washington, Seattle (WA), 1993.

[2] T. J. de Koning, L. Dorland, O. P. van Diggelen et al., "A novel disorder of N-glycosylation due to phosphomannose isomerase deficiency," *Biochemical and Biophysical Research Communications*, vol. 245, no. 1, pp. 38–42, 1998.

[3] G. Matthijs, E. Schollen, E. Pardon et al., "Mutations in *PMM2*, a phosphomannomutase gene on chromosome 16p13 in carbohydrate-deficient glycoprotein type I syndrome (Jaeken syndrome)," *Nature Genetics*, vol. 16, no. 1, pp. 88–92, 1997.

[4] M. Schiff, C. Roda, M. L. Monin et al., "Clinical, laboratory and molecular findings and long-term follow-up data in 96 French patients with PMM2-CDG (phosphomannomutase 2-congenital disorder of glycosylation) and review of the literature," *Journal of Medical Genetics*, vol. 54, no. 12, pp. 843–851, 2017.

[5] R. Altassan, R. Péanne, J. Jaeken et al., "International clinical guidelines for the management of phosphomannomutase 2-congenital disorders of glycosylation: diagnosis, treatment and follow up," *Journal of Inherited Metabolic Disease*, vol. 42, no. 1, pp. 5–28, 2019.

[6] P. Yuste-Checa, S. Brasil, A. Gámez et al., "Pharmacological chaperoning: a potential treatment for PMM2-CDG," *Human Mutation*, vol. 38, no. 2, pp. 160–168, 2017.

[7] A. Vilas, P. Yuste-Checa, D. Gallego et al., "Proteostasis regulators as potential rescuers of PMM2 activity," *Molecular Basis of Disease*, vol. 1866, no. 7, article 165777, 2020.

[8] G. Andreotti, E. Pedone, A. Giordano, and M. V. Cubellis, "Biochemical phenotype of a common disease-causing mutation and a possible therapeutic approach for the phosphomannomutase 2-associated disorder of glycosylation," *Molecular Genetics & Genomic Medicine*, vol. 1, no. 1, pp. 32–44, 2013.

[9] S. C. Grünert, T. Marquardt, E. Lausch et al., "Unsuccessful intravenous D-mannose treatment in PMM2-CDG," *Orphanet Journal of Rare Diseases*, vol. 14, no. 1, p. 231, 2019.

[10] Z. Li, C. Zhu, Y. Ding, Y. Fei, and B. Lu, "ATTEC: a potential new approach to target proteinopathies," *Autophagy*, vol. 16, no. 1, pp. 185–187, 2020.

[11] L. Huang, T. Agrawal, G. Zhu et al., "DAXX represents a new type of protein-folding enabler," *Nature*, vol. 597, no. 7874, pp. 132–137, 2021.

[12] S. Tomoshige and M. Ishikawa, "PROTACs and other chemical protein degradation technologies for the treatment of neurodegenerative disorders," *Angewandte Chemie International Edition*, vol. 60, no. 7, pp. 3346–3354, 2021.

[13] R. Sharma, T. Srivastava, A. R. Pandey et al., "Identification of natural products as potential pharmacological chaperones for protein misfolding diseases," *ChemMedChem*, vol. 16, no. 13, pp. 2146–2156, 2021.

[14] A. I. Vega, C. Pérez-Cerdá, D. Abia et al., "Expression analysis revealing destabilizing mutations in phosphomannomutase 2 deficiency (PMM2-CDG)," *Journal of Inherited Metabolic Disease*, vol. 34, no. 4, pp. 929–939, 2011.

[15] P. Yuste-Checa, A. Gámez, S. Brasil et al., "The effects of PMM2-CDG-causing mutations on the folding, activity, and stability of the PMM2 protein," *Human Mutation*, vol. 36, no. 9, pp. 851–860, 2015.

[16] A. Gámez, P. Yuste-Checa, S. Brasil et al., "Protein misfolding diseases: prospects of pharmacological treatment," *Clinical Genetics*, vol. 93, no. 3, pp. 450–458, 2018.

[17] K. Mukaigasa, T. Tsujita, V. T. Nguyen et al., "Nrf 2 activation attenuates genetic endoplasmic reticulum stress induced by a mutation in the phosphomannomutase 2 gene in zebrafish," *Proceedings of the National Academy of Sciences of the United States of America*, vol. 115, no. 11, pp. 2758–2763, 2018.

[18] C. Thiel, T. Lübke, G. Matthijs, K. von Figura, and C. Körner, "Targeted disruption of the mouse phosphomannomutase 2 gene causes early embryonic lethality," *Molecular and Cellular Biology*, vol. 26, no. 15, pp. 5615–5620, 2006.

[19] A. Briso-Montiano, F. Del Caño-Ochoa, A. Vilas et al., "Insight on molecular pathogenesis and pharmacochaperoning potential in phosphomannomutase 2 deficiency, provided by novel human phosphomannomutase 2 structures," *Journal of Inherited Metabolic Disease*, vol. 45, no. 2, pp. 318–333, 2022.

[20] M. Schwartz, "Carbohydrate-deficient glycoprotein syndrome type 1A: expression and characterisation of wild type and mutant PMM2 in *E. coli*," *European Journal of Human Genetics*, vol. 7, no. 8, pp. 884–888, 1999.

[21] C. Bjursell, A. Erlandson, M. Nordling et al., "PMM2 mutation spectrum, including 10 novel mutations, in a large CDG type 1A family material with a focus on Scandinavian families," *Human Mutation*, vol. 16, no. 5, pp. 395–400, 2000.

[22] C. Le Bizec, S. Vuillaumier-Barrot, A. Barnier, T. Dupre, G. Durand, and N. Seta, "A new insight into PMM2 mutations in the French population," *Human Mutation*, vol. 25, no. 5, pp. 504-505, 2005.

[23] J. M. Held, "Redox systems biology: harnessing the sentinels of the cysteine redoxome," *Antioxidants & Redox Signaling*, vol. 32, no. 10, pp. 659–676, 2020.

[24] L. B. Poole, "The basics of thiols and cysteines in redox biology and chemistry," *Free Radical Biology & Medicine*, vol. 80, pp. 148–157, 2015.

[25] D. E. Fomenko, S. M. Marino, and V. N. Gladyshev, "Functional diversity of cysteine residues in proteins and unique features of catalytic redox-active cysteines in thiol oxidoreductases," *Molecules and Cells*, vol. 26, no. 3, pp. 228–235, 2008.

[26] H. Qiu, D. M. Honey, J. S. Kingsbury et al., "Impact of cysteine variants on the structure, activity, and stability of recombinant human α-galactosidase A," *Protein Science*, vol. 24, no. 9, pp. 1401–1411, 2015.

[27] J. Veno, R. Rahman, M. Masomian, M. S. M. Ali, and N. H. A. Kamarudin, "Insight into improved thermostability of cold-adapted staphylococcal lipase by glycine to cysteine mutation," *Molecules*, vol. 24, no. 17, p. 3169, 2019.

[28] L. Xu, H. Cao, C. Huang, and L. Jia, "Oriented immobilization and quantitative analysis simultaneously realized in sandwich immunoassay via His-tagged nanobody," *Molecules*, vol. 24, no. 10, p. 1890, 2019.

[29] E. Bourdon, N. Loreau, L. Lagrost, and D. Blache, "Differential effects of cysteine and methionine residues in the antioxidant activity of human serum albumin," *Free Radical Research*, vol. 39, no. 1, pp. 15–20, 2005.

[30] S. Vuillaumier-Barrot, G. Hetet, A. Barnier et al., "Identification of four novel PMM2 mutations in congenital disorders of glycosylation (CDG) Ia French patients," *Journal of Medical Genetics*, vol. 37, no. 8, pp. 579-580, 2000.

[31] R. R. Burgess, "A brief practical review of size exclusion chromatography: rules of thumb, limitations, and troubleshooting," *Protein Expression and Purification*, vol. 150, pp. 81–85, 2018.

[32] E. R. S. Kunji, M. Harding, P. J. G. Butler, and P. Akamine, "Determination of the molecular mass and dimensions of membrane proteins by size exclusion chromatography," *Methods*, vol. 46, no. 2, pp. 62–72, 2008.

[33] P. G. Squire, "A relationship between the molecular weights of macromolecules and their elution volumes based on a model for Sephadex gel filtration," *Archives of Biochemistry and Biophysics*, vol. 107, no. 3, pp. 471–478, 1964.

[34] K. J. Wang, X. Y. Liao, K. Lin et al., "A novel F30S mutation in γS-crystallin causes autosomal dominant congenital nuclear cataract by increasing susceptibility to stresses," *International Journal of Biological Macromolecules*, vol. 172, pp. 475–482, 2021.

[35] K. K. Turoverov, S. Y. Haitlina, and G. P. Pinaev, "Ultra-violet fluorescence of actin. Determination of native actin content in actin preparations," *FEBS Letters*, vol. 62, no. 1, pp. 4–6, 1976.

[36] J. J. Gorman, T. P. Wallis, and J. J. Pitt, "Protein disulfide bond determination by mass spectrometry," *Mass Spectrometry Reviews*, vol. 21, no. 3, pp. 183–216, 2002.

[37] V. Westphal, S. Peterson, M. Patterson et al., "Functional significance of *PMM2* mutations in mildly affected patients with congenital disorders of glycosylation Ia," *Genetics in Medicine*, vol. 3, no. 6, pp. 393–398, 2001.

[38] J. Xu, H. Wang, A. Wang et al., "βB2 W151R mutant is prone to degradation, aggregation and exposes the hydrophobic side chains in the fourth Greek Key motif," *Biochimica et Biophysica Acta (BBA) - Molecular Basis of Disease*, vol. 1867, no. 2, article 166018, 2021.

[39] X. Li, Z. Xu, X. Hong, Y. Zhang, and X. Zou, "Databases and bioinformatic tools for glycobiology and glycoproteomics," *International Journal of Molecular Sciences*, vol. 21, no. 18, p. 6727, 2020.

[40] J. L. Wiggs and L. R. Pasquale, "Genetics of glaucoma," *Human Molecular Genetics*, vol. 26, no. R1, pp. R21–r27, 2017.

[41] H. Demirbilek and K. Hussain, "Congenital hyperinsulinism: diagnosis and treatment update," *Journal of Clinical Research in Pediatric Endocrinology*, vol. 9, Suppl 2, pp. 69–87, 2017.

[42] T. Peng, C. Lv, H. Tan et al., "Novel PMM2 missense mutation in a Chinese family with non-syndromic premature ovarian insufficiency," *Journal of Assisted Reproduction and Genetics*, vol. 37, no. 2, pp. 443–450, 2020.

[43] E. F. Carney, "*PMM2* mutation causes PKD and hyperinsulinism," *Nature Reviews. Nephrology*, vol. 13, no. 6, p. 321, 2017.

[44] L. Vaes, D. Rymen, D. Cassiman et al., "Genotype-phenotype correlations in PMM2-CDG," *Genes*, vol. 12, no. 11, p. 1658, 2021.

[45] T. Bosma, R. Rink, M. A. Moosmeier, and G. N. Moll, "Genetically encoded libraries of constrained peptides," *Chembiochem*, vol. 20, no. 14, pp. 1754–1758, 2019.

[46] L. Ning, J. Guo, N. Jin, H. Liu, and X. Yao, "The role of Cys179-Cys214 disulfide bond in the stability and folding of prion protein: insights from molecular dynamics simulations," *Journal of Molecular Modeling*, vol. 20, no. 2, p. 2106, 2014.

[47] W. J. Zhao and Y. B. Yan, "Increasing susceptibility to oxidative stress by cataract-causing crystallin mutations," *International Journal of Biological Macromolecules*, vol. 108, pp. 665–673, 2018.

[48] D. Das and J. Hong, "Irreversible kinase inhibitors targeting cysteine residues and their applications in cancer therapy," *Mini Reviews in Medicinal Chemistry*, vol. 20, no. 17, pp. 1732–1753, 2020.

[49] K. K. Hallenbeck, D. M. Turner, A. R. Renslo, and M. R. Arkin, "Targeting non-catalytic cysteine residues through structure-guided drug discovery," *Current Topics in Medicinal Chemistry*, vol. 17, no. 1, pp. 4–15, 2017.

[50] A. Carija, S. Navarro, N. S. de Groot, and S. Ventura, "Protein aggregation into insoluble deposits protects from oxidative stress," *Redox Biology*, vol. 12, pp. 699–711, 2017.

[51] H. Kikuchi, Y. Goto, and K. Hamaguchi, "Reduction of the buried intrachain disulfide bond of the constant fragment of the immunoglobulin light chain: global unfolding under physiological conditions," *Biochemistry*, vol. 25, no. 8, pp. 2009–2013, 1986.

[52] W. J. Zhao, J. Xu, X. J. Chen, H. H. Liu, K. Yao, and Y. B. Yan, "Effects of cataract-causing mutations W59C and W151C on βB2-crystallin structure, stability and folding," *International Journal of Biological Macromolecules*, vol. 103, pp. 764–770, 2017.

[53] Y. Tian, M. Fan, Z. Qin et al., "Hydrogen peroxide positively regulates brassinosteroid signaling through oxidation of the BRASSINAZOLE-RESISTANT1 transcription factor," *Nature Communications*, vol. 9, no. 1, p. 1063, 2018.

[54] A. I. Alayash, "βCysteine 93 in human hemoglobin: a gateway to oxidative stability in health and disease," *Laboratory Investigation*, vol. 101, no. 1, pp. 4–11, 2021.

[55] N. Fujiwara, M. Nakano, S. Kato et al., "Oxidative modification to cysteine sulfonic acid of Cys^{111} in human copper-zinc superoxide dismutase∗," *The Journal of Biological Chemistry*, vol. 282, no. 49, pp. 35933–35944, 2007.

[56] A. P. Vintém, N. T. Price, R. B. Silverman, and R. R. Ramsay, "Mutation of surface cysteine 374 to alanine in monoamine oxidase a alters substrate turnover and inactivation by cyclopropylamines," *Bioorganic & Medicinal Chemistry*, vol. 13, no. 10, pp. 3487–3495, 2005.

[57] X. Gao, X. Dong, X. Li, Z. Liu, and H. Liu, "Prediction of disulfide bond engineering sites using a machine learning method," *Scientific Reports*, vol. 10, no. 1, article 10330, 2020.

Hindawi
Oxidative Medicine and Cellular Longevity
Volume 2022, Article ID 2405972, 7 pages
https://doi.org/10.1155/2022/2405972

Research Article

Serum Lipopolysaccharide Is Associated with the Recurrence of Atrial Fibrillation after Radiofrequency Ablation by Increasing Systemic Inflammation and Atrial Fibrosis

Meng Wang,[1] **Hua Xiong**,[1] **Li Lu**,[1] **Tongjian Zhu**,[2] **and Hong Jiang**[1]

[1]*Department of Cardiology, Renmin Hospital of Wuhan University, Wuhan, China*
[2]*Department of Cardiology, Xiangyang Central Hospital, Affiliated Hospital of Hubei University of Arts and Science, Xiangyang, China*

Correspondence should be addressed to Tongjian Zhu; whuzhutongjian@126.com and Hong Jiang; hong-jiang@whu.edu.cn

Received 30 June 2022; Revised 13 September 2022; Accepted 28 September 2022; Published 15 October 2022

Academic Editor: Jianbo Wu

Objectives. The gut microbiota and its metabolites are linked to inflammation and contribute to the progression of atrial fibrillation (AF), but the predictive value of the gut microbiota-derived metabolite lipopolysaccharide (LPS) for AF recurrence (RAF) is unknown. This study is aimed at investigating (1) the correlation between LPS and RAF and (2) its relationship with inflammation and atrial fibrosis. *Method*. We performed a single-centre retrospective analysis in 159 AF patients. Fasting plasma samples were collected, and an enzyme-linked immunosorbent assay was used to determine the levels of serum LPS, interleukin-6 (IL-6), collagen type-1 C-terminal telopeptide (CITP), and transforming growth factor-β1 (TGFβ1). The cumulative risk for RAF was evaluated with Kaplan–Meier analysis. Cox proportional hazard analysis was carried out to predict the hazard of RAF. The correlations among LPS and IL-6, CITP, TGFβ1, and left atrial diameter (LAD) were analysed by Pearson's correlation coefficient. Subsequent univariate and multivariable linear regression analyses were carried out to evaluate the connection between clinical variables and Log-LPS. *Results*. All 159 AF patients were included in this study. The proportion of persistent atrial fibrillation was 40.3%, the mean age was 61.9 ± 10.1 years, the proportion of males was 61.6%, and the mean LPS was 56.5 ± 29.5 pg/mL. After all patients were divided into tertiles according to the circulating LPS level, a total of 44 RAF occurred: 10 in the first tertile, 15 in the second tertile, and 19 in the third tertile (log-rank test $P = 0.037$). Heart failure (hazard ratio 2.029, $P = 0.041$), LAD (hazard ratio 1.064, $P = 0.022$), Log-LPS (hazard ratio 5.686, $P = 0.043$), and CITP (hazard ratio 6.841, $P = 0.033$) independently predicted the risk of RAF. In all patients, univariate analysis showed that heart failure, LAD, hs-CRP, IL-6, CITP, and TGF-β1 were connected with Log-LPS. Multivariate linear regression analysis indicated that IL-6 and hs-CRP were independently and positively connected with Log-LPS. *Conclusions*. Our results indicated that circulating LPS was a predictor of RAF and may contribute to RAF incidence after ablation by increasing systemic inflammation and atrial fibrosis.

1. Introduction

Atrial fibrillation (AF) is associated with a high prevalence of arrhythmia, which is connected with heart failure, stroke, and mortality [1, 2]. Previous studies have shown that the gut microbiota and its metabolites are linked to inflammation and contribute to the progression of cardiovascular diseases [3]. Recent data have shown that gut microbiota-derived metabolites such as TMAO are connected with the occurrence and recurrence of atrial fibrillation (AF) [4]. Additionally, animal experiments have also shown that TMAO can promote the progression of AF by affecting systemic inflammation [5]. In addition, Li et al. [6] also demonstrated that a GM-based taxonomic scoring system can effectively predict the accuracy of AF recurrence (RAF) after primary ablation. Therefore, research is necessary to explore the effects of key gut microbiota-derived metabolites on RAF.

Lipopolysaccharide (LPS), a cell wall component from Gram-negative bacteria, is involved in various cardiovascular diseases [7]. Animal experiments have indicated that

LPS can increase the expression levels of inflammatory cytokines and L-type calcium channel proteins as well as shorten the atrial effective refractory period (ERP), thereby promoting the occurrence of atrial fibrillation [8, 9]. Additionally, Zhang et al. [10] demonstrated that age-related gut dysbiosis induces AF by increasing serum LPS and glucose, which could activate the atrial NLRP3 inflammasome and promote atrial fibrosis. In addition, Pastori et al. found that circulating LPS is significantly associated with major adverse cardiovascular events (MACEs) in AF patients by increasing platelet activation [11]. However, the association between LPS and RAF has not been revealed. In this study, we aimed to assess the effect of circulating LPS on RAF during follow-up.

2. Materials and Methods

2.1. Study Population. All 159 enrolled patients were diagnosed with AF according to the guidelines of the European Society of Cardiology [12]. All patients were scheduled for radiofrequency catheter ablation procedures at Renmin Hospital of Wuhan University between February 2019 and February 2021. Major exclusion criteria were as follows: heart failure, any structural heart disease, stroke, infectious diseases, postsurgery status, acute coronary syndrome, renal or hepatic impairment, lipid lowering medication, any autoimmune disease, and other inflammatory diseases.

2.2. Serum Lipopolysaccharide. Fasting venous blood was centrifuged and stored at -80°C until biochemical determination. Serum LPS was determined with commercially available ELISA (Cusabio, Wuhan, China) following the instructions. The detection range of the kit was 6.25 pg/ml-400 pg/ml. The intra-assay and interassay precision were < 8% and < 10%, respectively. The absorbance of the sample was detected at 450 nm within 5 minutes. All serum samples were analysed in duplicate.

2.3. Inflammatory and Fibrotic Biomarkers. Serum samples were diluted twice, and the level of transforming growth factor beta1 (TGF-β1) was measured with commercially available ELISA (Cusabio, Wuhan, China). The value was read at 450 nm, and the detection range was 0.78 ng/mL-50 ng/mL. The interleukin-6 (IL-6) and collagen type-1 C-terminal telopeptide (CITP) levels were measured with a sandwich enzyme immunoassay with a commercially available ELISA (ELK Biotechnology), following the instructions. The intra- and interassay precision of all assays were < 8% and < 10%, respectively.

2.4. Laboratory Analysis. Fasting venous blood was obtained at baseline, and the levels of blood glucose (mmol/L), LDL (mmol/L), HDL (mmol/L), TC (mmol/L), TG (mmol/L), high-sensitivity C-reactive protein (hs-CRP, mg/L), and creatinine (μmol/L) were determined through Dimension EXL with an LM automatic biochemical analyser (Siemens Healthcare Diagnostics).

2.5. Echocardiography. After admission, 2-dimensional transthoracic colour Doppler echocardiography was performed in all patients. Each echocardiographic result was analysed by two blinded experts. The left atrial diameter (LAD) was measured along the parasternal long-axis. The left ventricular (LV) diameters and wall thickness were measured, and the LV ejection fraction was quantitatively analysed according to the modified Simpson method.

2.6. Radiofrequency Catheter Ablation. The intracardiac electrograms were recorded by a computer-based electrophysiology system (Lead XP, Jinjiang Inc., Chengdu, China). We imported and constructed CT image of left atrium and pulmonary veins using CARTO Segmentation software (Biosense Webster, Inc.). Transseptal puncture was performed, and unfractionated heparin was started at 100 U/kg and thereafter at 1,000 U/h by intermittent boluses to maintain an activated clotting time > 250 s. The geometries of PVs were generated under the guidance of the Electroanatomical Mapping System (CARTO, Biosense Webster, Diamond Bar, CA, USA). Then, we merged the CT image and PV electroanatomical map to construct the left atrium anatomical model. Circumferential pulmonary vein isolation (CPVI) was performed using an irrigated catheter. At the endpoint of the procedure, the pulmonary vein spike potential and bidirectional block of the lines were assessed. Electrical cardioversion was performed in patients without restoring sinus rhythm.

2.7. Follow-Up. All participants were followed up for one year after ablation. In the first 3 months, amiodarone therapy was administered to prevent early atrial fibrillation recurrence. Patients with persistent AF receive oral anticoagulation (warfarin or new oral anticoagulants) for 3 months. After ablation, medical examination (24-hour Holter monitoring and 12-lead ECG) was routinely performed at 3, 6, 9, and 12 months. Additional ECGs are obtained if the patients have any suspected symptoms of RAF, such as palpitations and shortness of breath. RAF was defined as any atrial tachycardia lasting at least 30 s according to the ECG recording after the initial 3-month blanking period.

2.8. Statistical Analysis. All numerical analyses were conducted using SPSS 22.0 (SPSS, Inc., Chicago, IL, USA) and GraphPad prim 7.0 Software. The continuous variables are presented as the mean ± SD, and the differences were determined by Student's t test when these variables satisfied a normal distribution. If these variables determined by the Mann–Whitney U test were nonnormal distributions, these variables were presented as medians (interquartile range). The $\chi 2$ test or Fisher's exact test was carried out to compare the differences. All patients were divided into tertiles according to LPS level, and the Kaplan–Meier method was used to calculate the cumulative risk for RAF. The hazard of RAF was analysed using Cox proportional hazards analysis. Correlations among LPS and biomarkers of inflammation and atrial fibrosis were analysed by Pearson's correlation coefficient. Univariate and multivariable linear regression analyses were conducted to detect the clinical variables that were correlated with circulating LPS. Statistical significance was set as a P value < 0.05.

Table 1: Characteristics of subjects with AF study According to RAF.

Variables	All ($n = 159$)	SR maintenance ($n = 115$)	AF recurrence ($n = 44$)	P
Age (year)	61.9 ± 10.1	61.3 ± 10.2	63.3 ± 9.8	0.265
Male, *n* (%)	98 (61.6%)	72 (62.6%)	26 (59.1%)	0.638
Persistent AF, *n* (%)	64 (40.3%)	42 (36.8%)	22 (50.0%)	0.121
Hypertension, *n* (%)	85 (53.5%)	56 (49.1%)	29 (65.9%)	0.052
Diabetes, *n* (%)	21 (13.2%)	13 (11.3%)	8 (18.2%)	0.252
CHD, *n* (%)	35 (22.0%)	24 (20.9%)	11 (25.0%)	0.574
Heart failure, *n* (%)	34 (21.4%)	13 (11.3%)	21 (47.7%)	< 0.001
BMI (kg/m^2)	25.1 ± 3.1	24.8 ± 2.9	25.8 ± 3.5	0.082
Glu (mmol/L)	5.04 (4.64-5.79)	4.99 (4.64-5.79)	5.20 (4.59-5.82)	0.599
LDL (mmol/L)	2.39 ± 0.81	2.4 ± 0.8	2.5 ± 0.8	0.432
HDL (mmol/L)	1.07 (0.93-1.36)	1.08 (0.94-1.36)	1.06 (0.85-1.36)	0.437
TC (mmol/L)	4.11 ± 0.96	4.10 ± 0.94	4.1 ± 1.0	0.916
TG (mmol/L)	1.44 (0.99,2.25)	1.38 (1.01-1.36)	1.33 (0.98-2.05)	0.605
Cr (μmol/L)	71 (58-81)	69 (57-80)	72 (60-86)	0.127
LAD (mm)	39.6 ± 6.1	38.4 ± 5.5	42.7 ± 6.3	< 0.001
Hs-CRP (mg/L)	0.55 (0.41-0.72)	0.52 (0.40-0.68)	0.57 (0.47-0.79)	0.064
LPS (pg/mL)	56.5 ± 29.5	51.5 ± 29.2	69.5 ± 26.2	0.001
IL-6 (pg/mL)	56.8 ± 22.3	53.5 ± 20.8	64.8 ± 23.0	0.004
CITP (ng/mL)	0.62 ± 0.19	0.59 ± 0.19	0.69 ± 0.15	0.004
TGF-β1 (ng/mL)	41.1 ± 15.1	39.5 ± 14.4	45.2 ± 16.3	0.030

CHD: coronary heart disease; BMI: body mass index; LAD: left atrial diameter; IL-6: interleukin-6; CITP: collagen type-1 C-terminal telopeptide; TGF-β1: transforming growth factor beta1; LPS: lipopolysaccharide.

3. Results

3.1. Clinical Characteristics of AF Patients. The characteristics of all 159 enrolled AF patients are presented in Table 1. The mean age was 61.9 ± 10.1 years, 61.6% of the patients were male, and the proportion of persistent atrial fibrillation was 40.3%. The most common comorbidities were hypertension (53.5%), coronary heart disease (22.0%), and heart failure (21.4%). Compared with sinus rhythm (SR) maintenance patients, patients with AF recurrence had a greater LAD and higher levels of inflammatory and fibrotic biomarkers (Table 1).

3.2. LPS and RAF. During the 12-month follow-up period, 72.3% (115/159) of patients successfully maintained sinus rhythm. Of the 159 patients, the mean LPS was 56.5 ± 29.5 pg/mL, 25.2 ± 12.4 pg/mL in the first tertile, 54.9 ± 8.4 pg/mL in the second tertile, and 89.3 ± 17.8 pg/mL in the third tertile. Kaplan–Meier survival analysis indicated a significantly higher recurrence probability in patients with LPS levels in the third tertile. However, compared to the first tertiles, there were no significant differences in the second tertiles (Figure 1). The multivariable Cox regression analysis showed that Log-LPS, LAD, heart failure, and CITP were independent predictors of RAF (Table 2).

3.3. Association between Circulating LPS with Systemic Inflammation and Atrial Fibrosis. Log-LPS was significantly higher than that in patients with RAF (Table 1). Additionally, inflammatory biomarkers (hs-CRP and IL-6), atrial fibrotic biomarkers (CITP and TGF-β), and LAD were significantly increased in patients with RAF ($P < 0.05$, Table 1). Log-LPS was positively correlated with serum inflammatory biomarkers (IL-6: $r = 0.289$, $P < 0.001$; hs-CRP: $r = 0.271$, $P = 0.001$), fibrotic biomarkers (CITP: $r = 0.179$, $P = 0.024$; TGF-β1: $r = 0.197$, $P = 0.013$) and LAD ($r = 0.227$, $P = 0.004$) using Pearson's correlation analysis (Figures 2(a)–2(e)). Univariate linear regression analyses showed that Log-LPS was correlated with heart failure, LAD, hs-CRP, IL-6, CITP, and TGF-β ($P < 0.05$, Table 3). Subsequent multivariate analysis identified that heart failure, IL-6, and hs-CRP were independently related to Log-LPS ($P < 0.05$, Table 3).

4. Discussion

Accumulating evidence has shown that gut dysbiosis is related to the progression of RAF. The present study confirmed the findings that the gut microbiota-derived metabolite LPS is significantly positively correlated with RAF. Baseline LPS levels were higher in the RAF group than in the sinus rhythm group. In addition, we demonstrated that circulating LPS levels may promote RAF by increasing systemic inflammation and atrial fibrosis.

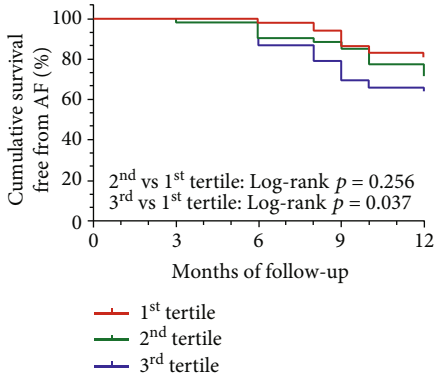

Figure 1: Kaplan–Meier curve for survival free from AF after ablation according to circulating LPS tertile.

Table 2: Multivariable Cox regression to predict RAF.

Variables	Hazard ratio (95% CI)	*P*
Age (year)	0.990 (0.954-1.027)	0.598
Persistent AF, *n* (%)	1.018 (0.520-1.992)	0.959
Hypertension, *n* (%)	1.117 (0.562-2.221)	0.752
Diabetes, *n* (%)	1.505 (0.596-3.796)	0.387
CHD, *n* (%)	0.794 (0.331-1.905)	0.606
Heart failure, *n* (%)	2.029 (1.030-3.997)	0.041
BMI (kg/m^2)	1.065 (0.972-1.167)	0.178
LAD (mm)	1.064 (1.009-1.123)	0.022
Hs-CRP (mg/L)	1.689 (0.456-6.253)	0.433
IL-6 (pg/mL)	1.009 (0.995-1.023)	0.226
CITP (ng/mL)	6.841 (1.168-40.069)	0.033
TGF-β1 (ng/mL)	1.021 (0.998-1.045)	0.079
Log-LPS (pg/mL)	5.686 (1.055-30.635)	0.043

CHD: coronary heart disease; BMI: body mass index; LAD: left atrial diameter; IL-6: interleukin-6; CITP: collagen type-1 C-terminal telopeptide; TGF-β1: transforming growth factor beta1; LPS: lipopolysaccharide.

In this study, we found a RAF rate of 27.7% after ablation during the one-year follow-up, which is in accordance with other experimental data. This study is consistent with the meta-analysis conducted by Turagam et al., who found a rate of 27.5% RAF in 1212 AF patients after one-year follow-up [13]. Similar evidence has been reported in 256 AF patients to evaluate the effect of perindopril on RAF. In the subgroup of 128 patients treated with placebo, the recurrence rate of atrial fibrillation was 28.5% during the one-year follow-up [14]. However, another prespecified study from the CABANA Trial showed that 12.6% of ablation patients experienced symptomatic AF, and atrial tachycardia occurred in 36.4% of patients [15]. Overall, our results are consistent with the findings of these studies.

Considerable evidence has indicated that disordered gut microbiota contributes to RAF. Catheter ablation has been used as a first-line treatment strategy. However, the high recurrence rate postablation requires the identification of novel biomarkers to select optimal patients to improve clinical outcomes. The novel finding of the current study is that the patients with RAF disclosed higher baseline LPS during follow-up. In particular, we demonstrated that the circulating levels of patients in the third tertile of LPS (> 67.3 pg/mL) had the highest risk of RAF. Our results extend current knowledge on the effect of gut microbiota-derived metabolites in RAF, suggesting that gut microbiota may not only play a pathogenetic role in AF development but may also affect clinical outcomes after ablation.

Inflammation and oxidative stress are central mediators of AF, which exacerbate cardiac remodelling and facilitate AF initiation [16]. Menichelli et al. [17] confirmed that circulating LPS could contribute to impaired antioxidant status in the ATHERO-AF study. In this study, we further assessed the association between LPS and inflammatory cytokines. Inflammatory biomarkers (hs-CRP and IL-6) and fibrotic biomarkers (TGFβ1 and CITP) were measured, which have proved to be an important mechanism leading to RAF [18, 19]. Previous studies have confirmed that a potential elevation in circulating hs-CRP and IL-6 has a higher risk of RAF [20]. Deftereos et al. found that colchicine can effectively prevent early AF recurrence by decreasing the levels of inflammatory mediators such as IL-6 and CRP [21]. Animal experiments found that LPS can stimulate M1 macrophage polarization to produce various proinflammatory cytokines. Additionally, TLR4 activation by LPS triggers consecutive MyD88 and TRIF-dependent signalling pathways, which synergistically promote the proinflammatory response [22]. In a canine model, inflammation induced by LPS could promote connexin 43 expression and cause heterogeneous atrial conduction, thereby increasing the risk of recurrence [23]. Consistent with previous studies, our data also indicated a significant association between circulating LPS and hs-CRP and IL-6. These studies showed that increasing chronic inflammation may be an important mechanism of LPS-induced recurrence of atrial fibrillation.

Clinical and animal evidence supports the viewpoint that atrial fibrosis is the hallmark of atrial structural remodelling and contributes to the occurrence and perpetuation of AF. The main pathological feature of atrial fibrosis was increased and disordered collagen deposition. CITP generated by the hydrolysis of type I collagen fiber, a serological marker of type I collagen degradation, has been demonstrated to be connected with the occurrence of AF [24, 25]. In addition, the progressive accumulation of the extracellular matrix produced by cardiac fibroblasts under profibrotic stimuli such as angiotensin II (Ang II) and TGF-β1 plays a pivotal role in promoting atrial fibrosis [26, 27]. Existing studies recognize the critical role played by TGF-β1 in inducing myocardial fibrosis [28]. In animal experiments, Zhang et al. demonstrated that gut dysbiosis induced AF partly through increased concentrations of circulating LPS and activated the atrial NLRP3 inflammasome, which promoted atrial fibrosis [10]. The present data demonstrated that circulating LPS levels were positively associated with the serum TGF-β1 and CITP levels. Subsequent multivariate analysis verified a significant independent association between LPS and the CITP levels. Another finding was that LAD is positively

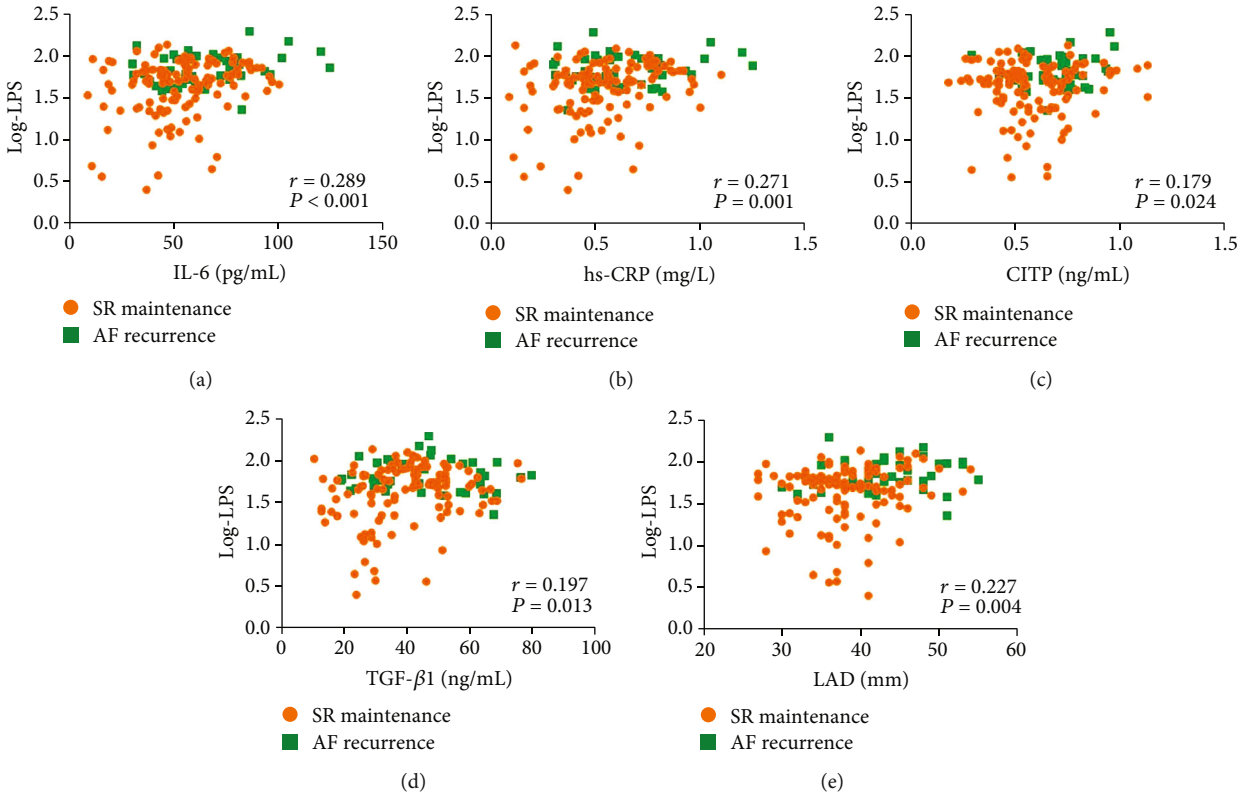

Figure 2: Scatter diagrams showing the association between the circulating LPS with the concentrations of inflammatory biomarker (IL-6 (a) and hs-CRP (b)), atrial fibrotic biomarkers (CITP (c) and TGF-β1 (d)), and LAD (e). Pearson's correlation coefficient and P values are indicated.

Table 3: Univariate and multivariable linear regression analysis for the correlation of between Log-LPS with anthropometric and biochemical variables.

Variables	Univariate			Multivariable		
	Standardized β	95% CI	P	Standardized β	95% CI	P
Age (year)	0.089	-0.002-0.008	0.267			
Male, n (%)	-0.057	-0.143-0.067	0.472			
Persistent AF, n (%)	0.132	-0.016-0.191	0.098			
Hypertension, n (%)	0.125	-0.020-0.183	0.116			
Diabetes, n (%)	0.121	-0.034-0.266	0.128			
CHD, n (%)	0.078	-0.062-0.184	0.328			
Heart failure, n (%)	0.255	0.081-0.323	0.001	0.138	-0.010-0.228	0.071
BMI (kg/m^2)	0.007	-0.016-0.017	0.926			
Glu (mmol/L)	-0.030	-0.029-0.021	0.743			
LDL (mmol/L)	0.087	-0.028-0.099	0.275			
TG (mmol/L)	0.078	-0.027-0.080	0.328			
Cr (μmol/L)	0.016	-0.002-0.003	0.837			
LAD (mm)	0.227	0.004-0.021	0.004	0.144	0.001-0.016	0.057
Hs-CRP (mg/L)	0.271	0.175-0.619	0.001	0.215	0.105-0.525	0.003
IL-6 (pg/mL)	0.289	0.002-0.007	< 0.001	0.182	0.001-0.005	0.016
CITP (ng/mL)	0.179	0.042-0.589	0.024	0.123	-0.036-0.469	0.092
TGF-β1 (ng/mL)	0.197	0.001-0.008	0.013	0.144	0.001-0.006	0.050

CHD: coronary heart disease; BMI: body mass index; LAD: left atrial diameter; IL-6: interleukin-6; CITP: collagen type-1 C-terminal telopeptide; TGF-β1: transforming growth factor beta1; LPS: lipopolysaccharide.

correlated with serum LPS levels. These results may further support the hypothesis that LPS induces RAF by promoting atrial fibrosis.

In addition, other mechanisms may contribute to the connection between LPS and RAF. Indeed, LPS may contribute to recurrence of AF through acceleration of heart failure and may induce myocardial infarction and left ventricular dysfunction, both of which could increase the recurrence risk of AF [29, 30]. Furthermore, there is an evidence that elevated circulating levels of LPS are connected with MACEs in AF patients. In the present study, our results demonstrate a significantly positive association between circulating LPS and heart failure and hypertension. Collectively, these studies confirm that promoting the occurrence of RAF-related risk factors may be an indirect mechanism leading to AF recurrence.

4.1. Study Limitations. The present study has several limitations. First, serum biomarkers of inflammation and atrial fibrosis are not heart specific. In addition, the findings were more convincing if measuring these biomarkers in the atrial tissue. Because of this potential limitation, we made strenuous efforts to exclude those patients with conditions related to inflammation and fibrosis. Second, the sample size was limited. Hence, more prospective studies are necessary to investigate the differences between paroxysmal AF patients and persistent AF patients in the future. Finally, we could not exclude other mechanisms by which LPS may contribute to RAF.

5. Conclusion

In conclusion, the results support the role of gut microbiota in the prognosis of AF postablation by demonstrating that baseline circulating LPS is associated with recurrence of AF during the one-year follow-up. Furthermore, baseline circulating LPS levels are associated with systemic inflammation and fibrotic biomarkers. However, further animal experiments are necessary to elucidate the potential mechanism of LPS-induced systemic inflammation and atrial fibrosis.

Data Availability

The datasets used and/or analyzed during this study are available from the corresponding author on reasonable request.

Conflicts of Interest

The authors declare that they have no conflict of interest.

Authors' Contributions

Meng Wang and Hua Xiong contributed equally to this work.

Acknowledgments

This work was supported by the National Natural Science Foundation of China (grant number 81970287).

References

[1] A. Beaser and A. Cifu, "Management of patients with atrial fibrillation," *JAMA*, vol. 321, no. 11, pp. 1100-1101, 2019.

[2] L. Staerk, J. Sherer, D. Ko, E. Benjamin, and R. Helm, "Atrial Fibrillation," *Circulation Research*, vol. 120, no. 9, pp. 1501–1517, 2017.

[3] W. H. Tang, T. Kitai, and S. L. Hazen, "Gut microbiota in cardiovascular health and disease," *Circulation Research*, vol. 120, no. 7, pp. 1183–1196, 2017.

[4] R. Huang, L. Yan, and Y. Lei, "The gut microbial-derived metabolite trimethylamine N-oxide and atrial fibrillation: relationships, mechanisms, and therapeutic strategies," *Clinical Interventions in Aging*, vol. Volume 16, pp. 1975–1986, 2021.

[5] W. Jiang, J. Huo, S. Wang et al., "Trimethylamine N-oxide facilitates the progression of atrial fibrillation in rats with type 2 diabetes by aggravating cardiac inflammation and connexin remodeling," *Journal of Physiology and Biochemistry*, 2022.

[6] J. Li, K. Zuo, J. Zhang et al., "Shifts in gut microbiome and metabolome are associated with risk of recurrent atrial fibrillation," *Journal of Cellular and Molecular Medicine*, vol. 24, no. 22, pp. 13356–13369, 2020.

[7] Z. Wang and Y. Zhao, "Gut microbiota derived metabolites in cardiovascular health and disease," *Protein & Cell*, vol. 9, no. 5, pp. 416–431, 2018.

[8] C. Yao, T. Veleva, L. Scott et al., "Enhanced cardiomyocyte NLRP3 inflammasome signaling promotes atrial fibrillation," *Circulation*, vol. 138, no. 20, pp. 2227–2242, 2018.

[9] R. Okazaki, Y. Iwasaki, Y. Miyauchi et al., "Lipopolysaccharide induces atrial arrhythmogenesis via down-regulation of L-type Ca2+ channel genes in rats," *International Heart Journal*, vol. 50, no. 3, pp. 353–363, 2009.

[10] Y. Zhang, S. Zhang, B. Li et al., "Gut microbiota dysbiosis promotes age-related atrial fibrillation by lipopolysaccharide and glucose-induced activation of NLRP3-inflammasome," *Cardiovascular Research*, vol. 118, no. 3, pp. 785–797, 2022.

[11] D. Pastori, R. Carnevale, C. Nocella et al., "Gut-derived serum lipopolysaccharide is associated with enhanced risk of major adverse cardiovascular events in atrial fibrillation: effect of adherence to Mediterranean diet," *Journal of the American Heart Association*, vol. 6, no. 6, 2017.

[12] G. Hindricks, T. Potpara, N. Dagres et al., "2020 ESC guidelines for the diagnosis and management of atrial fibrillation developed in collaboration with the European Association for Cardio-Thoracic Surgery (EACTS)," *European Heart Journal*, vol. 42, no. 5, pp. 373–498, 2021.

[13] M. Turagam, D. Musikantow, W. Whang et al., "Assessment of catheter ablation or antiarrhythmic drugs for first-line therapy of atrial Fibrillation," *JAMA Cardiology*, vol. 6, no. 6, pp. 697–705, 2021.

[14] Q. Wang, Y. Shang, Z. Wang et al., "Perindopril for the prevention of atrial fibrillation recurrence after radiofrequency catheter ablation: one-year experience," *Heart Rhythm*, vol. 13, no. 10, pp. 2040–2047, 2016.

[15] J. Poole, T. Bahnson, K. Monahan et al., "Recurrence of atrial fibrillation after catheter ablation or antiarrhythmic drug therapy in the CABANA trial," *Journal of the American College of Cardiology*, vol. 75, no. 25, pp. 3105–3118, 2020.

[16] B. Karam, A. Chavez-Moreno, W. Koh, J. Akar, and F. Akar, "Oxidative stress and inflammation as central mediators of

atrial fibrillation in obesity and diabetes," *Cardiovascular Diabetology*, vol. 16, no. 1, p. 120, 2017.

[17] D. Menichelli, R. Carnevale, C. Nocella et al., "Circulating lipopolysaccharides and impaired antioxidant status in patients with atrial fibrillation. Data from the ATHERO-AF study," *Frontiers in cardiovascular medicine*, vol. 8, article 779503, 2021.

[18] Y. Hu, Y. Chen, Y. Lin, and S. Chen, "Inflammation and the pathogenesis of atrial fibrillation," *Nature Reviews. Cardiology*, vol. 12, no. 4, pp. 230–243, 2015.

[19] G. Begg, R. Karim, T. Oesterlein et al., "Left atrial voltage, circulating biomarkers of fibrosis, and atrial fibrillation ablation. A prospective cohort study," *PLoS One*, vol. 13, no. 1, article e0189936, 2018.

[20] K. Henningsen, B. Nilsson, H. Bruunsgaard, X. Chen, B. Pedersen, and J. Svendsen, "Prognostic impact of hs-CRP and IL-6 in patients undergoing radiofrequency catheter ablation for atrial fibrillation," *Scandinavian Cardiovascular Journal*, vol. 43, no. 5, pp. 285–291, 2009.

[21] S. Deftereos, G. Giannopoulos, C. Kossyvakis et al., "Colchicine for prevention of early atrial fibrillation recurrence after pulmonary vein isolation: a randomized controlled study," *Journal of the American College of Cardiology*, vol. 60, no. 18, pp. 1790–1796, 2012.

[22] A. Ciesielska, M. Matyjek, and K. Kwiatkowska, "TLR4 and CD14 trafficking and its influence on LPS-induced pro-inflammatory signaling," *Cellular and Molecular Life Sciences*, vol. 78, no. 4, pp. 1233–1261, 2021.

[23] Y. Chen, Z. Sun, J. Jiang et al., "α-adrenoceptor-mediated enhanced inducibility of atrial fibrillation in a canine system inflammation model," *Molecular Medicine Reports*, vol. 15, no. 6, pp. 3767–3774, 2017.

[24] E. Kallergis, C. Goudis, E. Kanoupakis et al., "Sinus rhythm restoration affects collagen turnover in patients with persistent atrial fibrillation," *Europace*, vol. 16, no. 12, pp. 1726–1730, 2014.

[25] E. Kallergis, E. Manios, E. Kanoupakis et al., "Extracellular matrix alterations in patients with paroxysmal and persistent atrial fibrillation: biochemical assessment of collagen type-I turnover," *Journal of the American College of Cardiology*, vol. 52, no. 3, pp. 211–215, 2008.

[26] M. Dzeshka, G. Lip, V. Snezhitskiy, and E. Shantsila, "Cardiac fibrosis in patients with atrial fibrillation: mechanisms and clinical implications," *Journal of the American College of Cardiology*, vol. 66, no. 8, pp. 943–959, 2015.

[27] W. Kosmala, M. Przewlocka-Kosmala, H. Szczepanik-Osadnik, A. Mysiak, and T. Marwick, "Fibrosis and cardiac function in obesity: a randomised controlled trial of aldosterone blockade," *Heart*, vol. 99, no. 5, pp. 320–326, 2013.

[28] D. Rahmutula, G. Marcus, E. Wilson et al., "Molecular basis of selective atrial fibrosis due to overexpression of transforming growth factor-β1," *Cardiovascular Research*, vol. 99, no. 4, pp. 769–779, 2013.

[29] J. Jaw, M. Tsuruta, Y. Oh et al., "Lung exposure to lipopolysaccharide causes atherosclerotic plaque destabilisation," *The European Respiratory Journal*, vol. 48, no. 1, pp. 205–215, 2016.

[30] X. Zhou, J. Li, J. Guo et al., "Gut-dependent microbial translocation induces inflammation and cardiovascular events after ST-elevation myocardial infarction," *Microbiome*, vol. 6, no. 1, p. 66, 2018.

Hindawi
Oxidative Medicine and Cellular Longevity
Volume 2022, Article ID 5992436, 24 pages
https://doi.org/10.1155/2022/5992436

Research Article

Naringenin Alleviates Renal Ischemia Reperfusion Injury by Suppressing ER Stress-Induced Pyroptosis and Apoptosis through Activating Nrf2/HO-1 Signaling Pathway

Banghua Zhang,[1,2] **Shanshan Wan**,[3] **Hao Liu**,[1,2] **Qiangmin Qiu**,[1] **Hui Chen**,[1] **Zhiyuan Chen**,[1] **Lei Wang**,[1,4] **and Xiuheng Liu**[1,4]

[1]*Department of Urology, Renmin Hospital of Wuhan University, Wuhan 430060, China*
[2]*Hubei Key Laboratory of Digestive System Disease, Wuhan 430060, China*
[3]*Department of Ophthalmology, Renmin Hospital of Wuhan University, Wuhan 430060, China*
[4]*Wuhan University Institute of Urological Disease, Wuhan 430060, China*

Correspondence should be addressed to Zhiyuan Chen; chenzhiyuan163@163.com, Lei Wang; drwanglei@whu.edu.cn, and Xiuheng Liu; drliuxh@hotmail.com

Received 12 August 2022; Revised 8 September 2022; Accepted 15 September 2022; Published 10 October 2022

Academic Editor: En Yin Lai

Endoplasmic reticulum (ER) stress, pyroptosis, and apoptosis are critical molecular events in the occurrence and progress of renal ischemia reperfusion (I/R) injury. Naringenin (4′,5,7-trihydroxyflavanone) is one of the most widely consumed flavonoids with powerful antioxidant and anti-inflammatory activities. However, whether naringenin is able to relieve renal I/R injury and corresponding mechanisms have not been fully clarified. This study was aimed at exploring its role and relevant mechanisms in renal I/R injury. The C57Bl/6 mice were randomly assigned to receive administration with naringenin (50 mg/kg/d) or sterile saline (1.0 mL/d) for 3 d by gavage and suffered from renal I/R surgery. One specific ER stress inhibitor, 4-phenylbutyric acid (4-PBA, 100 mg/kg/d), was intraperitoneally administered to validate the regulation of ER stress on pyroptosis and apoptosis. Cultured HK-2 cells went through the process of hypoxia/reoxygenation (H/R) to perform cellular experiments with the incubation of naringenin (200 μM), 4-PBA (5 mM), or brusatol (400 nM). The animal results verified that naringenin obviously relieved renal I/R injury, while it refined renal function and attenuated tissue structural damage. Furthermore, naringenin treatment inhibited I/R-induced ER stress as well as pyroptosis and apoptosis as indicated by decreased levels of specific biomarkers such as GRP78, CHOP, caspase-12, NLRP3, ASC, caspase-11, caspase-4, caspase-1, IL-1β, GSDMD-N, BAX, and cleaved caspase-3 in animals and HK-2 cells. Besides, the upregulated expression of Nrf2 and HO-1 proteins after naringenin treatment suggested that naringenin activated the Nrf2/HO-1 signaling pathway, which was again authenticated by the usage of brusatol (Bru), one unique inhibitor of the Nrf2 pathway. Importantly, the application of 4-PBA showed that renal I/R-generated pyroptosis and apoptosis were able to be regulated by ER stress in vivo and in vitro. In conclusion, naringenin suppressed ER stress by activating Nrf2/HO-1 signaling pathway and further alleviated pyroptosis and apoptosis to protect renal against I/R injury.

1. Introduction

Acute kidney injury emerges as a fairly intractable and worrisome clinical problem, which is often accompanied by varieties of syndromes such as urinary tract obstruction, cardiorenal syndrome, and sepsis. AKI occurs in more than 50% of patients in intensive care and in 10-15% of patients [1]. Blood flow to the kidney is suddenly reduced or stopped in renal I/R injury. After blood supply is restored, the injury is further aggravated and can develop into acute kidney injury and other serious kidney diseases [2]. Although the pathogenesis of renal I/R injury remains to be clearly elucidated,

relevant studies have confirmed that oxidative stress, ER stress, mitochondrial dysfunction, ion accumulation, pyroptosis, and apoptosis are critical molecular mechanisms. Furthermore, relevant articles have authenticated that ER stress proves to be the critical regulatory mediator in renal I/R injury as evidenced by reduced renal I/R injury after effectively inhibiting ER stress [3–5]. In view of the significant mortality and morbidity of related diseases including AKI caused by renal I/R injury, it is increasingly necessary to completely understand its cellular pathophysiological mechanisms and persistently explore new therapeutic strategies of renal I/R injury [6, 7].

ER stress, pyroptosis, and apoptosis are substantial and interrelated processes in the occurrence and etiopathogenesis of renal I/R injury [3, 8]. When the internal environment has changes including disruption of calcium homeostasis, hypoxia, and oxidative stress, endoplasmic reticulum homeostasis is imbalanced, leading to an abnormal increase in intracellular misfolded or unfolded proteins, which ultimately induce ER stress [9]. When cells are continuously under pathological stress, apoptotic pathways are triggered, resulting in massive accumulation of unfolded proteins and apoptosis [10]. In addition, ER stress has been verified to have participation in the activation of NF-κB signaling pathway and NLRP3 inflammasome, which in turn cause pyroptosis [11, 12].

As one of the largely consumed flavonoids which widely exist in Citrus genus, naringenin possesses a broad prospect of clinical application owing to its excellent bioavailability, low cytotoxicity, and remarkable anti-inflammatory and antioxidant properties [13–15]. Recent researches in different fields have testified that naringenin has showed noteworthy protective effects in cardiovascular diseases, neurological disorders, diabetes mellitus, virus infection, and I/R injury. These functions are mainly achieved through mitigating inflammatory response, oxidative stress, ER stress, and apoptosis [16–18]. Meanwhile, naringenin is able to relieve myocardial I/R injury by inhibiting oxidative stress, ferroptosis, and ER stress via AMPK-SIRT3, Nrf2/GPX4, and PI3K/AKT pathways [19–21]. Pretreatment of naringenin protects retinal and brain against I/R injury as well as ameliorating ischemic stroke [22, 23]. Nevertheless, whether it can alleviate renal I/R injury and the corresponding mechanisms demands to be further authenticated.

Therefore, we innovatively investigated the protective influence and the underlying mechanisms of naringenin treatment on renal I/R-generated ER stress, pyroptosis, and apoptosis by establishing the typical renal I/R model in C57Bl/6 mice and an H/R model in HK-2 cells, so as to provide some new perspectives into the pathogenesis occurrence of renal I/R injury and a theoretical basis for naringenin in the clinical treatment of kidney ischemic diseases.

2. Materials and Methods

2.1. Antibodies and Reagents. Naringenin (HPLC $\geq$ 98%) used in this study was acquired from Solarbio (IN0350, Solarbio Life Sciences, Beijing). Annexin V-FITC/PI apoptosis kit that was applied in flow cytometry was supplied by Multi Sciences Biotech (Hangzhou, China). The 5x protein loading buffer, BCA protein quantification kit, radioimmunoprecipitation assay (RIPA) buffer, SDS-PAGE gel preparation kit, 10x TBS with Tween-20 buffer, and phenylmethanesulfonyl fluoride (PMSF) all were bought from Servicebio Technology (Wuhan, China). Fetal bovine serum was purchased from Invitrogen (MA, USA). Polyvinylidene difluoride (PVDF) membrane and chemiluminescent HRP substrate were obtained from Millipore (Billerica, MA, USA). Sources and usage of other reagents are described in detail in the following instructions.

2.2. Renal I/R Injury Mice Model. Eight-week-old adult male C57Bl/6 mice (22-24 g) were provided by the First Clinical College Experimental Animal Center of Wuhan University. The project was approved by Bioethics Committee of the Renmin Hospital of Wuhan University. These mice were provided with adequate food, sufficient water, appropriate room temperature (22-23°C), and light for a fixed period of time (the time is all 12 h of darkness or light for one cycle) according to the Laboratory Animal Guidelines.

The renal I/R model was built as we did in the previous studies; we selected 30 min of ischemia followed by suturing the incision and one full day (24 h) of reperfusion because renal I/R damage of this model was obvious [24, 25]. 0.2% pentobarbital sodium (60 mg/kg) was selected to anesthetize the mice in the experiments by intraperitoneal injection followed by placing the experimental mice on a thermostatic blanket. After skin preparation, a longitudinal abdominal incision was made to expose and separate bilateral kidneys and renal arteries. Only the right kidney was removed without subsequent treatment, and the mice were followed by the suture of abdominal incision in the Sham group. The left renal artery was clamped with a noninvasive vascular clip after right-sided nephrectomy in all I/R groups, and the kidney rapidly turned into black and purple after clamping. The arterial clamp was removed to restore blood supply after 30 min of ischemia, and the kidney quickly turned red. After the incision was sutured, 0.5 mL normal saline was injected intraperitoneally for liquid resuscitation. Blood and kidney tissue were collected immediately after 24 h of reperfusion.

2.3. Mice Treatment. All C57Bl/6 mice were randomly divided into 5 groups, which consisted of the Sham group, I/R group, I/R+NS (sterile saline) group, I/R+NRG (naringenin) group, and I/R+4-PBA (4-phenylbutyric acid) group, n=5. The Sham group received the above-mentioned treatment after normal feeding. Vehicle (1.0 mL/d, sterile saline) or naringenin (50 mg/kg/d, dilution in NS) was conducted by oral gavage for 3 d in the I/R+NS group or I/R+NRG group. Mice were injected intraperitoneally with 4-PBA (100 mg/kg, dilution in phosphate-buffered saline) 24 h before undergoing I/R surgery in the I/R+4-PBA group. The dose of 4-PBA was chosen for this study because there were previous articles about 4-PBA treatment in adult animals [26].

2.4. Assessment of Renal Function. Fresh blood from all experimental mice was collected immediately after 24 h

reperfusion, followed by 20 min of centrifugation at 3000 r/min. The corresponding kits were purchased from Jiancheng Bioengineering Institute in Nanjing of China to measure the creatinine (Cr) and blood urea nitrogen (BUN) levels according to the product instructions.

2.5. HE Staining. After embedding the formaldehyde-fixed mouse kidney tissues with paraffin, we prepared 4 μm thick sections and employed hematoxylin-eosin (H&E) to stain them. The pathological changes of renal tissue were observed under microscope. Two professional renal pathologists randomly selected 8 fields from each section to observe the pathological changes of renal tubule-interstitial lesions and performed semiquantitative scores of renal tubule-interstitial lesions.

2.6. Cell Culture and In Vitro H/R Model. As a cell line commonly used to construct in vitro model of renal I/R injury [27, 28], HK-2 cells utilized in H/R model were supplied by China Center for Type Culture Collection (CTCC, China). HK-2 cell line is also known as human renal proximal tubular epithelial cell line. DMEM medium called as Dulbecco's modified Eagle's medium was chosen to culture HK-2 cells, which need to undergo 12 h of incubation in serum-free medium in a three-gas incubator (5% CO_2, 94% N_2, 1% O_2) to complete this step of hypoxia. Reoxygenation was accomplished by changing the serum-free medium into normal medium containing 10% fetal bovine serum (FBS) immediately after completion of hypoxia, and then, HK-2 cells in the H/R groups were cultured normally in an ordinary incubator with 5% CO_2, 74% N_2, and 21% O_2 at 37°C. Meanwhile, HK-2 cells in the control group of cellular models were cultured in the normal environment using complete medium with 10% FBS at all times. The 12 h of hypoxia and 4 h of reoxygenation were chosen because our previous studies showed that both apoptosis and pyroptosis were relatively pronounced in such a model [25, 29]. Different concentrations of NRG or 4-PBA (5 mM, dilution in DMSO) were added to the medium 24 h before model construction [30], and then, they were incubated with or without brusatol (400 nM), 2 h before hypoxia [25].

2.7. Quantitative Real-Time PCR Analysis. RNA extraction kit (G3013, Servicebio, Wuhan) was purchased to extract the total RNA in relevant groups of animals and HK-2 cells according to the standard procedures. 1,000 ng of extracted RNA was then reversely transcribed into cDNA by the application of one SweScript RT II First Strand cDNA Synthesis Kit (G3333-100, Servicebio, Wuhan). Primers for human and mouse genes were designed and synthesized by Sangon Biotech (Shanghai, China). 20 μL qPCR reaction system including 2x Universal Blue SYBR Green qPCR Master Mix (G3326-05, Servicebio, Wuhan) was performed to detect the relative mRNA levels of target genes by qPCR Detection System (Bio-Rad, USA). $2^{-\triangle\triangle CT}$ method was selected to quantify the levels of gene mRNA expression relative to GAPDH. The sequences of primers used in our study are shown in Tables 1 and 2.

2.8. Western Blot Analysis. The kidney tissues that were preserved in liquid nitrogen at -80°C were cut and homogenized, followed by the addition of precooled RIPA buffer containing PMSF and centrifugation at 6,000 r/min for 20 min. The treated cells in all groups were collected for protein extraction following a standard procedure. After the protein content was determined through the utilization of the BCA kit, 30 μg of the unmeasured protein was mixed with the loading buffer 5x and then boiled in a water bath at 100°C for 10 min. The proteins were then separated using 10% sodium dodecyl sulfate-polyacrylamide gels (SDS-PAGE) and transferred electrophoretically to PVDF membranes. In order to eliminate nonspecific binding of the target proteins with the primary antibodies, Protein Free Rapid Blocking Buffer (1x) (PS108P, Epizyme Biomedical Technology, Shanghai) was used to block for 30 min at 37°C. Membranes were infiltrated with a specific dilution of primary antibodies overnight at 4°C. The dilutions and sources of all antibodies are as follows: GAPDH (10494-1-AP, 1 : 8000, Proteintech Group), GRP78 (11587-1-AP, 1 : 2000, Proteintech Group), CHOP (15204-1-AP, 1 : 2000, Proteintech Group), BAX (50599-2-Ig, 1 : 5000, Proteintech Group), cleaved caspase-3 (WL02117, 1 : 500, Wanleibio), HO-1 (10701-1-AP, 1 : 3000, Proteintech Group), Bcl-2 (26593-1-AP, 1 : 2000, Proteintech Group), Nrf2 (16396-1-AP, 1 : 5000, Proteintech Group), caspase-4 (sc-56056, 1 : 200, Santa Cruz), NLRP3 (#15101, 1 : 1000, Cell Signaling Technology), caspase-11 (sc-56038, 1 : 400, Santa Cruz), cleaved caspase-1 (sc-56036, 1 : 400, Santa Cruz), caspase-12 (sc-21747, 1 : 400, Santa Cruz), mature IL-1β (#12242, 1 : 1000, Cell Signaling Technology), ASC (sc-514414, 1 : 200, Santa Cruz), GSDMD-N (#39754, 1 : 1000, Cell Signaling Technology), and KIM-1 (AF1817, MAB1750, 1 : 1000, R&D Systems). The PVDF membranes were then placed into the diluted goat anti-rabbit or goat anti-mouse secondary antibody (SA00001-2, SA00001-1, 1 : 2000, Proteintech Group) and incubated for 1 h at 37°C. All membranes were flushed with TBST 1x buffer three times for 10 min each to lessen nonspecific binding. Chemiluminescent HRP substrate was applied to visualize all blots. Protein levels were analyzed and quantified by Image Lab Software (NIH, USA).

2.9. Detection of Caspase-1 Activity. The caspase-1 activity in various treatment groups was able to be detected by the caspase-1 activity assay kit (C1102, Beyotime, Shanghai) according to the attached detailed instructions. Briefly, after we collected the treated kidney tissue and HK-2 cells, the 100 μL reaction system was configured after successively adding the reagents from this kit according to the manufacturer's instructions. The samples were incubated at 37°C for 90 min. The absorbance at the wavelength of 405 nm was determined to assess the levels when the color change is obvious.

2.10. Cell Viability Assay. Cell viability in different groups of cellular experiments was measured by one CCK-8 cell viability assay kit, which was purchased from Nanjing Jiancheng Bioengineering Institute (Nanjing, China). The cell suspension of 10,000 cells was added to every well of the 96-well

Table 1: The primer sequences of human genes used in quantitative real-time PCR analysis.

Primer	Forward primer (5′ ->3′)	Reverse primer (5′ ->3′)	Amplicon size (bp)
GRP78	CACGGTCTTTGACGCCAAG	CCAAATAAGCCTCAGCGGTTT	215
CHOP	GGAAACAGAGTGGTCATTCCC	CTGCTTGAGCCGTTCATTCTC	116
Caspase-12	AACAACCGTAACTGCCAGAGT	CTGCACCGGCTTTTCCACT	118
NLRP3	CGTGAGTCCCATTAAGATGGAGT	CCCGACAGTGGATATAGAACAGA	191
ASC	TGGATGCTCTGTACGGGAAG	CCAGGCTGGTGTGAAACTGAA	110
Caspase-1	TTTCCGCAAGGTTCGATTTTCA	GGCATCTGCGCTCTACCATC	54
GAPDH	ACAACTTTGGTATCGTGGAAGG	GCCATCACGCCACAGTTTC	101

Table 2: The primer sequences of mouse genes used in quantitative real-time PCR analysis.

Primer	Forward primer (5′ ->3′)	Reverse primer (5′ ->3′)	Amplicon size (bp)
GRP78	ACTTGGGGACCACCTATTCCT	ATCGCCAATCAGACGCTCC	134
CHOP	CTGGAAGCCTGGTATGAGGAT	CAGGGTCAAGAGTAGTGAAGGT	121
Caspase-12	AGACAGAGTTAATGCAGTTTGCT	TTCACCCCACAGATTCCTTCC	106
NLRP3	ATTACCCGCCCGAGAAAGG	TCGCAGCAAAGATCCACACAG	141
ASC	CTTGTCAGGGGATGAACTCAAAA	GCCATACGACTCCAGATAGTAGC	154
Caspase-1	ACAAGGCACGGGACCTATG	TCCCAGTCAGTCCTGGAAATG	237
GAPDH	AGGTCGGTGTGAACGGATTTG	TGTAGACCATGTAGTTGAGGTCA	123

plates and cultured for 48 hours, followed by the various concentrations of NAR and relevant treatments. After being added with 10 μL of CCK-8 reagent per well, the cells were continued to be incubated in the dark for 4 hours. The absorbance of the treated cells in 96-well plates at 450 nm was quantified by the PerkinElmer Microplate reader (PerkinElmer Victor 1420, USA) to determine the cell viability.

2.11. Measurement of Caspase-3 Activity. One caspase-3 activity assay kit (C1116, Beyotime, Shanghai) was bought to assess the caspase-3 activity. According to the accompanying thorough instructions, tissue or cell samples treated with precooled RIPA buffer were centrifuged for 15 min at 12,000 r/min at 4° C, and the transferred supernatant was immediately used to configure the 100 μL system containing reagents in this kit. The samples were incubated at 37°C for 120 min. The levels were quantified by the utilization of the absorbance at 405 nm.

2.12. Flow Cytometry. Flow cytometry was taken to measure the apoptosis degree of HK-2 cells in various intervention groups through the Annexin V-FITC/PI apoptosis kit by referring to the attached instructions. HK-2 cells with different pretreatments were washed three times in PBS 1x buffer. Then, 5×10^3 cells including cells inside the culture supernatant were collected. After being resuspended by 1,000 μL of 1x binding buffer, cells in each group were added with 20 μL PI and 10 μL Annexin V-FITC, followed by 15 min incubation at 37°C in the dark. The FACS flow cytometer (Bio-Rad, USA) was applied to detect the apoptotic cells.

2.13. Statistical Analysis. The experimental data in animal and cell experiments were quantified and processed by software GraphPad Prism version 8.0 (CA, USA). The results were presented as mean + standard deviation (SD). One-way analysis of variance (ANOVA) followed by Tukey's test was used to perform the statistical analysis. $P < 0.05$ indicated a statistically significant comparison between the different groups.

3. Results

3.1. Naringenin Ameliorated Renal Ischemia Reperfusion Injury in Mice. The structural formula of naringenin as a flavonoid is as follows (Figure 1(a)). In order to determine the appropriate dose that could be administered in mice, we explored the concentration gradient to test effects of naringenin on renal function. The results of the pretest showed that naringenin did not significantly affect renal function at a dose of 50 mg/kg, as evidenced by Cr and BUN levels in normally fed mice (Figures 1(b) and 1(c)). Mice were then treated with NRG (50 mg/kg/d) or NS (1.0 mL/d) by gavage for 3 d as mentioned above, followed by construction of typical renal I/R model. Cr and BUN, the serum markers of kidney injury, were clearly increased in the renal I/R model, but their levels were obviously downregulated in the NRG+I/R group (Figures 1(d) and 1(e)). H&E staining authenticated that pretreatment with NRG effectively improved the renal tissue morphology, which exhibited loss of brush border and tubular dilatation in the kidneys exposed to I/R surgery (Figures 1(f) and 1(g)). Consistent with these results, there was also an evident reduction in the protein levels of kidney injury molecule 1 (KIM-1) after NRG administration (Figure 1(h)). In conclusion, these experimental results confirmed that NRG gavage treatment could availably alleviate the pathological damage and kidney dysfunction in mice after the construction of I/R model.

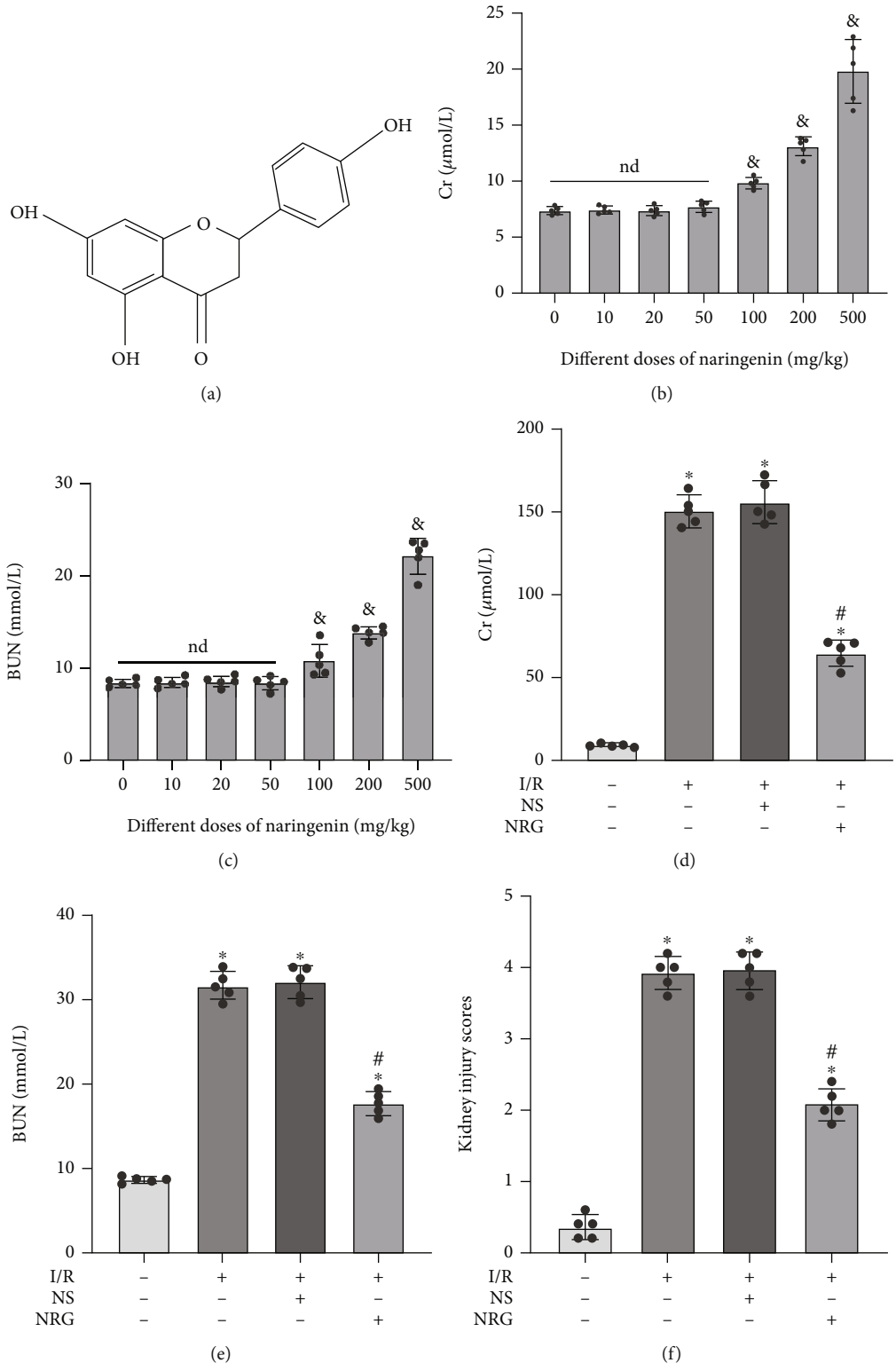

Figure 1: Continued.

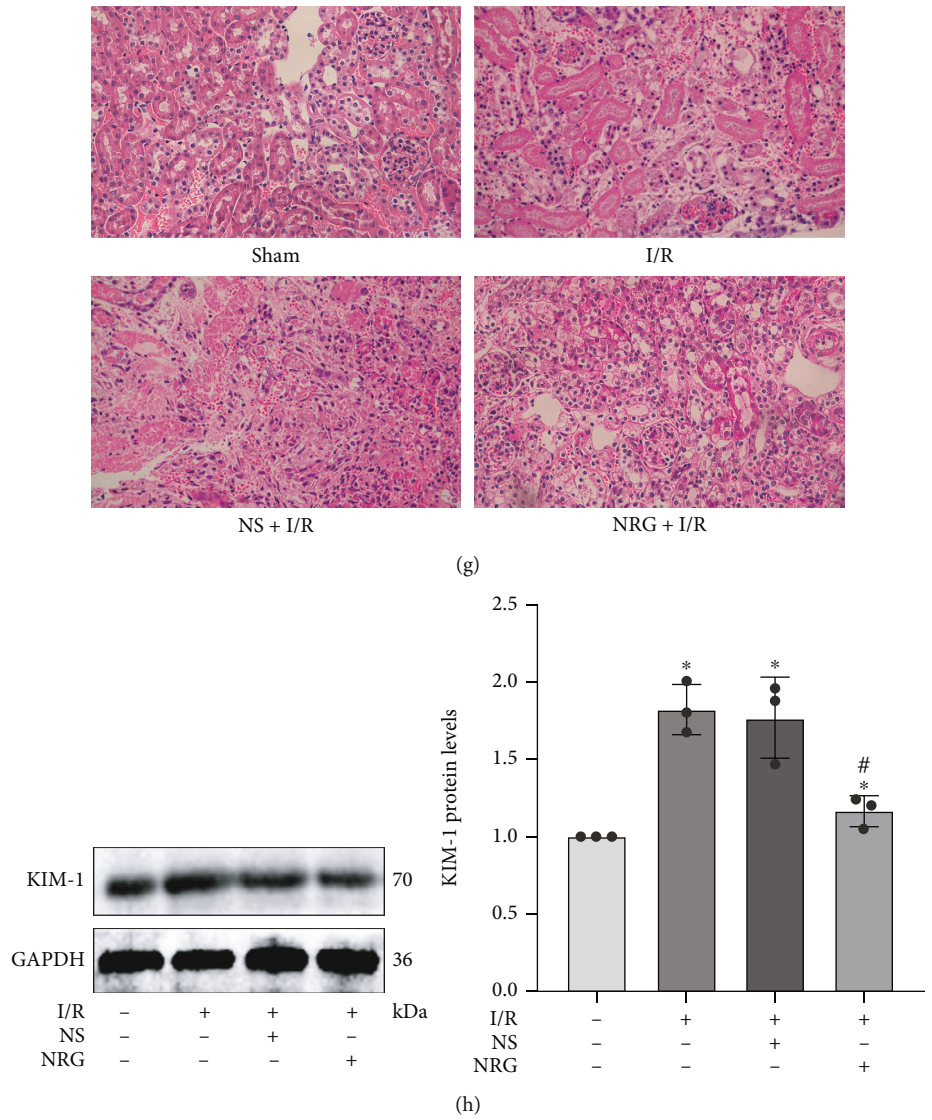

Figure 1: Naringenin ameliorated renal ischemia reperfusion injury in mice. (a) The structural formula of naringenin (NRG). (b, c) The influence about a variety of doses of naringenin on the levels of serum Cr as well as serum BUN in normally fed eight-week-old C57Bl/6 mice. (d, e) The levels of kidney biomarkers such as serum Cr and BUN declined notably in the NRG+I/R group. (f, g) H&E staining (×400) used in kidney histological staining showed that kidney tissue damage was mitigated in the NRG+I/R group. (h) Western blot analysis utilized in protein detection validated that the protein levels of KIM-1 decreased significantly in the NRG+I/R group. Values measured during animal experiments were carried out as mean ± SD, $n = 3 - 5$. $^{\&}P < 0.05$, compared with 0 mg/kg group; $^{*}P < 0.05$, compared with the Sham group; $^{\#}P < 0.05$, relative to the NS+I/R group; nd: no statistical difference.

3.2. Naringenin Effectively Attenuated Renal I/R-Generated ER Stress and Activated Nrf2/HO-1 Signaling Pathway in Mice. Subsequently, to identify corresponding mechanism by which NRG relieved renal I/R injury, members of this subject group performed qRT-PCR and western blot analysis to detect specific markers related to ER stress in renal I/R injury. Relevant studies revealed that ER stress plays the key role in renal I/R injury [3, 8], and NRG was testified by some studies to possess a meaningful role in regulating ER stress [31, 32]. By detecting the mRNA levels, we could clearly see that ER stress-specific markers including GRP78, CHOP, and caspase-12 were distinctly activated after I/R injury. Conversely, the results validated that NRG employment notably restrained the ER stress produced by I/R construction, as evidenced by the markedly lessened mRNA levels of both GRP78, CHOP, and caspase-12 (Figures 2(a)–2(c)). Western blot analysis further confirmed the effect of naringenin on inhibiting ER stress induced by renal I/R injury (Figures 2(d) and 2(e)). Moreover, we discovered that pretreatment of NRG reactivated restrained Nrf2/HO-1 signaling pathway in renal I/R injury (Figures 2(f) and 2(g)).

3.3. Naringenin Significantly Inhibited Pyroptosis and Apoptosis Induced by Renal I/R Injury in Mice. Next, pyroptosis-associated and apoptotic markers were further detected. The results suggested that the levels of caspase-1 activity in the I/R group exhibited obvious reduction after

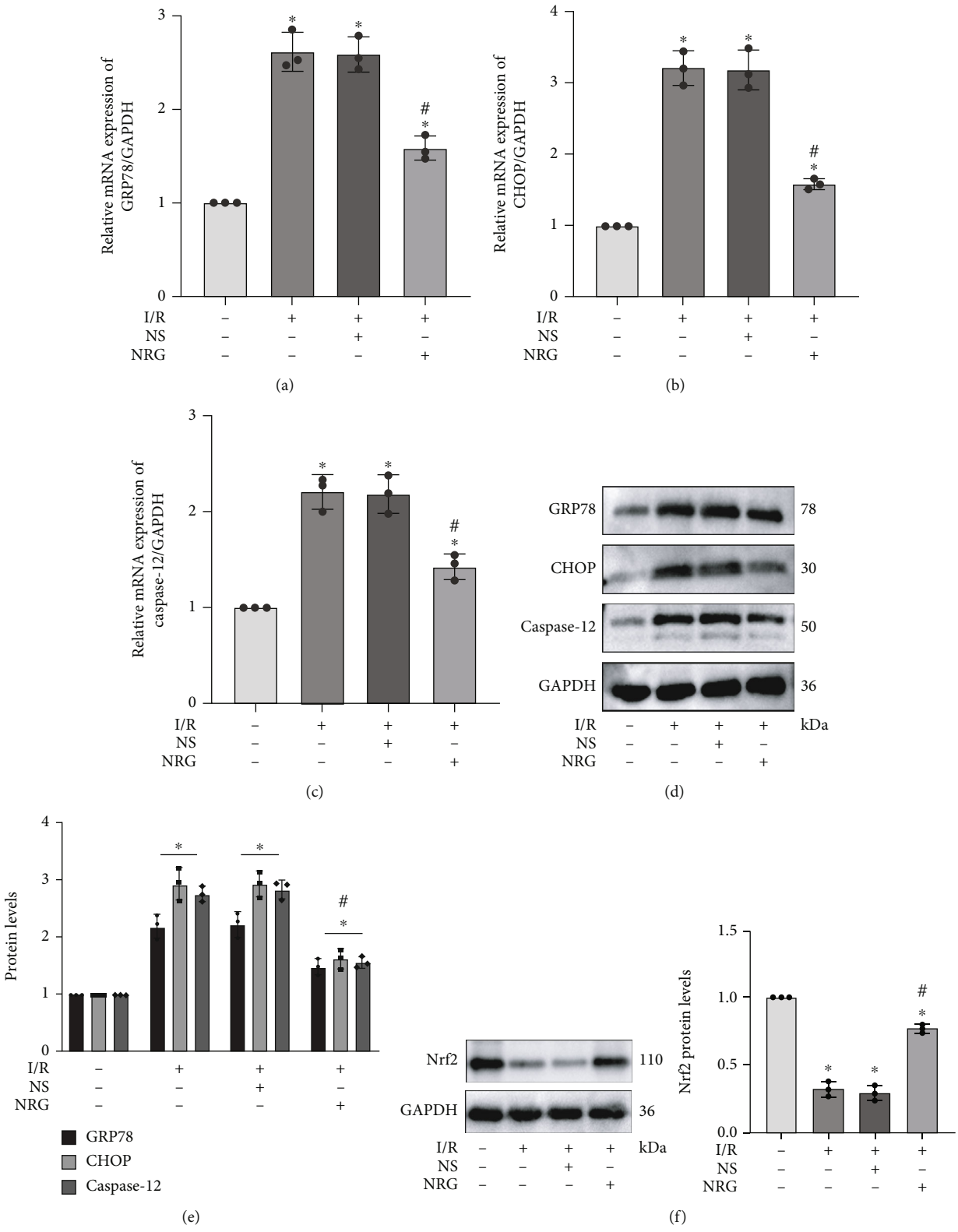

Figure 2: Continued.

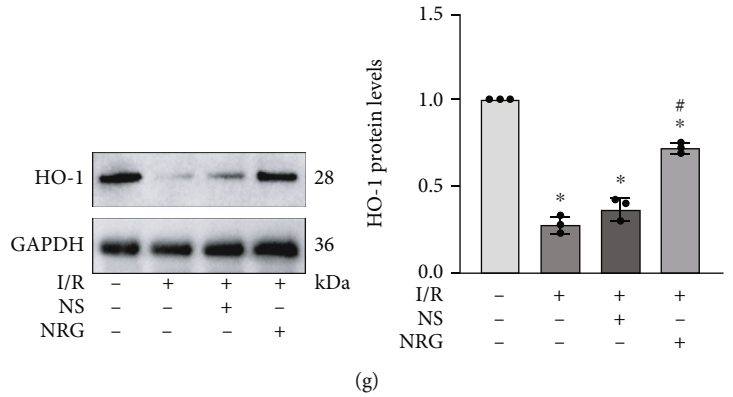

Figure 2: Naringenin effectively attenuated renal I/R-generated ER stress and activated Nrf2/HO-1 signaling pathway in mice. (a–c) qRT-PCR authenticated that pretreatment of naringenin effectively reduced the mRNA expression of GRP78, CHOP, and caspase-12 induced by renal I/R surgery. (d, e) Western blot analysis proved that naringenin administration downregulated ER stress-related proteins including GRP78, CHOP, and caspase-12 during renal I/R injury. (f, g) The protein levels of Nrf2 and HO-1 in renal tissues were displayed through western blot analysis in C57Bl/6 mice. Values measured during animal experiments were carried out as mean ± SD, $n = 3$ (three times measurements). $^{*}P < 0.05$, compared with the Sham group; $^{\#}P < 0.05$, relative to the NS+I/R group.

naringenin treatment (Figure 3(a)). The results of qRT-PCR authenticated that naringenin significantly inhibited the mRNA expression of pyroptosis-related markers such as NLRP3, ASC, and caspase-1 in renal I/R injury (Figures 3(b)–3(d)). The function of NRG on alleviating pyroptosis was again confirmed by the decreased protein expression of NLRP3, ASC, caspase-1 p10, GSDMD-N, caspase-11, and mature IL-1β in the NRG+I/R group (Figures 3(e) and 3(f)). Meanwhile, the usage of NRG remarkably restrained caspase-3 activity in renal I/R injury (Figure 3(g)). NRG application also abrogated the enhanced protein levels of apoptotic protein cleaved caspase-3 induced by I/R exposure as well as BAX, while the decreased expression of Bcl-2 protein in the I/R group was restored in the NAR+I/R group (Figure 3(h)).

3.4. Renal I/R-Generated Pyroptosis and Apoptosis Could be Regulated by ER Stress in Mice. The function of ER stress as a key mediator in renal I/R injury was investigated by the utilization of its established inhibitor, 4-PBA. In Figures 4(a) and 4(b), those results showed that preapplication of 4-PBA prior to establishment of renal I/R model clearly downregulated serum blood Cr and BUN levels. Moreover, H&E staining of the kidneys suggested that I/R-induced kidney tissue damage was evidently ameliorated after 4-PBA treatment (Figures 4(c) and 4(d)), which was again corroborated by the KIM-1 protein levels through detection using western blot analysis (Figure 4(e)). As shown in Figure 4(f), preapplication of 4-PBA prior to renal I/R model clearly prevented the initiation of ER stress, as summarized by the downregulated expression in GRP78, CHOP, and caspase-12 proteins. Interestingly, we further innovatively discovered that ER stress was capable of regulating pyroptosis and apoptosis in animal model of renal I/R injury. As confirmed by the experimental discoveries, the inhibition of ER stress by 4-PBA tremendously depressed the caspase-1 activity in mice with renal I/R surgery (Figure 4(g)). The noteworthy attenuation of elevated mRNA levels of NLRP3, ASC, and caspase-1 induced by I/R surgery was displayed after specific inhibition of ER stress using 4-PBA (Figure 4(h)). The remarkable differences in protein levels of NLRP3, ASC, cleaved caspase-1, GSDMD-N, caspase-11, and mature IL-1β between the NS+I/R group and 4-PBA+I/R group again testified that renal I/R-generated pyroptosis could be regulated by ER stress in mice (Figures 4(i) and 4(j)). 4-PBA administration also resulted in a striking diminution in the expression of BAX and cleaved caspase-3 proteins and a pronounced upregulation in protein expression of Bcl-2 in the 4-PBA+I/R group (Figure 4(k)).

3.5. Naringenin Effectively Alleviated ER Stress in H/R-Exposed HK-2 Cells. In addition, we constructed the H/R model in vitro to further verify the protective effects of naringenin in renal I/R injury. As shown in Figure 5(a), to find out the appropriate concentration that could be used for treating HK-2 cells, we selected CCK-8 assay to explore the effects of different concentrations of NRG on cell viability. The cell activity of HK-2 cells was not significantly affected by NAR at 200 μM, a concentration that was also selected in another study [33]. HK-2 cells were pretreated with 200 μM of NRG dissolved in DMSO and received H/R exposure 24 h later. Quantitative real-time PCR analysis demonstrated that NAR treatment noticeably alleviated the elevated mRNA levels of GRP78, CHOP, and caspase-12 in H/R injury (Figures 5(b)–5(d)). Consistent with mRNA levels, the protein expression of those specific markers of ER stress exhibited the obvious reduction in the NRG+H/R group (Figure 5(e)).

3.6. Naringenin Considerably Mitigated H/R-Induced Pyroptosis and Apoptosis In Vitro. In Figure 6(a), the obvious elevation of caspase-1 activity in H/R exposure was remarkably depressed after naringenin application in renal HK-2 cells. qRT-PCR revealed that the pretreatment of naringenin evidently lessened the mRNA levels of typical pyroptosis-related markers including ASC, NLRP3, and caspase-1 during H/R injury (Figure 6(b)). Besides, we authenticated that

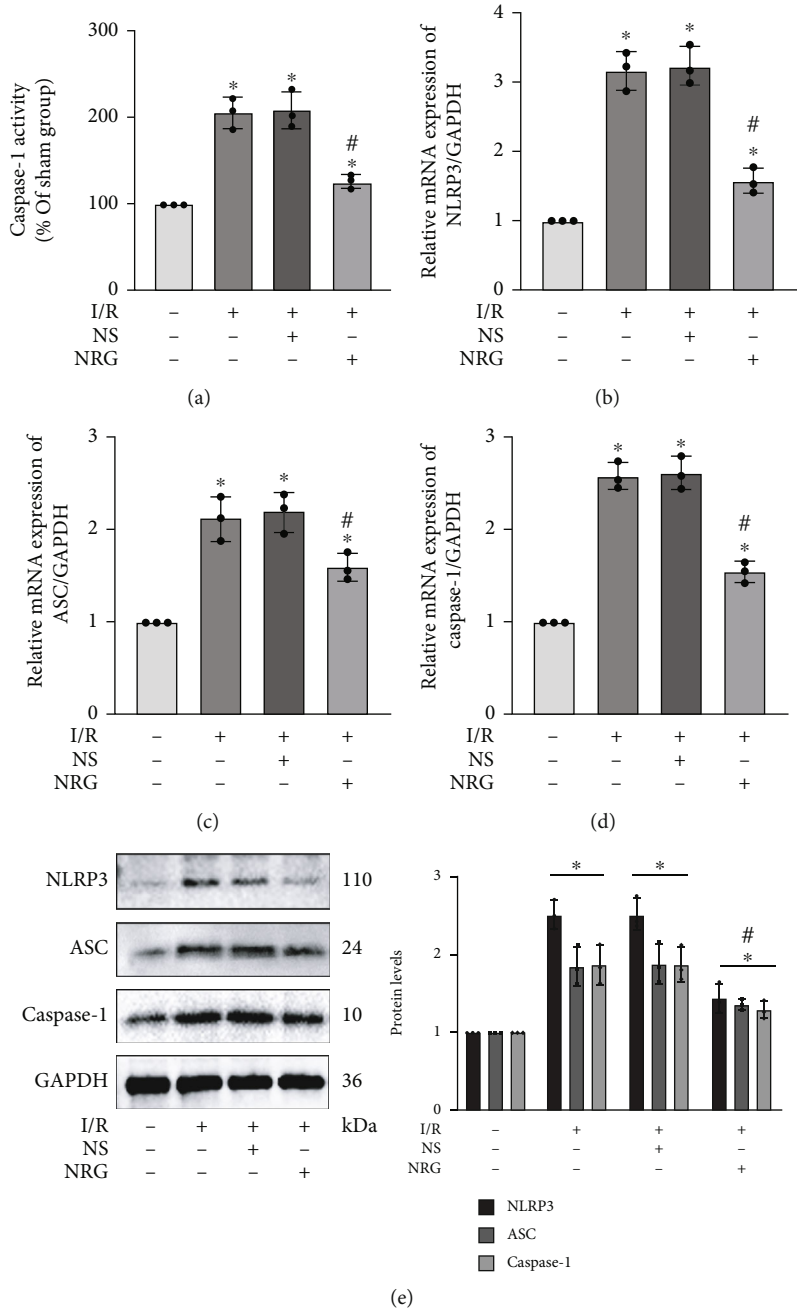

Figure 3: Continued.

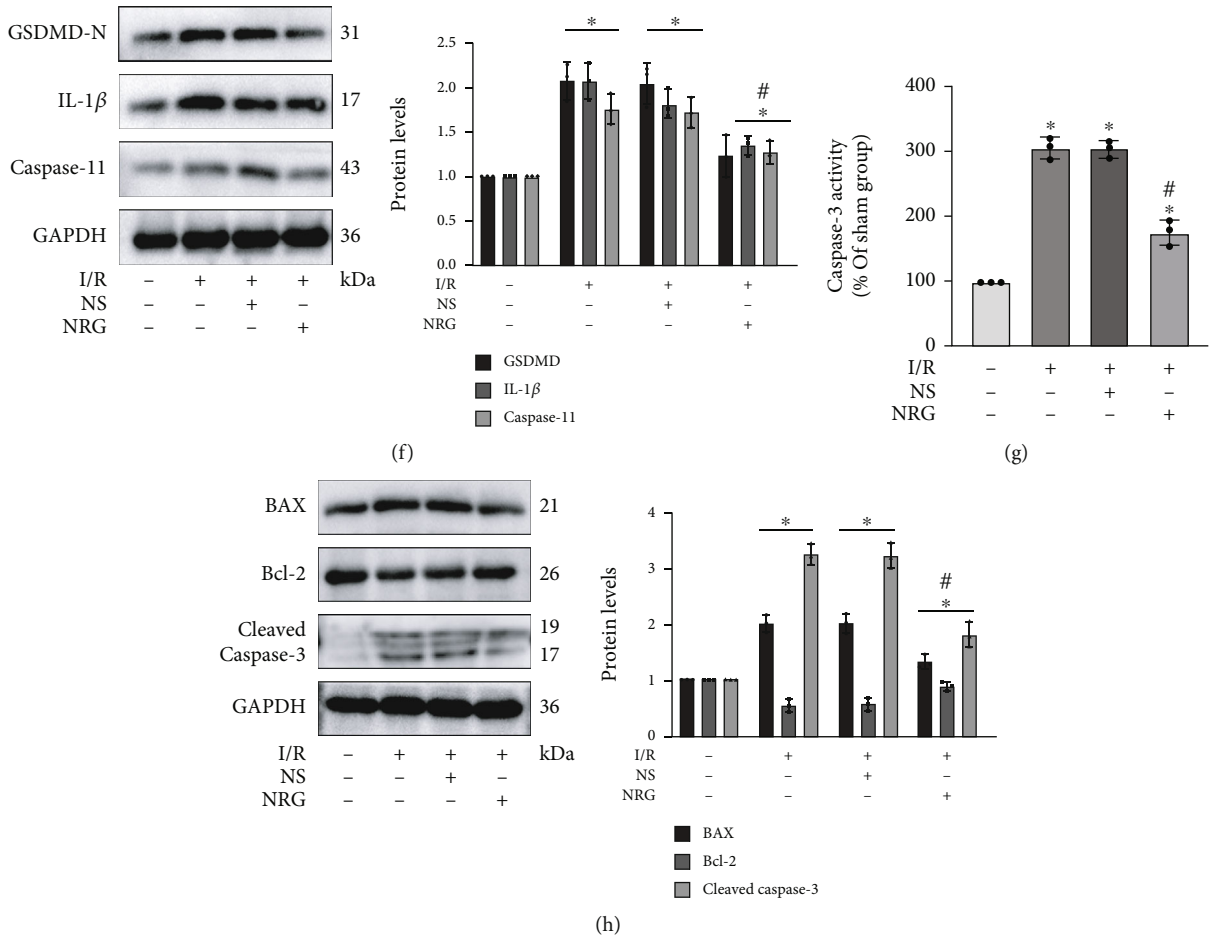

Figure 3: Naringenin significantly inhibited pyroptosis and apoptosis induced by renal I/R injury in mice. (a) The levels of caspase-1 activity in the I/R group exhibited obvious reduction after naringenin treatment. (b–d) Naringenin significantly inhibited the mRNA expression of pyroptosis-related markers such as NLRP3, ASC, and caspase-1 in renal I/R injury. (e, f) Renal I/R-generated pyroptosis was obviously ameliorated by naringenin application as evidenced by the decreased protein expression of NLRP3, ASC, caspase-1, GSDMD-N, caspase-11, and IL-1β in extracted kidney tissues. (g) The usage of naringenin remarkably restrained caspase-3 activity in renal I/R injury. (h) Western blot analysis utilized in protein detection of kidney tissue was selected to detect the protein levels of Bcl-2, BAX, and cleaved caspase-3 in the four groups. Values measured during animal experiments were carried out as mean ± SD, $n = 3$ (three times measurement). $^{*}P < 0.05$, compared with the Sham group; $^{\#}P < 0.05$, relative to the NS+I/R group.

NAR application was capable of attenuating H/R-induced activation of NLRP3 inflammasome in HK-2 cells (Figure 6(c)). Pretreatment of NRG on HK-2 cells prior to the establishment of H/R model remarkably depressed the expression of GSDMD-N, mature IL-1β, and caspase-4 proteins, which were crucial markers of pyroptosis (Figure 6(d)). The flow cytometry revealed that NAR administration tremendously mitigated H/R-stimulated apoptotic HK-2 cells (Figures 6(e) and 6(f)). The caspase-3 activity in H/R injury was effectively inhibited by NRG treatment in HK-2 cells (Figure 6(g)). The results of western blot analysis demonstrated that BAX protein levels as well as cleaved caspase-3 protein levels were obviously reduced in the NRG +H/R group versus DMSO+H/R group, whereas Bcl-2 protein levels were upregulated after NRG usage in vitro (Figure 6(h)).

3.7. H/R-Induced Pyroptosis and Apoptosis Depended on ER Stress In Vitro. A concentration at 5 mM of 4-PBA was taken to handle HK-2 cells that were followed by H/R treatment as described previously. Inhibition effect on ER stress of 4-PBA was verified by western blot analysis, as shown by remarkable reduction in expression levels of GRP78, CHOP, and caspase-12 proteins (Figure 7(a)). Notably, 4-PBA application significantly reduced caspase-1 activity and obviously decreased the relative mRNA levels of NLRP3, caspase-1, and ASC in H/R injury (Figures 7(b) and 7(c)). The preusage of 4-PBA also led to the restriction of activated protein markers of pyroptosis during H/R injury (Figures 7(d) and 7(e)). By performing flow cytometry, we could clearly observe that apoptosis rate in HK-2 cells increased considerably during H/R injury, whereas it was greatly reversed after ER stress inhibition through 4-PBA application (Figures 7(f) and 7(g)). The protein levels in different treatment groups confirmed that the administration of 4-PBA effectively restrained the expression of apoptotic markers including BAX and cleaved caspase-3, and the trend of Bcl-2 protein was elevated in the 4-PBA+H/R group (Figure 7(h)).

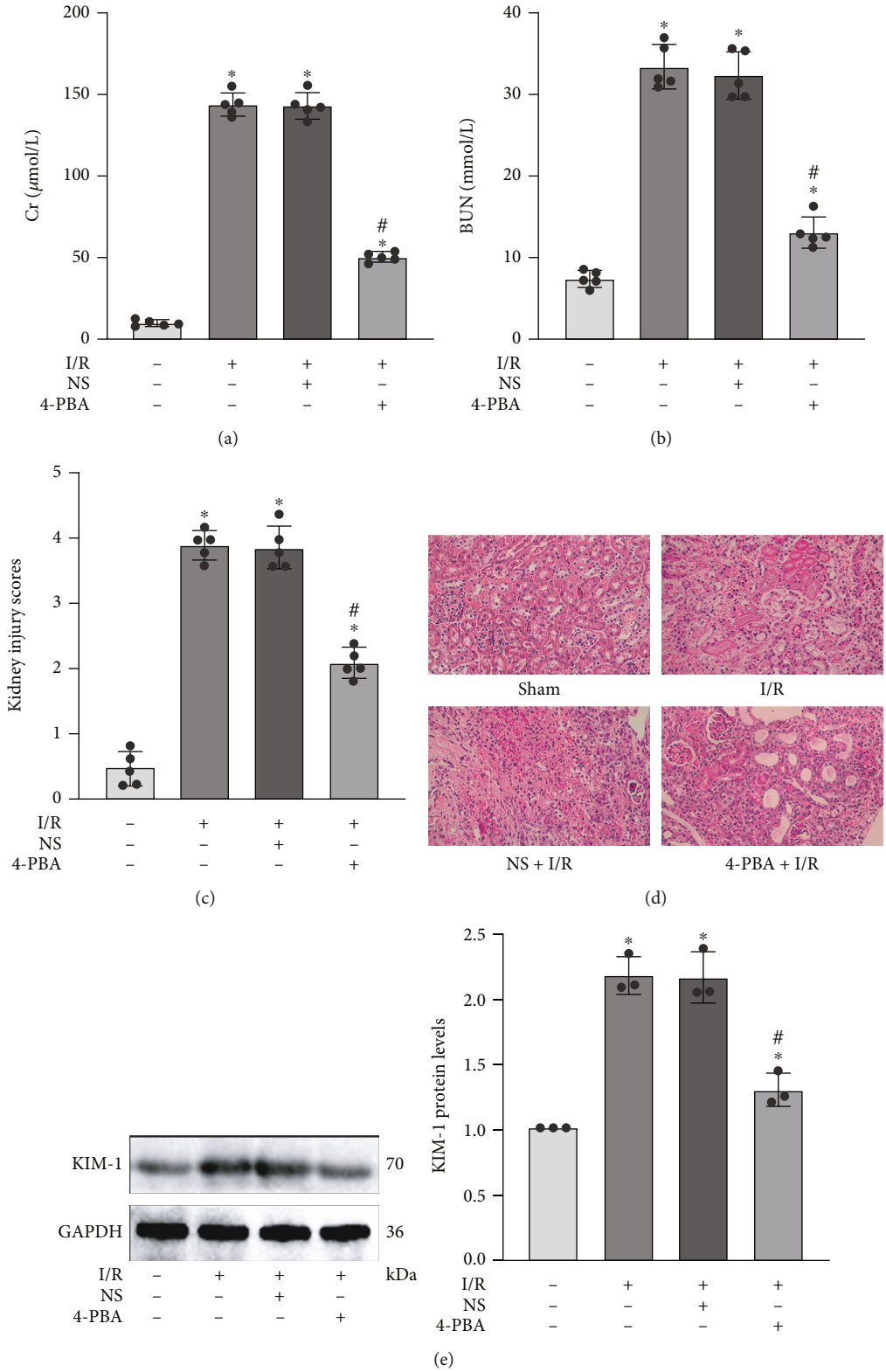

Figure 4: Continued.

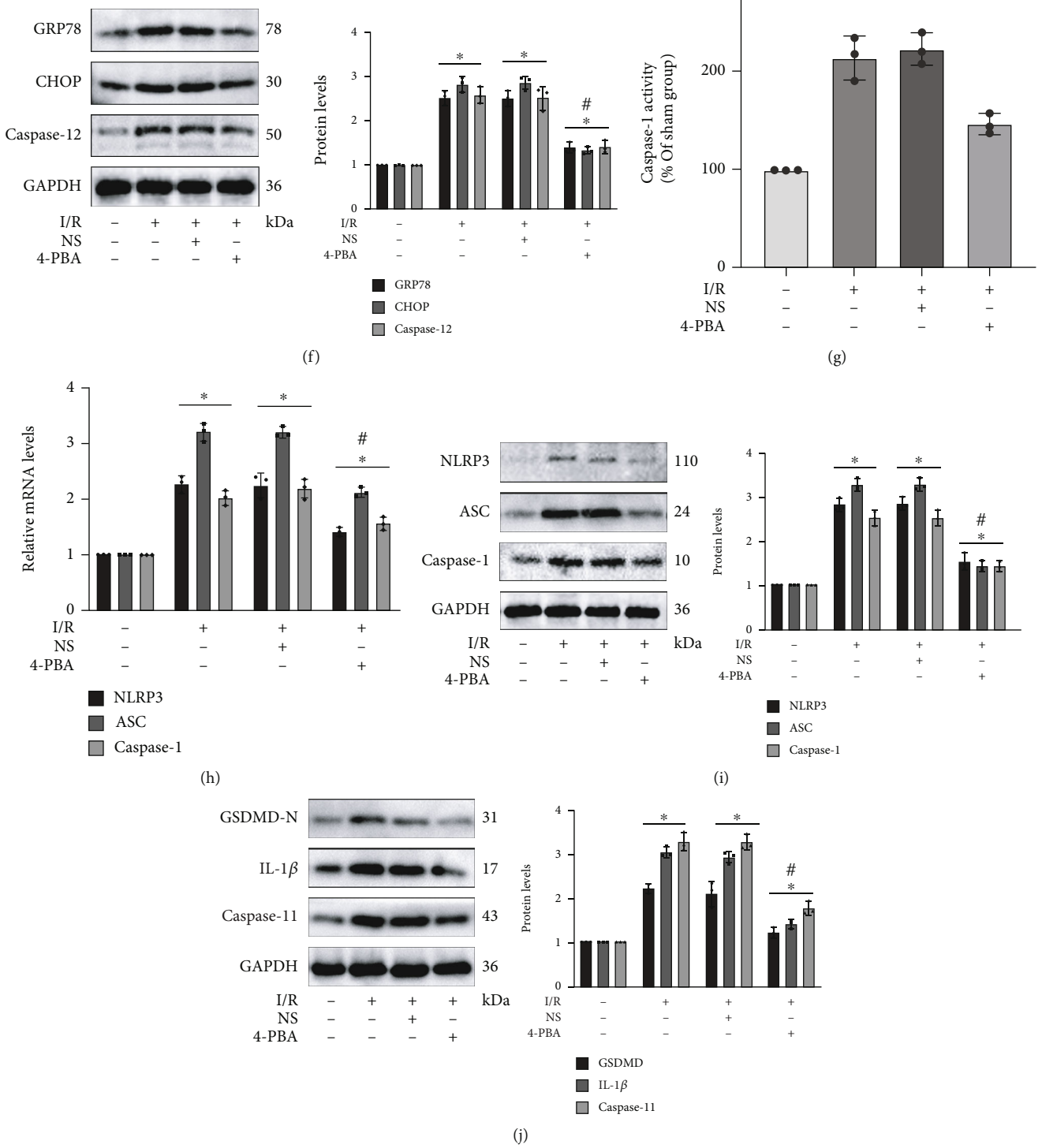

Figure 4: Continued.

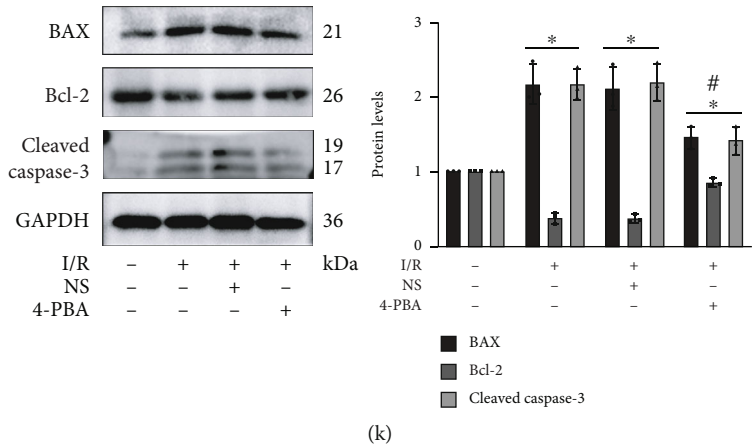

(k)

FIGURE 4: Renal I/R-generated pyroptosis and apoptosis could be regulated by ER stress in mice. Mice in the 4-PBA+I/R group were injected intraperitoneally with 4-PBA (100 mg/kg, dilution in phosphate-buffered saline) 24 h before undergoing renal I/R surgery. (a, b) The levels of serum Cr and serum BUN in renal I/R injury decreased notably after inhibiting ER stress by 4-PBA application. (c, d) Quantitative analysis of tubular injury scores and representative images of H&E staining in different groups. (e) KIM-1 protein levels were assessed by western blot analysis. (f) The established inhibitor 4-PBA effectively restrained the protein expression of GRP78, CHOP, and caspase-12 in renal I/R injury. (g) The inhibition of ER stress by 4-PBA tremendously depressed the caspase-1 activity in mice with renal I/R surgery. (h) The mRNA levels of NLRP3, ASC, and caspase-1 in the I/R group declined after the application of 4-PBA. (i, j) 4-PBA as one specific inhibitor of ER stress remarkably depressed the activation of pyroptosis-related protein markers including NLRP3, ASC, caspase-1, GSDMD-N, IL-1β, and caspase-11. (k) The protein levels of apoptotic markers consisting of BAX, Bcl-2, and cleaved caspase-3. Values measured during animal experiments were carried out as mean ± SD, $n = 3 - 5$. $^{*}P < 0.05$, compared with the Sham group; $^{\#}P < 0.05$, relative to the NS+I/R group.

3.8. Naringenin Activated Nrf2/HO-1 Signaling Pathway to Block Endoplasmic Reticulum Stress in HK-2 Cells. Next, subject members explored underlying mechanism by which NAR was capable of modulating ER stress. Since NAR could notably alleviate ER stress [34, 35] and Nrf2/HO-1 pathway had been demonstrated to be of great importance in regulating ER stress [36, 37], we examined the expression of relevant proteins after NAR usage in vitro. The protein expressions of Nrf2 and HO-1 were indeed visibly suppressed by H/R treatment, while pretreatment of NRG reactivated Nrf2/HO-1 signaling pathway in H/R injury (Figure 8(a)). We employed brusatol (Bru), an established inhibitor of Nrf2 pathway, to further investigate whether Nrf2/HO-1 signaling pathway exerted effect on NAR-regulated ER stress generated by H/R exposure. The triggering action of NRG on Nrf2/HO-1 signaling pathway was apparently abolished by Bru administration (Figure 8(b)). Interestingly, the abrogating consequence of Bru on Nrf2/HO-1 signaling pathway was accompanied by this striking reversal of NRG's impact on mitigating H/R-generated ER stress in vitro as well (Figure 8(c)).

3.9. Schematic Illustration of the Protective Effects of Naringenin on Renal I/R Injury. In vivo and in vitro, naringenin treatment reactivated Nrf2/HO-1 signaling pathway to block ER stress, thus attenuating pyroptosis and apoptosis to exert its protective effects on renal I/R injury (Figure 9).

4. Discussion

Renal I/R injury is seen as one complicated and intractable pathological process, and it is usually caused by sepsis, organ transplantation, and renal surgery [5, 7]. What is more serious and unacceptable is that if effective and timely measures are not taken to prevent it, renal I/R injury is prone to gradually develop into AKI, one clinic syndrome with noticeable hospital mortality due to its rapid kidney dysfunction and few satisfactory treatment strategies [1, 38, 39]. Encouragingly, there are also relevant clinical studies, which have demonstrated that some treatment strategies may be able to improve acute kidney injury to some extent by inhibiting pathological events such as ER stress, inflammatory response, and apoptosis in hospital patients. Tang et al. performed clinical trials to confirm that dexmedetomidine could attenuate AKI as well as postischemic myocardial injury, and the mechanisms may be related to the inhibition of ER stress, oxidative stress, and apoptosis [40]. 80 mg/d of atorvastatin may attenuate contrast-induced acute kidney injury by inhibiting apoptosis [41]. Remote ischemic preconditioning displayed significant anti-inflammatory effects [42] and could prevented contrast medium-induced nephropathy [43]. High-dose erythropoietin may be beneficial for some patients with sepsis-AKI possibly through anti-inflammatory effects in macrophage [44]. Naringenin was selected to investigate its role and involved mechanisms in renal I/R injury in our study, mainly because of its good bioavailability, powerful antioxidant, anti-inflammatory and antiapoptotic functions, and wide application prospects. In this research, we smoothly established classical animal model and HK-2 cell model to address the question whether naringenin could attenuate renal I/R injury and the underlying mechanisms behind its protective effects. Primarily, this study innovatively confirmed that NAR significantly improved tissue damage and renal function by inhibiting

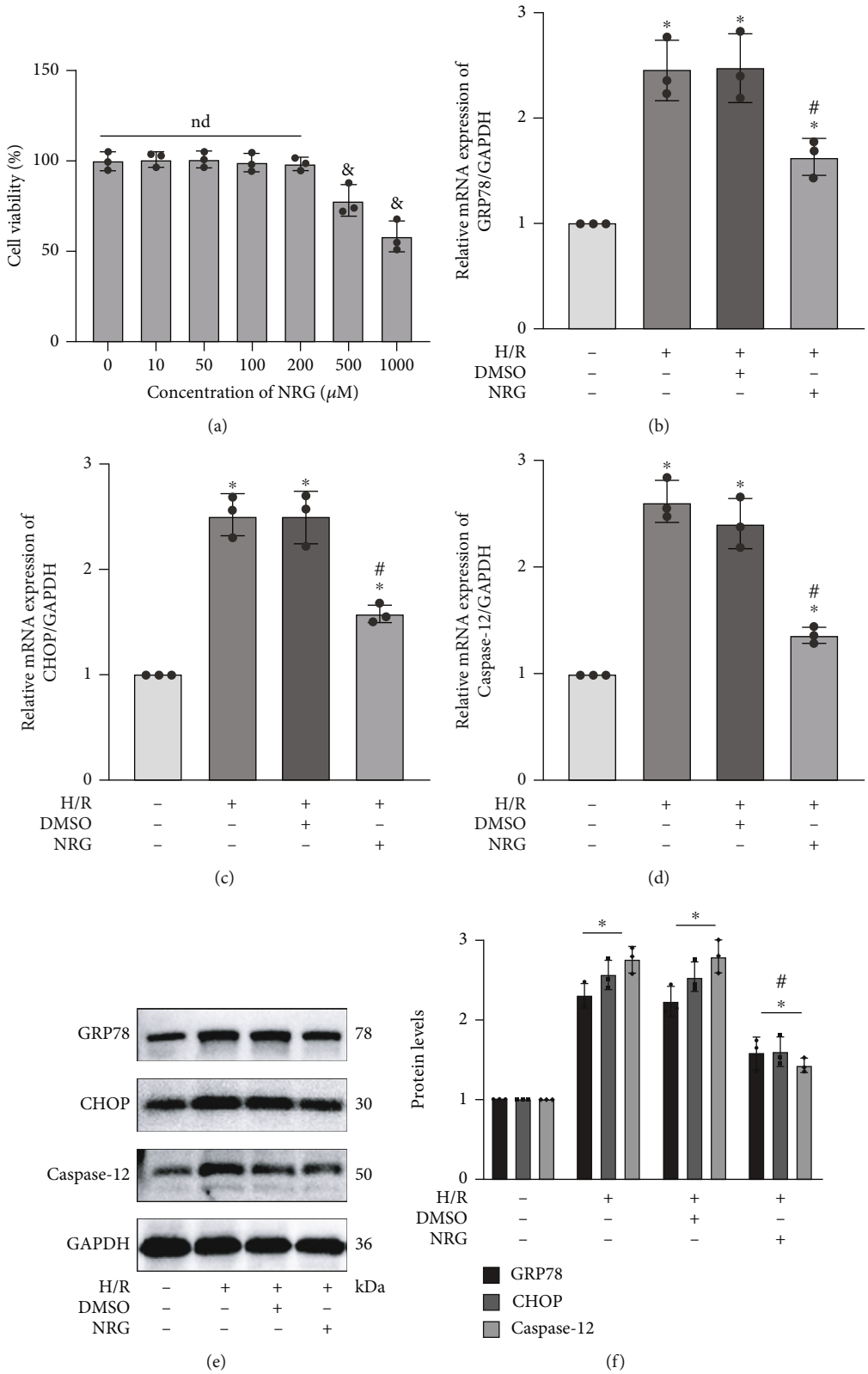

Figure 5: Naringenin effectively alleviated ER stress in H/R-exposed HK-2 cells. (a) CCK-8 assay explored the effects of different concentrations of NAR on cell viability. Concentration at 200 μM was selected in the following experiments. (b–d) The mRNA expression in GRP78, CHOP, and caspase-12 was explored by qRT-PCR. (e, f) Naringenin treatment noticeably alleviated the elevated protein levels of GRP78, CHOP, and caspase-12 in H/R injury. Values measured during cellular experiments were carried out as mean ± SD, $n = 3$ (three independent experiments). $^{\&}P < 0.05$, relative to 0 μM group; $^{*}P < 0.05$, compared with the control group; $^{\#}P < 0.05$, versus the DMSO+H/R group; nd: no statistical difference.

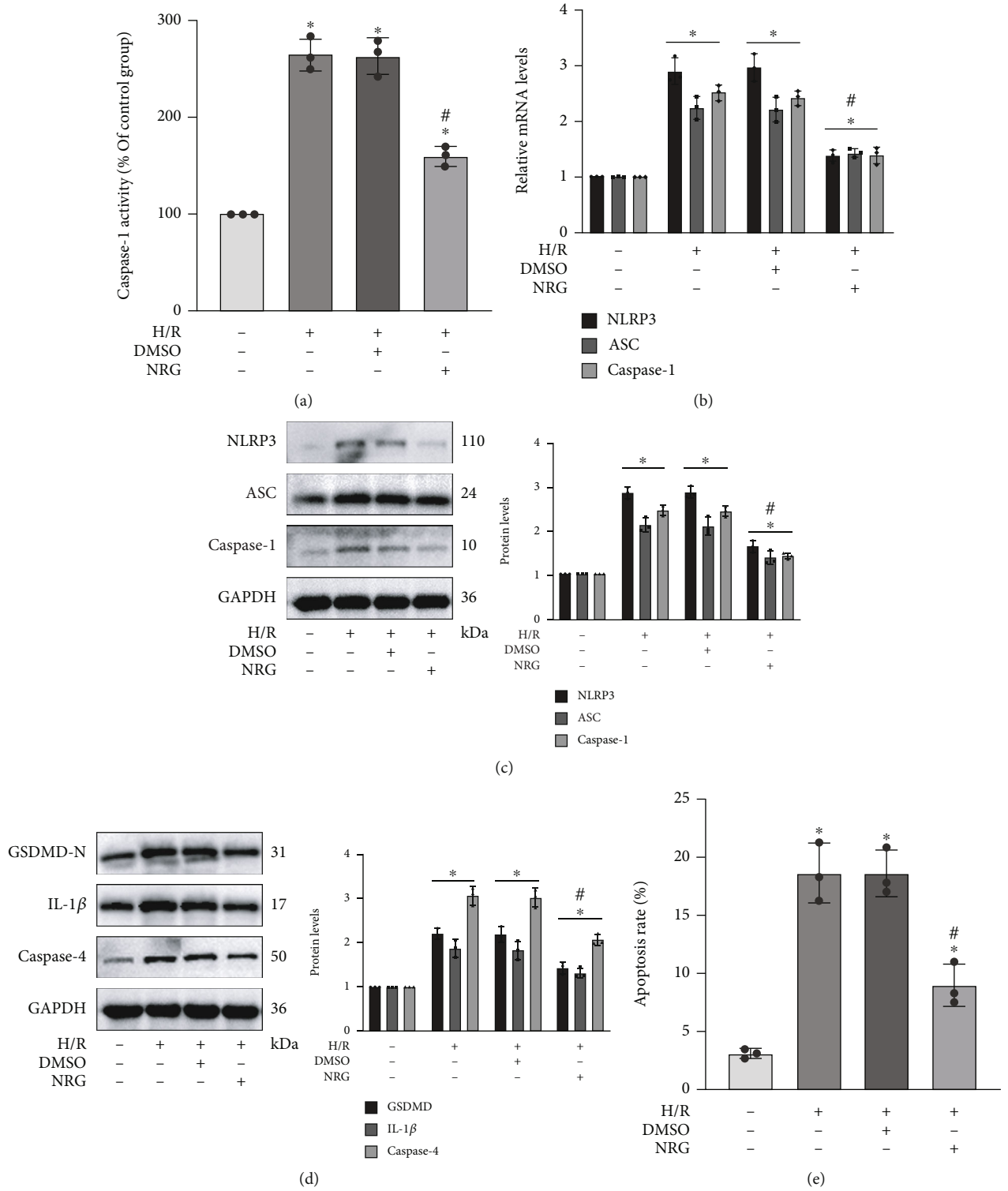

Figure 6: Continued.

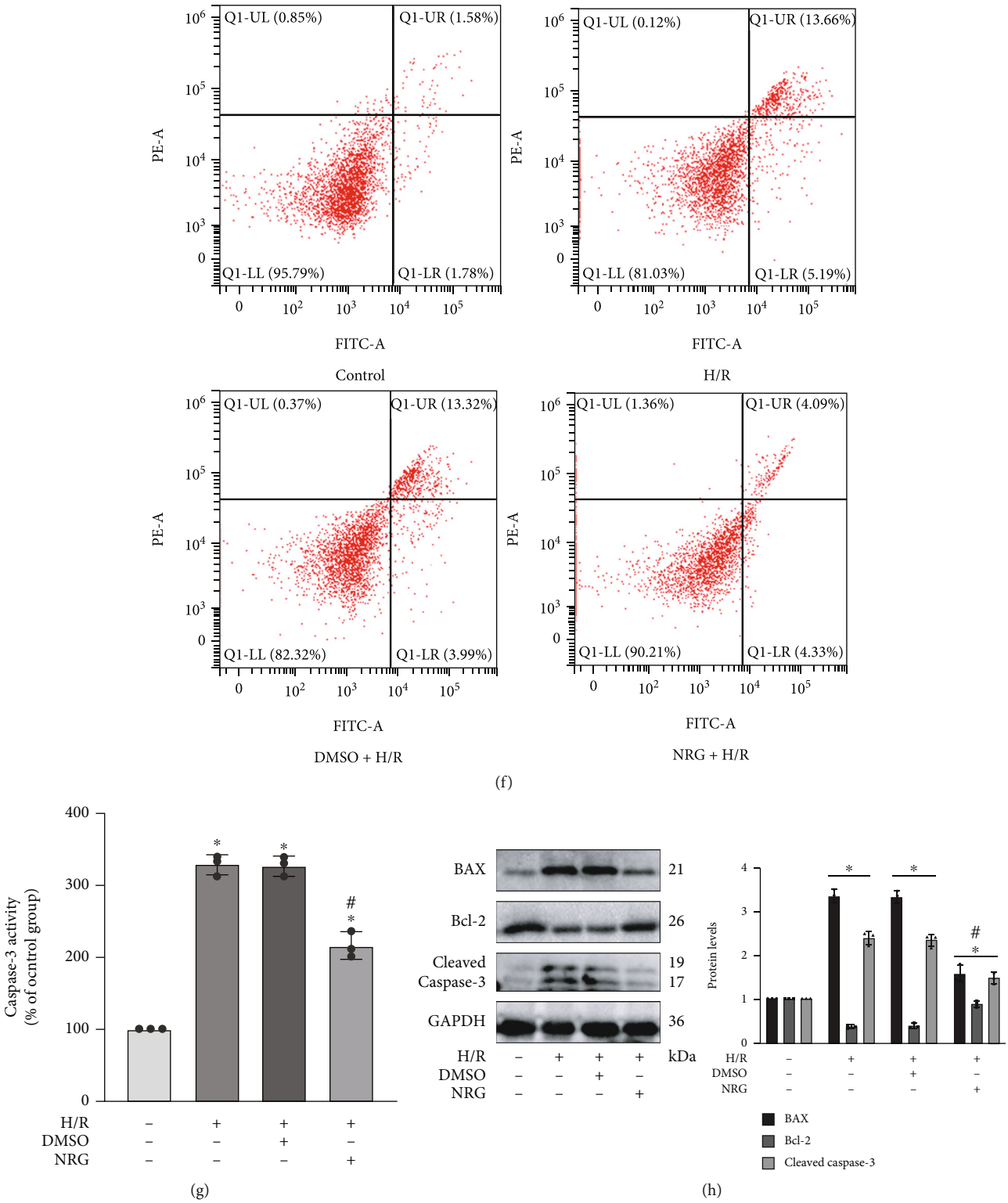

Figure 6: Naringenin considerably mitigated H/R-induced pyroptosis and apoptosis in vitro. (a) The obvious elevation of caspase-1 activity in H/R exposure was remarkably depressed after naringenin application in renal HK-2 cells. (b) The pretreatment of naringenin evidently lessened the mRNA levels of typical pyroptosis-related markers including ASC, NLRP3, and caspase-1 during H/R injury. (c, d) The usage of naringenin markedly decreased the protein levels of representative pyroptosis-related markers such as NLRP3, caspase-1, ASC, GSDMD-N, IL-1β, and caspase-4 after H/R exposure. (e, f) The flow cytometry revealed that naringenin administration tremendously mitigated H/R-generated apoptotic HK-2 cells. (g) The caspase-3 activity in various groups. (h) Western blot analysis utilized in protein detection of HK-2 cells was performed to quantify the protein levels of Bcl-2, cleaved caspase-3, and BAX in various group. Values measured during cellular experiments were carried out as mean ± SD, $n = 3$. $^{*}P < 0.05$, compared with the control group; $^{\#}P < 0.05$, versus the DMSO+H/R group.

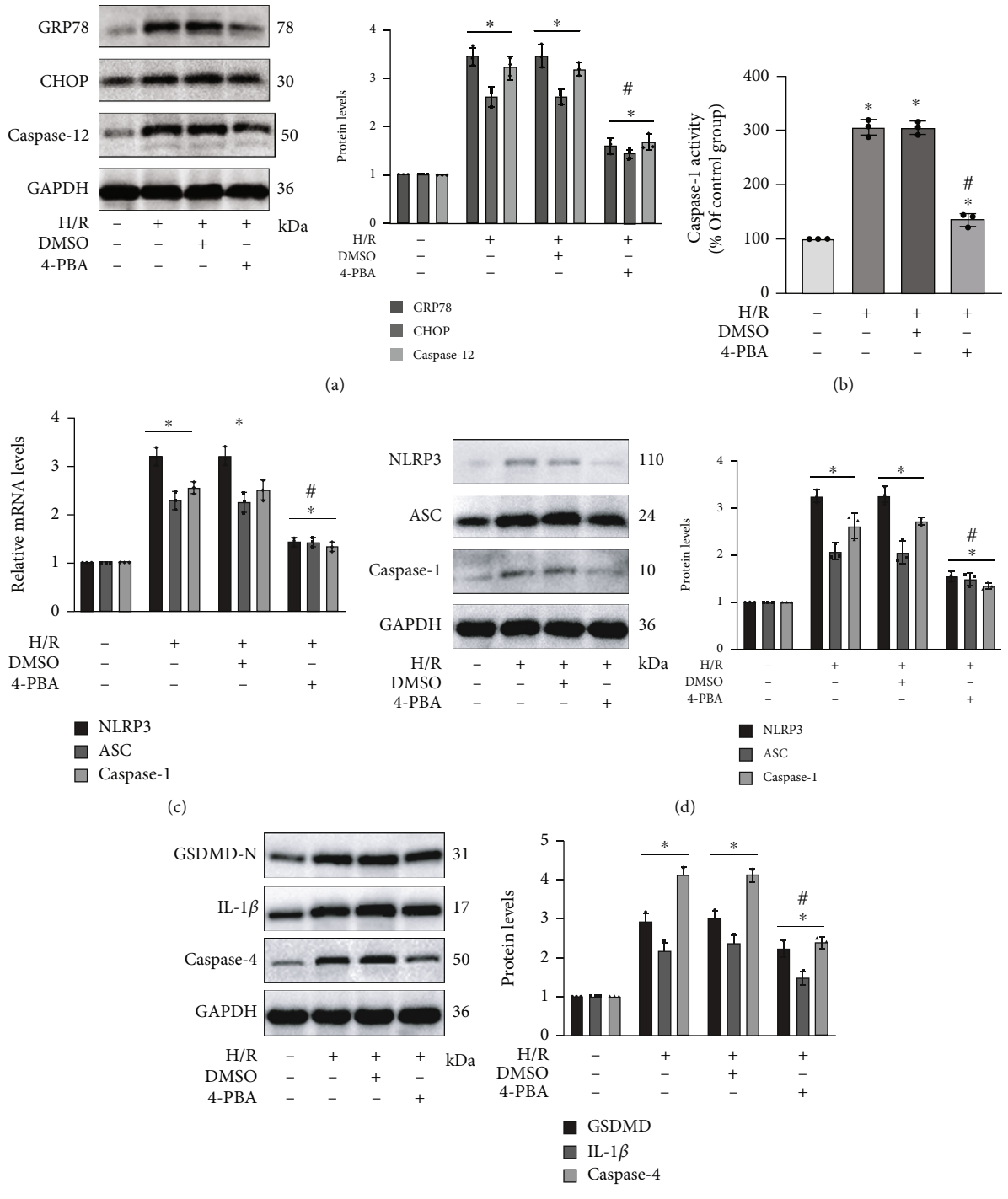

Figure 7: Continued.

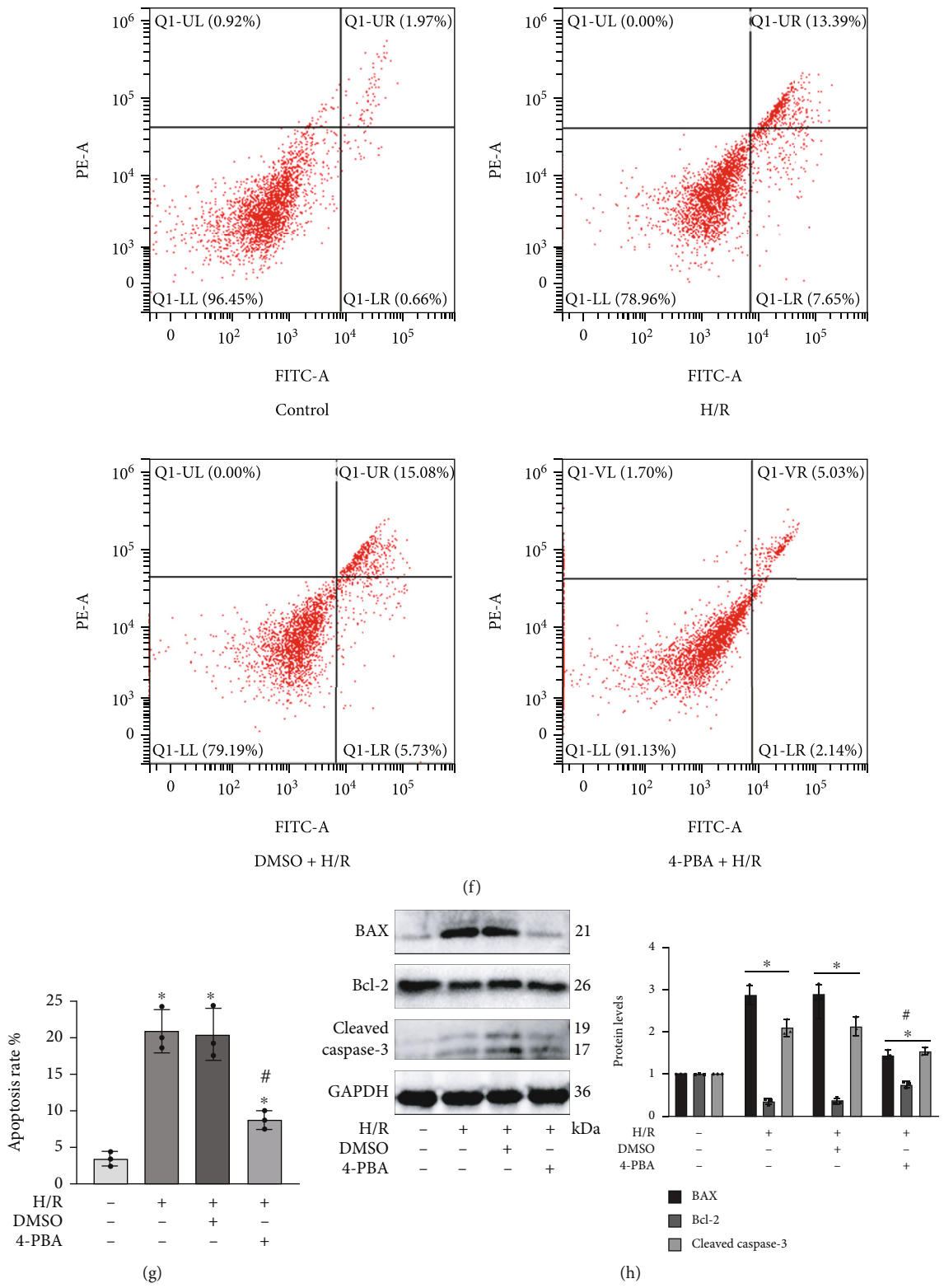

Figure 7: H/R-induced pyroptosis and apoptosis depended on ER stress in vitro. 5 mM of 4-PBA was taken to handle the HK-2 cells 24 h before H/R treatment as described previously. (a) The influence of 4-PBA on GRP78, CHOP, and caspase-12 proteins in H/R injury was verified by western blot analysis. (b) The levels of caspase-1 activity in the four groups. (c) 4-PBA application obviously decreased the relative mRNA levels of NLRP3, caspase-1, and ASC. (d, e) The rising levels of specific protein markers of pyroptosis in H/R injury declined after restraining ER stress by 4-PBA. (f, g) The apoptosis rate in relevant groups was revealed by the flow cytometry. (h) Protein levels of Bcl-2 and cleaved caspase-3 as well as BAX. Values measured during cellular experiments were carried out as mean ± SD, $n = 3$. $^{*}P < 0.05$, compared with the control group; $^{\#}P < 0.05$, versus the DMSO+H/R group.

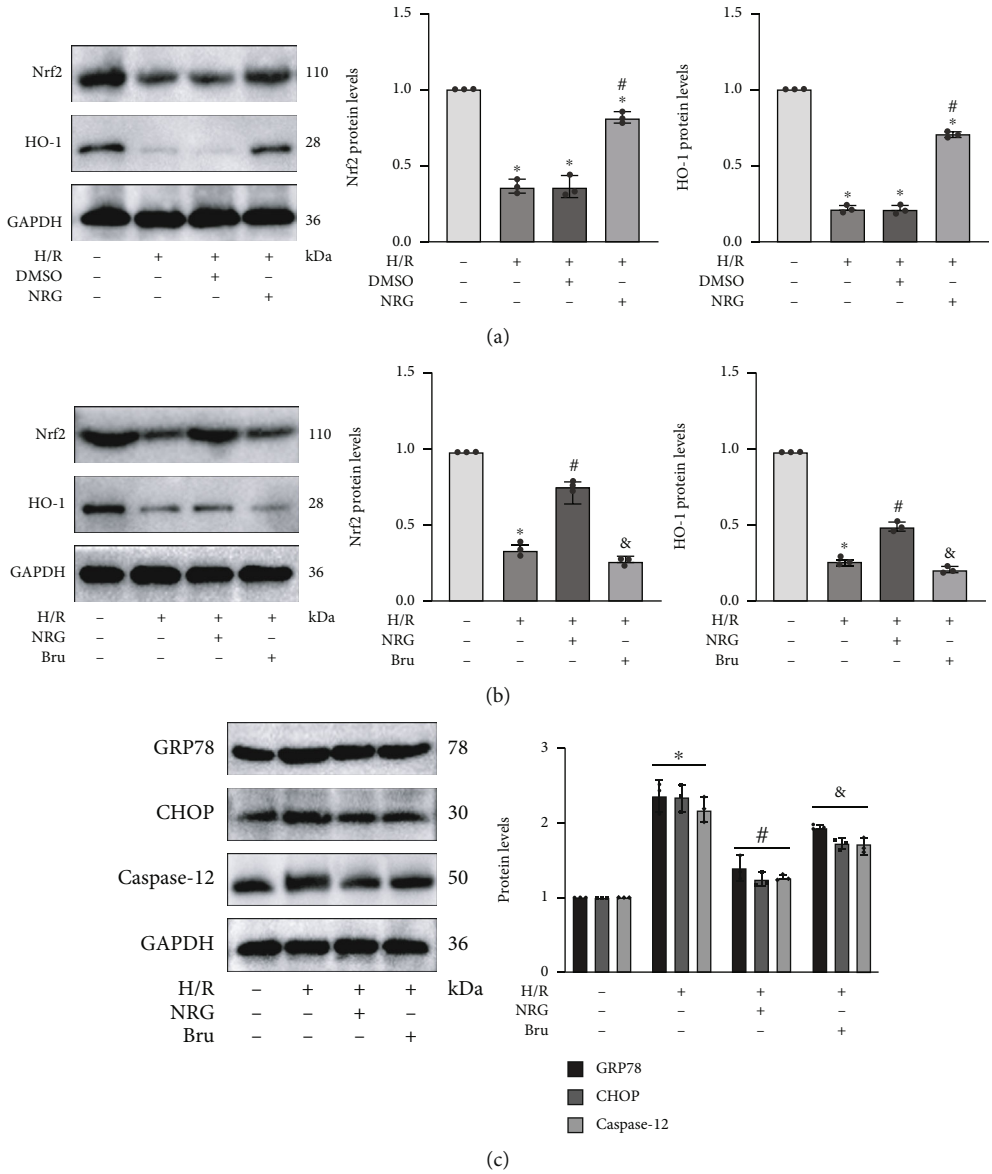

Figure 8: Naringenin activated Nrf2/HO-1 signaling pathway to block endoplasmic reticulum stress in HK-2 cells. 200 μM of NRG was added to the medium 24 h before model construction, and then, they were incubated with or without brusatol (400 nM) 2 h before hypoxia. (a) Naringenin activated Nrf2 and HO-1 after H/R injury. (b) Western blot analysis proved that Nrf2 and HO-1 protein levels were effectively prevented by brusatol (Bru) in HK-2 cells. (c) Inhibiting Nrf2/HO-1 signaling pathway reversed the function of naringenin on restraining ER stress. Values measured during cellular experiments were carried out as mean ± SD, $n = 3$. $^{*}P < 0.05$, versus the control group; $^{\#}P < 0.05$, compared with the H/R group; $^{\&}P < 0.05$, relative to the NRG+H/R group.

ER stress, pyroptosis and apoptosis induced by renal I/R injury both in vivo and in vitro. Interestingly, the application of 4-PBA as one characteristic inhibitor of ER stress clearly authenticated that renal I/R-generated pyroptosis and apoptosis were at least partially dependent on ER stress in animal and cell models. Furthermore, the reason for effective mitigation on renal I/R-induced ER stress by naringenin was found to be NAR's power in activating the antioxidant Nrf2/HO-1 signaling pathway. Taken together, the in vivo and in vitro experiments suggested that naringenin activated Nrf2/HO-1 pathway that was notably restrained during the process of renal I/R injury to relieve ER stress, thereby alleviating pyroptosis and apoptosis to protect the kidney against I/R injury.

ER stress, pyroptosis, and apoptosis are regarded as markedly crucial and interrelated molecular events in pathogenesis of renal I/R injury and have received increasing attention in recent years [3, 8, 45]. Endoplasmic reticulum (ER), one indispensable intracellular organelle, is capable of maintaining protein homeostasis such as polypeptide folding, protein modification and degradation, calcium storage, and lipid synthesis [46]. However, unfolded protein response (UPR) will be triggered by pathological conditions including severe hypoxia, persistent calcium imbalance, and

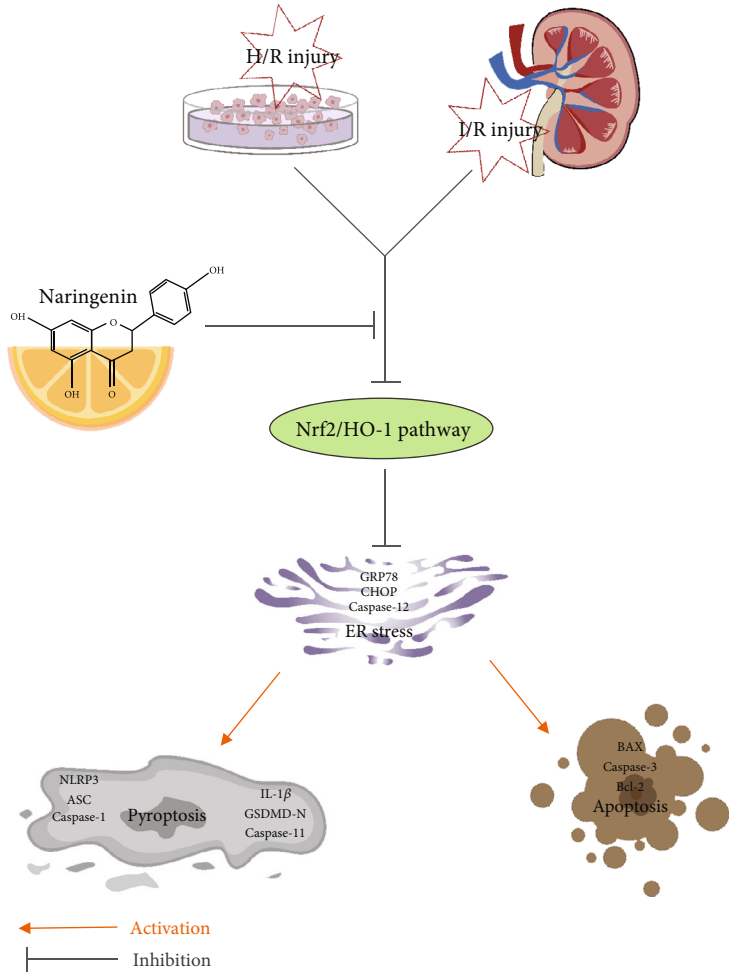

Figure 9: Schematic illustration of the protective effects of naringenin on renal I/R injury.

destroying ER homeostasis. The whole abnormal intracellular biological activities and stress stimuli in ER eventually induce what is known as endoplasmic reticulum stress [47]. GRP78 normally functions by binding to three major transmembrane protein sensors (ATF6, IRE1, and PERK) of ER stress in the endoplasmic reticulum lumen [48]. GRP78 is able to bind to unfolded proteins and lately could fold or degrade them through ER-related protein degradation pathways. Elevated expression of GRP78 is considered to be one significant marker of ER stress [49]. The degree and duration of pathogenic stimuli could largely determine the ultimate fate of cells, which means that sustained and extreme stress inevitably activates apoptotic UPR pathways to cause apoptosis [50]. Meantime, acting as one common element after the activation of 3 sensors of ER stress mentioned above, CHOP is treated as one crucial regulator of cellular apoptosis induced by ER stress because it could lend assistance in caspase activation, restraining the expression of antiapoptotic Bcl-2, leading to apoptotic cell death [51, 52]. Caspase-12 is a key molecule in the endoplasmic reticulum-specific apoptotic signaling pathway and is not associated with nonendoplasmic reticulum stress-mediated apoptosis. Caspase-12 is localized in the endoplasmic reticulum membrane and undergoes significant activation upon sustained ER stress, which ultimately induces the onset of apoptosis [53]. In I/R injury, related articles confirmed that inhibition of ER stress could effectively suppress apoptosis to alleviate I/R injury [54–56]. Consistent with these studies, our research demonstrated that the pretreatment of 4-PBA as one specific inhibitor of ER stress remarkably attenuated renal I/R-induced apoptosis, as indicated by flow cytometry, depressed expression of cleaved caspase-3, and BAX as well as the recovered levels of Bcl-2 in C57Bl/6 mice and HK-2 cells.

Pyroptosis, one unique form of cell death, is shown to be involved in the occurrence and pathogenesis of AKI along with apoptosis, ferroptosis, and necrosis [57]. Two major pathways are thought to have participated in the occurrence of pyroptosis. The classical signaling pathway is principally regulated through activating caspase-1, while caspase-11 or caspase-4 in human plays an important role inside the nonclassical pathway [8]. Interestingly, pyroptosis is characterized by the noteworthy involvement of inflammatory response especially the activation of NLRP3 inflammasome that was composed of procaspase-1, ASC, and NLRP3. Inactive NLRP3 that was localized in the ER and its adaptor protein ASC induced disruption of mitochondrial homeostasis and initiated pyroptosis upon the process of NLRP3 activation

[58]. In addition, ER stress occurring in the early stage is able to induce renal inflammation and activate NF-κB signaling pathway, which incidentally exacerbates the occurrence of pyroptosis [59, 60]. During the procedures of pyroptosis initiation, NLRP3 inflammasome naturally activates caspase-1, which not only drives IL-1β precursor into forming mature proinflammatory cytokine IL-1β but also cleaves gasdermin D and releases its N-terminal domain, one specific marker binding to membrane lipids, causing pyroptosis [61, 62]. In our investigation, the obvious participation of pyroptosis in renal I/R injury was verified by increased expressions of mentioned markers including caspase-1, ASC, NLRP3, GSDMD-N, caspase-11, caspase-4, and IL-1β in animal and cell models. These findings were in agreement with our published articles [25, 29]. Moreover, we innovatively revealed that inhibition of ER stress in renal I/R injury not only considerably relieved renal tissue damage but also successfully mitigated the outbreak of pyroptosis, as evidenced by distinguished alleviation of pyroptosis-related markers mentioned above in the 4-PBA +I/R (or H/R) group compared with the I/R (or H/R) group. Taken together, these data demonstrated that the inhibitory effect of NRG on pyroptosis and apoptosis was at least partially dependent on the alleviation of endoplasmic reticulum stress. The phenomenon that suppression of ER stress was capable of alleviating pyroptosis was also testified in other disease models [63–65].

Naringenin, one polyphenolic constituent existing in dietary citrus fruits, has attracted notable attention from researchers in various fields because of its powerful pharmacological activities and promising therapeutic prospects [32]. Naringenin was proved to regulate inflammatory response, oxidative stress, ER stress, and apoptosis as well as possessing protective effects against common clinical disorders including diabetes, carcinomas, cardiovascular, and neurodegenerative [17, 31]. Fortunately, more than ten clinical trials have been conducted to explore its specific outcome in hospital problems such as cardiovascular diseases, endothelial function, weight control, and HCV infection [14]. Nevertheless, there are no clinical trials of naringenin in kidney diseases, and what is more frustrating is that the role of naringenin in renal I/R injury has not even been fully clarified in basic studies in animal and cell models. During renal I/R injury, naringenin application mitigated the levels of kidney tissue damage, Cr, BUN, and KIM-1 as well as restraining the elevation of relevant markers including CHOP, GRP78, BAX, caspase-12, cleaved caspase-3, caspase-1, ASC, NLRP3, GSDMD-N, caspase-11, caspase-4, and IL-1β, indicating that naringenin administration by gavage noticeably attenuated renal tissue damage and improved impaired kidney function in renal I/R injury by preventing ER stress, pyroptosis, and apoptosis, which were proved again in HK-2 cell model.

Nrf2, one nuclear transcription factor, serves as a key regulator in mediating intracellular antioxidant defense system [66]. Although Nrf2 is bound to Keap1 in the cytoplasm and in an inactivated state, Nrf2 separates from its inhibitor protein Keap1 in response to pathological stimuli including oxidative stress and is transferred to the nucleus to activate the downstream genes to exert its antioxidant effects by forming a heterodimer with Maf protein [67]. Among these downstream targets, HO-1 is extremely susceptible to be activated by Nrf2 because it owns the highest number of AREs in the promoter, which is exactly the structure that Nrf2 needs to bind to activate antioxidant proteins [68]. Numerous studies pointed out that Nrf2/HO-1 activation was not only involved in various diseases, development, and oxidative stress response but also effective in relieving renal I/R injury [69]. In addition, with more and more in-depth studies, relevant articles revealed that apart from regulating oxidative stress, Nrf2/HO-1 pathway occupied an important position in regulating apoptosis, inflammation, and endoplasmic reticulum stress [36, 70, 71]. In this research, we observed that the crucial reason for NRG's ability to preserve kidney against I/R injury was its advantages in inhibiting pyroptosis and apoptosis by effectively reducing ER stress. It was frequently demonstrated that Nrf2/HO-1 signaling pathway took a momentous part in moderating ER stress [36, 37, 72], and NRG had been confirmed to have a talent in regulating Nrf2/HO-1 pathway to exert its protective effects [73–75]. The western blot analysis authenticated that decreased protein levels of Nrf2 and HO-1 during renal I/R injury were elevated again after pretreatment of naringenin in animals and HK-2 cells. Moreover, the experiments suggested that NRG could not exert an effect on suppressing H/R-generated ER stress after the addition of brusatol (a well-known Nrf2 inhibitor) in HK-2 cells. In other words, all those figures verified that naringenin blocked ER stress induced by renal I/R injury through activating Nrf2/HO-1 signaling pathway.

5. Conclusions

In conclusion, this implemented study innovatively confirmed that naringenin administration was capable of protecting kidney against I/R injury by attenuating pyroptosis and apoptosis via inhibiting ER stress through activating Nrf2/HO-1 signaling pathway. All this evidence could present novel mechanistic insights into the beneficial functions of naringenin, indicating the possibility of a new therapeutic drug for clinical treatment in hospital patients with ischemic kidney disease. However, whether naringenin can regulate other molecular mechanisms to relieve renal I/R injury and the corresponding clinical trials demands to be further explored.

Abbreviations

I/R: Ischemia reperfusion
NRG: Naringenin
H&E: Hematoxylin-eosin
ASC: Apoptosis-associated speck-like protein
AKI: Acute kidney injury
NS: Sterile saline
4-PBA: 4-Phenylbutyric acid
KIM-1: Kidney injury molecule 1
ER stress: Endoplasmic reticulum stress
Cr: Creatinine
GRP78: Glucose-regulated protein, 78 kDa

BUN: Blood urea nitrogen
NLRP3: NLR family pyrin domain containing 3
Nrf2: Nuclear factor- (erythroid-derived 2-) like 2
BAX: BCL2-associated X protein
Keap1: Kelch-like ECH-associated protein 1
GSDMD: Gasdermin D
IRE1: Inositol-requiring protein 1
Bcl-2: B-cell leukemia/lymphoma 2
IL-1β: Interleukin-1β
HCV: Hepatitis C virus
HO-1: Heme oxygenase (decycling) 1
CCK-8: Cell counting kit 8
ATF6: Activating transcription factor 6
SD: Standard deviation
CHOP: C/EBP-homologous protein
qRT-PCR: Quantitative real-time PCR analysis
Bru: Brusatol
PERK: Protein kinase R- (PKR-) like endoplasmic reticulum kinase
H/R: Hypoxia/reoxygenation
ARE: Antioxidant response element
HPLC: High-performance liquid chromatography
Maf: Muscle aponeurosis fibromatous.

Data Availability

Detailed data supporting the findings of this study are included in the manuscript.

Conflicts of Interest

The authors declare no competing interests.

Authors' Contributions

Banghua Zhang and Shanshan Wan contributed equally to this work. Xiuheng Liu, Zhiyuan Chen, and Lei Wang designed the protocol of this study and directed the experiments. Banghua Zhang and Shanshan Wan were responsible for conducting experiments and writing this article. Hao Liu, Qiangmin Qiu, and Hui Chen contributed to the collection, interpretation, and analysis of data throughout the experiments.

Acknowledgments

Our research was supported by the National Natural Science Foundation of China (No. 82000639), Innovation Project of Medical School of Wuhan University (TFZZ2018017), and Basic Research Project of Wuhan City (No. 2018060401011321).

References

[1] C. Ronco, R. Bellomo, and J. A. Kellum, "Acute kidney injury," *Lancet (London, England)*, vol. 394, no. 10212, pp. 1949–1964, 2019.

[2] A. Pefanis, F. L. Ierino, J. M. Murphy, and P. J. Cowan, "Regulated necrosis in kidney ischemia-reperfusion injury," *Kidney International*, vol. 96, no. 2, pp. 291–301, 2019.

[3] M. Yan, S. Shu, C. Guo, C. Tang, and Z. Dong, "Endoplasmic reticulum stress in ischemic and nephrotoxic acute kidney injury," *Annals of Medicine*, vol. 50, no. 5, pp. 381–390, 2018.

[4] N. Miao, F. Yin, H. Xie et al., "The cleavage of gasdermin D by caspase-11 promotes tubular epithelial cell pyroptosis and urinary IL-18 excretion in acute kidney injury," *Kidney International*, vol. 96, no. 5, pp. 1105–1120, 2019.

[5] G. J. Nieuwenhuijs-Moeke, S. E. Pischke, S. P. Berger et al., "Ischemia and reperfusion injury in kidney transplantation: relevant mechanisms in injury and repair," *Journal of Clinical Medicine*, vol. 9, no. 1, p. 253, 2020.

[6] H. Zhao, A. Alam, A. P. Soo, A. J. T. George, and D. Ma, "Ischemia-reperfusion injury reduces long term renal graft survival: mechanism and beyond," *eBioMedicine*, vol. 28, pp. 31–42, 2018.

[7] A. Hosszu, A. Fekete, and A. J. Szabo, "Sex differences in renal ischemia-reperfusion injury," *American Journal of Physiology. Renal Physiology*, vol. 319, no. 2, pp. F149–F154, 2020.

[8] N. Li, Y. R. Wang, X. Y. Wang, N. Sun, and Y. H. Gong, "Pathway network of pyroptosis and its potential inhibitors in acute kidney injury," *Pharmacological Research*, vol. 175, p. 106033, 2022.

[9] M. Schroder, "Endoplasmic reticulum stress responses," *Cellular and Molecular Life Sciences*, vol. 65, no. 6, pp. 862–894, 2008.

[10] J. Faitova, D. Krekac, R. Hrstka, and B. Vojtesek, "Endoplasmic reticulum stress and apoptosis," *Cellular & Molecular Biology Letters*, vol. 11, no. 4, pp. 488–505, 2006.

[11] Y. Zhou, Z. Tong, S. Jiang, W. Zheng, J. Zhao, and X. Zhou, "The roles of endoplasmic reticulum in NLRP3 inflammasome activation," *Cell*, vol. 9, no. 5, 2020.

[12] H. Jin, Y. Zhu, X.-d. Wang et al., "BDNF corrects NLRP3 inflammasome-induced pyroptosis and glucose metabolism reprogramming through KLF2/HK1 pathway in vascular endothelial cells," *Cellular Signalling*, vol. 78, p. 109843, 2021.

[13] M. Cavia-Saiz, M. D. Busto, M. C. Pilar-Izquierdo, N. Ortega, M. Perez-Mateos, and P. Muniz, "Antioxidant properties, radical scavenging activity and biomolecule protection capacity of flavonoid naringenin and its glycoside naringin: a comparative study," *Journal of the Science of Food and Agriculture*, vol. 90, no. 7, pp. 1238–1244, 2010.

[14] B. Salehi, P. V. T. Fokou, M. Sharifi-Rad et al., "The therapeutic potential of Naringenin: a review of clinical trials," *Pharmaceuticals*, vol. 12, no. 1, 2019.

[15] R. M. Martinez, F. A. Pinho-Ribeiro, V. S. Steffen et al., "Naringenin inhibits UVB irradiation-induced inflammation and oxidative stress in the skin of hairless mice," *Journal of Natural Products*, vol. 78, no. 7, pp. 1647–1655, 2015.

[16] S. Singh, A. Sharma, V. Monga, and R. Bhatia, "Compendium of naringenin: potential sources, analytical aspects, chemistry, nutraceutical potentials and pharmacological profile," *Critical Reviews in Food Science and Nutrition*, pp. 1–32, 2022.

[17] W. Zeng, L. Jin, F. Zhang, C. Zhang, and W. Liang, "Naringenin as a potential immunomodulator in therapeutics," *Pharmacological Research*, vol. 135, pp. 122–126, 2018.

[18] R. H. Moghaddam, Z. Samimi, S. Z. Moradi, P. J. Little, S. Xu, and M. H. Farzaei, "Naringenin and naringin in cardiovascular

disease prevention: a preclinical review," *European Journal of Pharmacology*, vol. 887, 2020.

[19] S. J. Xu, B. X. Wu, B. Y. Zhong et al., "Naringenin alleviates myocardial ischemia/reperfusion injury by regulating the nuclear factor-erythroid factor 2-related factor 2 (Nrf 2)/system xc-/glutathione peroxidase 4 (GPX4) axis to inhibit ferroptosis," *Bioengineered*, vol. 12, no. 2, pp. 10924–10934, 2021.

[20] L. M. Yu, X. Dong, J. Zhang et al., "Naringenin attenuates myocardial ischemia-reperfusion injury via cGMP-PKGI alpha signaling and in vivo and in vitro studies," *Oxidative Medicine and Cellular Longevity*, vol. 2019, Article ID 7670854, 15 pages, 2019.

[21] L.-M. Yu, X. Dong, X.-D. Xue et al., "Naringenin improves mitochondrial function and reduces cardiac damage following ischemia-reperfusion injury: the role of the AMPK-SIRT3 signaling pathway," *Food & Function*, vol. 10, no. 5, pp. 2752–2765, 2019.

[22] S. Kara, B. Gencer, T. Karaca et al., "Protective effect of hesperetin and naringenin against apoptosis in ischemia/reperfusion-induced retinal injury in rats," *The Scientific World Journal*, vol. 2014, Article ID 797824, 8 pages, 2014.

[23] S. S. Raza, M. M. Khan, A. Ahmad et al., "Neuroprotective effect of naringenin is mediated through suppression of NF-κB signaling pathway in experimental stroke," *Neuroscience*, vol. 230, pp. 157–171, 2013.

[24] H. Liu, L. Wang, X. D. Weng et al., "Inhibition of Brd4 alleviates renal ischemia/reperfusion injury-induced apoptosis and endoplasmic reticulum stress by blocking FoxO4-mediated oxidative stress," *Redox Biology*, vol. 24, p. 101195, 2019.

[25] C. H. Diao, Z. Y. Chen, T. Qiu et al., "Inhibition of PRMT5 attenuates oxidative stress-induced pyroptosis via activation of the Nrf2/HO-1 signal pathway in a mouse model of renal ischemia-reperfusion injury," *Oxidative Medicine and Cellular Longevity*, vol. 2019, Article ID 2345658, 18 pages, 2019.

[26] Y. Sun, J. Kang, Z. Tao et al., "Effect of endoplasmic reticulum stress-mediated excessive autophagy on apoptosis and formation of kidney stones," *Life Sciences*, vol. 244, article 117232, 2020.

[27] T. Tajima, A. Yoshifuji, A. Matsui et al., "β-hydroxybutyrate attenuates renal ischemia-reperfusion injury through its anti-pyroptotic effects," *Kidney International*, vol. 95, no. 5, pp. 1120–1137, 2019.

[28] S. W. Park, M. Kim, K. M. Brown, V. D. D'Agati, and H. T. Lee, "Inhibition of sphingosine 1-phosphate receptor 2 protects against renal ischemia-reperfusion injury," *Journal of the American Society of Nephrology*, vol. 23, no. 2, pp. 266–280, 2012.

[29] B. H. Zhang, H. Liu, Y. Yuan et al., "Knockdown of TRIM8 protects HK-2 cells against hypoxia/reoxygenation-induced injury by inhibiting oxidative stress-mediated apoptosis and pyroptosis via PI3K/Akt signal pathway," *Drug Design, Development and Therapy*, vol. Volume 15, pp. 4973–4983, 2021.

[30] S. J. Dong, X. Y. Gao, M. X. Pei et al., "Effects and mechanism of salvianolic acid B on the injury of human renal tubular epithelial cells induced by iopromide," *Frontiers in Pharmacology*, vol. 12, 2021.

[31] A. Arafah, M. U. Rehman, T. M. Mir et al., "Multi-therapeutic potential of naringenin (4 ',5,7-Trihydroxyflavonone): experimental evidence and mechanisms," *Plants-Basel*, vol. 9, no. 12, p. 1784, 2020.

[32] N. Rani, S. Bharti, B. Krishnamurthy et al., "Pharmacological properties and therapeutic potential of naringenin: a citrus flavonoid of pharmaceutical promise," *Current Pharmaceutical Design*, vol. 22, no. 28, pp. 4341–4359, 2016.

[33] Q. Y. Wang, Y. J. Ou, G. M. Hu et al., "Naringenin attenuates non-alcoholic fatty liver disease by down-regulating the NLRP3/NF-κB pathway in mice," *British Journal of Pharmacology*, vol. 177, no. 8, pp. 1806–1821, 2020.

[34] X. T. Xu, T. W. Lei, W. C. Li, and H. L. Ou, "Enhanced cellular cholesterol efflux by naringenin is mediated through inhibiting endoplasmic reticulum stress - ATF6 activity in macrophages," *Biochimica Et Biophysica Acta-Molecular and Cell Biology of Lipids*, vol. 1864, no. 10, pp. 1472–1482, 2019.

[35] B. L. Ha, Y. Wang, G. Yu et al., "Naringenin ameliorates insulin resistance by modulating endoplasmic reticulum stress in hepatitis C virus-infected liver," *Biomedicine & Pharmacotherapy*, vol. 115, p. 108848, 2019.

[36] J. C. Wang, L. Lu, S. S. Chen et al., "PERK overexpression-mediated Nrf2/HO-1 pathway alleviates hypoxia/reoxygenation-induced injury in neonatal murine cardiomyocytes via improving endoplasmic reticulum *stress*," *BioMed Research International*, vol. 2020, Article ID 6458060, 10 pages, 2020.

[37] H. Yu, G. Jiang, W. Hu, and C. Xu, "Pin1 aggravates renal injury induced by ischemia and reperfusion in rats via Nrf2/HO-1 mediated endoplasmic reticulum stress," *Acta Cirúrgica Brasileira*, vol. 37, no. 1, article e370101, 2022.

[38] Z. Zwaini, H. Y. Dai, C. Stover, and B. Yang, "Role of complement properdin in renal ischemia-reperfusion injury," *Current Gene Therapy*, vol. 17, no. 6, pp. 411–423, 2017.

[39] A. Zuk and J. V. Bonventre, "Acute kidney injury," *Annual Review of Medicine*, vol. 67, pp. 293–307, 2016.

[40] C. Tang, Y. Hu, J. Gao et al., "Dexmedetomidine pretreatment attenuates myocardial ischemia reperfusion induced acute kidney injury and endoplasmic reticulum stress in human and rat," *Life Sciences*, vol. 257, article 118004, 2020.

[41] C. Quintavalle, D. Fiore, F. De Micco et al., "Impact of a high loading dose of atorvastatin on contrast-induced acute kidney injury," *Circulation*, vol. 126, no. 25, pp. 3008–3016, 2012.

[42] A. Halapas, A. Kapelouzou, M. Chrissoheris, G. Pattakos, D. V. Cokkinos, and K. Spargias, "The effect of remote ischemic preconditioning (RIPC) on myocardial injury and inflammation in patients with severe aortic valve stenosis undergoing transcatheter aortic valve replacement (TAVIota)," *Hellenic Journal of Cardiology*, vol. 62, no. 6, pp. 423–428, 2021.

[43] F. Er, A. M. Nia, H. Dopp et al., "Ischemic preconditioning for prevention of contrast medium-induced nephropathy: randomized pilot RenPro trial (renal protection trial)," *Circulation*, vol. 126, no. 3, pp. 296–303, 2012.

[44] W. Chancharoenthana, K. Udompronpitak, Y. Manochantr et al., "Repurposing of high-dose erythropoietin as a potential drug attenuates sepsis in preconditioning renal injury," *Cell*, vol. 10, no. 11, 2021.

[45] A. Linkermann, G. C. Chen, G. E. Dong, U. Kunzendorf, S. Krautwald, and Z. Dong, "Regulated cell death in AKI," *Journal of the American Society of Nephrology*, vol. 25, no. 12, pp. 2689–2701, 2014.

[46] R. Bravo, V. Parra, D. Gatica et al., "Endoplasmic reticulum and the unfolded protein response: dynamics and metabolic integration," *International Review of Cell and Molecular Biology*, vol. 301, pp. 215–290, 2013.

[47] C. Y. Xu, B. Bailly-Maitre, and J. C. Reed, "Endoplasmic reticulum stress: cell life and death decisions," *Journal of Clinical Investigation*, vol. 115, no. 10, pp. 2656–2664, 2005.

[48] F. Prischi, P. R. Nowak, M. Carrara, and M. M. U. Ali, "Phosphoregulation of Ire1 RNase splicing activity," *Nature Communications*, vol. 5, 2014.

[49] R. Friedlander, E. Jarosch, J. Urban, C. Volkwein, and T. Sommer, "A regulatory link between ER-associated protein degradation and the unfolded-protein response," *Nature Cell Biology*, vol. 2, no. 7, pp. 379–384, 2000.

[50] C. Hetz, "The unfolded protein response: controlling cell fate decisions under ER stress and beyond," *Nature Reviews Molecular Cell Biology*, vol. 13, no. 2, pp. 89–102, 2012.

[51] X. Wang, L. Xu, T. G. Gillette, X. Jiang, and Z. V. Wang, "The unfolded protein response in ischemic heart disease," *Journal of Molecular and Cellular Cardiology*, vol. 117, pp. 19–25, 2018.

[52] K. D. McCullough, J. L. Martindale, L. O. Klotz, T. Y. Aw, and N. J. Holbrook, "Gadd153 sensitizes cells to endoplasmic reticulum stress by down-regulating Bcl2 and perturbing the cellular redox state," *Molecular and Cellular Biology*, vol. 21, no. 4, pp. 1249–1259, 2001.

[53] Y. Tian, L. Wang, Z. Qiu, Y. Xu, and R. Hua, "Autophagy triggers endoplasmic reticulum stress and C/EBP homologous protein-mediated apoptosis in OGD/R-treated neurons in a caspase-12-independent manner," *Journal of Neurophysiology*, vol. 126, no. 5, pp. 1740–1750, 2021.

[54] M. M. Guo, S. B. A. Qu, H. L. Lu et al., "Biochanin a alleviates cerebral ischemia/reperfusion injury by suppressing endoplasmic reticulum stress-induced apoptosis and p38MAPK signaling pathway in vivo and in vitro," *Frontiers in Endocrinology*, vol. 12, 2021.

[55] X. W. Sun, H. Liu, Z. R. Sun et al., "Acupuncture protects against cerebral ischemia-reperfusion injury via suppressing endoplasmic reticulum stress-mediated autophagy and apoptosis," *Molecular Medicine*, vol. 26, no. 1, p. 105, 2020.

[56] B. Dong, H. L. Zhou, C. H. Han et al., "Ischemia/reperfusion-induced CHOP expression promotes apoptosis and impairs renal function recovery: the role of acidosis and GPR4," *PLoS One*, vol. 9, no. 10, p. e110944, 2014.

[57] G. Priante, L. Gianesello, M. Ceol, D. Del Prete, and F. Anglani, "Cell death in the kidney," *International Journal of Molecular Sciences*, vol. 20, no. 14, p. 3598, 2019.

[58] R. B. Zhou, A. S. Yazdi, P. Menu, and J. Tschopp, "A role for mitochondria in NLRP3 inflammasome activation," *Nature*, vol. 469, no. 7329, pp. 221–225, 2011.

[59] S. Fougeray, N. Bouvier, P. Beaune et al., "Metabolic stress promotes renal tubular inflammation by triggering the unfolded protein response," *Cell Death & Disease*, vol. 2, no. 4, article e143, 2011.

[60] C. Lebeaupin, E. Proics, C. H. D. de Bieville et al., "ER stress induces NLRP3 inflammasome activation and hepatocyte death," *Cell Death & Disease*, vol. 6, no. 9, p. e1879, 2015.

[61] T. Horng, "Calcium signaling and mitochondrial destabilization in the triggering of the NLRP3 inflammasome," *Trends in Immunology*, vol. 35, no. 6, pp. 253–261, 2014.

[62] D. P. Zhang, J. H. Qian, P. Zhang et al., "Gasdermin D serves as a key executioner of pyroptosis in experimental cerebral ischemia and reperfusion model both in vivo and in vitro," *Journal of Neuroscience Research*, vol. 97, no. 6, pp. 645–660, 2019.

[63] X. Le, J. Mu, W. Peng et al., "DNA methylation downregulated ZDHHC1 suppresses tumor growth by altering cellular metabolism and inducing oxidative/ER stress-mediated apoptosis and pyroptosis," *Theranostics*, vol. 10, no. 21, pp. 9495–9511, 2020.

[64] Y. Tang, Q. Wa, L. Peng et al., "Salvianolic acid B suppresses ER stress-induced NLRP3 inflammasome and pyroptosis via the AMPK/FoxO4 and syndecan-4/Rac1 signaling pathways in human endothelial progenitor cells," *Oxidative Medicine and Cellular Longevity*, vol. 2022, Article ID 8332825, 8332822 pages, 2022.

[65] M. Shi, L. Liu, X. Min et al., "Activation of sigma-1 receptor alleviates ER-associated cell death and microglia activation in traumatically injured mice," *Journal of Clinical Medicine*, vol. 11, no. 9, p. 2348, 2022.

[66] Y.-S. Chiou, M.-L. Tsai, K. Nagabhushanam et al., "Pterostilbene is more potent than resveratrol in preventing azoxymethane (AOM)-induced colon tumorigenesis via activation of the NF-E2-related factor 2 (Nrf2)-mediated antioxidant signaling pathway," *Journal of Agricultural and Food Chemistry*, vol. 59, no. 6, pp. 2725–2733, 2011.

[67] Y. A. Hou, X. M. Li, S. J. Peng, J. Yao, F. F. Bai, and J. G. Fang, "Lipoamide ameliorates oxidative stress via induction of Nrf2/ARE signaling pathway in PC12 cells," *Journal of Agricultural and Food Chemistry*, vol. 67, no. 29, pp. 8227–8234, 2019.

[68] Z. A. Shah, R. C. Li, A. S. Ahmad et al., "The flavanol (-)-epicatechin prevents stroke damage through the Nrf2/HO1 pathway," *Journal of Cerebral Blood Flow and Metabolism*, vol. 30, no. 12, pp. 1951–1961, 2010.

[69] A. Loboda, M. Damulewicz, E. Pyza, A. Jozkowicz, and J. Dulak, "Role of Nrf2/HO-1 system in development, oxidative stress response and diseases: an evolutionarily conserved mechanism," *Cellular and Molecular Life Sciences*, vol. 73, no. 17, pp. 3221–3247, 2016.

[70] L. Wang, Y. Yao, R. He et al., "Methane ameliorates spinal cord ischemia-reperfusion injury in rats: antioxidant, anti-inflammatory and anti-apoptotic activity mediated by Nrf2 activation," *Free Radical Biology & Medicine*, vol. 103, pp. 69–86, 2017.

[71] W. Sun, Z. Wang, M. Sun, W. Huang, Y. Wang, and Y. Wang, "Aloin antagonizes stimulated ischemia/reperfusion-induced damage and inflammatory response in cardiomyocytes by activating the Nrf2/HO-1 defense pathway," *Cell and Tissue Research*, vol. 384, no. 3, pp. 735–744, 2021.

[72] Y. Liang, C. Fan, X. Yan et al., "Berberine ameliorates lipopolysaccharide-induced acute lung injury via the PERK-mediated Nrf2/HO-1 signaling axis," *Phytotherapy Research*, vol. 33, no. 1, pp. 130–148, 2019.

[73] S. Habtemariam, "The Nrf2/HO-1 Axis as targets for flavanones: neuroprotection by pinocembrin, naringenin, and eriodictyol," *Oxidative Medicine and Cellular Longevity*, vol. 2019, Article ID 4724920, 15 pages, 2019.

[74] Y. Li, Y. Pan, L. Gao et al., "Naringenin protects against acute pancreatitis in two experimental models in mice by NLRP3 and Nrf2/HO-1 pathways," *Mediators of Inflammation*, vol. 2018, Article ID 3232491, 13 pages, 2018.

[75] M. R. de Oliveira, C. M. B. Andrade, and C. R. Furstenau, "Naringenin exerts anti-inflammatory effects in paraquat-treated SH-SY5Y cells through a mechanism associated with the Nrf2/HO-1 axis," *Neurochemical Research*, vol. 43, no. 4, pp. 894–903, 2018.

Hindawi
Oxidative Medicine and Cellular Longevity
Volume 2022, Article ID 1200602, 17 pages
https://doi.org/10.1155/2022/1200602

Research Article

PCAF Accelerates Vascular Senescence via the Hippo Signaling Pathway

Chaohua Kong, Dongchen Wang, Feng Wang, Yifei Lv, Wenying Zhou, Peng Ye, Yue Gu, Xiaomin Jiang, Linlin Zhu, Zhen Ge, Yuelin Chao, and Shaoliang Chen

Department of Cardiology, Nanjing First Hospital, Nanjing Medical University, Nanjing, China

Correspondence should be addressed to Linlin Zhu; zhulinlin_007@sina.com, Zhen Ge; gezhen666@163.com, Yuelin Chao; chaoyuelincchy@163.com, and Shaoliang Chen; chmengx@126.com

Received 11 May 2022; Revised 13 August 2022; Accepted 30 August 2022; Published 6 October 2022

Academic Editor: Jianbo Wu

P300/CBP-Associated Factor (PCAF), one of the histone acetyltransferases (HATs), is known to be involved in cell growth and/or differentiation. PCAF is reported to be involved in atherosclerotic plaques and neointimal formation. However, its role in cellular senescence remains undefined. We investigated the potential mechanism for PCAF-mediated cellular senescence. Immunohistochemical (IHC) analysis showed PCAF was distinctly increased in the endothelia of aorta in aged mice. Palmitate acid (PA) or X radiation significantly induced the expression of senescence-associated markers and PCAF in human umbilical vein endothelial cells (HUVECs). PCAF silence in PA-treated HUVECs significantly rescued senescence-associated phenotypes, while PCAF overexpression accelerated it. Additionally, our results showed that Yes1 Associated Transcriptional Regulator (YAP) that acts as end effector of the Hippo signaling pathway is crucial in PCAF-mediated endothelial senescence. YAP activity declining was observed in aged vascular endothelia. Overexpression of YAP partially ameliorated PCAF-induced endothelial senescence. In vivo, endothelial-(EC-) specific PCAF downregulation in aged mice using adeno-associated virus revealed less vascular senescence-associated phenotypes. These results suggested that PCAF mediated endothelial senescence through the Hippo signaling pathway, implying that PCAF may become a potential target for the prevention and treatment of vascular aging.

1. Introduction

Cellular senescence is an irreversible form of cell cycle arrest that cells lose their replicative capacity and halt cell cycle in the G1 and G2 phases [1]. It is evoked during embryonic development as well as by various stressors, including oxidative stress, inflammation, UV and/or ionizing radiation, chemotherapeutic agents, aberrant activation of oncogenes, and inactivation of tumor suppressor genes [2]. Cellular senescence influences organic senescence, result in a series of disorders like obesity, cardiovascular diseases, diabetes, and neurodegeneration.

Endothelial cell is one of the main cell types that constitutes the vascular system. Senescent endothelial cells exhibit impaired homeostatic functions including reduced nitric oxide production and increased generation and secretion of ROS and a wide range of cytokines and chemokines like interleukin (IL)-1β and interleukin (IL)-6 [3–6]. Accumulating evidence suggests endothelial senescence renders the vessels prone to profound functional and morphological disturbances that ultimately bring about various cardiovascular diseases. Thus, understanding the mechanism of endothelial senescence is critical to prevent senescence-associated cardiovascular disease. Several senescence drivers and relevant pathways have been summarized to be associated with senescence establishment, including two classical tumor suppressor pathways, p53/p21 and Rb/p16 [7]. However, the specific molecular mechanisms remain poorly elucidated.

P300/CBP-Associated Factor (PCAF), a member of the GCN5-related N-acetyltransferase family, functions as a histone acetyltransferase (HAT) to promote transcriptional activity [8]. Apart from its role in acetylating core histones

(H3 and H4), it can also interact with many nonhistone proteins. PCAF has been shown to participate in the modulation of arteriogenesis, cell cycle progression, differentiation, gluconeogenesis, and tumorigenesis [9–11]. Intriguingly, several studies indicate that PCAF is implicated in the activation of p53-dependent transcription of the cyclin-dependent kinase inhibitor p21 and p16, which are highly associated with senescence establishment [12, 13]. Therefore, we hypothesized that inhibition of PCAF in endothelial cell may attenuate cellular senescence.

The aim of this study was to reveal the underlying molecular mechanism by which PCAF contributes to cellular senescence. By using PA-induced cellular senescence and aged mouse model [14, 15], we identified a novel and unrecognized role for PCAF in promoting cellular senescence through the Hippo signaling pathway. Our findings indicated that PCAF may become a promising therapeutic target for senescence-associate vascular disease.

2. Materials and Methods

2.1. Animal Tissues and Experiments. All experimental protocols and animal use were approved by the Institutional Animal Care and Use Committee of Nanjing Medical University. One and half-year-old and 4w C57BL/6 male wild-type mice ($n = 21$) were purchased from the Model Animal Research Centre of Nanjing University. Mice were housed in a specific pathogen-free room with an ambient temperature of 25°C and a humidity between 30% and 70%. They were exposed to 12-h light–dark cycles and fed with rodent food and adequate water. All animals were allocated randomly into three groups based on a single sequence of random assignments. Aortic arteries were dissected and fixed in 4% paraformaldehyde overnight at 25°C, and then embedded in paraffin.

2.2. Cell Culture. Human umbilical vein endothelial cells (HUVECs; Cellbank of Chinese Academy of Sciences, Shanghai) were cultured at 37°C in a humidified 5% CO_2 incubator. Cells were cultured with endothelial culture medium (ECM) with 5% fetal bovine serum and 1% penicillin-streptomycin (Sciencell, USA). When the cells reached 80–90% confluence, they were trypsinized and subcultured.

2.3. Materials and Reagents. Primary antibody against PCAF (3305, CST), p53 (sc-126, santa cruz), p21 (sc-6246, santa cruz), p16 (sc-166760, santa cruz), Ubiquitin (sc-53509, santa cruz), phosphor-Histone H2A.X(Ser139) (#2577, CST), YAP (#14074, CST), MDM2 (BS-1223, Biogot), phospho-YAP (#13008, CST), TAZ (#83669, CST), phospho-TAZ (#59971, CST), clathrin (ab21679, abcam), caveolae (ab2910, abcam), mTOR (ab2732, abcam), p-mTOR (Ser2448) (ab109268, abcam), p-mTOR(Ser2481) (ab137133, abcam), IL-1β (sc-12742, snata cruz), IL-6 (sc-130326, santa cruz), GAPDH (#AP0063, Biogot), histone H3(BS3718, Biogot), and PA (P0500, Sigma-Aldrich) were purchased commercially.

2.4. Western Blotting. Cells were lysed in a mixture of RIPA and proteinase inhibitor (100 : 1) for 20 min prior to centrifugation at 15 000 × g for 15 min at 4°C, as described in the previous studies. Protein concentration was determined by a bicinchoninic acid protein assay. Protein lysates were boiled in sodium dodecyl sulfate (SDS) sample buffer at 94°C for 7 min. 40 μg proteins were resolved on 10% sodium dodecyl sulfate-polyacrylamide gels, and then transferred to PVDF membrane. After that, the membranes were blocked in 1 × TBST containing 5% skim milk for 1 hour at room temperature before incubated with indicated primary antibodies at 4°C overnight.

2.5. Quantitative Real-Time PCR. Total RNA was isolated using Trizol reagent (Vazyme, R401-01, Shanghai, China) according to the manufactures' protocols [16]. RNA was reverse transcribed using HiScript II Q Select RT SuperMix (Vazyme, Shanghai, China) for qPCR and qPCR was performed on a Fast 7500 cycler (Applied Biosystems) using the resultant cDNA along with Taq Pro Universal SYBR qPCR Master Mix (Vazyme, R232-01, Shanghai, China) and gene-specific primers. PCR primers used are listed as follows:

IL-1β: Froward: ATGATGGCTTATTACAGTGGCAA.
Reverse: GTCGGAGATTCGTAGCTGGA.
IL-6: Froward: ACTCACCTCTTCAGAACGAATTG.
Reverse: CCATCTTTGGAAGGTTCAGGTTG.
GAPDH: Forward: GGAGCGAGATCCCTCCAAAAT.
Reverse: GGCTGTTGTCATACTTCTCATGG.
PCAF: Forward: CGAATCGCCGTGAAGAAAGC.
Reverse: CTTGCAGGCGGAGTACACT.

Results were qualified using a delta-delta-cycle threshold (Ct) method ($\Delta\Delta$Ct). All experiments were performed in triplicate and GAPDH was used as an internal control.

2.6. Cell Transfection. HUVECs were transfected with 3.75 μl PCAF/YAP or negative control siRNA using Lipo3000 after cell confluence reached 70–80% according to the manufactures' protocols. When cell confluence was 90%, 2.5 ng plasmid and corresponding control plasmid along with 3.75 μl Lipo3000 and p3000 (L3000-015, Thermo Fisher) were cocultured with HUVECs in opti-MEMI medium (Gibco,31985070) for 6 hours then refreshed with ECM. Cell lysates were collected after 48 h infection.

siRNA was purchased from Gene Pharma (Shanghai, China) siRNA targeting

PCAF#1: AGAGCAGUCCUGGAUUA,
PCAF#2: UCGCCGUGAAGAAAGCGCATT,
PCAF#3: GGCUACGUCCAGGAGCGCACC,
YAP#1: GACAUCUUCUGGUCAGAGA,
YAP#2: CUGGUCAGAGAUACUUCUU.

2.7. SAβG Staining for Cells and Tissues. SaβG staining (Beyotime, C0602, Shanghai, China) of HUVECs, aorta, and frozen tissue sections was performed according to the manufactures' instructions. SaβG staining activity was measured as previously described [17].

2.8. Immunohistochemistry. The aorta arch was embedded with in paraffin as described above. The paraffin block then

dissected into 4 μM thickness. Paraffin sections underwent deparaffinization, rehydration, and exposure to alkaline phosphatase block buffer for heat-induced epitope retrieval. Next, the sections were incubated in 0.3% hydrogen peroxide for 30 minutes, followed by incubation with 5% BSA for another 30 minutes, and primary antibody at 4°C overnight (anti-PCAF, anti-YAP, 1 : 200). The next day, sections were incubated with the corresponding second antibodies (ZSGB-BIO, Beijing, China) and counterstained with hematoxylin.

2.9. mRNA Decay Assays. The stability of mRNA was performed by treating cells with Actinomycin D (100 μg/mL) (MCE, HY-17559, Shanghai, China), a general RNA polymerase inhibitor. After 48 h incubation with PA, cells were treated with Actinomycin D for 0, 6, and 12 hours. Then mRNA levels were measured by qPCR.

2.10. Stability of Protein. To measure the effect of PA treatment on regulating the stability of PCAF protein, control and PA-stimulated HUVECs for 48 h before being treated with 35 μmol/L cycloheximide (CHX) (MCE, HY-12320, Shanghai, China) for 0, 6, and 12 h or MG132 (10 μM) for 0, 4, and 8 h. The total protein was extracted from whole-cell lysates and then prepared for western blotting analysis.

2.11. Co-Immunoprecipitation. Cells were transfected with corresponding plasmids (Addgene, #8941, #13054, #17793) and lysed in co-IP buffer containing protease inhibitor cocktail tablets. The indicated Flag-tagged magnetic beads or His-tagged beads (Bimake, Shanghai, China) were incubated with cell lysates at 4°C overnight. Next day, the lysates were removed to 1.5 ml tube to detect if targeted proteins were fully combined with the magnetic beads and PBST was used to wash the beads for 5 minutes three times. Then, 1 × SDS were added for boiling. The immunocomplexes were subjected to western blotting using the indicated antibodies.

2.12. Biochemistry and Enzyme-Linked Immunosorbent Assay (ELISA). Serum samples were collected from 4w, aged+AAV9-Luc and aged+AAV9-PCAF mice. Total IL-1β was determined by mouse IL-1β ELISA kits (R&D systems, Cat #PMLB00C, USA) following the manufacturer's instructions [18].

2.13. Pathway Enrichment Analysis. The data were downloaded from GEO database (GSE47179). Kyoto Encyclopedia of Genes and Genomes (KEGG) pathway analysis was used to determine the associated biological pathways after PCAF silence. In addition, the DAVID online tool was applied to KEGG pathway analysis [19, 20]. A P value of <0.05 was considered significant.

2.14. Statistical Analysis. At least 6 biological replicates and 3 replicates were done for each experiment. Results are presented as the means ± standard deviations (SDs). Student-t test or one-way ANOVA analysis were used for statistical analysis where appropriate.

3. Results

3.1. PCAF Was Increased in Aged Vascular Tissues and HUVECs Underwent X Radiation or Palmitate Acid Treatment. To explore the role of PCAF in endothelial senescence, we first investigated PCAF expression in vascular vessels between young (4 w) and aged mice (one and half-year-old). Immunohistochemical (IHC) analysis revealed that PCAF expression was significantly upregulated in the aortic endothelia of aged mice (Figure 1(d)). Then, we examined PCAF mRNA and protein expression in actively dividing young HUVECs (defined as cells used before passage 5), young HUVECs underwent palmitate acid (PA) treatment or X radiation (15 gray). HUVECs developed stress-induced premature senescence after X radiation and PA treatment featured by reduced proliferation and increased SaβG staining activity (Figure 1(f)), remarkable upregulation of senescence-associated p53, p21, P16 gene, and DNA damage marker pH2AX (a phosphorylated form of the histone variant H2AX, which is increased in DNA damage response) (Figures 1(a) and 1(b)) [21]. This demonstrated that PA treatment can imitate cellular senescence induced by X radiation. So, in this study, PA treatment was used to induce cellular senescence. Meanwhile, Western blotting showed that PCAF expression was increased in PA-treated/X radiated cells than the control young cells (Figures 1(a) and 1(b)). In addition, palmitate or X radiation promoted IL-6 and IL-1β mRNA expression in young HUVECs (Figure 1(c)). These results suggested PCAF may participate in the process of cellular senescence.

3.2. PCAF Regulated PA-Induced Cellular Senescence in HUVECs. We next investigated whether PCAF promoted PA-induced cellular senescence in HUVECs. First, silencing of PCAF significantly decreased the levels of p53, p21, p16, and pH2AX in PA-stimulated HUVECs (Figure 2(a)). PCR results also showed that inhibition of PCAF in HUVECs decreased PA-induced upregulation of IL-1β and IL-6 mRNA levels (Figure 2(b)). Moreover, the silence of PCAF decreased SaβG staining in PA-stimulated HUVECs (Figure 2(e)), while overexpression of PCAF in PA-stimulated HUVECs upregulated the levels of p53, p21, p16, and pH2A.X protein levels, IL-1β and IL-6 mRNA and SaβG staining (Figures 2(c), 2(d), and 2(f)). Taken together, these gain and loss-of-function experiments suggested that PCAF mediated PA-induced endothelial senescence.

3.3. PA Upregulated PCAF in HUVECs Depended on Decreased MDM2 Mediated Ubiquitination. Further, we determined the potential mechanism of PA-stimulated PCAF expression. We investigated if PA stimulation influenced PCAF mRNA or protein stability in HUVECs. HUVECs were stimulated with PA before treatment with actinomycin D (100 μg/ml) or not. Our results revealed that PA stimulation did not affect PCAF mRNA degradation (Figure 3(b)). Meanwhile the half-life of PCAF protein was also explored after PA treatment or not. PA treatment increased PCAF protein stability (Figures 3(a), 3(c)). Then

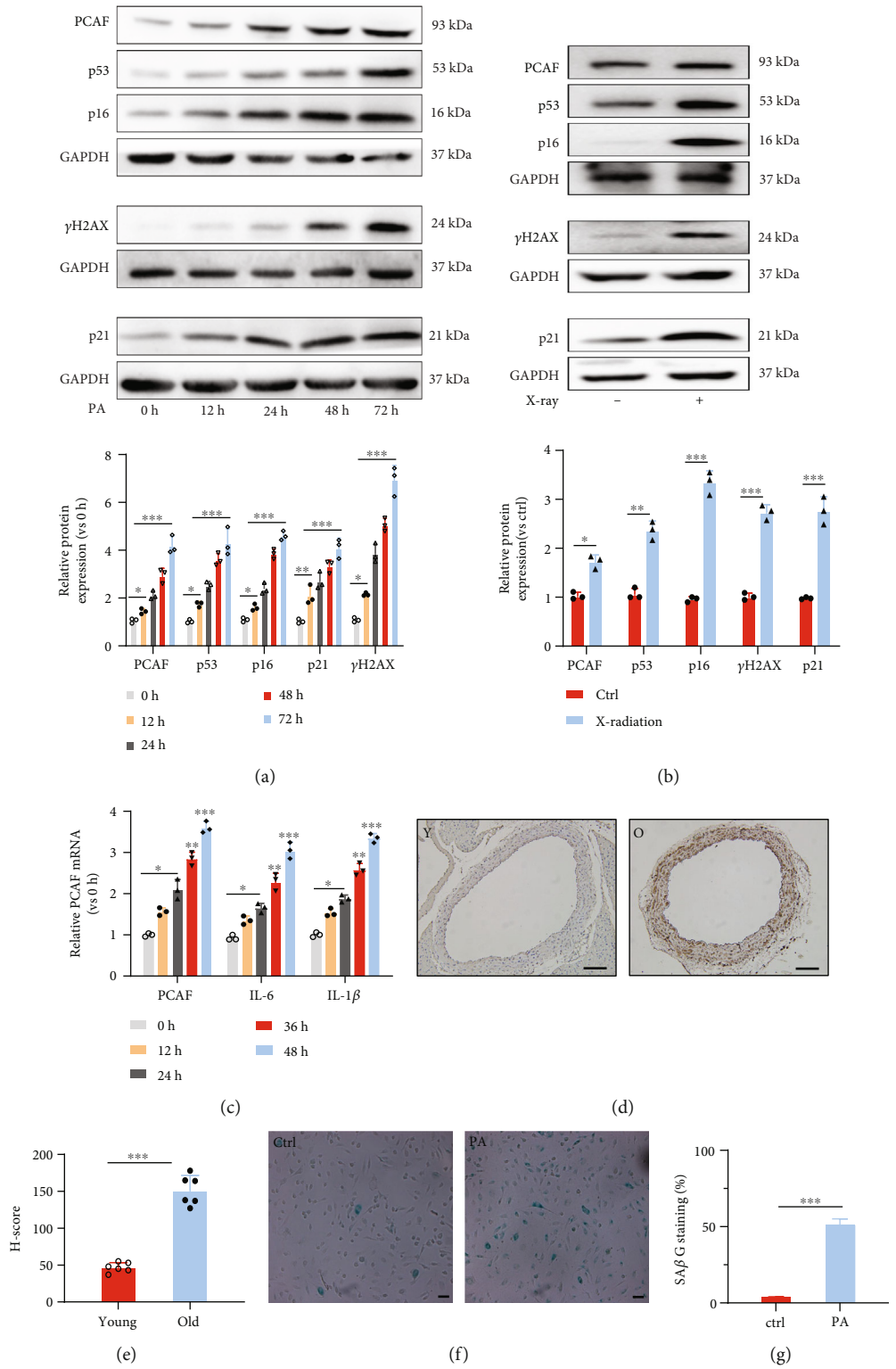

FIGURE 1: Increased PCAF expression in endothelia of aged mice and palmitate acid (PA) or X radiation treated HUVECs. (a) Western blotting analysis and qualification of PCAF and senescence-associated protein expression in HUVECs stimulated with PA (0.3 mM) for the indicated time points. (b) Western blotting analysis and qualification of PCAF and senescence-associated protein expression in HUVECs treated with or without X radiation (15 gray). (c) mRNA levels of PCAF, IL-6, and IL-1β in HUVECs treated with vehicle or PA for indicated time points. (d) and (e) Immunohistochemical (IHC) stain and quantitative analysis of blood vessels from young (4 w) and old (one and half-year-old) mice with PCAF antibody. Scale bars: 100 μm. (f) and (g) SaβG staining and quantitative analysis of vector and PA-treated HUVECs. Scale bars, 20 μm. Y: young mice; O: old mice. Data are expressed as mean ± SEM ($^{*}P < 0.05$, $^{**}P < 0.01$, $^{***}P < 0.001$, n.s. $P > 0.05$).

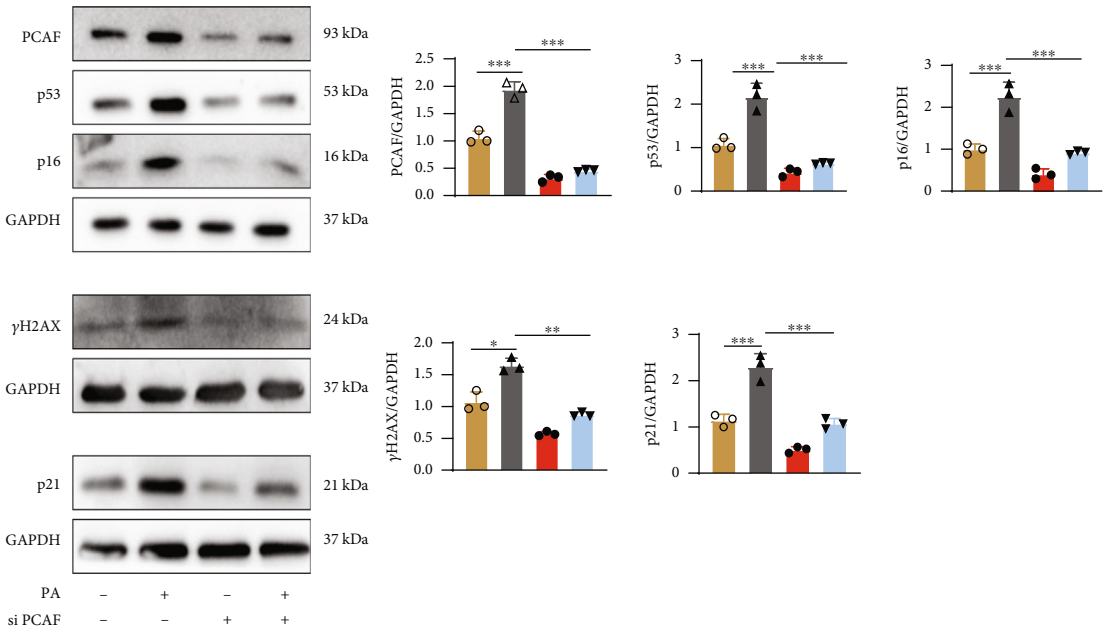

(a)

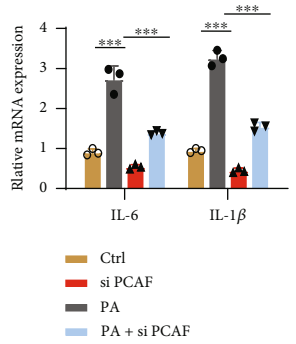

(b)

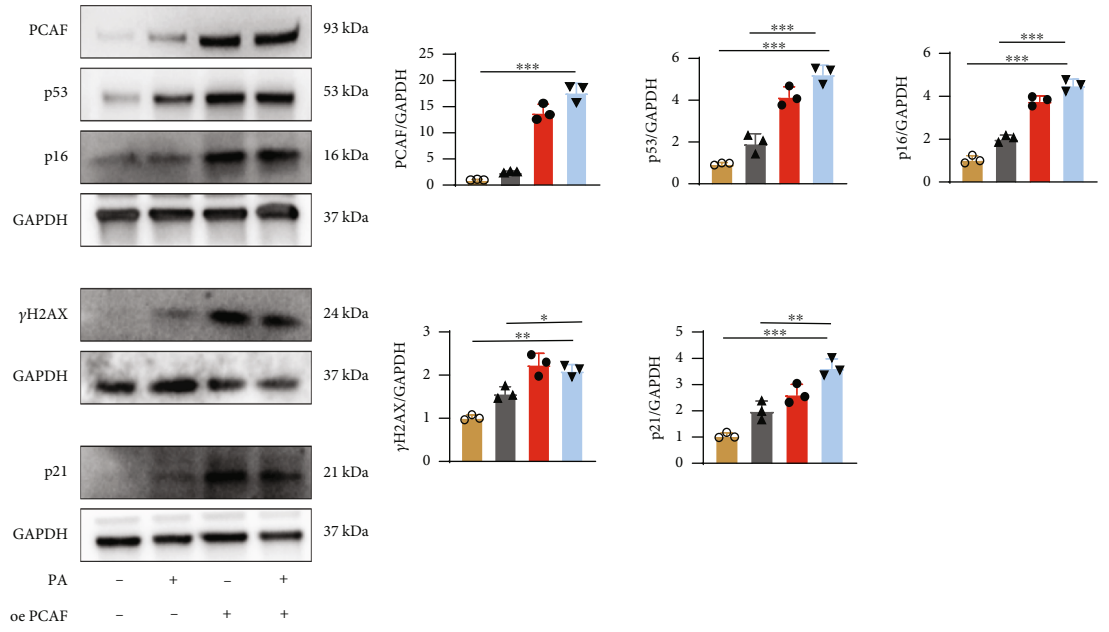

(c)

Figure 2: Continued.

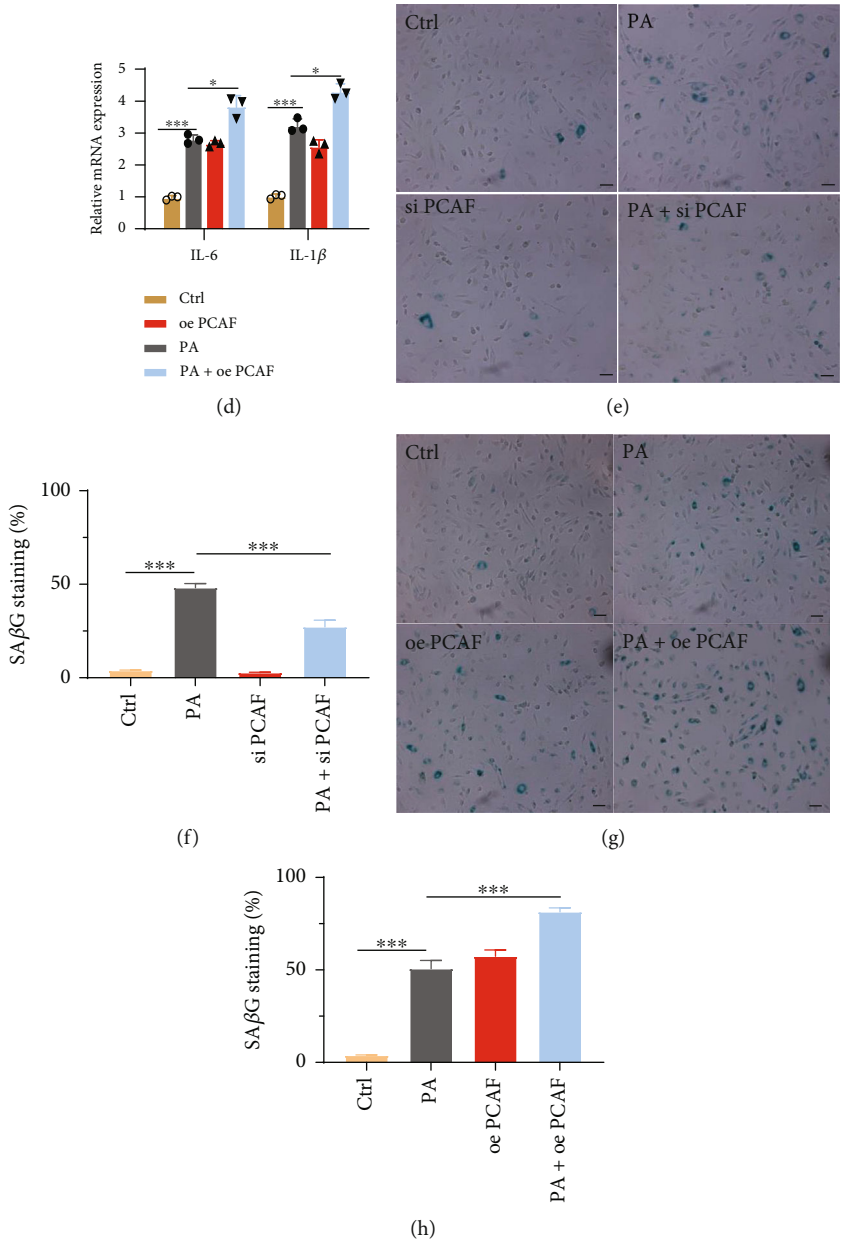

Figure 2: PCAF were involved in the regulation of endothelial senescence. (a) and (b) Western blotting analysis and qualification of p53, p16, pH2A.X, and p21 protein expression and relative mRNA expression of IL-6 and IL-1β in PA-treated HUVECs transfected with scramble or PCAF siRNA. (c) and (d) Western blotting analysis and qualification of p53, p16, pH2A.X, and p21 protein expression and relative mRNA expression of IL-6 and IL-1β in PA-treated HUVECs transfected with vector or PCAF plasmid. (e) and (f) SaβG staining and quantitative analysis in HUVECs transfected with scramble or PCAF siRNA in the presence of PA or not. Scale bars, 20 μm. (g) and (h) SaβG staining and quantitative analysis in HUVECs transfected with vector or PCAF plasmid in the presence of PA or not. Scale bars, 20 μm. Data are expressed as mean ± SEM ($n = 3$ for each experiment. ($^*P < 0.05$, $^{**}P < 0.01$, $^{***}P < 0.001$, n.s. $P > 0.05$).

we tested whether PA increased PCAF protein stability via reduced ubiquitination. HUVECs were transfected with His-tagged ubiquitin plasmid in the presence of PA or not for 48 hours, MG132 then was added 12 h before cells were harvested. Ubiquitin was co-immunoprecipitated by His-tagged magnetic beads. Co-IP showed PA stimulation evidently reduced overall ubiquitination level. Interestingly, previous studies have documented that MDM2 is a nuclear-localized E3 ubiquitin ligase that mediates the ubiquitination of many proteins including PCAF [22, 23]. Thus, we validated the potential interaction between PCAF and MDM2. Co-immunoprecipitation (Co-IP) experiments revealed that compared with control group, PA stimulation decreased the interaction between PCAF and MDM2 (Figures 3(e) and 3(f)). To sum up, PA-stimulated PCAF upregulation was dependent on decreased MDM2 mediated ubiquitination.

3.4. PCAF Mediated PA-Induced Endothelial Senescence through Hippo Signaling Pathway. To further understand

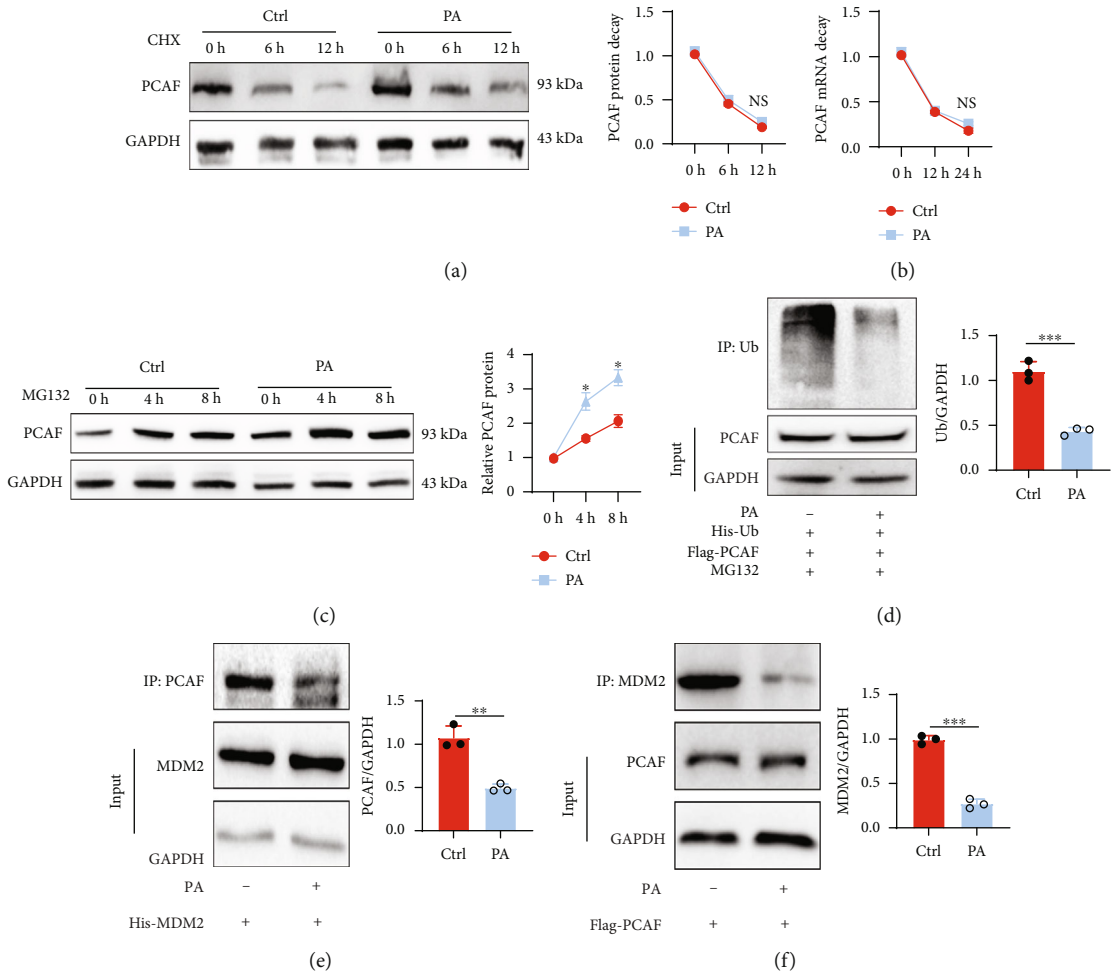

Figure 3: PA upregulated PCAF in HUVECs depended on decreased MDM2 mediated ubiquitination. (a) HUVECs were treated with cycloheximide (35 μmol/L) to block nascent protein synthesis for indicated time points in the presence of PA or not. Stability of PCAF protein was assessed by western blotting. (b) The stability of PCAF mRNA was assessed in HUVECs treated with actinomycin D (100 μg/ml) by RT-PCR in the presence of PA or not. (c) Western blotting was used to assess the expression of PCAF in HUVECs treated with MG132 (10 μM) for indicated times points in the presence of PA or not. (d) His-tagged ubiquitin plasmid and flag-tagged PCAF plasmid were cotransfected into HUVECs, PBS, or PA were then stimulated for 48 h. 12 h before cells were harvested, MG132 was added into the culture dishes. Flag-tagged magnetic beads were used to bind to PCAF, total Ub level was detected by western blotting. (e) and (f) His-tagged MDM2 plasmid or Flag-tagged PCAF plasmid was transfected into HUVECs before stimulated with PBS or PA for 48 h, Co-IP were performed by using corresponding magnetic beads. Data are expressed as mean ± SEM ($n = 3$ for each experiment. $^{*}P < 0.05$, $^{**}P < 0.01$, $^{***}P < 0.001$, n.s. $P > 0.05$).

the molecular mechanism by which PCAF modulated endothelial senescence, we predicted the potential pathways PCAF may participate in by using Gene Ontology annotation and predicted that PCAF may mainly regulate endothelial senescence via endocytosis and the Hippo signaling pathway (Figure 4(a)). Clathrin-mediated endocytosis (CME) and caveolae-mediated endocytosis (CavME) represent major types of endocytosis that are implicated in senescence [24]. Knockdown of PCAF had no significant effect on clathrin and caveolae protein expression, indicating PCAF-mediated endothelial senescence may not influence endocytosis (Suppl. Figure 2C). YAP plays a central role in the Hippo signaling pathway [25]. So, we tested whether PCAF regulated endothelial senescence via Hippo-YAP pathway. Western blotting and immunofluorescence revealed that PA stimulation reduced the transportation of YAP into the nucleus (Figures 4(c) and 4(d)). In addition, the phosphorylation of YAP was upregulated upon PA treatment (Figure 4(b)). Then, we knocked down YAP using siRNA in HUVECs, silence of YAP significantly increased the expression of p53, p21, p16, and pH2AX (Figure 4(e)). Real-time PCR revealed that YAP knockdown upregulated the mRNA levels of IL-1β and IL-6 (Figure 4(f)). In addition, YAP overexpression in HUVECs using plasmid prevented these senescence-associated gene expression and the mRNA levels of IL-1β and IL-6 (Figures 4(g) and 4(h)). IHC analysis also revealed that there was less expression of YAP in the vascular endothelia from aged mice than the control group (Figure 4(i)). To investigate if PCAF regulated cellular

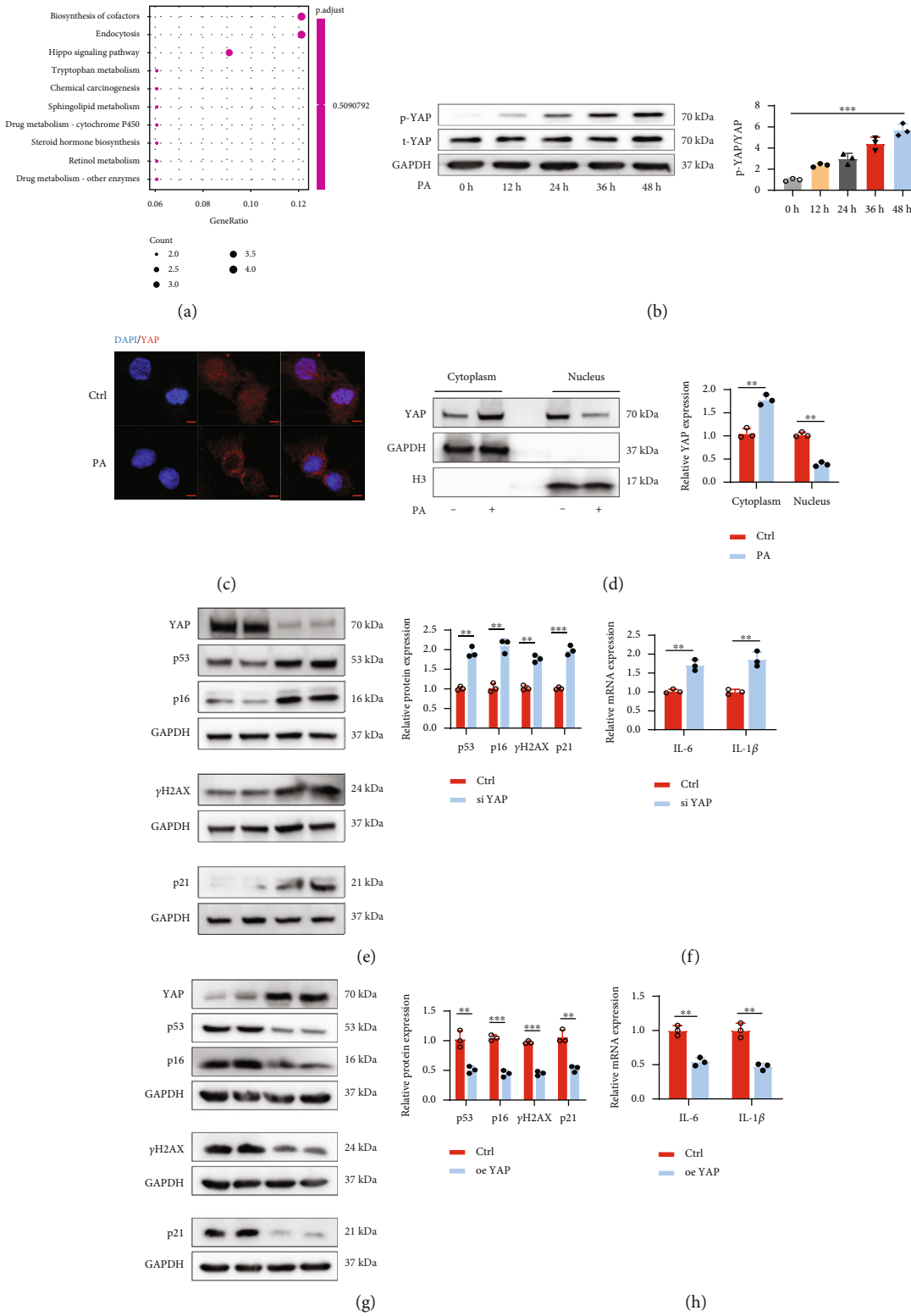

Figure 4: Continued.

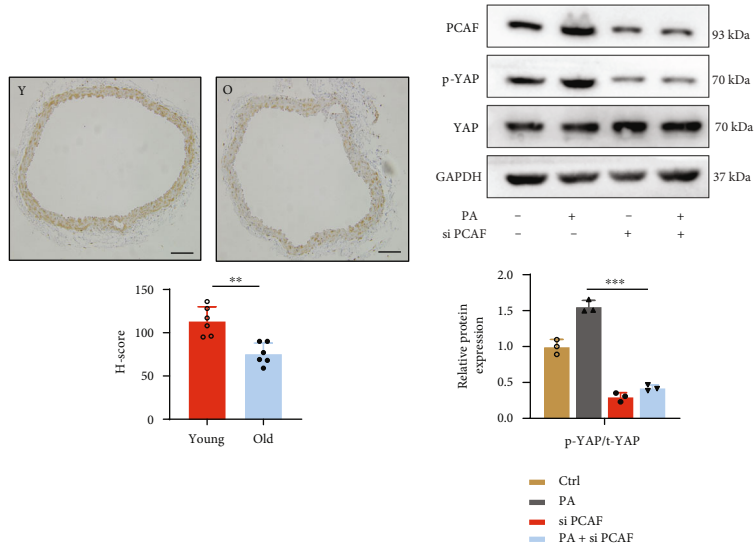

(i) (j)

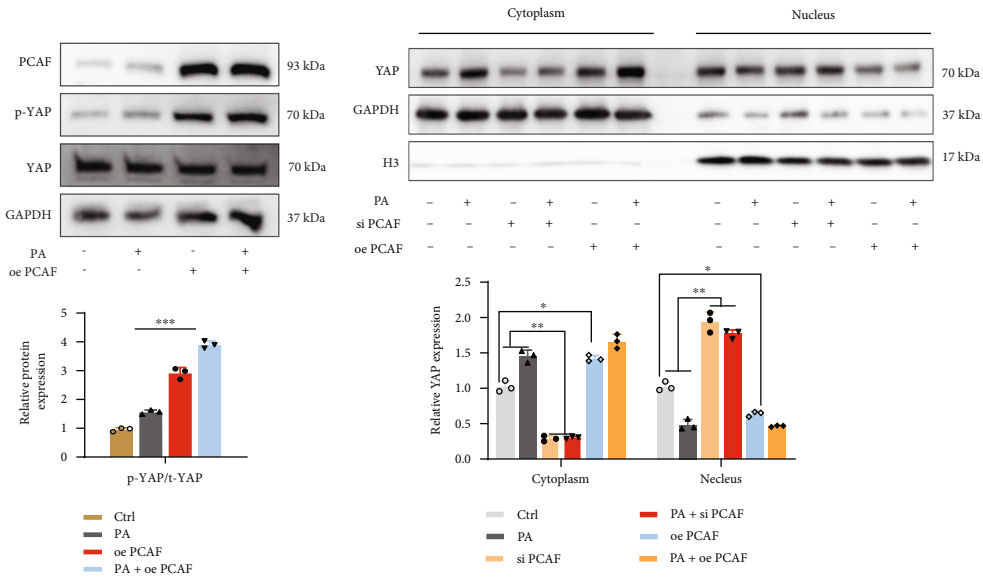

(k) (l)

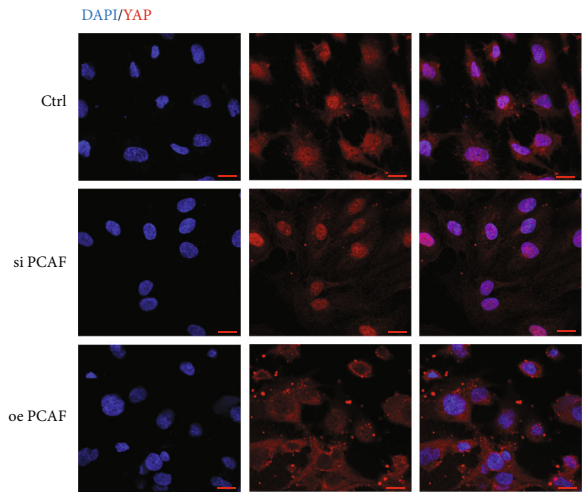

(m)

Figure 4: Continued.

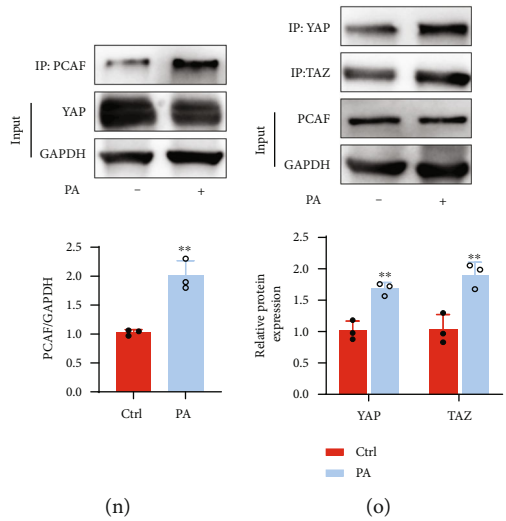

(n) (o)

Figure 4: PCAF mediated PA-induced endothelial senescence through Hippo signaling pathway. (a) KEGG analysis showed that PCAF may regulate endothelial senescence via Hippo-YAP pathway. (b) Western blotting analysis and qualification of phosphorylated YAP expression in HUVECs treated with PA for the indicated time points. (c) Immunofluorescence of YAP localization in HUVECs treated with or without PA. Scar bars, 10 μm. (d) Expression of total YAP proteins was analyzed by immunoblot in nuclear and cytoplasmic protein extractions from in HUVECs treated with or without PA. (e) and (f): HUVECs were transfected with YAP siRNA or overexpression plasmid. The expression of p53, p16, pH2A.X and p21 protein were by immunoblotting. (g) and (h) HUVECs were transfected with YAP siRNA or overexpression plasmid, IL-6 and IL-1β mRNA expression were analyzed by RT-PCR. (i) IHC staining and its qualification of vessels from 4w and one and half-year-old mice with YAP antibody. Scale bars, 100 μm. (j) and (k) HUVECs were transfected with PCAF siRNA or overexpression plasmid, the expression of p-YAP and t-YAP protein were by immunoblotting. (l) HUVECs were transfected with PCAF siRNA or overexpression plasmid treated with or without PA. Expression of YAP proteins was analyzed by immunoblot in nuclear and cytoplasmic protein extractions. (m) Immunofluorescence of YAP localization in HUVECs infected with si PCAF or PCAF plasmid or vector. Scar bars, 10 μm. (n) and (o) Flag-tagged YAP or Flag-tagged PCAF was transfected into HUVECs before stimulated with PBS or PA for 48 h, Co-IP were performed by using corresponding magnetic beads. t-YAP: total YAP; p-YAP: phosphorylated YAP. Data are expressed as mean ± SEM ($n = 3$ for each experiment. $^*P < 0.05$, $^{**}P < 0.01$, $^{***}P < 0.001$, n.s. $P > 0.05$).

senescence through Hippo signaling pathway, we knocked down PCAF in HUVECs. Our results showed PACF silence decreased YAP phosphorylation and its nucleus exporting (Figures 4(j), 4(m)). Accordingly, overexpression of PCAF in HUVECs promoted YAP phosphorylation and its transportation to the cytoplasm (Figures 4(k) and 4(l)). Additionally, PCAF knockdown or overexpression can also influence the activation of PDZ-binding motif (TAZ; also known as WWTR1) (Suppl. Figures 2A and 2B), which often acts as a coactivator with YAP to regulate various cellular process. Co-IP results showed that PCAF can bind to YAP and TAZ in HUVECs and their binding increased when PA stimulated (Figures 4(n) and 4(o)). In all, these results indicated that PCAF may regulate endothelial senescence via the Hippo signaling pathway.

3.5. YAP Is the Downstream Target of PCAF in PA-Stimulated Senescence-Associated Phenotypes in HUVECs. To confirm that YAP was the downstream of PCAF in PA-stimulated cellular senescence, PCAF knockdown significantly reduced PA-induced the upregulation of p53, p21, and p16 expression, and YAP silence remarkably reversed the reduced expression of these senescence-associated proteins (Figure 5(a)). As compared with silence control, YAP silence reversed PCAF-silencing-reduced SaβG staining in PA-treated HUVECs (Figure 5(d)). The mRNA and protein levels of IL-1β and IL-6 expression showed the similar trend (Figures 5(c) and 5(c)). Then, we forced the expression of PCAF and YAP in HUVECs. Compared with vector plasmid, the overexpression of YAP significantly abolished PCAF-induced senescence-associated phenotypes in HUVECs (Figures 5(e), 5(h)). Similarly, the upregulation of YAP also reduced the increased mRNA and protein levels of IL-1β and IL-6 mediated by PCAF in PA-treated HUVECs (Figures 5(f) and 5(g)). To sum up, this demonstrated that YAP is the downstream of PCAF in PA-induced cellular senescence.

3.6. Knockdown of PCAF Ameliorated Vascular Senescence. In PA-stimulated HUVECs, PCAF overexpression significantly accelerated cellular senescence and its downregulation ameliorated cellular senescence. Therefore, we tested if PCAF EC-specific downregulation using adeno-associated virus (AAV) can ameliorate vascular endothelial senescence in vivo. One and half-year-old C57BL6 male mice were injected with AAV-tie-PCAF virus or control virus and then fed with rodent diet for 16 weeks. Primary endothelial cells were isolated and vascular senescence-associated phenotypes and inflammatory factors were investigated by western blotting (Suppl. Figures 2E and 2F). Circulated IL-1β concentration in plasma was slightly reduced in PCAF-knockdown mice but with no significance (Figure 6(a)). No significance in body weight, blood glucose, serum triglyceride, total cholesterol levels, LDL, and HDL were

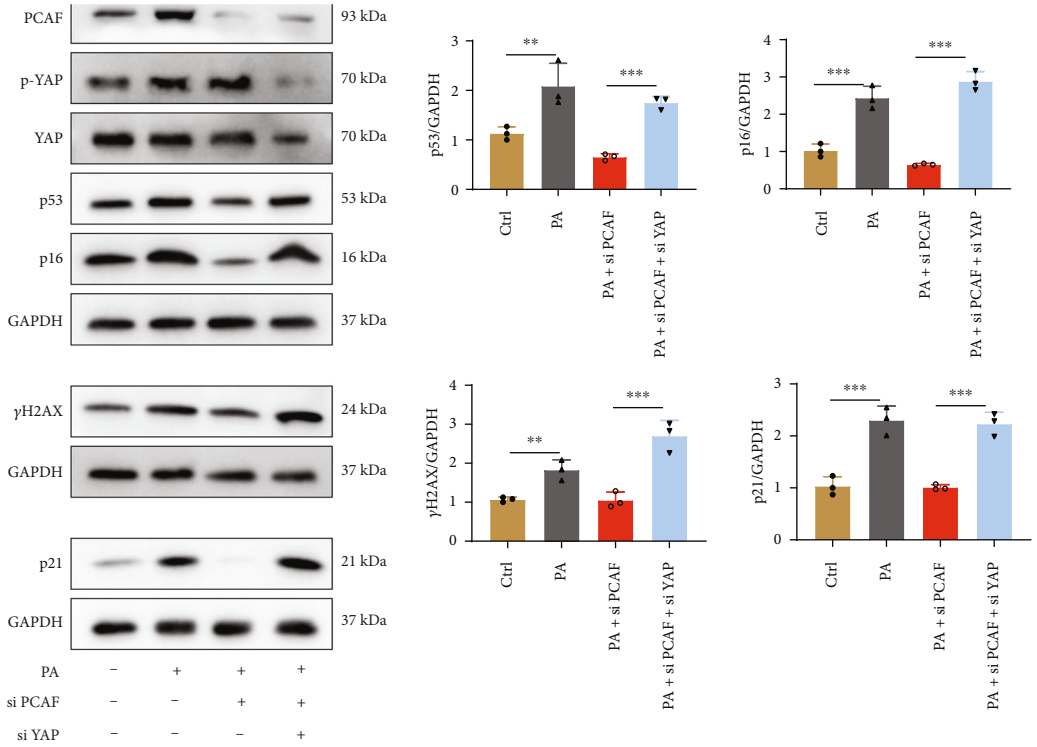

(a)

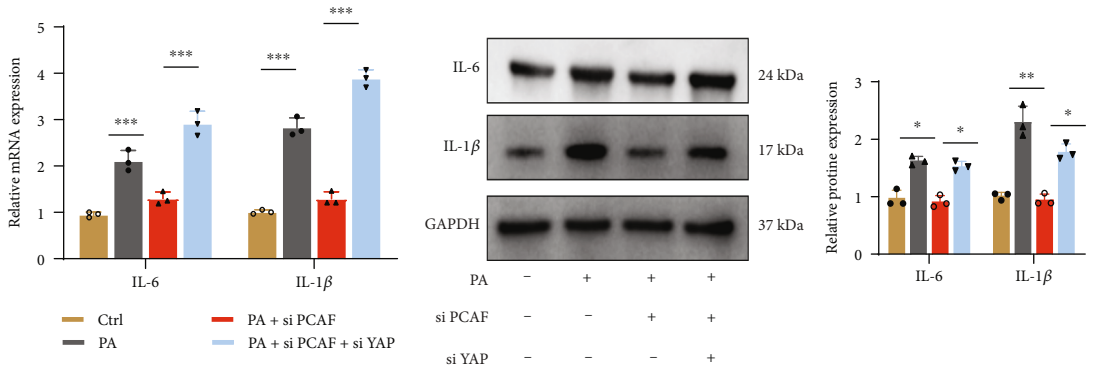

(b) (c)

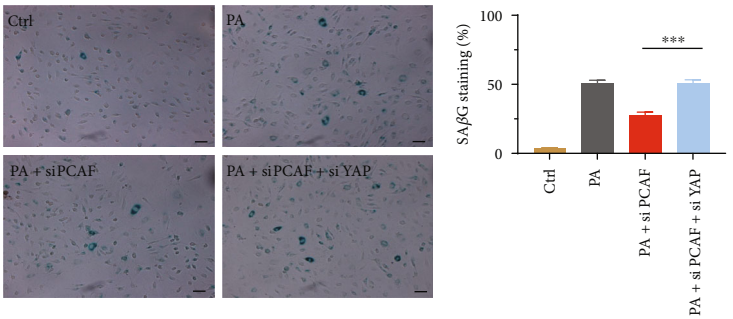

(d)

Figure 5: Continued.

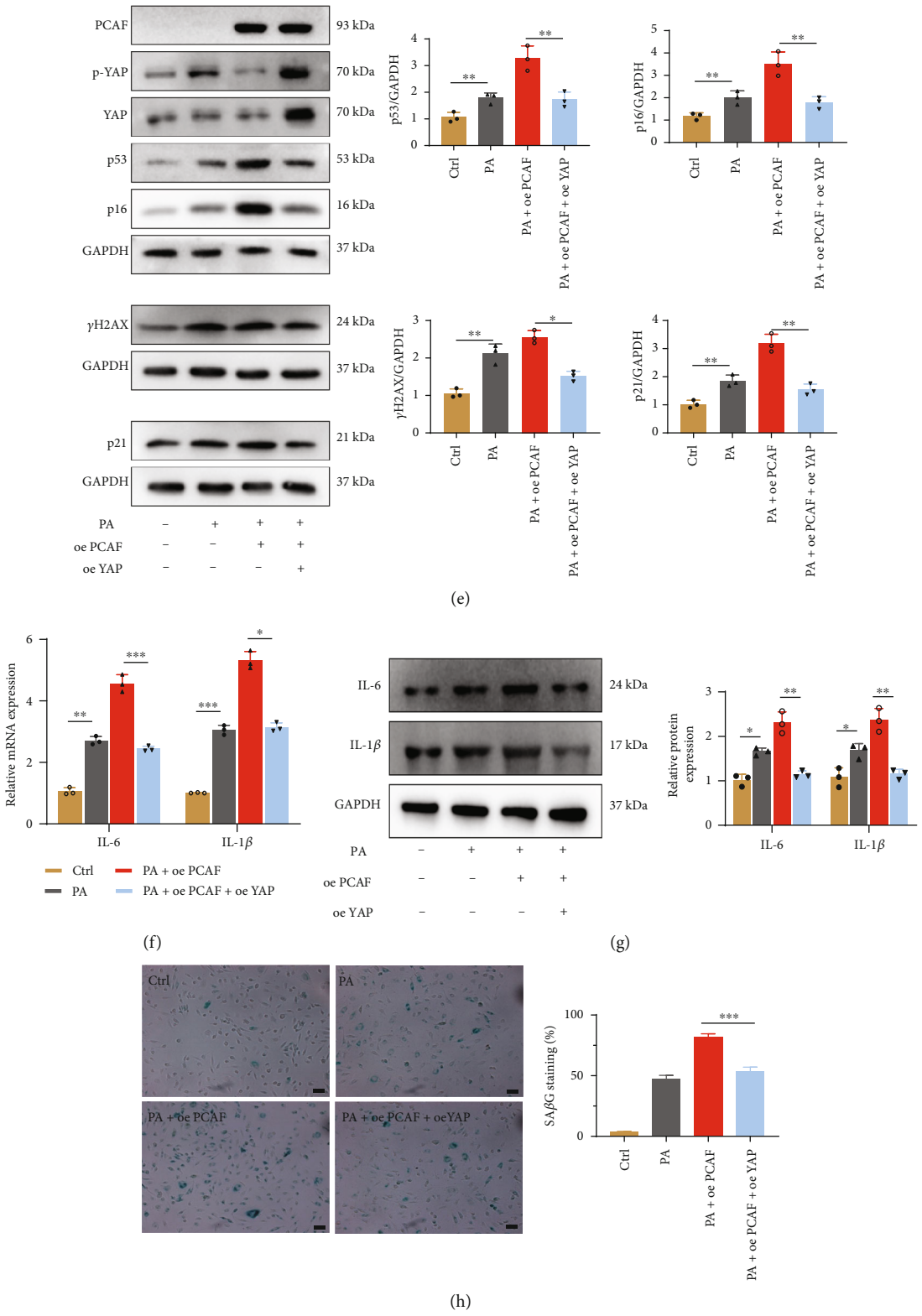

Figure 5: YAP is the downstream of PCAF in PA-stimulated senescence in HUVECs. (a)–(c) PCAF and YAP were knocked down in HUVECs using siRNA in the treatment of PA or not. The expression of p53, p16, pH2A.X, and p21 protein were by immunoblotting (a), relative IL-6 and IL-1β mRNA expression were analyzed by RT-PCR (b) and immunoblotting (c). (d) Quantitative analysis of SaβG staining. Scale bars, 20 μm. E-G: PCAF and YAP were overexpressed in HUVECs using plasmids in the treatment of PA or not. The expression of p53, p16, pH2A.X, and p21 protein were by immunoblotting (e), relative IL-6 and IL-1β mRNA expression were analyzed by RT-PCR (f) and immunoblotting (g). (h) Quantitative analysis of SaβG staining. Scale bars, 20 μm. Data are expressed as mean ± SEM ($n = 3$ for each experiment. $^{*}P < 0.05$, $^{**}P < 0.01$, $^{***}P < 0.001$, n.s. $P > 0.05$).

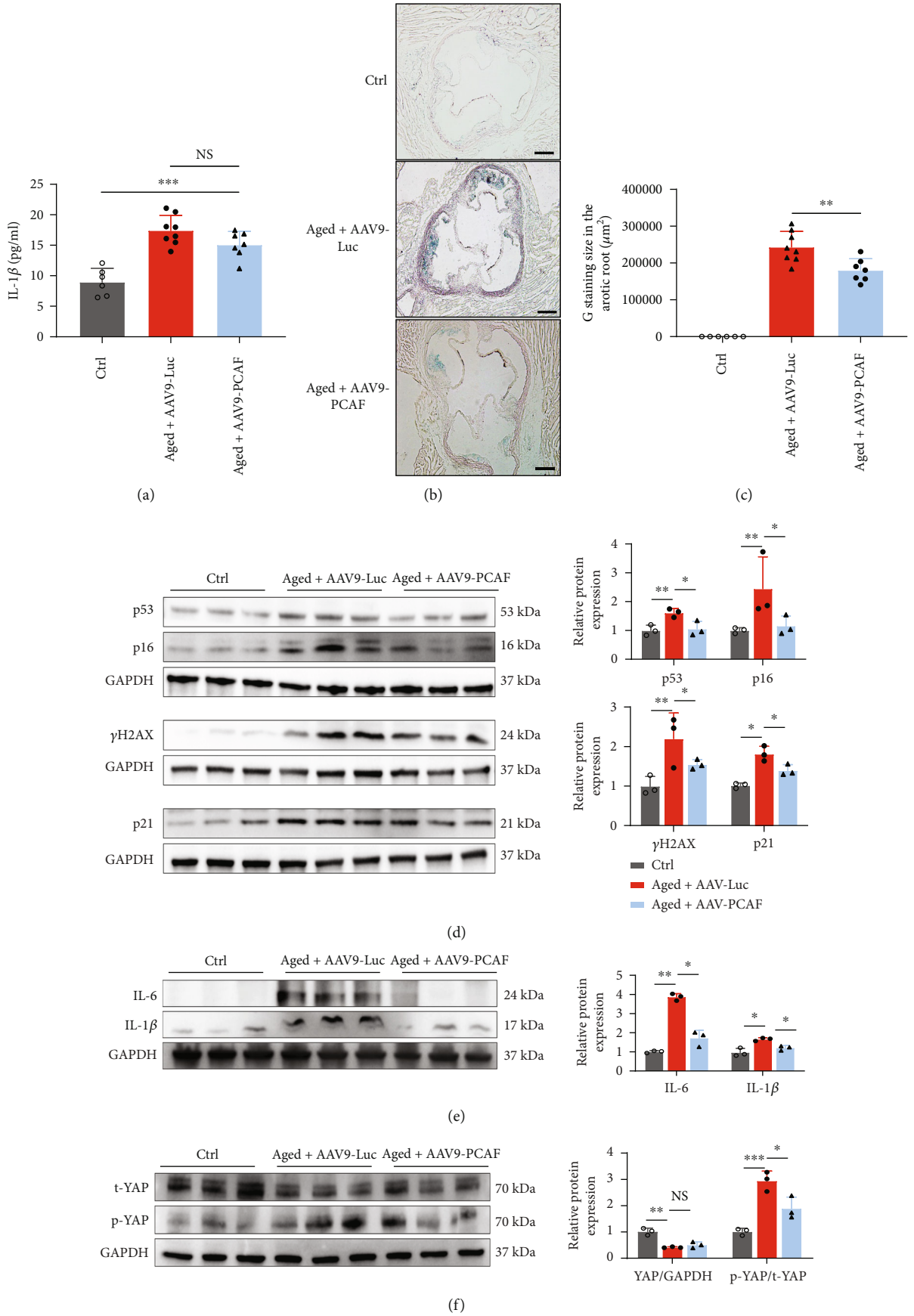

Figure 6: Continued.

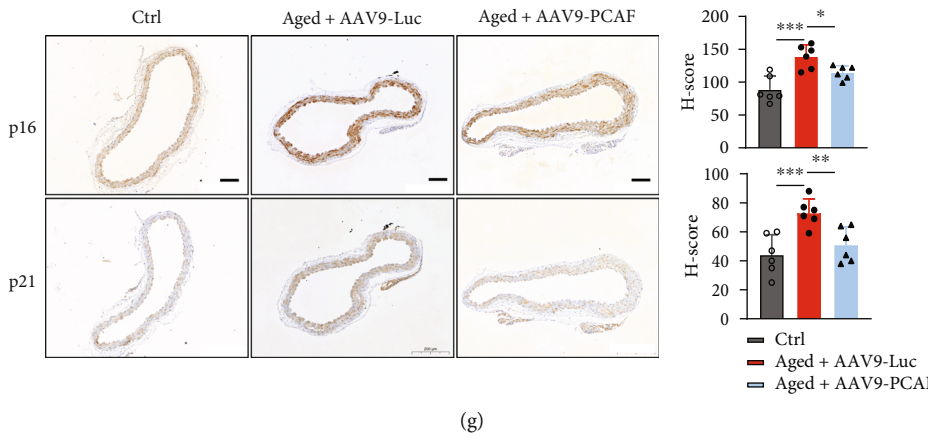

(g)

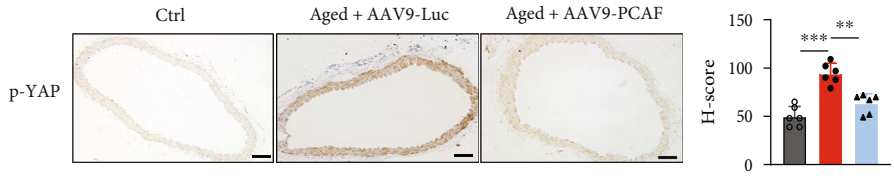

(h)

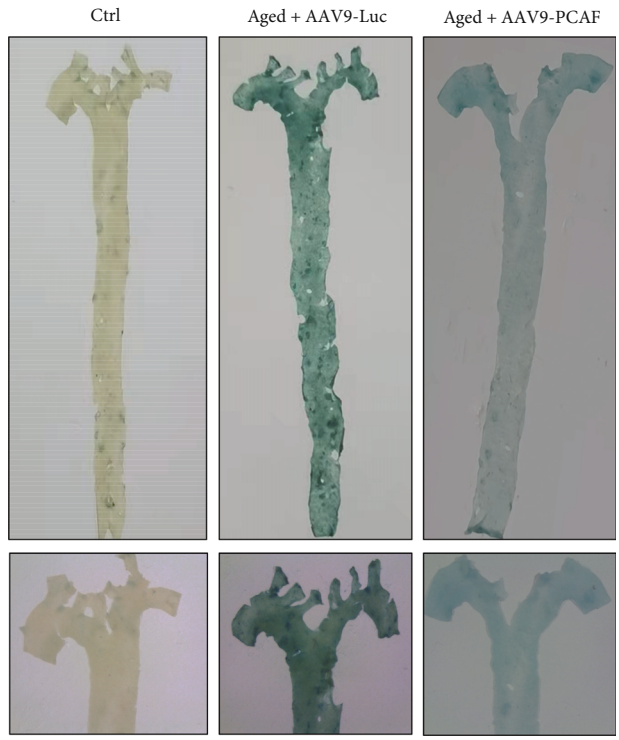

(i)

FIGURE 6: Knockdown of PCAF ameliorated vascular senescence. (a) The concentration of IL-1β in the plasma from ctrl ($n = 6$), aged+AAV9-Luc ($n = 8$), and aged+AAV9-PCAF ($n = 7$) mice were determined by ELISA kit according to its instruction. (b) and (c) Representative SaβG staining of aortic sinus sections (b) and its qualification analysis and thoracoabdominal aorta (i). Scale bars, 20 μm. (d) and (e): The expression of senescence-associated markers (d) and inflammatory factors (e) in the aorta from each group were assessed by immunoblotting. (f) The expression of YAP and p-YAP were investigated by immunoblotting. (g) and (h) The expression of p16, p21 (g) and p-YAP (h) were detected by IHC. Scale bars, 20 μm. Data are expressed as mean ± SEM ($^{*}P < 0.05$, $^{**}P < 0.01$, $^{***}P < 0.001$, n.s. $P > 0.05$).

found between the two groups of aged mice (Suppl. Figures 1E and 1F). Western blotting analysis suggested that senescence-associated markers were downregulated in the aorta of PCAF-knockdown mice (Figure 6(d) and 6(e)). The level of p-YAP/YAP was upregulated in the aorta of aged mice and downregulated in endothelial PCAF-

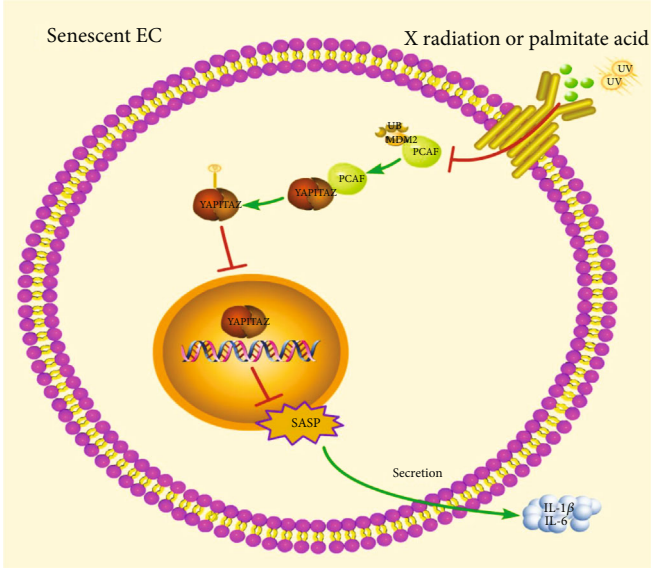

Figure 7: A proposed model for the role of PCAF in endothelial senescence. PCAF is upregulated in senescent endothelial cells by decreased coupling with DMD2 to inhibit the transportation of YAP/TAZ into nucleus, thereby promoting cellular senescence.

knockdown mice (Figure 6(f)). IHC analysis of p16 and p21 and p-YAP revealed the same trend. (Figure 6(g) and 6(h)). There was a remarkable reduction of SaβG staining of aortas and frozen tissue sections of aortic sinus in PCAF-knockdown mice than the control aged mice (Figure 6(b), 6(i)). These in vivo experiments suggested that PCAF might aggravate vascular senescence.

4. Discussion

Cellular senescence is a continuously irreversible process that chronically leads to organ dysfunction. The way to slow down this process at a systemic or tissue level has attracted much concern over the past decades. Cardiovascular disease, the most common cause of death, is also age-related disease [26]. Aged vascular tissues can bring about a series of diseases including atherosclerosis and vascular calcification [27, 28]. Thus, it is important to understand the mechanisms behind cellular senescence.

PCAF, a member of the GCN5-related N-acetyltransferase family with histone acetyltransferase activity, has been shown to be involved in cell growth and differentiation, tumorigenesis, and transcriptional regulation [8]. Prior works show that PCAF can regulate the activation of p53/p21 and Rb/p16 signaling pathway. PCAF downregulation can also inhibit NF-κB-mediated vascular inflammation, which is a critical cause of cellular senescence [29]. These results have put PCAF in the spotlight of the aging process. However, the specific role of PCAF in regulating cellular senescence is unclear. In this study, we found that (a) PCAF was highly expressed in aged vascular artery and its expression was closely related with the upregulation senescence-associated phenotype markers and inflammatory factors in palmitate acid-induced aged HUVECs, (b) genetical silence of PCAF significantly attenuated cellular senescence-associated phenotypes in vivo, and (c) PCAF regulated cellular senescence via the Hippo signaling pathway. The possible mechanism of this study is summarized in Figure 7.

In our preliminary study, we found that PCAF could be activated by PA or UV stimulation in HUVECs, along with increased senescence-associated markers like p53, p21, p16, and DNA damage marker pH2AX. Knockdown of PCAF in PA-stimulated HUVECs alleviated senescence-associated phenotypes and overexpression of PCAF accelerated it. Excitingly, in aged mice injected with AAV-tie-PCAF virus, SaβG staining showed PCAF downregulation in endothelial cells obviously alleviated vascular senescence. Therefore, our results indicated that PCAF can affect cellular senescence and the key role of PCAF in this process may provide a therapeutic target for the prevention of senescence-associated vascular diseases.

Based on transcriptional microarray analysis, Kyoto Encyclopedia of Genes and Genomes pathway enrichment analysis showed that genes were mainly enriched in endocytosis and the Hippo signaling pathway. Our results indicated that PCAF might induce cellular senescence via the Hippo signaling pathway without affecting endocytosis in HUVECs. Studies over the past decade have uncovered the critical role of the Hippo-YAP signaling pathway in the regulation of development, regeneration, and homoeostasis [30, 31]. When the Hippo pathway is active, the Hippo kinase cascade phosphorylates YAP and TAZ, resulting in their cytoplasmic retention and proteolytic degradation. When the Hippo pathway is inactive, YAP and TAZ translocate into the nucleus and interact with transcription factors to regulate the expression of target genes. Previous works also manifested the effectiveness of YAP and TAZ in cellular senescence [32]. However, it seems that in various types of cells, the effects of YAP in modulating cellular senescence are quite different. For instance, downregulation of YAP in IMR90 tumor cells increased cellular senescence, whereas

upregulation of YAP in Werner syndrome-derived fibroblasts accelerated cellular senescence [33, 34]. Recent work indicated that the upregulation of YAP may regulate cellular senescence through YAP-mTOR-autophagic flux signaling pathway [35].

In our study, we found that PCAF-induced cellular senescence was repressed by YAP overexpression. PCAF upregulated the phosphorylation of YAP and TAZ in PA-induced senescent HUVECs while not apparently affecting the mTOR pathway, which was documented to have a direct link with the Hippo signaling pathway and play an important role in cellular senescence (Suppl. Figure 2D). PCAF silence promoted YAP and TAZ nucleus transportation, result in lessened senescence-associated secretory phenotype (SASP) and reduced IL-1β and IL-6 production. Regarding to how PCAF affecting YAP and TAZ activity, our Co-IP results revealed that PCAF can bind to YAP and TAZ in HUVECs, implying PCAF may directly regulate the activation YAP and TAZ, result in increased phosphorylation of YAP and TAZ. However, the specific mechanism between PCAF and YAP/TAZ needs further study. In addition to our in vitro study for the modulation of PCAF in cellular senescence, we demonstrated that PCAF increased in the endothelia of aorta in aged mouse and EC-specific knockdown of PCAF evidently neutralized vascular senescence. The limitation of this study is that mice injected with adeno-associated virus (AAV)-tie-YAP are not included in this study to further verify our hypothesis in vivo.

In conclusion, our study revealed a previously unknown, but potentially crucial role of PCAF in regulating endothelial cell senescence. We propose that inhibition the PCAF in endothelial cell might provide a novel strategy for prevention and treatment of senescence-associated vascular disease.

5. Conclusions

Our study indicated that PCAF was closely related to vascular senescence. Its upregulation in vascular tissue accelerated vascular senescence and PCAF inhibition effectively alleviated vascular senescence. In addition, YAP inactivation was observed during PCAF-promoted vascular senescence. These findings indicated a fundamentally important function of PCAF as a potent target for controlling endothelial cell senescence. We propose that inhibition of PCAF might provide a novel strategy for prevention and treatment of vascular senescence.

Data Availability

The data used for pathway enrichment analysis were downloaded from GEO database (GSE47179).

Conflicts of Interest

The authors declare that there is no conflict of interest regarding the publication of this paper.

Authors' Contributions

CK performed most of the in vitro experiments and drafted the manuscript. DW, FW, and WZ conducted the in vivo experiments and part of the in vitro experiments, including cell culture and harvest. YL and PY analyzed data. YG, LZ, and XJ performed bioinformatic analysis and edited the manuscript. SC, YC, and ZG developed the original hypothesis and supervised the experimental design. Chaohua Kong, Dongchen Wang and Feng Wang contributed equally to this work. Yuelin Chao and Shaoliang Chen jointly directed this work.

Acknowledgments

This work was supported by grants from the National Natural Science Foundation of China (No. 82000416) and Natural Science Foundation of Jiangsu Province (No. BK20191117). We would like to thank Yuelin Chao for his excellent technical assistance.

Supplementary Materials

Supplemental Figure 1–A and B: PCAF and YAP siRNA efficiency was tested via western blotting in HUVECs. C and D: Body weight, serum triglyceride, total cholesterol, LDL and HDL levels of each group are shown. Supplemental Figure 2–A and B: Western blotting analysis and qualification of p-TAZ and TAZ in PA-treated HUVECs transfected with scramble or PCAF siRNA. C: Western blotting analysis and qualification of clathrin and caveolin in HUVECs transfected with scramble or PCAF siRNA. D: Western blotting analysis and qualification of p-mTOR and mTOR in HUVECs transfected with scramble or PCAF siRNA. E and F: Primary endothelial cells were isolated and vascular senescence-associated phenotypes (E) and inflammatory factors (F) were investigated by western blotting. Physiological parameters of experimental mice. *(Supplementary Materials)*

References

[1] F. Rodier and J. Campisi, "Four faces of cellular senescence," *The Journal of Cell Biology*, vol. 192, no. 4, pp. 547–556, 2011.

[2] J. van Deursen, "The role of senescent cells in ageing," *Nature*, vol. 509, no. 7501, pp. 439–446, 2014.

[3] A. Donato, D. Machin, and L. Lesniewski, "Mechanisms of dysfunction in the aging vasculature and role in age-related disease," *Circulation Research*, vol. 123, no. 7, pp. 825–848, 2018.

[4] E. Lakatta and D. Levy, "Arterial and cardiac aging: major shareholders in cardiovascular disease enterprises," *Circulation*, vol. 107, no. 2, pp. 346–354, 2003.

[5] B. van Bussel, F. Schouten, R. Henry et al., "Endothelial dysfunction and low-grade inflammation are associated with greater arterial stiffness over a 6-year period," *Hypertension (Dallas, Tex. : 1979)*, vol. 58, no. 4, pp. 588–595, 2011.

[6] J. D. Erusalimsky, "Vascular endothelial senescence: from mechanisms to pathophysiology," *Journal of Applied Physiology (Bethesda, MD: 1985)*, vol. 106, no. 1, pp. 326–332, 2009.

[7] I. Ben-Porath and R. A. Weinberg, "The signals and pathways activating cellular senescence," *The International Journal of Biochemistry & Cell Biology*, vol. 37, no. 5, pp. 961–976, 2005.

[8] V. Ogryzko, R. Schiltz, V. Russanova, B. Howard, and Y. Nakatani, "The transcriptional coactivators p300 and CBP are histone acetyltransferases," *Cell*, vol. 87, no. 5, pp. 953–959, 1996.

[9] A. J. Bastiaansen, M. M. Ewing, H. C. de Boer et al., "Lysine acetyltransferase PCAF is a key regulator of arteriogenesis," *Arteriosclerosis, Thrombosis, and Vascular Biology*, vol. 33, no. 8, pp. 1902–1910, 2013.

[10] Y. Sunami, M. Araki, S. Kan et al., "Histone Acetyltransferase p300/CREB-binding Protein-associated Factor (PCAF) Is Required for All- *trans* -retinoic Acid-induced Granulocytic Differentiation in Leukemia Cells," *The Journal of Biological Chemistry*, vol. 292, no. 7, pp. 2815–2829, 2017.

[11] C. Sun, M. Wang, X. Liu et al., "PCAF improves glucose homeostasis by suppressing the gluconeogenic activity of PGC-1α," *Cell Reports*, vol. 9, no. 6, pp. 2250–2262, 2014.

[12] I. M. Love, P. Sekaric, D. Shi, S. R. Grossman, and E. J. Androphy, "The histone acetyltransferase PCAF regulates p21 transcription through stress-induced acetylation of histone H3," *Cell Cycle*, vol. 11, no. 13, pp. 2458–2466, 2012.

[13] H. J. Fei, L. D. Zu, J. Wu et al., "PCAF acts as a gastric cancer suppressor through a novel PCAF-p16-CDK4 axis," *American Journal of Cancer Research*, vol. 6, no. 12, pp. 2772–2786, 2016.

[14] J. Lee, J. H. Yoo, H. S. Kim et al., "C1q/TNF-related protein-9 attenuates palmitic acid-induced endothelial cell senescence via increasing autophagy," *Molecular and Cellular Endocrinology*, vol. 521, p. 111114, 2021.

[15] X. Xiao, M. Xu, H. Yu et al., "Mesenchymal stem cell-derived small extracellular vesicles mitigate oxidative stress-induced senescence in endothelial cells via regulation of miR-146a/Src," *Signal Transduction and Targeted Therapy*, vol. 6, no. 1, p. 354, 2021.

[16] S. Luo, F. Wang, S. Chen et al., "NRP2 promotes atherosclerosis by upregulating PARP1 expression and enhancing low shear stress-induced endothelial cell apoptosis," *The FASEB Journal*, vol. 36, no. 2, article e22079, 2022.

[17] R. X. Wu, C. S. Bi, Y. Yu, L. L. Zhang, and F. M. Chen, "Age-related decline in the matrix contents and functional properties of human periodontal ligament stem cell sheets," *Acta Biomaterialia*, vol. 22, pp. 70–82, 2015.

[18] O. J. Sul, J. H. Kim, T. Lee et al., "SPE protects against bleomycin-induced pulmonary fibrosis in mice via ameliorating epithelial apoptosis through inhibition of oxidative stress," *Oxidative Medicine and Cellular Longevity*, vol. 2022, Article ID 8200189, 16 pages, 2022.

[19] D. W. Huang, B. T. Sherman, and R. A. Lempicki, "Systematic and integrative analysis of large gene lists using DAVID bioinformatics resources," *Nature Protocols*, vol. 4, no. 1, pp. 44–57, 2009.

[20] D. W. Huang, B. T. Sherman, and R. A. Lempicki, "Bioinformatics enrichment tools: paths toward the comprehensive functional analysis of large gene lists," *Nucleic Acids Research*, vol. 37, no. 1, pp. 1–13, 2009.

[21] M. Löbrich, A. Shibata, A. Beucher et al., "γH2AX foci analysis for monitoring DNA double-strand break repair: strengths, limitations and optimization," *Cell Cycle (Georgetown, Texas)*, vol. 9, no. 4, pp. 662–669, 2010.

[22] Y. Jin, S. Zeng, M. Dai, X. Yang, and H. Lu, "MDM2 inhibits PCAF (p300/CREB-binding protein-associated factor)-mediated p53 acetylation," *The Journal of Biological Chemistry*, vol. 277, no. 34, pp. 30838–30843, 2002.

[23] M. Li, C. Brooks, N. Kon, and W. Gu, "A dynamic role of HAUSP in the p53-Mdm2 pathway," *Molecular Cell*, vol. 13, no. 6, pp. 879–886, 2004.

[24] E. Y. Shin, N. K. Soung, M. A. Schwartz, and E. G. Kim, "Altered endocytosis in cellular senescence," *Ageing Research Reviews*, vol. 68, p. 101332, 2021.

[25] B. Zhao, X. Wei, W. Li et al., "Inactivation of YAP oncoprotein by the hippo pathway is involved in cell contact inhibition and tissue growth control," *Genes & Development*, vol. 21, no. 21, pp. 2747–2761, 2007.

[26] P. Mistriotis and S. Andreadis, "Vascular aging: Molecular mechanisms and potential treatments for vascular rejuvenation," *Ageing Research Reviews*, vol. 37, pp. 94–116, 2017.

[27] J. Leopold, "Vascular calcification," *Circulation*, vol. 127, no. 24, pp. 2380–2382, 2013.

[28] S. Stojanović, J. Fiedler, J. Bauersachs, T. Thum, and D. Sedding, "Senescence-induced inflammation: an important player and key therapeutic target in atherosclerosis," *European Heart Journal*, vol. 41, no. 31, pp. 2983–2996, 2020.

[29] S. Park, Y. Lee, A. Seong, J. Lee, W. Jun, and H. Yoon, "Selective inhibition of PCAF suppresses microglial-mediated β-amyloid neurotoxicity," *International Journal of Molecular Medicine*, vol. 32, no. 2, pp. 469–475, 2013.

[30] I. M. Moya and G. Halder, "Hippo-YAP/TAZ signalling in organ regeneration and regenerative medicine," *Nature Reviews. Molecular Cell Biology*, vol. 20, no. 4, pp. 211–226, 2019.

[31] F. X. Yu, B. Zhao, and K. L. Guan, "Hippo Pathway in Organ Size Control, Tissue Homeostasis, and Cancer," *Cell*, vol. 163, no. 4, pp. 811–828, 2015.

[32] H. L. Sladitschek-Martens, A. Guarnieri, G. Brumana et al., "YAP/TAZ activity in stromal cells prevents ageing by controlling cGAS-STING," *Nature*, vol. 607, no. 7920, pp. 790–798, 2022.

[33] F. Fausti, S. Di Agostino, M. Cioce et al., "ATM kinase enables the functional axis of YAP, PML and p53 to ameliorate loss of Werner protein-mediated oncogenic senescence," *Cell Death and Differentiation*, vol. 20, no. 11, pp. 1498–1509, 2013.

[34] Q. Xie, J. Chen, H. Feng et al., "YAP/TEAD–mediated transcription controls cellular senescence," *Cancer Research*, vol. 73, no. 12, pp. 3615–3624, 2013.

[35] X. Pan, B. Wu, X. Fan, G. Xu, C. Ou, and M. Chen, "YAP accelerates vascular senescence via blocking autophagic flux and activating mTOR," *Journal of Cellular and Molecular Medicine*, vol. 25, no. 1, pp. 170–183, 2021.

Hindawi
Oxidative Medicine and Cellular Longevity
Volume 2022, Article ID 4631983, 12 pages
https://doi.org/10.1155/2022/4631983

Research Article

Antidyslipidemic, Antioxidant, and Anti-inflammatory Effects of Jelly Drink Containing Polyphenol-Rich Roselle Calyces Extract and Passion Fruit Juice with Pulp in Adults with Dyslipidemia: A Randomized, Double-Blind, Placebo-Controlled Trial

Jurairat Khongrum,[1] **Pratoomporn Yingthongchai**,[1] **Kongsak Boonyapranai**,[2] **Wachira Wongtanasarasin**,[3] **Nowwapan Donrung**,[4] **Wanida Sukketsiri**,[5] **Aree Prachansuwan**,[6] **and Pennapa Chonpathompikunlert**[4]

[1]*Science and Technology Research Institute, Chiang Mai University, Chiang Mai 50200, Thailand*
[2]*Research Institute for Health Science Chiang Mai University, Chiang Mai 50200, Thailand*
[3]*Department of Emergency Medicine, Faculty of Medicine, Chiang Mai University, Chiang Mai 50200, Thailand*
[4]*Expert Center of Innovative Health Food and Biodiversity Research Centre, Thailand Institute of Scientific and Technological Research, 12120, Thailand*
[5]*Division of Health and Applied Sciences, Faculty of Science, Prince of Songkla University, Songkhla 90110, Thailand*
[6]*Institute of Nutrition, Mahidol University, Nakhon Pathom 73170, Thailand*

Correspondence should be addressed to Jurairat Khongrum; jurairat.kh@cmu.ac.th
and Pennapa Chonpathompikunlert; pennapa@tistr.or.th

Received 23 May 2022; Accepted 1 September 2022; Published 21 September 2022

Academic Editor: Michael A. Hill

Oxidative stress and inflammation play key roles in the pathophysiology in the pathophysiology of dyslipidemia, which are positive risks that increase atherosclerosis leading to important healthcare problems. Therefore, we aimed to study the antioxidant, anti-inflammatory, and lipid-lowering effects of jelly drink containing polyphenol-rich roselle calyces extract and passion fruit juice with pulp concentrate (RP jelly drink) in comparison to a placebo jelly drink for 8 weeks. Forty-three adults with dyslipidemia were randomly assigned into two groups: the RP jelly drink group and the placebo group. Glucose, total cholesterol (TC) triglyceride (TG), low-density lipoprotein-cholesterol (LDL-C), high-density lipoprotein-cholesterol (HDL-C), oxidative stress biomarkers, inflammatory parameters, and monocyte chemotactic protein-1 (MCP-1) were measured with fasting blood samples at baseline, 4 weeks and 8 weeks of intervention. Results showed a significant decrease in LDL-C and TG, respectively, after 8 weeks of RP jelly drink consumption (LDL-C: $107.63 \pm 22.98\, mg/dL$; TG: $109.79 \pm 38.83\, mg/dL$) compared to baseline measurements (LDL-C: $128.43 \pm 32.74\, mg/dL$; TG: $132.33 \pm 75.11\, mg/dL$). These may be possible due to reduced inflammation and improvements in oxidative stress, as demonstrated by the reduction of tumor necrosis factor-(TNF-) α and malondialdehyde (MDA), and the enhancement of glutathione (GSH) after consuming the RP jelly drink for 8 weeks. However, no significant differences of treatment on glucose, total cholesterol, MCP-1, interleukin-6, and interleukin-10 were observed. In conclusion, daily consumption of RP jelly drink for 8 weeks resulted in significant improvement in lipid profiles in subjects with dyslipidemia. However, more research is needed to assess its nutritional and functional potential.

1. Introduction

Cardiovascular disease has become life-threatening worldwide with high morbidity and mortality rates. Positive risk factors can be grouped into metabolic syndromes, including abdominal obesity, high blood pressure, hyperglycemia, and dyslipidemia for the onset of atherosclerosis, which may lead to a series of cardiovascular events [1]. Dyslipidemia is recognized as a risk factor related with atherosclerosis and is characterized by an abnormal lipid profile in which the level of serum cholesterol, triglycerides, or both are elevated, or the level of high-density lipoprotein cholesterol (HDL-C) is reduced [2]. Consumption of foods high in fat and cholesterol and lack of exercise cause high blood lipid levels [3]. Furthermore, the occurrence of increased oxidative stress and inflammation is associated with the regulation of lipid metabolism, and these are major contributors to the incidence of dyslipidemia [4, 5].

The imbalance between oxygen free radicals and antioxidant defenses is negatively altered within cells, on cell membranes and receptors, proteins, lipids, lipoproteins, carbohydrates, and DNA strands [6, 7]. Previous studies have revealed that an increase in lipid peroxidation such as malondialdehyde (MDA) is associated with the serum total cholesterol (TC), triglyceride (TG), and low-density lipoprotein cholesterol (LDL-C) [8]. Likewise, inflammation is recognized as a key role in abnormal lipid metabolism. Higher production of inflammatory cytokines, including tumor necrosis factor- (TNF-) α and less potent anti-inflammatory properties such as interleukin-10 (IL-10), induced severe high-density lipoprotein cholesterol (HDL-C) deficiency, LDL-C, and elevated TG. [9, 10]. Furthermore, LDL-C accumulated in the intimal layer of blood vessels was oxidized that caused oxidized low-density lipoproteins (OxLDL) forming in microphages and vascular smooth muscle cells. An excessive OxLDL accumulation could further stimulate proinflammatory signaling pathway because the OxLDL could bind to the monocyte chemoattractant protein-1 (MCP-1) and form a monocyte-attracting lipoprotein which can induce a much stronger chemotactic effect on monocytes than that of OxLDL alone. Either OxLDL or OxLDL-bound MCP-1 play a key role in the initiation and progression of atherosclerosis by promoting the direct migration of inflammatory cell [11]. It is known that lipid-lowering drugs can effectively reduce serum LDL-C levels; however, the adverse effects of the drugs have raised concerns about its use. Therefore, alternative strategies are presented especially in dietary polyphenol and vitamin C that play a role in antioxidant defenses showed high activity of glutathione (GSH) and superoxide dismutase (SOD) along with the reduction of TC, TG, and LDL-C [12–14]. Dietary polyphenols such as fruits, vegetables, legumes, nuts, and plant-derived beverages [15] have received much attention in disease prevention due to their potential therapeutic effects. Roselle calyces (*Hibiscus sabdariffa*) is an important source of vitamins, minerals, and bioactive compounds, such as organic acids, phytosterols, and polyphenols as well [16]. There are many pharmacological actions on the health effects of rosella petals, such as cardioprotective action, antihypertensive effect, and inhibition of LDL-C oxidation [17]. Passion fruit (*Passiflora edulis*) is a tropical fruit composed of polyphenols, flavonoids, alkaloids, carotenoids, tocopherols, and ascorbic acid. These compounds have been recognized for their health effects and biological activity such as antioxidant, antihypertensive, antitumor, antidiabetic, hypolipidemic, and anti-inflammatory activities [14, 18].

However, there are no reports on the benefits of a combination of rosella calyces extract and passion fruit containing bioactive components in functional food products regarding the effects of hypolipidemia. We therefore performed a double-blind randomized, two-arm parallel-group, placebo-controlled trial study to evaluate the hypolipidemic, antioxidant, and anti-inflammatory effects of jelly drink containing polyphenol-rich rosella calyces extract and passion fruit juice with pulp (RP) on repeated intake over a period of 8-week among hyperlipidemic adults.

2. Materials and Methods

2.1. Study Design. A randomized double-blind, two-arm parallel-group, placebo-controlled trial was conducted with an 8-week intervention among Thai adults with dyslipidemia. The study was performed according to the Good Clinical Practice (GCP) Guideline with fully complied with the ethical guidelines of a clinical trial study according to the Declaration of Helsinki. All procedures involving human subjects were approved by the Health Sciences Human Experimentation Committee under the auspices of the Office of Research Ethics, Research Institute for Health Sciences, Chiang Mai University, Thailand (Code: HSHEC-23/63). All subjects written informed consent before inclusion in the study. The trial was registered at https://www.thaiclinicaltrials.org as TCTR20220326001.

2.2. Subjects and Interventions. Forty Thai adults were recruited via poster advertisement from the community around Chiang Mai University. Eligibility criteria were aged 35-60 years, dyslipidemia based on the criteria: serum total cholesterol ($TC \geq 200\, mg/dL$) and/or triglycerides ($TG \geq 150\, mg/dL$) and/or LDL cholesterol ($LDL - C \geq 100\, mg/dL$) and/or HDL cholesterol ($HDL\text{-}C < 40\, mg/dL$), not currently taking drugs for lowering cholesterol or triglycerides such as statins and fenofibrate and not with a vegan or vegetarian diet. The exclusion criteria included *body mass index* (BMI) $> 35\, kg/m^2$, smokers, athletes, diabetes, multiple allergies, traumatic injury, gastrointestinal disease, cancer, central nervous system or psychiatric disorders, and having been treated with herbal medicines and dietary supplements affecting the lipid metabolism in the previous 14 days. The randomization was performed using a computer-generated code with Random Allocation Software. Each subject was blinded and randomly assigned to receive either the RP-jelly drink (300 mL; 100 Kcal) or a placebo jelly drink (300 mL; 100 Kcal) once daily for a period of 8 weeks.

Table 1: The total phenolic contents, flavonoids contents, and antioxidant activity of RP jelly drink and placebo jelly drink.

Parameters	RP jelly drink	Placebo jelly drink	P value
Total phenolic content, mg GAE/g DW	1.97 ± 0.03	0.98 ± 0.01	<0.001
Flavonoid content, mg QE/g DW	1.79 ± 0.20	0.87 ± 0.12	0.002
DPPH (IC_{50}), mg/mL	2.87 ± 0.05	4.79 ± 0.02	<0.001

Data are expressed as *mean ± standard deviations*. Data were analyzed using independent t -test for comparing the parameters between study groups. GAE: gallic acid equivalent; DW: dried weight; QE: quercetin equivalent; DPPH: 2, 2-diphenyl-1-picrylhydrazyl.

2.3. Study Protocol. During the baseline visit, the subject's demographic information and medical history were obtained.

Body weight, height, body mass index (BMI), and blood pressure were assessed individually. Subjects fasted overnight for 10-12 h before venous blood collection. Fasting plasma glucose, serum lipid profile, oxidative stress status, inflammation parameters, and a key chemokine of atherosclerotic lesions were measured before received any treatments, 4-week, and 8-week of intervention. All subjects were asked not to change their dietary and physical activity patterns during the study period.

All subjects were asked not to change their dietary and physical activity patterns during the study period. To ensure the influence of dietary and physical activity patterns on this study, all subjects received a questionnaire about dietary behavior and physical activity patterns. The frequency and quantity of dietary including rice, meat, egg, milk, coconut curry, vegetable, fruits, and dessert at a recalling 7 days before visiting in represent energy intake. The frequency and duration of physical activity including strenuous activities, moderate sport, walking, and sitting at a recalling 7 days before visiting in represent physical activity.

2.4. Dietary Interventions. Subjects in the treatment and placebo group were given packs of 300 mL RP jelly drink and placebo jelly drink, respectively. Two products were isocaloric jelly drinks of 100 kcal. The 300 mL RP jelly drink for the treatment group was developed and supported by Expert Center of Innovative Health Food, Thailand Institute of Scientific and Technological Research, Thailand. RP jelly drink was prepared by using water, sweetener, gelling agent, flavoring agent, multivitamin, the roselle extract powder of 0.18%, and the freeze-dried passion fruit juice plus pulp of 0.37%.

Calyces of roselle (*Hibiscus sabdariffa*) were collected from Prachuap Khiri Khan, Thailand, by P. Chonpathompikunlert and authenticated by a taxonomist from the Plant Varieties Protection Office with identification as voucher specimen BK No. 071159 and deposited at the Forest Herbarium, Royal Forest Department, Ministry of Agriculture and Cooperatives, Bangkok, Thailand. Briefly, the roselle calyces were dried in hot air oven 50°C for 24 h. Dehydrated roselle calyces were ground into powder, then mixed with water 1 : 10% (w/v) ratio, followed by double extraction via maceration method. The aqueous extracts of roselle calyces were filtered (Whatman®, No. 1). The solvent was evaporated to concentrate using stirrer under heat 50°C for 6 h and kept in a freezer, then freeze-dried by the lyophilizer (Alpha 2-4 LSCplus freeze dryer, An der Unteren SÖse, Germany), and the powder was kept in a dark bottle at -20°C until used for RP jelly production. The percentage yield of roselle calyces aqueous extract was 44.53% (w/w) of the dry powder.

Freeze-dried passion fruit juice plus pulp was obtained from *Passiflora edulis* f. *flavicarpa* Deg. L. plants in Chiang Mai, Thailand, collected by P. Chonpathompikunlert, then authenticated by a taxonomist staff of plant varieties protection office with its identification as A voucher specimen BK No. 082283 and deposited at the Forest Herbarium, Royal Forest Department, Ministry of Agriculture and Cooperatives, Bangkok, Thailand. The purple passion fruit juice and pulp (4.5 kg) was blended, filtered 3 times, then freeze dried, and kept in a dark bottle at -20°C until used for RP jelly production. The percentage yield of the passion fruit juice and pulp was 12.12% (w/w) of the fresh juice and pulp.

Placebo was prepared by Expert Center of Innovative Health Food, Thailand Institute of Scientific and Technological Research, Thailand, in the same manner of RP jelly without the roselle extract powder and the freeze-dried passion fruit juice plus pulp.

Both RP jelly drink and placebo jelly drink were lyophilized using a Heto Powerdry PL9000 freeze dryer (Allerod, Denmark) at −80°C for 48 h for determination of total phenolic contents using the Folin–Ciocalteu reagent [19], flavonoid content according to spectrophotometric methods based on the formation of aluminium-flavonoid complexes [20], and antioxidant potential using the 2,2′-diphenyl-1-picrylhydrazyl (DPPH) radical scavenging method [21].

Data of total phenolic contents, flavonoid content, and antioxidant activity were presented as the mean of five separate experiments and error bars are displayed with standard error. In order to compare the difference in total phenolic contents, flavonoid contents, and antioxidant activity between RP jelly drink and placebo jelly drink, the statistical significance of the data was analyzed using an independent t -test. P value < 0.05 was considered as statistical significance, and the results are shown in Table 1.

In addition, they were identified and quantified the contents of gallic acid, quercetin, and ascorbic acid using high-performance liquid chromatography (HPLC) with Agilent Por shell 120 EC-C18, $4.6 \times 100\,mm$, $2.7\,\mu$m column (Agilent 1260 Infinity LC system, Waldbronn, Germany). The separation was performed using ternary linear elution gradient with 20 mM KH2PO4, 60% methanol, and 40%

acetonitrile at 284 nm. Standards were run in similar conditions of chromatography to match the retention items [22] and to calculate the quantification.

2.5. Blood Analysis. Whole blood samples were collected intravenously by a registered nurse into sodium fluoride containing tubes and clotted blood tubes. The separated plasma/serum determined the biochemical results including glucose, TG, TC, HDL-C, and LDL-C at Chiang Mai Medical Lab, Chiang Mai, Thailand. Another sample of whole blood was collected into an EDTA plasma tube for oxidative stress, antioxidant activity, inflammatory markers, and MCP-1, placed immediately on ice, and centrifuged within 30 min (3600 rpm for 10 minutes at 4°C) to separate plasma. Plasma then was stored at -80°C until analysis.

Oxidative stress was evaluated by lipid peroxidation level as thiobarbituric acid reactive substances (TBARS) method. Malondialdehyde (MDA) assay was adapted from the procedure previously described [23]. The plasma was prepared by mixing with 20% trichloroacetic acid (TCA) and incubated for 15 min at room temperature. The supernatant of mixed plasma was collected after centrifugation. Thiobarbituric acid (TBA) was added to supernatant sample in test tube before boiling at 100°C for 30 min for measuring lipid peroxidation. The MDA value was determined at wavelength of 530 nm and expressed in nmol/L.

Antioxidant activity was determined by glutathione (GSH) level according to the procedure previously described [24]. The assay of GSH with DTNB was performed by following the standard method of Ellman [25] and slightly modified method of Tipple and Rogers [24]. A 20 μL of sample was added into 96-well plate with 10 μL of solution of 10 mM NaH2PO4 and 1 mM dithiothreitol, 100 μL of 1 mM sodium azide dissolved 40 mM potassium phosphate buffer (pH 7.0), 10 μL of 50 mM glutathione, and 100 μL of 30% H2O2. Then, it was shaken for 10 minutes before adding 10 μL of 10 mM 5,5-dithiobis-2-nitrobenzoic acid (DTNB) and immediately measured for absorbance. Later, the GSH level in samples was calculated using A412 nm from standard curve of GSH concentration.

Inflammatory markers including IL-10, IL-6 and TNF-alpha were measured by enzyme-linked immunosorbent assay kit using paired antibodies. (Abcam®, Waltham, MA, USA, for IL-10 and Elabscience®, Houston, Texas, USA, for IL-6 and TNF-α).

A key chemokine of atherosclerotic lesion, MCP-1 expression, was also evaluated via enzyme linked immunosorbent assay kit (Elabscience®, Houston, Texas, USA).

2.6. Statistical Analysis

2.6.1. Sample Size. A total sample size of 40 subjects was estimated based on calculation of sample size by comparing two means according to sample size estimation in clinical trial [26] with a power of 80%, a significant level of 0.05, and dropout of 10%.

2.6.2. Data Analysis. A statistician was blinded to analyze the results of randomized participants who have received RP jelly drink and placebo treatment. Statistical analyses were being conducted by SPSS software version 22 (SPSS Inc., Chicago, IL, USA) for windows licensed, Chiang Mai University. The minimum level of statistical significance was set to $P < 0.05$.

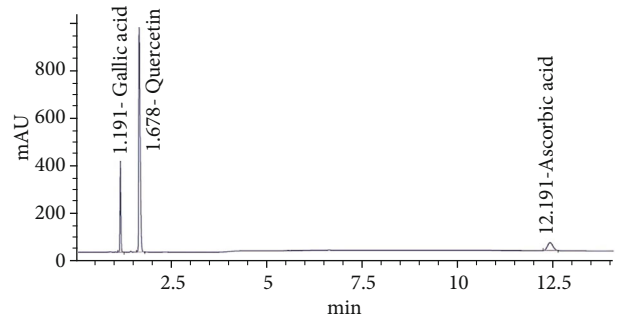

Figure 1: HPLC chromatogram of RP jelly drink for gallic acid, quercetin, and ascorbic acid.

The data of total phenolic compounds, flavonoid, and antioxidant activity were expressed as *means ± standard deviation* of at least three replicates. The difference when compared between RP jelly drink and placebo product was analyzed by independent *t*-test.

For continuous variables, we expressed data as *mean ± standard deviation* and coefficient of variation. Kolmogorov-Smirnov test was applied to ensure the normal distribution of variables, and nonnormally distributed data were log-transformed. Differences between the intervention and placebo groups were analyzed on an intention-to-treat (ITT) basis. Missing data was imputed following the last observation carried forward (LOCF) principle. We performed sensitivity analysis with per protocol (PP) principle in which the missing values were not imputed ($n = 20$ in placebo group, $n = 20$ in RP jelly drink group). The comparability of general characteristics of subjects at baseline was assessed by independent *t*-test. A repeated measure one-way ANOVA with a Greenhouse-Geisser correction and followed by the Bonferroni *post hoc* test in pairwise comparisons was performed to identify significant differences at different consumption (treatment) times and to analyze main effective differences between groups.

For quantitative data analysis, dietary intake and physical activity questionnaire were used for monitoring the subject's nutrition intake and energy expenditure. We expressed data as *mean ± standard deviation* in the range of a data set, and independent *t*-test was performed to analyze the significant difference of between groups.

3. Results

3.1. Bioactive Compounds and Antioxidant Activities of RP Jelly Drink. The chromatographic profiles of the RP jelly drink showed three types of the phytoconstituents, gallic acid, quercetin, and ascorbic acid (Figure 1). The retention time of gallic acid, quercetin, and ascorbic acid in RP jelly drink was found to be 1.191, 1.678, and 12.191, and it matched with standard retention time values, respectively. The amount of gallic acid, quercetin, and ascorbic acid in RP jelly drink was found to

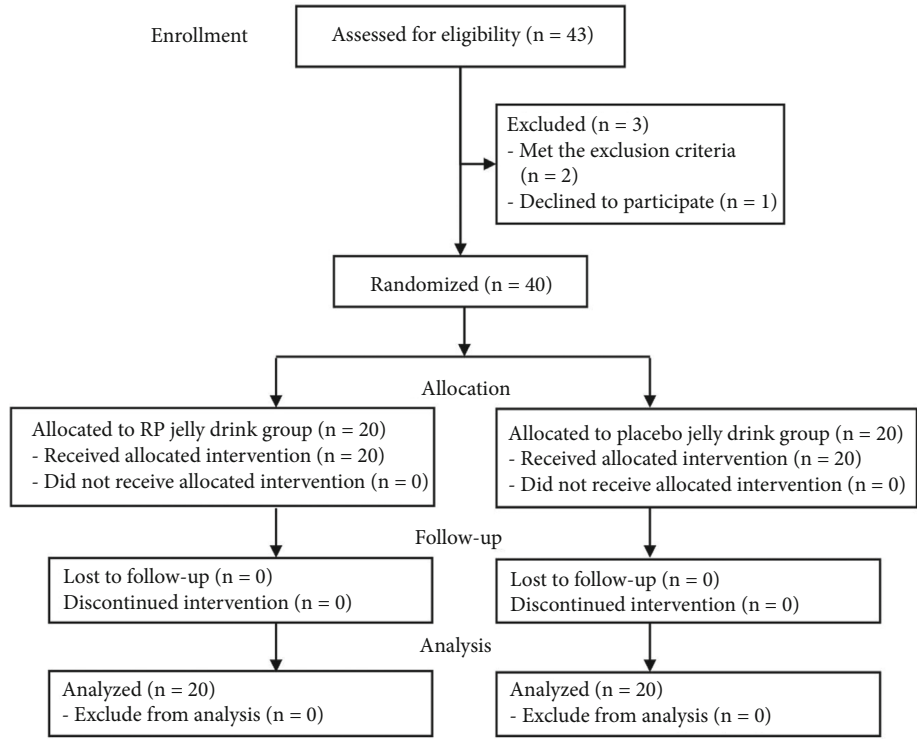

Figure 2: CONSORT flow diagram for the study.

Table 2: General characteristics of subjects participated in the study ($n = 40$).

Parameters	RP jelly drink ($n = 20$)	Placebo jelly drink ($n = 20$)	P value
AGE, years	37.00 ± 3.61	36 ± 6.14	0.469
BMI, kg/m^2	24.685 ± 4.35	24.145 ± 4.53	0.881
SBP, mmHg	119.58 ± 11.82	118.90 ± 3.47	0.875
DBP, mmHg	71.48 ± 2.01	69.43 ± 1.92	0.712
FPG, mg/dL	79.50 ± 13.76	78.28 ± 2.71	0.702
TC, mg/dL	203.76 ± 38.04	199.8 ± 35.12	0.731
TG, mg/dL	132.33 ± 75.11	130.73 ± 29.50	0.425
HDL-C, mg/dL	47.00 ± 14.40	49.70 ± 10.62	0.500
LDL-C, mg/dL	128.43 ± 32.74	126.75 ± 31.76	0.869

Data are expressed as mean ± standard deviations. Data were analyzed using independent t -test for comparing the parameters between study groups. BMI: body mass index; SBP: systolic blood pressure; DBP: diastolic blood pressure; FPG: fasting plasma glucose; TC: total cholesterol; TG: triglyceride; HDL-C: high-density lipoprotein cholesterol; LDL-C: low-density lipoprotein cholesterol.

be $0.001 \pm 0.000\,\mu g/mg$, $0.02 \pm 0.000\,\mu g/mg$, and $0.0006 \pm 0.000\,\mu g/mg$. Total phenolic compounds, flavonoid contents, and antioxidant activity of the RP jelly drink are shown in Table 1. The data showed that total phenolic contents and flavonoid contents and antioxidant activity by DPPH radical scavenging of RP jelly drink were $1.97 \pm 0.03\,mg$ GAE/g DW and $1.79 \pm 0.20\,mg$ QE/g DW, respectively. Antioxidant activity by DPPH radical scavenging shown in IC_{50} value was $2.87 \pm 0.05\,mg/mL$ jelly drink.

3.2. General Characteristics of Subjects. A total of 43 subjects were enrolled in the study as shown in Figure 2. Two subjects met the exclusion criteria, and one subject declined to participate the study. Finally, 40 subjects (20 RP jelly drink; 20 placebo jelly drink) were included, and no withdrawal events were observed. Subjects were 15 women and 5 men in RP jelly group and 14 women and 6 men in placebo jelly drink group. General characteristics of subjects participated in the study are summarized in Table 2.

3.3. Effect of Jelly Drinks on Lipid Profiles, Inflammatory Markers, and Other Parameters. Effects of jelly drinks on lipid profiles, inflammatory markers, and other parameters within each group at different times are shown in Table 3. After a 4-week consumption period, the subjects who consumed RP jelly drinks showed a significant reduction in LDL-C ($P < 0.05$) and an enhancement of HDL-C ($P < 0.05$). Noticeably, LDL-C and TG were significantly reduced after 8 weeks of RP jelly drink consumption (16% and 17%, respectively), while LDL-C was unchanged, and it was likely that TG increased over the time of the placebo group. However, after 4 and 8 weeks of intervention, no differences were found in BMI, blood pressure, fasting plasma glucose, and TC in each study group (Table 3).

After consuming the RP jelly drink, plasma MDA was significantly lower ($P < 0.001$) at the time of the intervention and noticed a significant difference compared to the placebo group. With respect to antioxidant enzymes, subjects who

Table 3: Lipid profiles, inflammatory markers, and other parameters of the subjects within each group at different times and between groups.

Parameters	RP jelly drink ($n = 20$)			P value within group	Placebo jelly drink ($n = 20$)			P value within group	P value between group
	Baseline (CV%)	4 weeks (CV%)	8 weeks (CV%)		Baseline (CV%)	4 weeks (CV%)	8 weeks (CV%)		
BMI, kg/m^2	24.685 ± 4.35 (17.62)	24.42 ± 4.84 (19.82)	24.34 ± 3.82 (15.69)	0.895	24.145 ± 4.53 (18.02)	24.9 ± 4.27 (17.15)	24.81 ± 4.34 (17.49)	0.832	0.950
SBP, mmHg	119.58 ± 11.82 (9.89)	116.25 ± 17.57 (15.11)	112.21 ± 31.09 (27.97)	0.543	118.90 ± 3.47 (2.92)	110.00 ± 28.38 (21.25)	115.95 ± 16.55 (14.27)	0.230	0.945
DBP, mmHg	71.48 ± 2.01 (2.81)	78.55 ± 15.34 (19.53)	79.89 ± 15.89 (19.89)	0.818	69.43 ± 1.92 (2.77)	76.35 ± 8.40 (11.00)	77.84 ± 12.29 (15.79)	0.234	0.464
FPG, mg/dL	79.50 ± 13.76 (17.35)	82.25 ± 18.52 (22.52)	81.58 ± 15.12 (14.11)	0.094	78.28 ± 2.71 (3.46)	79.15 ± 11.91 (15.05)	80.68 ± 17.08 (21.17)	0.506	0.357
TC, mg/dL	203.76 ± 38.04 (18.67)	198.35 ± 35.59 (17.94)	192.79 ± 27.08 (14.05)	0.727	199.8 ± 35.12 (17.57)	214.62 ± 39.12 (18.23)	201.95 ± 43.54 (21.56)	0.214	0.530
TG, mg/dL	132.33 ± 75.11 (56.76)	142.55 ± 54.00 (37.88)	109.79 ± 38.83^{a} (36.28)	0.020*	130.73 ± 29.50 (22.57)	164.95 ± 41.85^{a} (25.37)	145.84 ± 48.90 (33.53)	0.775	0.016*
HDL-C, mg/dL	47.00 ± 14.40 (30.64)	55.81 ± 10.35^{a} (18.55)	51.29 ± 10.52 (20.51)	0.014*	49.70 ± 10.62 (21.37)	51.70 ± 11.45 (22.15)	51.11 ± 11.24 (21.99)	0.447	0.780
LDL-C, mg/dL	128.43 ± 32.74 (25.49)	107.47 ± 20.87^{aa} (19.42)	107.63 ± 22.98^{aa} (21.35)	0.0.29*	126.75 ± 31.76 (25.06)	133.39 ± 31.49 (23.61)	128.11 ± 34.56 (26.98)	0.766	0.018*
MDA, nmol/mL	0.516 ± 0.032 (6.20)	0.415 ± 0.010^{a} (2.41)	0.471 ± 0.024 (5.10)	0.001***	0.524 ± 0.042 (8.02)	0.512 ± 0.016 (3.13)	0.553 ± 0.021 (3.80)	0.493	0.032
GSH, μg/mL	0.554 ± 0.084 (15.16)	1.024 ± 0.141^{a} (13.77)	1.09 ± 0.148^{a} (14.52)	0.091	0.577 ± 0.072 (12.48)	0.607 ± 0.048 (7.91)	0.428 ± 0.053 (12.38)	0.518	0.020*
TNF-α, pg/mL	14.75 ± 1.97 (13.36)	12.47 ± 1.89 (15.16)	6.06 ± 0.34^{a} (5.61)	0.025*	13.68 ± 2.18 (15.94)	14.05 ± 1.92 (13.67)	11.19 ± 1.15 (10.28)	0.586	0.026
IL-6, pg/mL	1.02 ± 0.10 (9.80)	1.04 ± 0.05 (18.29)	1.05 ± 0.09 (8.57)	0.810	0.95 ± 0.06 (6.32)	1.04 ± 0.13 (12.50)	1.05 ± 0.06^{a} (15.70)	0.003**	0.096
IL-10, pg/mL	5.62 ± 0.96 (17.08)	6.07 ± 1.11 (13.77)	7.07 ± 1.04 (14.71)	0.516	5.34 ± 0.73 (13.67)	6.06 ± 1.61 (26.57)	7.09 ± 0.95 (13.40)	0.638	0.854
MCPL-1, pg/mL	7.77 ± 0.70 (9.91)	8.51 ± 0.38 (4.46)	7.14 ± 0.72 (10.08)	0.193	7.38 ± 0.34 (4.61)	9.43 ± 0.28 (2.97)	7.65 ± 0.72 (9.41)	0.585	0.673

Data expressed as *mean ± standard deviations* and the coefficient of variation percent (CV%). Data were analyzed using repeated-measured ANOVA for comparing the changes over time within and between study groups. [a] indicates the significant differences within each group at different times when compared to baseline (P value <0.05). BMI: body mass index; SBP: systolic blood pressure; DBP: diastolic blood pressure; FPG: fasting plasma glucose; TC: total cholesterol; TG: triglyceride; HDL-C: high-density lipoprotein cholesterol; LDL-C: low-density lipoprotein cholesterol; MDA: malondialdehyde; GSH: glutathione reduced; IL: interleukin; TNF-α: tumor necrosis factor alpha; MCP-1: monocyte chemoattractant protein-1.

Table 4: Frequency and quantity of dietary items including rice, meat, eggs, milk, coconut-based curry, vegetable, fruits, and dessert at as recalled for 7 days prior to visit (baseline, 4 weeks, and 8 weeks).

Dietary		Treatment group	Baseline	*P* value	4 weeks	*P* value	8 weeks	*P* value
Rice	Frequency (score)	Placebo	5.65 ± 0.11	0.230	5.76 ± 0.10	0.617	5.76 ± 0.11	0.284
		RP jelly drink	5.48 ± 0.10		5.84 ± 0.15		5.44 ± 0.20	
	Quantity (score)	Placebo	2.64 ± 0.14	0.302	2.63 ± 0.13	0.248	2.65 ± 0.13	0.610
		RP jelly drink	2.40 ± 0.13		2.36 ± 0.14		2.36 ± 0.13	
Meat	Frequency (score)	Placebo	4.76 ± 0.23	0.559	4.76 ± 0.27	0.403	5.18 ± 0.23	0.930
		RP jelly drink	4.84 ± 0.25		4.92 ± 0.32		5.20 ± 0.19	
	Quantity (score)	Placebo	1.76 ± 0.14	0.922	1.64 ± 0.13	0.852	1.80 ± 0.12	0.707
		RP jelly drink	1.80 ± 0.13		1.76 ± 0.14		1.68 ± 0.13	
Egg	Frequency (score)	Placebo	3.36 ± 0.32	0.683	2.96 ± 0.35	0.527	2.92 ± 0.31	0.579
		RP jelly drink	3.20 ± 0.34		2.86 ± 0.35		2.88 ± 0.21	
	Quantity (score)	Placebo	2.36 ± 0.14	0.566	2.24 ± 0.19	0.693	2.16 ± 0.16	0.438
		RP jelly drink	2.60 ± 0.12		2.44 ± 0.14		2.48 ± 0.13	
Milk	Frequency (score)	Placebo	3.84 ± 0.34	0.907	3.52 ± 0.33	0.936	3.28 ± 0.33	0.898
		RP jelly drink	3.72 ± 0.36		3.22 ± 0.40		3.10 ± 0.24	
	Quantity (score)	Placebo	2.20 ± 0.13	0.895	1.92 ± 0.16	0.687	1.88 ± 0.12	0.895
		RP jelly drink	2.32 ± 0.16		1.92 ± 0.17		2.16 ± 0.11	
Coconut curry	Frequency (score)	Placebo	1.96 ± 0.38	0.149	1.94 ± 0.43	0.836	1.92 ± 0.36	0.535
		RP jelly drink	1.84 ± 0.36		1.88 ± 0.40		1.88 ± 0.38	
	Quantity (score)	Placebo	1.22 ± 0.20	0.139	1.16 ± 0.21	0.994	1.00 ± 0.17	0.885
		RP jelly drink	1.64 ± 0.14		1.16 ± 0.21		1.04 ± 0.18	
Vegetable	Frequency (score)	Placebo	4.44 ± 0.36	0.741	5.08 ± 0.29	0.148	4.88 ± 0.32	0.615
		RP jelly drink	5.04 ± 0.20		5.24 ± 0.19		4.84 ± 0.19	
	Quantity (score)	Placebo	1.84 ± 0.14	0.230	1.88 ± 0.13	0.627	1.80 ± 0.13	0.193
		RP jelly drink	2.24 ± 0.16		1.96 ± 0.15		1.88 ± 0.12	
Fruits	Frequency (score)	Placebo	3.46 ± 0.37	0.695	3.84 ± 0.30	0.920	3.84 ± 0.25	0.935
		RP jelly drink	3.42 ± 0.34		3.80 ± 0.33		3.88 ± 0.25	
	Quantity (score)	Placebo	1.78 ± 0.18	0.870	1.80 ± 0.10	0.334	1.80 ± 0.13	0.783
		RP jelly drink	1.76 ± 0.21		2.08 ± 0.15		1.84 ± 0.11	
Dessert	Frequency (score)	Placebo	1.38 ± 0.35		1.08 ± 0.37	0.696	1.84 ± 0.35	0.911
		RP jelly drink	1.76 ± 0.39	0.279	1.00 ± 0.41		1.04 ± 0.36	
	Quantity (score)	Placebo	1.36 ± 0.15		1.56 ± 0.18	0.450	1.48 ± 0.14	0.580
		RP jelly drink	1.24 ± 0.14	0.219	1.48 ± 0.15		1.40 ± 0.15	

P value is a statistical measurement value used to represent the difference between groups by independent *t*-test. Data were expressed as *mean* ± *SD* in the range of a data set. Frequency scores were calculated from a ranking of 0 = not consume, 1 = 1-2 times a week, 2 = 3-4 times a week, 3 = 5-6 times a week, 4 = 1 time a day, 5 = 2 times a day, 6 = 3 times a day, and 7 = more than 3 times a day. Quantity score was calculated from a ranking of 1 = less than a half rice plate, 2 = a half plate to 1 plate, 3 = 1 and a half plate, and 4 = more than 1 and a half plate.

drank the RP jelly products showed significantly higher plasma GSH levels at the 4 weeks and 8 weeks of the study period compared to baseline measurements. This change was seen only in the RP jelly drink group than in the placebo group.

Inflammatory cytokines, including IL-6, TNF-α, and IL-10, which may contribute to the acceleration of abnormal lipid metabolism, have also been evaluated. Results revealed that those who consumed the RP jelly drink had a significant reduction in TNF-α levels at 8 weeks of the study duration ($P < 0.05$). No significant changes in IL-6, IL-10, and MCP-1 levels were observed after consuming the RP jelly drink.

Energy intake and physical activity did not change over time or between groups during the study period (Tables 4 and 5).

4. Discussion

In this randomized, double-blind controlled trial, consuming a jelly drink containing polyphenol-rich roselle extract

Table 5: The frequency and duration of physical activity including strenuous activities, moderate sport, walking, and sitting as recalled for 7 days prior to visit (baseline, 4 weeks, and 8 weeks).

Activities		Treatment group	Baseline	*P* value	4 weeks	*P* value	8 weeks	*P* value
Strenuous activities	Frequency	Placebo	3.40 ± 0.30	0.707	3.16 ± 0.36	0.943	3.44 ± 0.35	0.974
		RP jelly drink	3.35 ± 0.36		3.28 ± 0.33		3.28 ± 0.33	
	Duration	Placebo	1.64 ± 0.43	0.880	2.48 ± 0.35	0.799	2.28 ± 0.34	0.981
		RP jelly drink	1.83 ± 0.27		2.68 ± 0.42		2.24 ± 0.36	
Moderate sport	Frequency	Placebo	1.64 ± 0.36	0.957	3.56 ± 0.32	0.088	3.60 ± 0.34	0.432
		RP jelly drink	4.00 ± 0.31		3.80 ± 0.34		3.32 ± 0.33	
	Duration	Placebo	1.40 ± 0.28	0.534	1.92 ± 0.23	0.265	1.64 ± 0.18	0975
		RP jelly drink	1.58 ± 0.18		1.76 ± 0.20		1.68 ± 0.19	
Walking	Frequency	Placebo	6.88 ± 0.12	0.738	6.92 ± 0.08	0.957	6.88 ± 0.12	0.794
		RP jelly drink	6.56 ± 0.23		6.96 ± 0.04		6.92 ± 0.08	
	Duration	Placebo	2.20 ± 0.39	0.391	2.28 ± 0.34	0.562	1.76 ± 0.19	0.445
		RP jelly drink	2.33 ± 0.39		1.68 ± 0.20		1.88 ± 0.22	
Sitting	Frequency	Placebo	6.52 ± 0.16	0.568	6.80 ± 0.14	0.316	6.88 ± 0.12	0.770
		RP jelly drink	6.56 ± 0.22		6.96 ± 0.04		6.92 ± 0.08	
	Duration	Placebo	4.36 ± 0.46	0.468	3.60 ± 0.39	0.676	3.12 ± 0.28	0.585
		RP jelly drink	3.25 ± 0.39		3.00 ± 0.37		2.76 ± 0.27	

P value is a statistical measurement value used to represent the difference between groups by independent *t* -test. Data were expressed as mean ± SD in the range of a data set. Frequency scores were calculated from a ranking of 0 = not activity, 1 = 1-2 times a week, 2 = 3-4 times a week, 3 = 5-6 times a week, 4 = 1 time a day, 5 = 2 times a day, 6 = 3 times a day, and 7 = more than 3 times a day. Quantity score of quantity was calculated from ranking of 0 = not activity, 1 = 1-10 minutes, 2 = 10-20 minutes, 3 = 20-30 minutes, 4 = 30-40 minutes, 5 = 40-50 minutes, 6 = 50-60 minutes, and 7 = more than 1 hour.

and passion fruit juice plus pulp concentrate (RP jelly drink) once daily for 8 weeks, clearly demonstrated a significant reduction in LDL-C and TG levels when compared to either baseline measurements or jelly drink placebo in Thai adults with dyslipidemia, whereas the changes in fasting plasma glucose, total cholesterol, HDL-C, MCP-1, interleukin-6, and interleukin-10 indicated no significant difference between the RP jelly drink and the placebo group. Furthermore, we also found lower inflammatory markers and improved oxidative stress, which were seen in the reduction of tumor necrosis factor- (TNF-) α and malondialdehyde (MDA), and the enhancement of glutathione (GSH) after the ingestion of the RP jelly drink for 8 weeks. This investigation emphasized the impact of a polyphenol-rich product supplementation on the beneficial effect of lowering blood lipids resulting in a protective effect against atherosclerosis that might help to primary prevention of cardiovascular disease.

Numerous observational studies indicated that polyphenol-rich foods were strongly associated with a lower incidence of cardiovascular diseases, metabolic syndrome, and diabetes [27–29]. Consistency with knowledge that Passion fruit and roselle calyces have been well-documented to improve serum HDL-C and reduce LDL-C levels [30–32]. This might be associated with the presence of quercetin and gallic acid [33–35] in RP jelly drink consumption. Additionally, a recent meta-analysis study of 34 randomized controlled trials reported that consuming polyphenol-containing supplements significantly improved blood lipid levels (LDL-C: -4.39 mg/dL, $P = 0.009$; HDL-C: 2.68 mg/dL, $P < 0.001$) in comparison with the placebo group [36]. This observation may be related to lipoprotein metabolism by increasing fecal cholesterol elimination and impeding apolipoprotein production [36] or enhancement of the cholesterol efflux capacity [37]. Another possible mechanism may be involved with the effect of intestinal microbiota on lipid homeostasis by increasing polyphenol bioavailability and promoting polyphenol metabolites production, which includes bile acids, lactic acids, and short-chain fatty acids [38, 39]. These studies support that polyphenol-containing products may benefit people with high cholesterol levels or those at risk of heart diseases.

It has been suggested that the polyphenols, anthocyanins, and other bioactive compounds found in roselle calyces (*Hibiscus sabdariffa*) may contribute to lipid-lowering and inhibition of LDL-C oxidation through its antioxidant activity or other mechanisms [40]. A human trial conducted by Lin et al. [41] revealed that taking one or two capsules of roselle extract reduced TC by 11-15% after 4 weeks of supplementation; however, there were no reports for LDL-C, HDL-C, and TG. In a recent meta-analysis of 9 clinical trials, the efficacy of roselle supplementation in regulating cholesterol levels in patients with metabolic syndrome and related diseases showed a reduction in total cholesterol, LDL-C, and HDL-C but not TG [42]. In our study, daily consumption of an RP jelly drink containing polyphenol-rich roselle extract for 8 weeks tends to have a positive effect on the changes in LDL-C, TG, TC, and HDL-C, levels as time passed; nevertheless, no significant differences were found in TC and HDL-C between study

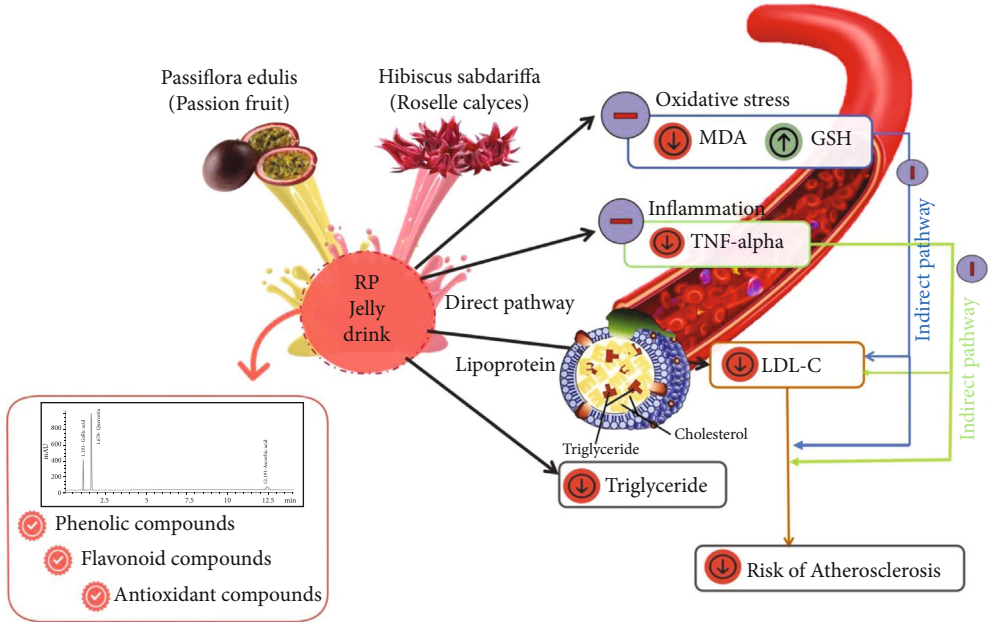

Figure 3: The framework of potential components in RP jelly drink.

groups. Our results were consistent with a meta-analysis studied by Aziz et al. [43], when we focused on the pooled results of two placebo-controlled studies [44, 45]. Nonetheless, this meta-analysis concluded that the limited evidence from clinical studies cannot support the effect of *Hibiscus sabdariffa* on blood lipids.

For passion fruit, an animal study performed by Souza et al. 2012 [30] revealed that the treatment group that received concentrated passion fruit juice twice daily for 28 days had better antioxidant activity and lipid profiles compared to the control group. Similar to another study, passion fruit juice was be able to improve lipid and blood glucose levels in offspring from diabetic and nondiabetic mothers of Wistar rats [46]. These effects may be attributed to the presence of flavonoids, consequently showing antioxidant and anti-inflammatory properties derived from passion fruit juice. Interestingly, several *in vivo* studies have shown that flavonoids have a strong inhibitory effect on 3-hydroxy 3-methylglutaryl coenzyme A (HMG-CoA) reductase and increased activity of lecithin cholesterol acyltransferase (LCAT); thereby, changes in blood lipid levels were observed [47, 48]. It might be one of the explanations why RP jelly drink, which combined passion fruit juice and roselle calyces, demonstrated a significant reduction in LDL-C and TG levels. However, the efficacy of *Passiflora edulis* juice alone has not been investigated in human clinical studies.

Oxidative stress has been associated with many pathologies especially cardiovascular disease. The balance between reactive oxygen species (ROS) and antioxidants are important to prevent the pathological progression [49]. With regard to the reduction of malondialdehyde (MDA) and the enhancement of glutathione (GSH), the present findings supported that consuming RP jelly drinks can improve oxidative stress in the body. It is well-known that polyphenols play an important role in inhibiting oxidative stress and are also connected to anti-inflammatory effects in order to remain cellular homeostasis [50]. Oxidative stress and inflammation are not only related to dyslipidemia but also contribute to the onset and progression of atherosclerosis [51]. As we have known that TNF-α can trigger the cytokine cascade and contribute to regulate the production of another inflammatory cytokine [52, 53]. Remarkably, the abnormality of TNF-α level and signaling cause the development of disease, such as rheumatoid arthritis, psoriasis, Crohn's disease, atherosclerosis, and cancer [53]. In our study, plasma tumor necrosis factor- (TNF-) α was decreased after the ingestion of the RP jelly drink for 8 weeks. This observation may be explained by the natural active ingredients presented in RP jelly drinks exert anti-inflammatory effects through multitargeted action in the inflammatory pathway [54]. Consistent with the study of Herranz-Lopez et al. (2017), the effects of *Hibiscus sabdariffa*-derived polyphenols on specific cellular pathways have been reviewed, particularly in pathways associated with chronic inflammation and energy metabolism [55]. A metabolomics and gene-expression study has demonstrated that *Hibiscus sabdariffa* polyphenols can downregulate genes involved in cholesterol and TG synthesis and exert a multitarget lipid-lowering effect [56]. In addition, it has been proposed that TNF-α itself can suppress free fatty acid uptake, inhibit the activity of enzymes involved in lipid metabolism, and regulate cholesterol metabolism [57]. Moreover, Passion fruit has been evaluated to have anti-inflammatory activity by reducing the level of proinflammatory IL-1β and TNF-α in an *in vivo* study [58, 59] and decrease IL-17A in human [32]. This could be attributed to the presence of bioactive compounds like C-glycosyl flavonoids vicenin, orientin, isoorientin, vitexin, and isovitexin [59]. Therefore, the reductions in TNF-α, LDL-C, and TG as seen in our study appeared to be consistent.

This study has some strengths. First, the double-blind, placebo-controlled study was conducted with the subjects with no differences in baseline general characteristics between groups. Participants in this study did not require a wash-out period between placebo and treatment as a cross-over design, resulting in no dropping out from the trial. Second, two kinds of jelly drinks (RP jelly drink and placebo) were prepared with isocaloric and iso-macronutrients (carbohydrates, proteins, and fats) in the same format. Roselle extract powder and the dried passion fruit juice with pulp are used only in RP jelly drink which is different from placebo; hence, we can ensure the effectiveness of the intervention provided in the lipid-lowering function. Nevertheless, there are limitations. First of all, due to the study not being conducted in an inpatient setting, the participants' diet and physical activity could not be rigorously controlled during the study period. Natural polyphenols or other bioactive substances presented in common diets may interfere with our study. However, we asked participants to refrain from changing their diet and exercise patterns throughout the 8-week study. Secondly, the long-term effects of RP jelly drink supplementation on lipid-lowering and other relevant clinical endpoints should be performed. Thirdly, several factors including short duration of the study, a lack of consideration of sex-related effects, homogenous ethnic background, and the relatively small study numbers might associate with the lipid-lowering effect. Therefore, any direct cause-effect relationships or precise mechanisms including reduced lipid content of 3-hydroxyl-3-methylglutaryl coenzyme A reductase (HMGCR) activity and sterol regulatory element binding protein-2 (SREBP2) also require further investigation.

5. Conclusion

Our findings indicated that once-daily consumption of RP jelly drink for eight weeks improved blood lipid profiles compared to placebo among Thai adults with dyslipidemia in uncontrolled nutrition intake. The possible underlying mechanism of improved blood lipid levels is unclear. However, it can be concluded that a RP jelly drink product, which contains large amounts of phytoconstituents (quercetin, gallic, and ascorbic acid), total phenolic, and flavonoid compound exhibiting antioxidant activities could represent another polyphenol-rich food product with antioxidant and anti-inflammatory effects, which in turn may indirectly enhance lowering blood lipid levels resulting in decreased risk of the initiation of atherosclerosis (Figure 3). Further study of the nutritional qualities of RP jelly drink and the mechanisms underlying its action in reducing lipids in the body should be performed to evaluate its potential role in the prevention of cardiovascular disease.

Data Availability

All data supporting the conclusions of this work were included within the article. Further inquiries can be directed to the corresponding authors.

Consent

Written informed consent of participates has been obtained for this study. All listed authors consent to the submission, and all data are used with the consent of the authors.

Conflicts of Interest

The authors declare no conflict of interest.

Authors' Contributions

Jurairat Khongrum and Pennapa Chonpathompikunlert designed the study. Jurairat Khongrum, Pratoomporn Yingthongchai, Kongsak Boonyapranai, Wachira Wongtanasarasin, Nowwapan Donrung, and Pennapa Chonpathompikunlert performed experiments. Jurairat Khongrum analyzed the data. Jurairat Khongrum and Pennapa Chonpathompikunlert drafted the manuscript. Jurairat Khongrum, Pennapa Chonpathompikunlert, Wanida Sukketsiri, and Aree Prachansuwan edited and revised the manuscript. All authors have read and approved the final submitted manuscript.

Acknowledgments

We thank all the participants of this study for full cooperation. This work was supported by the Expert Center of Innovative Health Food, Thailand Institute of Scientific and Technological Research, Thailand; Science and Technology Research Institute, Chiang Mai University; and Functional Food Research Center for Well-Being, Chiang Mai University, and partially supported by the Chiang Mai University.

References

[1] C. P. Cannon, "Cardiovascular disease and modifiable cardiometabolic risk factors," *Clinical Cornerstone*, vol. 8, no. 3, pp. 11–28, 2007.

[2] S. Koba and T. Hirano, "Dyslipidemia and atherosclerosis," *Japanese Journal of Clinical Medicine*, vol. 69, no. 1, pp. 138–143, 2011.

[3] K. M. Huffman, V. H. Hawk, S. T. Henes et al., "Exercise effects on lipids in persons with varying dietary patterns–does diet matter if they exercise? Responses in studies of a targeted risk reduction Intervention through defined exercise I," *American Heart Journal*, vol. 164, no. 1, pp. 117–124, 2012.

[4] N. D. Vaziri, "Role of dyslipidemia in impairment of energy metabolism, oxidative stress, inflammation and cardiovascular disease in chronic kidney disease," *Clinical and Experimental Nephrology*, vol. 18, no. 2, pp. 265–268, 2014.

[5] M. H. Kim and W. S. Choi, "The association between subclinical inflammation and abnormal glucose and lipid metabolisms in normal-weight Korean individuals," *Nutrition, Metabolism and Cardiovascular Diseases*, vol. 28, no. 11, pp. 1106–1113, 2018.

[6] P. Moriel, F. L. Plavnik, M. T. Zanella, M. C. Bertolami, and D. S. Abdalla, "Lipid peroxidation and antioxidants in hyperlipidemia and hypertension," *Biological Research*, vol. 33, no. 2, pp. 105–112, 2000.

[7] N. H. Al-Rawi, "Oxidative stress, antioxidant status and lipid profile in the saliva of type 2 diabetics," *Diabetes and Vascular Disease Research*, vol. 8, no. 1, pp. 22–28, 2011.

[8] G. Teto, G. D. Kanmogne, J. N. Torimiro et al., "Lipid peroxidation and total cholesterol in HAART-naïve patients infected with circulating recombinant forms of human immunodeficiency virus type-1 in Cameroon," *The Public Library of Science*, vol. 8, no. 6, article e65126, 2013.

[9] R. J. Torres, A. Luchini, L. Y. Barberini et al., "Expression of TNF-α and IL-6 cytokines in the choroid and sclera of hypercholesterolemic rabbits," *Arquivos Brasileiros de Oftalmologia*, vol. 77, no. 3, pp. 168–172, 2014.

[10] A. G. Moraitis, L. A. Freeman, R. D. Shamburek et al., "Elevated interleukin-10: a new cause of dyslipidemia leading to severe HDL deficiency," *Journal of Clinical Lipidology*, vol. 9, no. 1, pp. 81–90, 2015.

[11] P. Wiesner, M. Tafelmeier, D. Chittka et al., "MCP-1 binds to oxidized LDL and is carried by lipoprotein(a) in human plasma," *Journal of Lipid Research*, vol. 54, no. 7, pp. 1877–1883, 2013.

[12] M. Gobert, D. Rémond, M. Loonis, C. Buffière, V. Sante-Lhoutellier, and C. Dufour, "Fruits, vegetables and their polyphenols protect dietary lipids from oxidation during gastric digestion," *Food and Function*, vol. 5, no. 9, pp. 2166–2174, 2014.

[13] A. A. Tareke and A. A. Hadgu, "The effect of vitamin C supplementation on lipid profile of type 2 diabetic patients: a systematic review and meta-analysis of clinical trials," *Diabetology and Metabolic Syndrome.*, vol. 13, no. 1, pp. 1–7, 2021.

[14] X. He, F. Luan, Y. Yang et al., "Passiflora edulis: an insight into current researches on phytochemistry and pharmacology," *Frontiers in Pharmacology*, vol. 11, p. 617, 2020.

[15] K. B. Pandey and S. I. Rizvi, "Plant polyphenols as dietary antioxidants in human health and disease," *Oxidative Medicine and Cellular Longevity*, vol. 2, no. 5, Article ID 897484, 2009.

[16] P. Singh, M. Khan, and H. Hailemariam, "Nutritional and health importance of Hibiscus sabdariffa: a review and indication for research needs," *Journal of Nutritional Health and Food Engineering*, vol. 6, no. 5, pp. 125–128, 2017.

[17] C. C. Chen, J. D. Hsu, S. F. Wang et al., "Hibiscus sabdariffa extract inhibits the development of atherosclerosis in cholesterol-fed rabbits," *Journal of Agricultural and Food Chemistry*, vol. 51, no. 18, pp. 5472–5477, 2003.

[18] P. B. Pertuzatti, M. Sganzerla, A. C. Jacques, M. T. Barcia, and R. C. Zambiazi, "Carotenoids, tocopherols and ascorbic acid content in yellow passion fruit (_Passiflora edulis)_ grown under different cultivation systems," *LWT-Food Science and Technology*, vol. 64, no. 1, pp. 259–263, 2015.

[19] H. Noreen, N. Semmar, M. Farman, and J. S. McCullagh, "Measurement of total phenolic content and antioxidant activity of aerial parts of medicinal plant _Coronopus didymus_," *Asian Pacific Journal of Tropical Medicine*, vol. 10, no. 8, pp. 792–801, 2017.

[20] A. Pękal and K. Pyrzynska, "Evaluation of aluminium complexation reaction for flavonoid content assay," *Food Analytical Methods*, vol. 7, no. 9, pp. 1776–1782, 2014.

[21] R. Scherer and H. T. Godoy, "Antioxidant activity index (AAI) by the 2,2-diphenyl-1-picrylhydrazyl method," *Food Chemistry*, vol. 112, no. 3, pp. 654–658, 2009.

[22] G. Shui and L. P. Leong, "Separation and determination of organic acids and phenolic compounds in fruit juices and drinks by high-performance liquid chromatography," *Journal of Chromatography*, vol. 977, no. 1, pp. 89–96, 2002.

[23] Y. Bhutia, A. Ghosh, M. L. Sherpa, R. Pal, and P. K. Mohanta, "Serum malondialdehyde level: surrogate stress marker in the Sikkimese diabetics," *Journal of Natural Science, Biology, and Medicine*, vol. 2, no. 1, pp. 107–112, 2011.

[24] T. E. Tipple and L. K. Rogers, "Methods for the determination of plasma or tissue glutathione levels," *Methods in Molecular Biology*, vol. 889, pp. 315–324, 2012.

[25] G. L. Ellman, "Tissue sulfhydryl groups," *Archives of Biochemistry and Biophysics*, vol. 82, no. 1, pp. 70–77, 1959.

[26] D. Messina, C. Soto, A. Mendez et al., "Lipid-lowering effect of mate tea intake in dyslipidemic subjects," *Nutricion Hospitalaria*, vol. 31, no. 5, pp. 2131–2139, 2015.

[27] G. Grosso, U. Stepaniak, A. Micek, D. Stefler, M. Bobak, and A. Pajak, "Dietary polyphenols are inversely associated with metabolic syndrome in Polish adults of the HAPIEE study," *European Journal of Nutrition*, vol. 56, no. 4, pp. 1409–1420, 2017.

[28] M. Lajous, E. Rossignol, G. Fagherazzi et al., "Flavonoid intake and incident hypertension in women," *The American Journal of Clinical Nutrition*, vol. 103, no. 4, pp. 1091–1098, 2016.

[29] A. Tresserra-Rimbau, M. Guasch-Ferré, J. Salas-Salvadó et al., "Intake of total polyphenols and some classes of polyphenols is inversely associated with diabetes in elderly people at high cardiovascular disease risk," *The Journal of Nutrition*, vol. 146, no. 4, pp. 767–777, 2015.

[30] S. S. Maricelma, S. M. Barbalho, D. C. Damasceno et al., "Effects of Passiflora edulis (yellow passion) on serum lipids and oxidative stress status of Wistar rats," *Journal of Medicinal Food*, vol. 15, no. 1, pp. 78–82, 2012.

[31] A. Diantini, S. Rahmat, A. Alpiani, S. A. Sumiwi, L. Lubis, and J. Levita, "Effect of the roselle (Hibiscus sabdariffa L.) calyces drink on the physiological parameters of healthy adult subjects," *Biomedical Reports*, vol. 15, no. 5, p. 89, 2021.

[32] I. A. E. Duarte, D. Milenkovic, T. K. D. S. Borges et al., "Acute effects of the consumption of Passiflora setacea juice on metabolic risk factors and gene expression profile in humans," *Nutrients*, vol. 12, no. 4, p. 1104, 2020.

[33] J. Chao, T. I. Huo, H. Y. Cheng et al., "Gallic acid ameliorated impaired glucose and lipid homeostasis in high fat diet-induced NAFLD mice," *PLoS ONE*, vol. 9, no. 6, article e96969, 2014.

[34] S. Egert, C. Boesch-Saadatmandi, S. Wolffram, G. Rimbach, and M. J. Müller, "Serum lipid and blood pressure responses to quercetin vary in overweight patients by apolipoprotein E genotype," *The Journal of Nutrition*, vol. 140, no. 2, pp. 278–284, 2010.

[35] E. Talirevic and S. Jelena, "Quercetin in the treatment of dyslipidemia," *Medical Archives*, vol. 66, no. 2, pp. 87-88, 2012.

[36] F. Potì, D. Santi, G. Spaggiari, F. Zimetti, and I. Zanotti, "Polyphenol health effects on cardiovascular and neurodegenerative disorders: a review and meta-analysis," *International Journal of Molecular Sciences*, vol. 20, no. 2, p. 351, 2019.

[37] Á. Hernáez, S. Fernández-Castillejo, M. Farràs et al., "Olive oil polyphenols enhance high-density lipoprotein function in humans," *Arteriosclerosis, Thrombosis, and Vascular Biology*, vol. 34, no. 9, pp. 2115–2119, 2014.

[38] J. Fernandes, W. Su, S. Rahat-Rozenbloom, T. M. S. Wolever, and E. M. Comelli, "Adiposity, gut microbiota and faecal short chain fatty acids are linked in adult humans," *Nutrition and Diabetes*, vol. 4, no. 6, article e121, 2014.

[39] S. Castro-Barquero, R. M. Lamuela-Raventós, M. Doménech, and R. Estruch, "Relationship between Mediterranean dietary polyphenol intake and obesity," *Nutrients*, vol. 10, no. 10, p. 1523, 2018.

[40] I. Da-Costa-Rocha, B. Bonnlaender, H. Sievers, I. Pischel, and M. Heinrich, "Hibiscus sabdariffa L. – A phytochemical and pharmacological review," *Food Chemistry*, vol. 165, pp. 424–443, 2014.

[41] T. L. Lin, H. H. Lin, C. C. Chen, M. C. Lin, M. C. Chou, and C. J. Wang, "Hibiscus sabdariffa extract reduces serum cholesterol in men and women," *Nutrition Research*, vol. 27, no. 3, pp. 140–145, 2007.

[42] B. Zhang, R. Yue, Y. Wang et al., "Effect of Hibiscus sabdariffa (Roselle) supplementation in regulating blood lipids among patients with metabolic syndrome and related disorders: a systematic review and meta-analysis," *Phytotherapy Research*, vol. 34, no. 5, pp. 1083–1095, 2020.

[43] Z. Aziz, S. Y. Wong, and N. J. Chong, "Effects of Hibiscus sabdariffa L. on serum lipids: A systematic review and meta-analysis," *Journal of Ethnopharmacology*, vol. 150, no. 2, pp. 442–450, 2013.

[44] R. Kuriyan, D. R. Kumar, and A. V. Kurpad, "An evaluation of the hypolipidemic effect of an extract of Hibiscus sabdariffa leaves in hyperlipidemic Indians: a double blind, placebo controlled trial," *BMC Complementary and Alternative Medicine*, vol. 10, no. 1, pp. 1–8, 2010.

[45] A. M. Sabzghabaee, E. Ataei, R. Kelishadi et al., "Effect of Hibiscus sabdariffa calices on dyslipidemia in obese adolescents: a triple-masked randomized controlled trial," *Materia Socio-Medica*, vol. 25, no. 2, pp. 76–79, 2013.

[46] S. M. Barbalho, D. C. Damasceno, A. P. M. Spada et al., "Effects of Passiflora edulis on the metabolic profile of diabetic Wistar rat offspring," *Journal of Medicinal Food*, vol. 14, no. 12, pp. 1490–1495, 2011.

[47] P. Prince and N. K. Kannan, "Protective effect of rutin on lipids, lipoproteins, lipid metabolizing enzymes and glycoproteins in streptozotocin-induced diabetic rats," *Journal of Pharmacy and Pharmacology*, vol. 58, pp. 1373–1383, 2006.

[48] C. L. You, C. L. Su, and C. L. Zhou, "Study on effect and mechanisms of Scutellaria baicalensis stem-leaf total flavonoid in regulating lipid metabolism," *Journal of Chinese Medicinal Materials*, vol. 33, pp. 1064–1066, 2008.

[49] E. Dubois-Deruy, V. Peugnet, A. Turkieh, and F. Pinet, "Oxidative stress in cardiovascular diseases," *Antioxidants*, vol. 9, no. 9, p. 864, 2020.

[50] I. Rahman, S. K. Biswas, and P. A. Kirkham, "Regulation of inflammation and redox signaling by dietary polyphenols," *Biochemical Pharmacology*, vol. 72, no. 11, pp. 1439–1452, 2006.

[51] A. Lozhkin, A. E. Vendrov, H. Pan, S. A. Wickline, N. R. Madamanchi, and M. S. Runge, "NADPH oxidase 4 regulates vascular inflammation in aging and atherosclerosis," *Journal of Molecular and Cellular Cardiology*, vol. 102, pp. 10–21, 2017.

[52] L. Chen, H. Deng, H. Cui et al., "Inflammatory responses and inflammation-associated diseases in organs," *Oncotarget*, vol. 9, no. 6, pp. 7204–7218, 2018.

[53] K. Urschel and I. Cicha, "TNF-α in the cardiovascular system: from physiology to therapy," *International Journal of Interferon, Cytokine and Mediator Research*, vol. 7, pp. 9–25, 2015.

[54] A. García-Lafuente, E. Guillamón, A. Villares, M. A. Rostagno, and J. A. Martínez, "Flavonoids as anti-inflammatory agents: implications in cancer and cardiovascular disease," *Inflammation Research*, vol. 58, no. 9, pp. 537–552, 2009.

[55] M. Herranz-López, M. Olivares-Vicente, J. A. Encinar et al., "Multi-targeted molecular effects of Hibiscus sabdariffa polyphenols: an opportunity for a global approach to obesity," *Nutrients*, vol. 9, no. 8, p. 907, 2017.

[56] R. Beltrán-Debón, E. Rodríguez-Gallego, S. Fernández-Arroyo et al., "The acute impact of polyphenols from Hibiscus sabdariffa in metabolic homeostasis: an approach combining metabolomics and gene-expression analyses," *Food and Function*, vol. 6, no. 9, pp. 2957–2966, 2015.

[57] X. Chen, K. Xun, L. Chen, and Y. Wang, "TNF-α, a potent lipid metabolism regulator," *Cell Biochemistry and Function*, vol. 27, no. 7, pp. 407–416, 2009.

[58] C. B. Cazarin, J. K. da Silva, T. C. Colomeu et al., "Intake of _Passiflora edulis_ leaf extract improves antioxidant and anti-inflammatory status in rats with 2,4,6-trinitrobenzenesulphonic acid induced colitis," *Journal of Functional Foods*, vol. 17, pp. 575–586, 2015.

[59] R. O. Silva, S. R. Damasceno, T. V. Brito et al., "Polysaccharide fraction isolated from Passiflora edulis inhibits the inflammatory response and the oxidative stress in mice," *Journal of Pharmacy and Pharmacology*, vol. 67, no. 7, pp. 1017–1027, 2015.

Hindawi
Oxidative Medicine and Cellular Longevity
Volume 2022, Article ID 6742792, 17 pages
https://doi.org/10.1155/2022/6742792

Review Article

Diagnostic and Therapeutic Roles of Extracellular Vesicles in Aging-Related Diseases

Zixuan Sun,[1,2] **Xiaomei Hou**,[2] **Jiaxin Zhang**,[2] **Jiali Li**,[2] **Peipei Wu**,[2] **Lirong Yan**,[1] **and Hui Qian**[2]

[1]*Department of Gerontology, Affiliated Hospital of Jiangsu University, Zhenjiang 212001, China*
[2]*Key Laboratory of Laboratory Medicine of Jiangsu Province, School of Medicine, Jiangsu University, Zhenjiang 212013, China*

Correspondence should be addressed to Lirong Yan; zjdwylr@126.com and Hui Qian; lstmmmlst@163.com

Received 27 May 2022; Accepted 19 July 2022; Published 8 August 2022

Academic Editor: Jianbo Wu

Aging shows a decline in overall physical function, and cellular senescence is the powerful catalyst leading to aging. Considering that aging will be accompanied with the emergence of various aging-related diseases, research on new antiaging drugs is still valuable. Extracellular vesicles (EVs), as tools for intercellular communication, are important components of the senescence-associated secretory phenotype (SASP), and they can play pathological roles in the process of cellular senescence. In addition, EVs are similar to their original cells in functions. Therefore, EVs derived from pathological tissues or body fluids may be closely related to the progression of diseases and become potential biomarkers, while those from healthy cells may have therapeutic effects. Moreover, EVs are satisfactory drug carriers. At present, numerous studies have supported the idea that engineered EVs could improve drug targeting ability and utilization efficiency. Here, we summarize the characteristics of EVs and cellular senescence and focus on the diagnostic and therapeutic potential of EVs in various aging-related diseases, including Alzheimer disease, osteoporosis, cardiovascular disease, diabetes mellitus and its complications, and skin aging.

1. Introduction

Extending the human lifespan is a major goal of medical research, and aging seems to be a stumbling block to human longevity. It is a multifactorial biological process accompanied with the accumulation of senescent cells and the decline of body function [1, 2]. The physiological role of cellular senescence depends on the recruitment of immunocytes by senescent cell-secreted senescence-associated secretory phenotype (SASP) factors. However, after exerting their beneficial effects, the senescent cells cannot be completely cleared by the immune system [3]. Sustained secretion of SASP factors could lead to chronic inflammation, which is an essential contributor to aging-related diseases [4]. Senescent cells are mainly characterized by changes in nuclear genes, mitochondrial and lysosomal system dysfunction, and increased SASP factor secretion [5, 6]. Numerous studies have confirmed the key roles of extracellular vesicles (EVs) in DNA damage repair, inflammatory regulation, and epigenetic alterations, showing their great medical value in aging-related diseases.

EVs are diverse nanoscale membrane vesicles secreted by most cell types [7]. Based on their biogenesis, size, and biophysical properties, they can be classified into apoptotic bodies, exosomes, and microvesicles (MVs) [8]. In the process of the synthesis and secretion of EVs, signaling molecules such as DNA, RNA, functional proteins, and lipids can be selectively encapsulated, indicating the sharing of biological information among cells [9]. EVs are important components of SASP factors, and their information transmission function plays a vital role in cellular senescence [5, 10]. Particularly, senescent cells can promote the senescence of surrounding bystander cells by secreting SASP factors [11]. In addition, senescence manifests a decline or even loss of stem cell proliferative capacity, so stem-cell therapy has also emerged. However, due to the uncontrollable differentiation of stem cells, it may have carcinogenic and teratogenic effects, and the surgical cost is high. Compared with cell

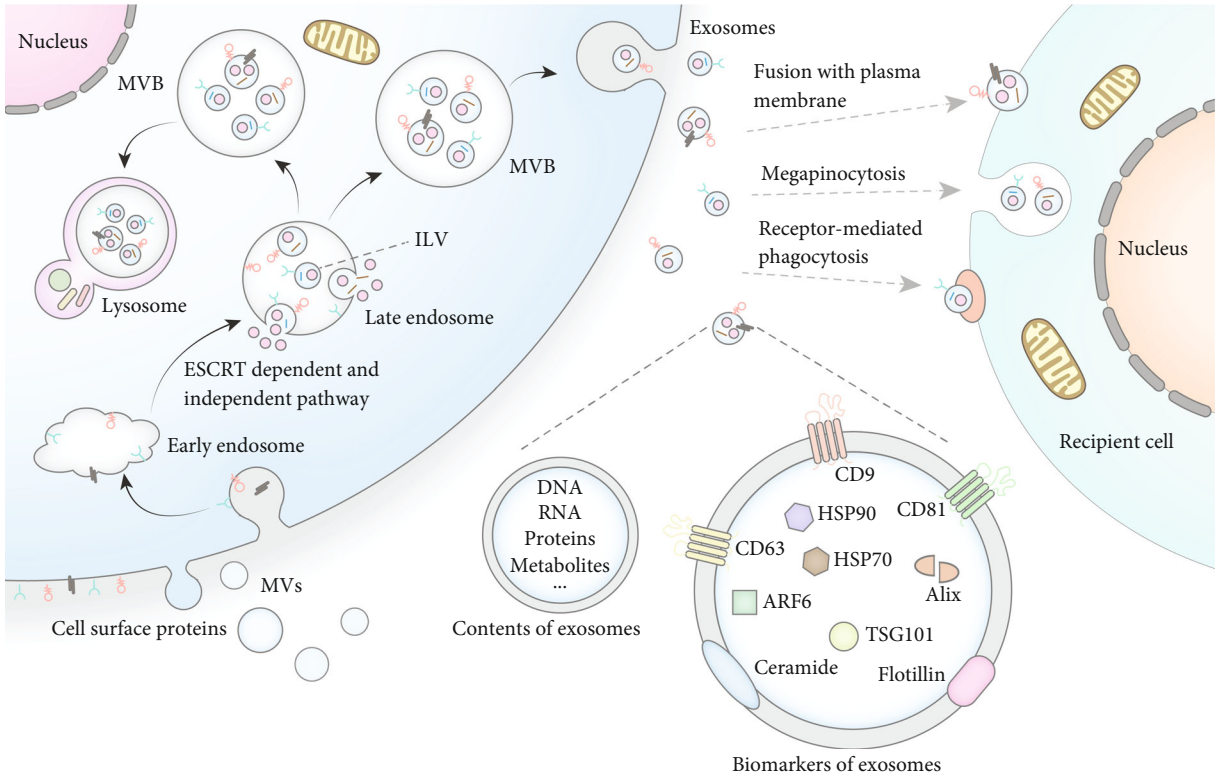

Figure 1: Biogenesis, secretion, and uptake of exosomes. Exosome is a subset of EVs. The biogenesis of exosomes mainly goes through the stages of endocytosis and MVB formation. Different nucleic acids or proteins are loaded during the formation of exosomes. These cargoes can be internalized into recipient cells through different mechanisms, thus realizing the information transmission function of exosomes. Moreover, some cargo proteins can also be used as biomarkers for the identification of exosomes.

therapy, EVs are similar to their parent cells in functions, and they have the advantages of low carcinogenicity and no blockage of blood vessels, which make EVs become promising antiaging agents [12]. In this review, we summarize the roles of different sources of EVs as biomarkers and treatments of various aging-related diseases, and the current knowledge around the challenges and prospects of EVs are also discussed.

2. EVs as Biological Tools for Cell Communication

The effectiveness of EVs mainly depends on which cargoes they carry. In fact, the current researches on the pathogenic and therapeutic effects of EVs are mainly based on the belief that EVs can be used as tools for intercellular information transmission. As an important member of EVs, the exosome also plays a major role in cell communication. At present, it is believed that the biogenesis of exosomes originates from the endosomal pathway [13] (Figure 1). Endocytic vesicles form and fuse on the plasma membrane to form early endosomes. Next, early endosomes sink again and mature to form late endosomes. These late endosomes are also known as multivesicular bodies (MVBs) [14], which contain intraluminal vesicles (ILVs) formed through endosomal sorting complex required for transport- (ESCRT-) dependent and ESCRT-independent pathways [15–17]. The formation of ILVs is accompanied by cargo loading, which is crucial for cell communication. After vesicular accumulation, some MVBs are degraded in lysosomes, and the other MVBs release ILVs out of cells by fusing with the plasma membrane. These ILVs are the precursors of exosomes [18]. The uptake of exosomes by recipient cells is another important step in cell communication (Figure 1). Exosomal cargoes are internalized into recipient cells through a variety of mechanisms: (i) receptor-mediated phagocytosis of special cells, (ii) megapinocytosis of plasma membrane invagination, and (iii) direct fusion with the plasma membrane [19]. The cargoes of exosomes could change the state of recipient cells or make them obtain new abilities, which reflects the medical value of exosomes [20].

3. Stimuli and Characteristics of Cellular Senescence

The accumulation of senescent cells *in vivo* is an essential mechanism of aging [21], and it is also the culprit of aging-related diseases. Although cell senescence has certain physiological effects [2, 22], excessive senescent cell accumulation can create a proinflammatory environment conducive to the occurrence and development of aging-related diseases [23] (Figure 2).

Although cellular senescence is a complicated process [6, 24], it can be summarized into two basic events: the change of nuclear genes and the transformation of mitochondria [5]. The changes of nuclear genes include DNA damage,

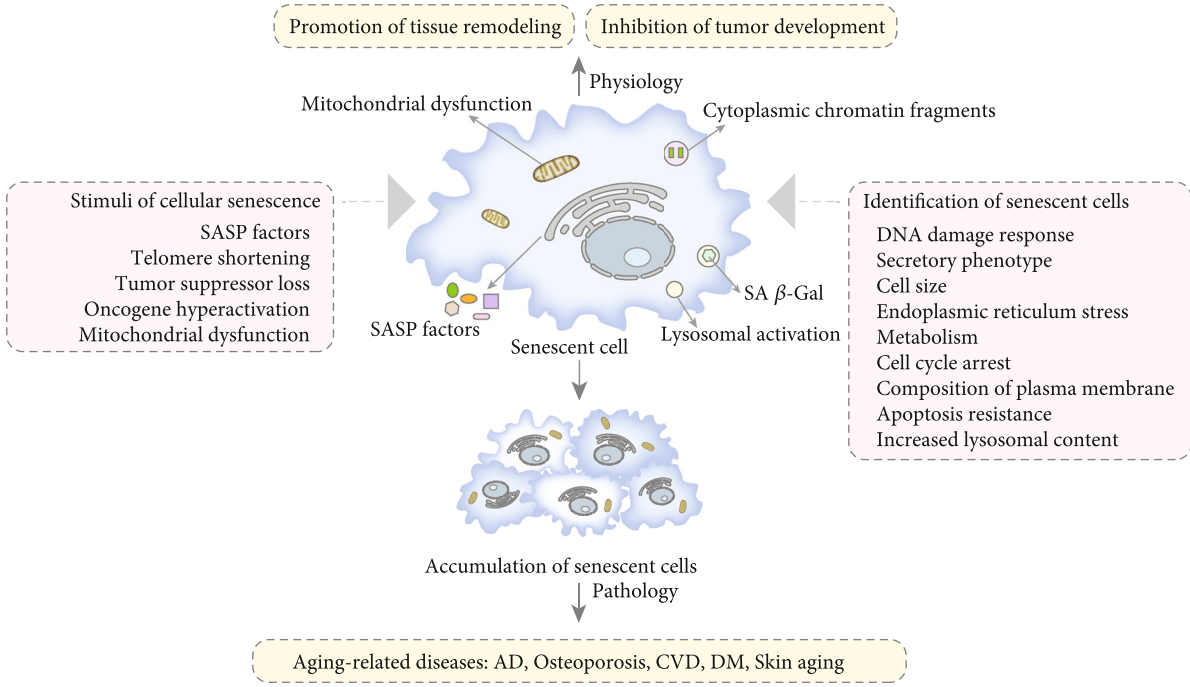

Figure 2: The stimuli and identification of cellular senescence. Cellular senescence has two sides. On the one hand, cellular senescence can promote tissue remodeling and inhibit tumor development. On the other hand, accumulation of senescent cells can lead to a variety of aging-related diseases. Cellular senescence is caused by different stimuli, and the mechanism of cellular senescence is very complex. Therefore, the identification of senescent cells needs to be analyzed from different aspects.

telomere shortening, and epigenetic change [25]. The mitochondrion is a multifaceted regulator of aging [26]. The loss of mitochondrial DNA integrity and destruction of mitochondrial metabolism are regarded as evolutionarily conserved senescent mechanisms [27]. In fact, mitochondrial dysfunction is associated with low NAD^+/NADH ratios [28] and high level of SASP factors and reactive oxygen species (ROS) [29, 30]. Because of the complexity of the cellular senescence mechanism, the characteristic of senescent cells shows complex dynamics and heterogeneity. Therefore, the identification of senescent cells involves many aspects [21] (Figure 2). There is still no gold standard for identifying senescent cells [31], and the combination of multiple aging phenotypes to identify senescent cells is still the best choice at present [32]. In order to further explore the diagnosis and treatment of aging-related diseases, it is very important to clarify the stimuli and characteristics of cellular senescence.

4. EVs in Aging-Related Diseases

Aging is characterized by the disorder of various biological functions, which leads to an increased risk of osteoporosis, diabetes mellitus (DM), cardiovascular diseases (CVDs), Alzheimer disease (AD), and other chronic diseases [33]. Increasing researches have demonstrated that EVs can serve as potential biomarkers and therapeutic reagents in aging-related diseases. Here, we introduce the most studied aging-related diseases in the field of EVs (Figure 3).

4.1. Roles of EVs in AD. Around the world, AD is a leading cause of disability in people over 65 years old [34]. Two main histopathological features of AD are (i) senile plaques formed by increased deposition of the amyloid beta (Aβ) peptide and (ii) intracellular neurofibrillary tangle (NFT) caused by tau hyperphosphorylation [35]. Aging is a major risk factor for AD [36], and cellular senescence is one of the hallmarks of aging, which increases susceptibility to AD. Enrichment of senescent astrocytes, microglia, and neurons, as well as the expression of senescence-associated β-galactosidase (SA β-Gal), were observed in the brain tissue of AD patients [37]. Senescent astrocytes and microglia could promote tau hyperphosphorylation [38]. It is suggested that clearing senescent nerve cells might be helpful to inhibit the occurrence of AD. In addition, AD has a longer preclinical phase [39], and the onset of clinical symptoms can be alleviated if treatment is available in this period [34]. Therefore, biomarkers for the early diagnosis of AD is urgently needed.

4.1.1. EVs as Low-Invasive Markers for Early Diagnosis of AD. At present, the combined detection of Aβ42, total tau (t-tau), and phosphorylated Thr181 tau (p181-tau) in the cerebrospinal fluid is the gold standard for the diagnosis of AD [40]. However, this method requires invasive lumbar puncture to obtain cerebrospinal fluid, limiting its clinical application. Positron emission tomography (PET) has been proven to have high accuracy in AD diagnosis *in vivo*, but it is not available in most medical settings [41]. Therefore, the detection of blood-based biomolecules that are less invasive and easy to implement have become alternative methods for AD diagnosis.

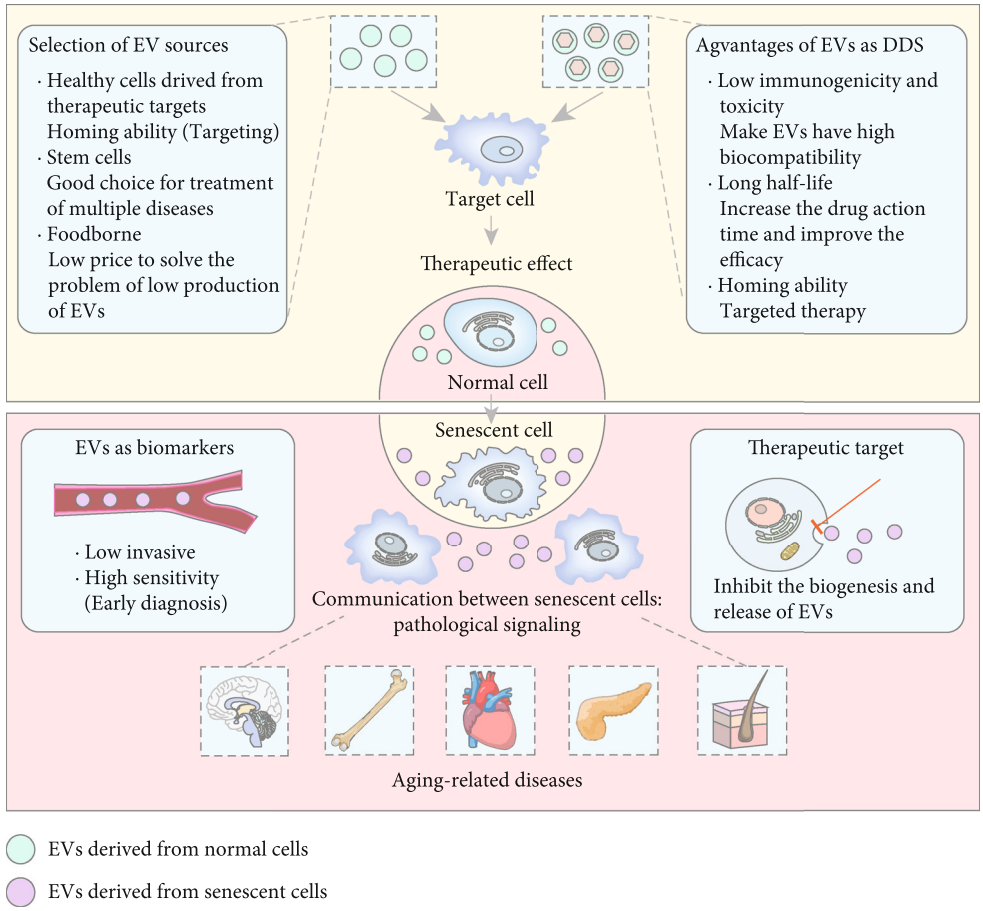

Figure 3: The roles of EVs in aging-related diseases. EVs derived from normal cells have therapeutic effects on aging-related diseases. There are many sources of natural EVs, and the optimal selection should consider the yield, targeting, and curative effect. In addition, EVs are also high-quality drug delivery systems (DDSs), which can target the delivery of therapeutic drugs through engineered EVs. EVs derived from senescent cells will contribute to the transmission of aging information and further promote the accumulation of senescent cells, which may eventually lead to aging-related diseases. Significantly, EVs derived from these senescent cells are also potential diagnostic biomarkers and therapeutic targets.

Recently, EVs isolated from peripheral blood have aroused the interest of researchers. Longobardi et al. [42] found that patients with different types of dementia have differences in the size and number of blood-derived EVs, indicating that their physical characteristics might be promising markers for dementia. In addition, EVs contain the Aβ peptide and tau that play important roles in the occurrence of AD. This presents their great potential in the diagnosis of AD. Delgado-Peraza et al. [43] reported that in AD mouse models, plasma neuronal EVs (NEVs) carry higher levels of t-tau, p181-tau, and Aβ42, and those astrocytic EVs (AEVs) carry higher levels of complement proteins. The levels of these markers in plasma NEVs and AEVs are correlated with their levels in brain tissue, thus supporting the use of plasma EV biomarkers for detecting brain pathology. Similarly, changes in other forms of Aβ peptide and tau have also been found in AD patients [39, 41, 44]. Besides, there are several other promising biomarkers based on EVs for AD diagnosis, such as matrix metalloproteinase 9 (MMP-9), growth-associated protein 43 (GAP43), neurogranin, synaptosome-associated protein 25 (SNAP25), and synaptophysin 1 [34, 41]. Notably, in addition to using EVs alone, some researchers have combined olfactory functions with Aβ1-42 and Sniffin' Sticks (SS-16) to more accurately predict the transition from mild cognitive impairment to AD dementia [45] (Table 1).

4.1.2. Roles of EVs from Different Sources in AD Treatment. Due to the heterogeneity of EVs, those EVs from healthy cells can act therapeutically on AD. Li et al. [46] injected neural stem cell-derived EVs (NSC-EVs) into the lateral ventricle of AD mice and found that the mouse inflammatory response was reduced and cognitive impairment was rescued. Similarly, Apodaca et al. [47] injected NSC-EVs intravenously into 5xFAD mice. And EV treatment reversed the cognitive impairment of AD mice by reducing Aβ plaques, inhibiting microglia activation, and promoting synaptophysin recovery in the brain. Several potential therapeutic EV cargoes were identified by using TaqMan Advanced miRNA Assays, including miR-125b-5p, miR-124-3p, and miR-125a-5p, thereby providing candidate miRNAs for follow-up studies. In addition, EVs derived from mesenchymal

Table 1: EVs and their cargoes as biomarkers of aging-related diseases.

Disease	Nanovesicle	Source of EVs	Biomarkers	Refs.
AD	NDEs	Human blood	GAP43, neurogranin, SNAP25 and synaptophysin 1↓	[34]
	Exosomes	Human serum	Gelsolin↓	[40]
	NDEVs	Human plasma	Aβ42, p181-tau, and MMP-9↑	[41]
	EVs	Human plasma	The size of EVs↑ The number of EVs↓	[42]
	NEVs	Mouse plasma	t-tau, p181-tau, and Aβ42↑	[43]
	NEVs	Human serum	p181-tau, p231-tau, and annual rate of change in insulin signaling biomarkers↑	[39, 44]
	NDEs	Human plasma	Aβ1-42↑ SS-16 scores↓	[45]
Hypertension	Exosomes	Urine	PTC-EMPs↑	[53]
	EVs	Urine	$p16^+$ EVs↑	[54]
	Exosomes	Urine	miR-192-5p and miR-204-5p↓	[55]
T2DM	EVs	Human plasma	IGHG-1, miR-324-5p, miR-376c-3p, and miR-374b-5p↓ ITIH2 protein, serum ferritin, miR-141-3p, and miR-26b-5p↑	[56]
DN	Exosomes	Urine	miR-4534↑	[57]
DR	EVs	Human serum	miR-431-5p↑	[58]
	EVs	Human plasma	miR-150-5p↓ miR-21-3p, and miR-30b-5p↑	[59, 60]
	Small EVs	Human plasma	TNFAIP8↑	[61]

Abbreviations: NEVs: neuronal extracellular vesicles; NDEVs: neuronally derived extracellular vesicles; NDEs: neuronal-derived exosomes; IGHG-1: immunoglobulin heavy constant gamma 1; ITIH2 protein: interalpha-trypsin inhibitor heavy chain H2 protein; TNFAIP8: tumor necrosis factor-α-induced protein 8.

stromal cells (MSC-EVs) have shown good therapeutic effects on AD [48–50]. Besides, a recent study found that ultrasound could increase the release of exosomes derived from human astrocytes (HAs) by nearly five times, and these exosomes demonstrated excellent therapeutic effects, suggesting that applying physical methods may help solve the problem of low EV yields [51].

Because of EVs' advantages of homing ability, good biocompatibility, and blood-brain barrier penetration, they can serve as excellent drug carriers. By using plasma exosomes to load quercetin (Que), Qi et al. [52] found that Exo-Que could remarkably improve brain targeting and bioavailability of Que. Compared with free Que, Exo-Que inhibited tau phosphorylation and the formation of NFT, which could better alleviate the symptoms of AD, indicating that Exo-Que has better potential for the treatment of AD (Table 2). This represents the positive function of EVs in drug delivery, but the loading efficiency should also be considered.

4.2. Roles of EVs in Osteoporosis. Osteoporosis can lead to bone fragility and an increased risk of fractures [62, 63]. Osteoporotic fractures are most commonly found in the spine, hip, or wrist [64], and it is a major cause of global health expenditures. As a unique tissue form, the bone can heal without fibrous scars. But healing disorders associated with osteoporotic fractures, especially nonunion, will prolong treatment time and increase the socioeconomic burden [65]. The risk of fracture in patients with osteoporosis is mainly due to the increased bone resorption caused by the increased activity of osteoclasts. Moreover, that osteoblasts cannot make up for this bone loss in time will result in serious delays of bone reconstruction [66].

4.2.1. Pathological Roles of EVs in Osteoporosis. At present, the researches on the pathological mechanisms of osteoporosis mainly focus on the functional imbalance between osteoblasts and osteoclasts, as well as the imbalance between osteogenic differentiation and adipogenic differentiation of bone marrow MSCs (BMSCs) [67, 68]. DNA damage, apoptosis, and cellular senescence induced by oxidative stress are important reasons for the imbalance of the bone tissue environment [69]. As essential participants in the aging process, EVs make a difference in the imbalance of bone homeostasis and the occurrence and development of osteoporosis. Additionally, the communication function of EVs determines their crosstalk abilities between cells and tissues in the pathological process of osteoporosis. Crosstalk between the bone and muscle is a new research direction. Some researchers have reported that muscle-derived EVs carrying miR-34a could induce BMSC aging by reducing sirtuin 1 (SIRT1) expression in BMSCs, thus decreasing bone mass [70]. Angiogenesis, a key factor in bone reconstruction, can be regulated by the bone itself. Senescence osteoblast-derived exosomes could upregulate miR-139-5p expression in vascular endothelial cells. miR-139-5p acts on the target gene TBX1, which could increase aging and apoptosis and reduce the proliferation and migration of vascular endothelial cells, thus affecting the process of osteoporosis [71]. Therefore, blocking the transmission of harmful EV has become a potential therapeutic target for osteoporosis.

Table 2: Therapeutic effects of EVs from different sources in aging-related diseases.

Disease	Source of EVs	Animal model	Mechanism(s) and effect(s)	Refs.
AD	NSCs	APP/PS1 mice	Increased the metabolism and function of mitochondria, the activation of SIRT1, and the activity and integrity of synapses; decreased the oxidative damage of cerebral cortex and the inflammatory response	[46]
	hNSCs	5xFAD mice	Mitigated AD-related behavioral and molecular neuropathologies	[47]
	MSCs	J20 AD transgenic (Tg) mice	Improved brain metabolism and cognitive function; reduced Aβ plaque load and inhibited astrocyte activation	[48]
	MSCs	3xTg AD mice	Dampened microglia activation and reduced dendritic spine loss	[49]
	ADMSCs	APP/PS1 mice	Decreased the release of inflammatory factors by inhibiting pyroptosis	[50]
	HAs	APP/PS1 mice	HA-Exo provided neuroprotective effects to reverse oligomeric amyloid-β-induced cytotoxicity *in vitro*	[51]
	Mouse plasma	OA-induced AD mice	Reduced the formation of insoluble NFTs and inhibited CDK5-mediated phosphorylation of tau	[52]
Osteoporosis	BMSCs	OVX-induced postmenopausal osteoporosis mice	miR-29b-3p in EVs potentiated osteogenic differentiation through SOCS1/NF-κB pathway	[63]
	Serum of young rats	OVX-induced postmenopausal osteoporosis mice	miR-19b-3p in EVs promoted the osteogenic differentiation of BMSCs	[78]
	hucMSCs	OVX-induced postmenopausal osteoporosis mice and TS-induced hindlimb disuse osteoporosis mice	CLEC11A in EVs promoted the shift from adipogenic to osteogenic differentiation of BMSCs and inhibited bone resorption	[81]
	BMSCs	OVX-induced postmenopausal osteoporosis mice	MALAT1 in EVs promoted osteoblast activity through microRNA-34c/SATB2 axis	[82]
	SHED	OVX-induced postmenopausal osteoporosis mice	miR-346 in EVs rescued impaired BMSC function and recovered bone loss	[83]
	Mid-to-late stage of osteoblasts	OVX-induced postmenopausal osteoporosis mice	Enhanced osteogenesis	[84]
	BMSCs	OVX-induced postmenopausal osteoporosis mice	miR-150-3p in EVs promoted osteoblast proliferation and differentiation	[85]
	BMSCs	OVX-induced postmenopausal osteoporosis mice	miR-29a in EVs promoted angiogenesis and osteogenesis by acting on human venous endothelial cells	[86]
	BMSCs	OVX-induced postmenopausal osteoporosis mice	miR-22-3p in EVs promoted osteogenic differentiation through MYC/PI3K/AKT pathway	[87]
	ECs	OVX-induced postmenopausal osteoporosis mice	miR-155 in EVs inhibited osteoclasts activity by acting on BMMs	[88]
	Bovine milk	OVX-induced postmenopausal osteoporosis mice	Reduced osteoclast presence through RANKL/OPG system	[90]

Table 2: Continued.

Disease	Source of EVs	Animal model	Mechanism(s) and effect(s)	Refs.
	Bovine colostrum	GIOP mice	Facilitated preosteoblast proliferation and inhibited osteoclast differentiation	[91]
	hAFSCs	GIOP mice	Ameliorated the differentiation ability of HOB through a redox-dependent regulation of SIRT1	[92]
	hUCB	OVX-induced postmenopausal osteoporosis mice	miR-3960 in EVs promoted osteogenesis and inhibited osteoclastogenesis	[93]
Hypertension	Plasma from WKY	SHR and WKY	Modulated systemic blood pressure as well as structure and function of cardiovascular tissues in both normotensive and hypertensive rats	[94]
	CDCs	Ang II-induced male C57BL/6J mice	EV-YF1 attenuated cardiac hypertrophy and renal injury induced by Ang II infusion, without affecting blood pressure	[95]
	iPS-MSCs	Young and old male C57BL/6 mice	Attenuated aging-associated vascular endothelial dysfunction, arterial stiffness, and hypertension through SIRT1-AMPKα-eNOS pathway	[96]
	Vascular adventitial fibroblasts of normal rats	SHR and WKY	miR-155-5p in EVs inhibited cell migration and proliferation in VSMCs of SHR through suppressing ACE expression, oxidative stress, and inflammation	[97, 98]
HF	hBMSCs	TAC-operated C57B6/J male mice	Regulated the fibrogenic and adhesion pathways, and cellular metabolic process in the damaged heart	[99]
	Normal human cardiomyocytes	Diseased heart tissues received from patients who underwent heart transplantation at UNC Hospital after heart failure	Promoted cardiomyocyte proliferation, decreased programmed cell death, and stimulated angiogenesis *in vitro* through phosphatase and tensin homolog/Akt pathway	[100]
	iPSC-Pg and iPSC-CMs	Nude mice with permanent left anterior coronary artery occlusion	miRNAs in EVs are effective in the treatment of CHF	[101]
T2DM	hucMSCs	Low concentrations of TNF-α and high glucose medium were used to simulate insulin resistance in human adipocytes	The insulin-stimulated glucose uptake↑ The level of leptin↓ The mRNA expression of sirtuin-1 and insulin receptor substrate-1↑	[102]
	Pancreatic β cells	β cell-specific miR-29a/b/c transgenic mouse (βTG) model	Prediabetic β cells release exosomal miR-29 to reset macrophage inflammatory tone	[103]

Abbreviations: hNSCs: human neural stem cells; ADMSCs: adipose-derived mesenchymal stem cells; OA: okadaic acid; CDK-5: cyclin-dependent kinase 5; OVX-induced: ovariectomized-induced; GIOP: glucocorticoid-induced osteoporosis; SHED: stem cells from human exfoliated decimal teeth; BMMs: bone marrow-derived macrophages; TS-induced: tail suspension-induced; SHR: spontaneous hypertensive rat; WKY: Wistar-Kyoto rat; iPS-MSCs: induced pluripotent stem cell-derived mesenchymal stem cells; SIRT1-AMPKα-eNOS: sirtuin type 1-AMP-activated protein kinase alpha-endothelial nitric oxide synthase; ACE: angiotensin-converting enzyme; CDCs: cardiosphere-derived cells; Ang II: angiotensin II; TAC: transverse aortic constriction; iPSC-Pg: human induced pluripotent stem cell-derived cardiovascular progenitor; iPSC-CM: human induced pluripotent stem cell-derived cardiomyocyte; CHF: chronic heart failure.

4.2.2. Calcification Paradox in Aging. The great significance of the calcification paradox in aging deserves attention. The calcification paradox means that vascular calcification (VC) and osteoporosis are often accompanied in the elderly population. VC is an early pathological change in many CVDs [72], and it also promotes osteoporosis by damaging the blood and nutrient supply of cortical bone [73]. A recent study revealed the molecular mechanism of the calcification paradox: (i) miR-483-5p in the aged bone matrix-derived EV (AB-EV) targets BMSCs to promote their adipogenic differentiation rather than osteogenic differentiation, thus promoting osteoporosis, and (ii) miR-2861 in AB-EVs promotes the ossification of vascular smooth muscle cells, thus promoting vascular calcification [74]. Notably, young BMSC-EVs not only promote osteogenesis in bone but also inhibit phosphate-induced VC in the vascular system [75, 76]. This suggests that young BMSC-EVs can regulate mineral disorders, and we should also pay attention to the impact on other systems when studying the effect of EVs on one disease.

4.2.3. Targeted Therapy of EVs from Different Sources in Osteoporosis. The treatment of osteoporosis depends on drugs, mainly antiresorptive agents, such as bisphosphonates, while the drugs approved by the FDA to restore bone loss are only parathyroid hormones (PTHs) [77, 78]. In addition to medication, physical therapy for osteoporosis, such as external mechanical load, can improve bone quality by promoting angiogenesis and driving BMSC recruitment and differentiation [79, 80]. The osteoporosis model used in a recent study is based on this principle. Specifically, this model suspended the hind legs of mice to eliminate mechanical load [81]. However, Xun et al. [78] found that this method was not effective at all ages. By contrast, fatigue load aggravated the microdamage of tibias in elderly osteoporotic rats, and the osteogenic differentiation ability of BMSCs was also decreased. In general, the therapeutic methods of osteoporosis still need to be expanded.

The therapeutic effect of EVs on osteoporosis is mainly reflected in promoting angiogenesis, inhibiting proliferation and differentiation of osteoclasts, and promoting the proliferation and osteogenic differentiation of BMSCs (Table 2). In addition to osteoblasts and osteoclasts, BMSCs are also key components in new bone formation. The adipogenic differentiation tendency of BMSCs is considered an essential cause of osteoporosis [82]. This is consistent with increased adipogenesis and decreased bone formation in osteoporosis [63]. Therefore, BMSC is the preferred therapeutic target for osteoporosis. Sonoda et al. [83] first demonstrated that systemic infusion of EVs derived from stem cells from human exfoliated decimal teeth could regulate telomerase activity, thereby improving the damaged function of BMSCs. Similarly, EVs derived from the mid-to-late stages of osteoblast differentiation could be helpful to restore the normal osteogenic differentiation level of BMSCs [84]. Although many studies have confirmed the therapeutic effect of EVs on osteoporosis, there is still a lack of optimal choice of the source of EVs. Good bone targeting is the guarantee for EVs to treat osteoporosis *in vivo*. Considering the homing ability of MSC-EVs, EVs from BMSCs are mostly selected in EV research on osteoporosis [63, 82, 85–87]. Although the bone-targeting ability of BMSC-derived exosomes (BMSC-Exos) is greatly improved compared with first-line osteoporosis drugs, such as bisphosphonates, their targeting ability may need further confirmation. EVs derived from vascular endothelial cells (ECs) and mid-to-late stages of osteoblast differentiation also exhibit innate bone-targeting potential [84, 88]. Notably, Lou et al. noted that although bone marrow stromal cell- (ST-) derived exosomes have a therapeutic effect *in vitro*, they failed to prevent postmenopausal osteoporosis induced by ovariectomy in the mouse model [77]. However, by binding BMSC-targeting aptamers to ST-derived exosomes, this complex could effectively accumulate in the bone marrow and showed a therapeutic effect *in vivo*. This suggests that engineering EVs to enhance their bone targeting is feasible. Similarly, Wang et al. linked alendronate to mouse MSC- (mMSC-) derived EVs by click chemistry, which not only improved bone targeting but also alleviated the side effects of alendronate [89]. While ensuring the efficacy, the availability of EV sources is another consideration. Human umbilical cord mesenchymal stromal cells (hucMSCs) [81], bovine milk [90], bovine colostrum [91], human amniotic fluid stem cells (hAFSCs) [92], and human umbilical cord blood (hUCB) [93] have unique source advantages. Since EVs derived from senescent cells carry aging information and have pathogenic potential, it is necessary to ensure that EVs come from young cells or body fluids [93]. In conclusion, the ideal source of EVs should have the characteristics of good bone targeting, easy availability, and coming from young individuals. Unfortunately, the study on the molecular mechanism of EVs in the treatment of osteoporosis is still very limited. This is undoubtedly a future research direction.

4.3. Roles of EVs in CVDs. Age is the primary risk factor for CVDs [104]. By 2030, 23.6 million people are expected to die annually from CVDs [105], which has aroused great attention to cardiovascular health all over the world. Recently, EVs have emerged as new players in the researches on pathology, diagnosis, and treatment of CVDs.

4.3.1. Cardiovascular Aging. Vascular aging occurs before clinical diseases and can lead to serious CVDs [106, 107]. It mainly occurs in the inner and middle layers of the vascular wall [107]. Therefore, as the main cells of the blood vessel wall, ECs and vascular smooth muscle cells (VSMCs) play vital roles in vascular aging. During vascular aging, tube wall stiffness and compliance decrease. Women exhibit higher wall hardness than men [108]. The mechanism underlying this association may explain sexual differences in the incidence rate of CVD. In addition to blood vessels, the function of the heart decreases with age. Increases in heart mass and volume and a decreased maximum heart rate are the main characteristics of heart aging [108]. Notably, changes in the cardiomyocyte structure and function precede anatomical and functional changes in the heart [109]. Mitochondria are critical for heart aging, which is consistent with the mechanism of cellular senescence. Apart from affecting the energy transfer efficiency of cardiomyocytes [110], mitochondrial acetaldehyde dehydrogenase (ALDH2) can also influence cardiac aging by affecting autophagy [111]. Dysfunction associated with cardiovascular aging will lead to various CVDs.

4.3.2. Hypertension. The main harm of hypertension is to damage cardiovascular and renal health [112]. Since the etiology of hypertension is still not clear, the current research on EVs in the treatment of hypertension is mainly aimed at the accompanying cardiovascular and renal injury. For example, plasma exosomes could regulate the structure and function of cardiovascular tissue and systemic blood pressure in hypertensive rats [94]. And exosomes secreted by cardiosphere cells could treat angiotensin II-induced hypertension-related myocardial hypertrophy and renal injury [95]. Vascular remodeling is a key event in the development of hypertension. Considering that ECs and VSMCs are essential in vascular remodeling, these two cells are important therapeutic targets for vascular injury induced by hypertension [113]. In addition, in view of the correlation

between hypertension and aging, cellular senescence-related signal pathways and molecules deserve attention while studying the specific mechanism of EVs on hypertension. There is no doubt about the close relationship between MMPs and aging. In fact, MMPs can participate in skin aging [114], neurodegenerative diseases [115], and hypertension. By activating the SIRT1-AMPKα-eNOS pathway and downregulating MMPs, EVs from induced pluripotent stem cell- (iPSC-) derived MSCs could reduce aging-related vascular endothelial dysfunction and hypertension [96]. Besides, oxidative stress [116] and chronic inflammation [117], the risk factors of aging are also the targets of EVs in the treatment of hypertension. miR-155-5p in adventitia fibroblast-derived EVs under normal blood pressure could inhibit the proliferation and migration of VSMCs under hypertension by inhibiting oxidative stress, inflammation, and the expression of the angiotensin-converting enzyme [97, 98]. It should be noted that different hypertensive mouse models may reveal different results in the study of hypertension mechanisms and treatment, and the impact of this difference should be excluded as far as possible in practical research (Table 2).

The early diagnosis of aging-related diseases is of great significance for disease intervention. EVs are expected to become early diagnostic biomarkers of hypertension-induced chronic kidney disease [118]. Urine is an ideal specimen for detecting renal injury. In addition to the advantage of noninvasiveness, the EV-derived proteins which are contained in urine could also reflect the damage of renal cells [119]. Moreover, the level of PTC-EMPs (peritubular capillary endothelial microparticles), which are urinary exosomes positive for the peritubular capillary marker plasmalemmal-vesicle-associated protein, may be early biomarkers of renal injury independent of proteinuria in patients with hypertension [53]. The cyclin-dependent kinase (Cdk) inhibitor, $p16^{Ink4a}$ (p16), is an ideal biomarker of cellular senescence [120]. The elevated level of $p16^{+}$ EVs in the urine of patients with hypertension could reflect the increased proximal tubular cellular senescence [54]. In addition to the changes of EVs' own level, the miRNA contained in EV is also helpful to the diagnosis of hypertension [121]. The downregulated expression level of miR-192-5p and miR-204-5p from urinary exosomes would be helpful to diagnose patients with "nonclassical" apparent mineralocorticoid excess [55]. Early recognition of this phenotype helps to prevent the progression of arterial hypertension. These examples demonstrate the unique diagnostic potential of EVs in hypertensive chronic kidney disease (Table 1).

4.3.3. HF. Heart failure (HF) is a kind of myocardial systolic dysfunction caused by multiple factors, and it is also the last stage of various CVDs [97, 122]. Similar to other aging-related diseases, oxidative stress plays an important pathological role in CVDs. Exosomal miRNAs play pathogenic roles in HF by participating in oxidative stress [123, 124]. Nrf2 is considered as an amplifier of the antioxidant pathway [125], while miR-27a, miR-28-3p, and miR-34a contained in exosomes could mediate Nrf2 imbalance thereby promoting the development of HF [124].

As to the treatment of HF, EVs are favorable agents. Nakamura et al. [99] found that intravenous injection of human BMSCs could play a therapeutic role in mice with HF through EVs. Moreover, adiponectin can stimulate EV biogenesis and secretion by binding to T-cadherin on human BMSCs, thereby enhancing the curative effect. This provides a new strategy for solving the problem of EVs' production. Compared with other cell sources, cardiogenic EVs may have more therapeutic advantages [100, 126]. Studies have shown that exosomes derived from cardiac fibroblast-iPSCs have a better effect than those from dermal fibroblast-iPSCs in reducing cardiac remodeling [126]. Although the specific therapeutic mechanism of EVs remains unclear, it may be associated with the miRNAs in EVs [101]. Future studies should focus on elucidating the underlying molecular mechanisms (Table 2). At present, the evidence of EVs for HF diagnosis is not sufficient. Oh et al. [127] predicted miRNAs from EVs that may be biomarkers for HF diagnosis by comparing the EV miRNA expression profiles between normal mouse hearts and HF mouse hearts. However, further verification is still needed.

4.4. Roles of EVs in DM and Its Complications. DM is an aging-related metabolic disorder marked by a chronic elevation of blood glucose levels caused by insufficient insulin secretion or function defects [128]. At present, the prevalence of type 2 DM (T2DM) is the highest, followed by type 1 DM (T1DM), while other types of DM account for a small proportion [128]. Chronic hyperglycemia in DM causes damage to blood vessels, which can lead to a series of DM-associated complications [129]. Diabetes is considered as an inducement to accelerate cellular senescence, and it is associated with aging-related cardiovascular diseases and kidney diseases caused by hyperglycemia [130]. This highlights the link between aging-related diseases. DM has become a global health problem in recent years due to aging populations, which makes it essential to identify effective molecular markers and drug targets for DM.

4.4.1. T2DM. The onset of T2DM usually occurs after the age of 40, and it is considered to be a typical aging-related disease [131]. With the development of T2DM and its cardiovascular complications, EVs change both in quantity and quality [132]. By analyzing EVs isolated from patients' plasma, Masi et al. [56] reported an EV biomarker combination containing five differentially expressed miRNAs (miR-141-3p, miR-324-5p, miR-376c-3p, miR-26b-5p, and miR-374b-5p) and three proteins (immunoglobulin heavy constant gamma 1, interalpha-trypsin inhibitor, and heavy chain H2 and serotransferrin), which had a good indication effect on the prognosis of DM complications. Aside from being biomarkers, EVs can also be used as therapeutic targets for DM. T2DM is characterized by insulin resistance, and Kumar et al. [133] reported that high-fat diet-induced exosomes might contribute to insulin resistance. As a result, intestinal exosomes can serve as a wide range of therapeutic targets. In addition, EVs from other sources may be available for T2DM treatment [102, 103, 134] (Table 2).

4.4.2. Diabetic Foot Ulcer. There is no doubt that diabetic foot ulcer is a serious complication of DM that negatively impacts patients' quality of life. In recent years, increasing evidence has pointed that MSC-EVs could be a potentially effective agent for diabetic wounds [135]. For example, Pomatto et al. [136] found that BMSC-EVs primarily promoted cell proliferation, while ADSC-derived EVs (ADSC-EVs) showed significant ability to promote endothelial cell migration and angiogenesis, which may be related to their expression of specific molecules. Notably, studies have shown that pretreatment of MSCs with chemical or biological factors could enhance the biological activity of MSC-Exos. For example, BMSC-Exos pretreated with atorvastatin (ATV) had better effects than nonpretreated BMSC-Exos both *in vivo* and *in vitro* [137]. Furthermore, the combination of pluronic F-127 (PF-127) hydrogel and hucMSC-derived exosomes could significantly enhance wound healing and promote granulation tissue regeneration [138]. PF-127 thermosensitive hydrogels could carry and sustainably release exosomes, so biomaterial-based exosome therapy may be helpful for diabetic wound healing. In addition to MSC-EVs, circulating exosomes isolated from patients with DM may also be used for treating diabetic foot ulcers [139, 140]. Taken together, the available evidence encourages further studies to explore the potential of EVs as a future diagnostic and therapeutic tool for diabetic foot ulcer.

4.4.3. Diabetic Nephropathy. Diabetic nephropathy (DN) is one of the microvascular complications of DM, which causes end-stage renal disease [141]. Its clinical diagnosis mainly depends on the presence of proteinuria and the estimated decrease in the glomerular filtration rate [142]. However, renal function may deteriorate before microalbuminuria can be detected [143]. Therefore, more sensitive biomarkers are required for DN diagnosis. According to recent studies, urinary EVs might be potential noninvasive biomarkers for early diagnosis and treatment of DN [57, 144].

Currently, the treatment of DN is divided into two main areas: (i) early treatments that include strict control of blood sugar and blood pressure to prevent DN from developing and (ii) comprehensive treatments for advanced DN that include dialysis or kidney transplantation [145]. However, the incidence of end-stage renal disease remains high. BMSCs-Exos have been proven to participate in slowing down the progression of DN by controlling hyperglycemia and protecting kidney function [141]. In addition, exosomes derived from ADSCs and hucMSCs have also been confirmed to be used for the treatment of DN [146, 147] (Table 2). These studies have laid the foundation for the application of EVs as a new biological therapy for DN. However, the protective mechanism of EVs on DN requires further researches.

4.4.4. Diabetic Retinopathy. The early stages of diabetic retinopathy (DR) do not cause any symptoms, but if left unchecked, it can cause significant retinal damage [148]. Recently, researchers have found that miR-431-5p in serum-derived EVs is upregulated in proliferative diabetic retinopathy (PDR) patients [58]. In addition, two other studies also reported that miR-150-5p, miR-21-3p, and miR-30b-5p extracted from circulating EVs may serve as biomarkers for predicting DR [59, 60]. Except for miRNAs, it is indicated that TNFAIP8 was upregulated in both plasma small extracellular vesicle and vitreous of DR patients [61]. The collection of these molecules will be helpful to DR diagnosis. In the treatment of DR, miR-192 in MSC-EVs could target and negatively regulate ITGA1, thereby ameliorating diabetic retinal damage by decreasing the inflammatory response and angiogenesis [149]. Similarly, hucMSC-derived small EVs could upregulate miR-18b and reduce retinal vascular leakage and retinal thickness [150]. Overall, these findings provide new insights into EV-based therapy for DR.

4.4.5. Diabetic Macrovascular Complications. Macrovascular complications of DM include accelerated cardiovascular disease, which causes myocardial infarction, and cerebrovascular disease, which manifests as stroke. It has been reported that EVs could be used to treat diabetic macrovascular diseases. For example, Venkat et al. [151] reported that $CD133^+$ exosomes upregulated miR-126 expression and reduced the expression of myocardial inflammatory factors, thus improving cardiac function of T2DM stroke mice. Other studies have also reported favorable therapeutic effects of EVs [12, 152]. Liu et al. [153] proved that increased levels of miR-1443p in diabetic exosomes could weaken endothelial progenitor cells' ability to mobilize. It may be possible to improve cardiac repair after myocardial infarction by using enriched miR-1443p.

4.5. Roles of EVs in Skin Aging. Human skin is a finely structured organ that acts as a natural shield, sensor, and alarm of the body [154]. Both internal and external factors are strong incentives for skin changes. As the main external cause of skin aging, ultraviolet (UV) has strong skin penetration ability and induces skin photoaging [155]. Although there are differences in the clinical features and histological characteristics in intrinsic and extrinsic skin aging [156], the underlying molecular pathways are similar: extracellular matrix (ECM) degradation caused by MMP overexpression [157]. Furthermore, aging skin shows a higher proportion of senescent cells, and aging microenvironment constructed by gradually accumulated senescent cells is easier to accelerate skin aging [32].

Stem cells can theoretically solve the problem of collagen loss in aging skin. At present, stem cells for injection mainly come from autologous adipose tissue [158], but this method is expensive and risky, thereby limiting its prevalence. Besides, the clinical safety of iPSC therapy remains uncertain due to the introduction of oncogenes. Skin antiaging goes through a complex process of skin tissue repair and skin function recovery. Under this complexity, efficient communication between skin cells is essential. EV-mediated cell information exchange is widely involved in the regulation of skin cell function [159]. In recent years, their strong roles in the proliferation of epidermal cells and the recovery of dermal cells' vitality made them potential drugs to reverse skin aging. Here, we explored the different effects of several EVs against skin aging.

UV can directly contribute to the decline of human dermal fibroblast (HDF) function. Choi et al. [160] observed that human ADSC-EVs could alleviate the damage of HDF migration and proliferation ability caused by UVB irradiation. Further study revealed that EV treatment could upregulate the level of tissue inhibitors of MMP-1 and TGF-β1 in UV-irradiated HDF cells and then inhibit the degradation of collagen. In addition, the increase of ROS induced by UV has a major influence in photoaging [157]. On the one hand, ROS may be a necessary signal messenger for melanin production, which protects against UVA-induced skin reaction [161]. However, on the other hand, excessive ROS will lead to DNA damage, inflammatory reactions, decreased production of antioxidants, and increased MMP expression in skin cells. Our past study have shown that hucMSC-Exos rich in 14-3-3ζ could upregulate the expression of SIRT1 in skin keratinocytes, thereby inhibiting oxidative stress and autophagy activation induced by UV irradiation [162]. Besides, exosomes derived from HDF could reduce skin wrinkles in nude mice caused by UVB irradiation, and some SASP factors were also relatively reduced [163]. Aging skin appears as functional deterioration and shows an increased proportion of senescent skin cells [164, 165]. The immune homeostasis function of macrophages is impaired with age, resulting in the decline of its selective scavenging ability to aging cells. This will contribute to the abnormal accumulation of senescent cells in skin [166]. However, there is little research on how UV-induced senescent cells bypass immune clearance. An effective skin rejuvenation strategy may involve applying EVs to restore the immune surveillance ability from aging skin. It may be feasible to externally supplement EVs from young macrophages to promote the recovery of the function of aging macrophages. And it may be an important research direction to analyze the differences between homogeneous EVs from young and aging macrophages to find possible beneficial molecules. Hence, further research is required to elucidate how to delay skin aging by regulating the immune activity of macrophages through EVs. Because of the existence of the skin barrier, simply applying EVs to the skin surface will sharply reduce its effectiveness. Studies have shown that ADSC-EVs combined with a microneedle roller can effectively reduce the aging phenotype of SKH-1 mice [167], but this method of promoting EV absorption could easily increase skin sensitivity. And in recent years, the microneedle patch has become a research hotspot in the field of dermatology based on its advantages of minimal invasiveness, painlessness, and high drug loading. However, this transdermal drug delivery system requires special equipment and faces the risk of failure of preloaded active substances. Thus, modifying the physical properties of EVs while maintaining its activity has become a challenge for the exogenous supplement of EVs in the field of skin antiaging.

5. Conclusions and Perspectives

Cellular senescence and aging are inseparable. Although some mechanisms leading to cellular senescence and many antiaging targets have been found, this may only be the tip of the iceberg of aging. Further clarifying the aging mechanism is still the basis of antiaging treatment. EVs, especially exosomes, have been proven to participate in the regulation of various diseases and have shown their great potential in becoming biomarkers and therapeutic agents in aging-related diseases. Some studies on EVs have entered the stage of clinical trials, but challenges continue to exist when meeting clinical requirements. First, the current research of EVs mainly focused on whether they have curative effects, but which component of EVs take effect is not comprehensive. This unknown factor raises doubts about the safety and effectiveness of EVs. Second, there is still a lack of strict standard in EVs' quality management. Different tissue sources, donor cells, and preparation methods will produce heterogeneous EVs, and with the inconsistency of the *in vivo* and *in vitro* models between laboratories, the effective concentration and intervention methods of EVs in different diseases have not been finalized, which hinders their clinical transformation. Moreover, EVs are natural drug carriers, and the appropriate ratio to drugs is the important premise for their function; therefore, a scientific matching system is needed. Besides, regarding the problem of low EV yield and purification efficiency, some researchers found that human iPSC could produce EVs several times higher than MSC under specific culture conditions, and these iPSC-EVs could be efficiently ingested by target cells [168]. This suggests that human iPSC as the source cell of EVs may become a more promising choice in the field of antiaging. Finally, the role of standalone therapy is always limited. Exploring the combined medication of EVs and other effective drugs may become the trend of development in the future.

Despite the challenges, beneficial achievements have been made in the field of EVs in recent years. With the continuous maturity in separation, purification, and identification standards, EVs are expected to be candidates for the diagnosis and treatment of clinical aging-related diseases. Moreover, preventing aging is an urgent need of developed society, and the research on the preventive efficacy of EVs in aging-related diseases may become a new research direction of modern medicine.

Conflicts of Interest

The authors declare that there is no conflict of interest regarding the publication of this paper.

Authors' Contributions

Zixuan Sun, Xiaomei Hou, and Jiaxin Zhang contributed equally to this article. All authors have read and agreed to the published version of the manuscript.

Acknowledgments

This work was supported by the National Natural Science Foundation of China (grant number 82003379), Zhenjiang Key Laboratory of High Technology Research on Exosomes Foundation and Transformation Application (grant number SS2018003), Jiangsu Gerontology Clinical Technology

Application Research Project Unit (grant number LD2021011), Entrusted Project of Jiangsu Population Society (grant number JSPA2019015), and Priority Academic Program Development of Jiangsu Higher Education Institutions Project (Phase III).

References

[1] D. Saul and R. L. Kosinsky, "Epigenetics of aging and aging-associated diseases," *International Journal of Molecular Sciences*, vol. 22, no. 1, p. 401, 2021.

[2] D. Muñoz-Espín and M. Serrano, "Cellular senescence: from physiology to pathology," *Nature Reviews. Molecular Cell Biology*, vol. 15, no. 7, pp. 482–496, 2014.

[3] A. Kowald, J. F. Passos, and T. B. L. Kirkwood, "On the evolution of cellular senescence," *Aging Cell*, vol. 19, no. 12, article e13270, 2020.

[4] R. J. Pignolo, J. F. Passos, S. Khosla, T. Tchkonia, and J. L. Kirkland, "Reducing senescent cell burden in aging and disease," *Trends in Molecular Medicine*, vol. 26, no. 7, article S1471491420300770, pp. 630–638, 2020.

[5] Y. Yin, H. Chen, Y. Wang, L. Zhang, and X. Wang, "Roles of extracellular vesicles in the aging microenvironment and age-related diseases," *Journal of Extracellular Vesicles*, vol. 10, no. 12, article e12154, 2021.

[6] R. I. Martínez-Zamudio, L. Robinson, P.-F. Roux, and O. Bischof, "SnapShot: cellular senescence pathways," *Cell*, vol. 170, no. 4, pp. 816–816.e1, 2017.

[7] H. Shao, H. Im, C. M. Castro, X. Breakefield, R. Weissleder, and H. Lee, "New technologies for analysis of extracellular vesicles," *Chemical Reviews*, vol. 118, no. 4, pp. 1917–1950, 2018.

[8] P. Hu, Q. Yang, Q. Wang et al., "Mesenchymal stromal cells-exosomes: a promising cell-free therapeutic tool for wound healing and cutaneous regeneration," *Burns & Trauma*, vol. 7, p. 38, 2019.

[9] Y. Yang, Y. Hong, E. Cho, G. B. Kim, and I. S. Kim, "Extracellular vesicles as a platform for membrane-associated therapeutic protein delivery," *Journal of Extracellular Vesicles*, vol. 7, no. 1, p. 1440131, 2018.

[10] T. Misawa, Y. Tanaka, R. Okada, and A. Takahashi, "Biology of extracellular vesicles secreted from senescent cells as senescence-associated secretory phenotype factors," *Geriatrics & Gerontology International*, vol. 20, no. 6, pp. 539–546, 2020.

[11] T. Kadota, Y. Fujita, Y. Yoshioka, J. Araya, K. Kuwano, and T. Ochiya, "Emerging role of extracellular vesicles as a senescence-associated secretory phenotype: insights into the pathophysiology of lung diseases," *Molecular Aspects of Medicine*, vol. 60, pp. 92–103, 2018.

[12] P. Venkat, A. Zacharek, J. Landschoot-Ward et al., "Exosomes derived from bone marrow mesenchymal stem cells harvested from type two diabetes rats promotes neurorestorative effects after stroke in type two diabetes rats," *Experimental Neurology*, vol. 334, p. 113456, 2020.

[13] R. Kalluri and V. S. LeBleu, "The biology, function, and biomedical applications of exosomes," *Science*, vol. 367, no. 6478, 2020.

[14] A. S. Jadli, N. Ballasy, P. Edalat, and V. B. Patel, "Inside(sight) of tiny communicator: exosome biogenesis, secretion, and uptake," *Molecular and Cellular Biochemistry*, vol. 467, no. 1-2, pp. 77–94, 2020.

[15] T. Wollert and J. H. Hurley, "Molecular mechanism of multivesicular body biogenesis by ESCRT complexes," *Nature*, vol. 464, no. 7290, pp. 864–869, 2010.

[16] Z. Sun, J. Zhang, J. Li et al., "Roles of mesenchymal stem cell-derived exosomes in cancer development and targeted therapy," *Stem Cells International*, vol. 2021, Article ID 9962194, 10 pages, 2021.

[17] K. Trajkovic, C. Hsu, S. Chiantia et al., "Ceramide triggers budding of exosome vesicles into multivesicular endosomes," *Science*, vol. 319, no. 5867, pp. 1244–1247, 2008.

[18] C. Hsu, Y. Morohashi, S. I. Yoshimura et al., "Regulation of exosome secretion by Rab35 and its GTPase-activating proteins TBC1D10A-C," *The Journal of Cell Biology*, vol. 189, no. 2, pp. 223–232, 2010.

[19] L. A. Mulcahy, R. C. Pink, and D. R. F. Carter, "Routes and mechanisms of extracellular vesicle uptake," *Journal of Extracellular Vesicles*, vol. 3, no. 1, 2014.

[20] L. A. Mulcahy, R. C. Pink, and D. R. F. Carter, "Exosomes: composition, biogenesis and function," *Nature Reviews. Immunology*, vol. 2, no. 8, pp. 569–579, 2002.

[21] A. Hernandez-Segura, J. Nehme, and M. Demaria, "Hallmarks of cellular senescence," *Trends in Cell Biology*, vol. 28, no. 6, pp. 436–453, 2018.

[22] T. M. Loo, K. Miyata, Y. Tanaka, and A. Takahashi, "Cellular senescence and senescence-associated secretory phenotype via the cGAS-STING signaling pathway in cancer," *Cancer Science*, vol. 111, no. 2, pp. 304–311, 2020.

[23] P. Lecot, F. Alimirah, P. Y. Desprez, J. Campisi, and C. Wiley, "Context-dependent effects of cellular senescence in cancer development," *British Journal of Cancer*, vol. 114, no. 11, pp. 1180–1184, 2016.

[24] J. L. Tarry-Adkins, C. E. Aiken, L. Dearden, D. S. Fernandez-Twinn, and S. Ozanne, "Exploring telomere dynamics in aging male rat tissues: can tissue-specific differences contribute to age-associated pathologies?," *Gerontology*, vol. 67, no. 2, pp. 233–242, 2021.

[25] L. B. Chen, S. Ma, T. X. Jiang, and X. B. Qiu, "Transcriptional upregulation of proteasome activator Blm10 antagonizes cellular aging," *Biochemical and Biophysical Research Communications*, vol. 532, no. 2, pp. 211–218, 2020.

[26] Z. R. Jarrell, M. R. Smith, X. Hu et al., "Plasma acylcarnitine levels increase with healthy aging," *Aging (Albany NY)*, vol. 12, no. 13, pp. 13555–13570, 2020.

[27] L. N. Lakshmanan, Z. Yee, L. F. Ng, R. Gunawan, B. Halliwell, and J. Gruber, "Clonal expansion of mitochondrial DNA deletions is a private mechanism of aging in long-lived animals," *Aging Cell*, vol. 17, no. 5, article e12814, 2018.

[28] C. D. Wiley, M. C. Velarde, P. Lecot et al., "Mitochondrial dysfunction induces senescence with a distinct secretory phenotype," *Cell Metabolism*, vol. 23, no. 2, article S1550413115005781, pp. 303–314, 2016.

[29] T. Nacarelli, L. Lau, T. Fukumoto et al., "NAD^+ metabolism governs the proinflammatory senescence-associated secretome," *Nature Cell Biology*, vol. 21, no. 3, pp. 397–407, 2019.

[30] J. M. Son and C. Lee, "Mitochondria: multifaceted regulators of aging," *BMB Reports*, vol. 52, no. 1, pp. 13–23, 2019.

[31] F. Galkin, P. Mamoshina, A. Aliper, J. P. de Magalhães, V. N. Gladyshev, and A. Zhavoronkov, "Biohorology and

biomarkers of aging: current state-of-the-art, challenges and opportunities," *Ageing Research Reviews*, vol. 60, p. 101050, 2020.

[32] C. Y. Ho and O. Dreesen, "Faces of cellular senescence in skin aging," *Mechanisms of Ageing and Development*, vol. 198, article S004763742100097X, p. 111525, 2021.

[33] A. Picca, F. Guerra, R. Calvani et al., "Mitochondrial dysfunction and aging: insights from the analysis of extracellular vesicles," *International Journal of Molecular Sciences*, vol. 20, no. 4, p. 805, 2019.

[34] L. Jia, M. Zhu, C. Kong et al., "Blood neuro-exosomal synaptic proteins predict Alzheimer's disease at the asymptomatic stage," *Alzheimers Dement*, vol. 17, no. 1, pp. 49–60, 2021.

[35] T. Soares Martins, D. Trindade, M. Vaz et al., "Diagnostic and therapeutic potential of exosomes in Alzheimer's disease," *Journal of Neurochemistry*, vol. 156, no. 2, pp. 162–181, 2021.

[36] A. Guerrero, B. de Strooper, and I. L. Arancibia-Cárcamo, "Cellular senescence at the crossroads of inflammation and Alzheimer's disease," *Trends in Neurosciences*, vol. 44, no. 9, pp. 714–727, 2021.

[37] Y. Hou, X. Dan, M. Babbar et al., "Ageing as a risk factor for neurodegenerative disease," *Nature Reviews. Neurology*, vol. 15, no. 10, pp. 565–581, 2019.

[38] S. Saez-Atienzar and E. Masliah, "Cellular senescence and Alzheimer disease: the egg and the chicken scenario," *Nature Reviews. Neuroscience*, vol. 21, no. 8, pp. 433–444, 2020.

[39] E. Eren, J. F. V. Hunt, M. Shardell et al., "Extracellular vesicle biomarkers of Alzheimer's disease associated with subclinical cognitive decline in late middle age," *Alzheimers Dement*, vol. 16, no. 9, pp. 1293–1304, 2020.

[40] T. Soares Martins, R. Marçalo, M. Ferreira et al., "Exosomal Aβ-Binding Proteins Identified by "In Silico" Analysis Represent Putative Blood-Derived Biomarker Candidates for Alzheimer's Disease," *International Journal of Molecular Sciences*, vol. 22, no. 8, p. 3933, 2021.

[41] D. Gu, F. Liu, M. Meng et al., "Elevated matrix metalloproteinase-9 levels in neuronal extracellular vesicles in Alzheimer's disease," *Annals of Clinical Translational Neurology*, vol. 7, no. 9, pp. 1681–1691, 2020.

[42] A. Longobardi, L. Benussi, R. Nicsanu et al., "Plasma extracellular vesicle size and concentration are altered in Alzheimer's disease, dementia with Lewy bodies, and frontotemporal dementia," *Frontiers in Cell and Development Biology*, vol. 9, p. 667369, 2021.

[43] F. Delgado-Peraza, C. J. Nogueras-Ortiz, O. Volpert et al., "Neuronal and astrocytic extracellular vesicle biomarkers in blood reflect brain pathology in mouse models of Alzheimer's disease," *Cell*, vol. 10, no. 5, p. 993, 2021.

[44] D. Kapogiannis, M. Mustapic, M. D. Shardell et al., "Association of extracellular vesicle biomarkers with Alzheimer disease in the Baltimore longitudinal study of aging," *JAMA Neurology*, vol. 76, no. 11, pp. 1340–1351, 2019.

[45] A. Zhao, Y. Li, Y. Yan et al., "Increased prediction value of biomarker combinations for the conversion of mild cognitive impairment to Alzheimer's dementia," *Translational Neurodegeneration*, vol. 9, no. 1, p. 30, 2020.

[46] B. Li, J. Liu, G. Gu, X. Han, Q. Zhang, and W. Zhang, "Impact of neural stem cell-derived extracellular vesicles on mitochondrial dysfunction, sirtuin 1 level, and synaptic deficits in Alzheimer's disease," *Journal of Neurochemistry*, vol. 154, no. 5, pp. 502–518, 2020.

[47] L. A. Apodaca, A. A. D. Baddour, C. Garcia Jr. et al., "Human neural stem cell-derived extracellular vesicles mitigate hallmarks of Alzheimer's disease," *Alzheimer's Research & Therapy*, vol. 13, no. 1, p. 57, 2021.

[48] Y. A. Chen, C. H. Lu, C. C. Ke et al., "Mesenchymal stem cell-derived exosomes ameliorate Alzheimer's disease pathology and improve cognitive deficits," *Biomedicine*, vol. 9, no. 6, p. 594, 2021.

[49] M. Losurdo, M. Pedrazzoli, C. D'Agostino et al., "Intranasal delivery of mesenchymal stem cell-derived extracellular vesicles exerts immunomodulatory and neuroprotective effects in a 3xTg model of Alzheimer's disease," *Stem Cells Translational Medicine*, vol. 9, no. 9, pp. 1068–1084, 2020.

[50] L. Zhai, H. Shen, Y. Sheng, and Q. Guan, "ADMSC Exo-microRNA-22 improve neurological function and neuroinflammation in mice with Alzheimer's disease," *Journal of Cellular and Molecular Medicine*, vol. 25, no. 15, pp. 7513–7523, 2021.

[51] Z. Deng, J. Wang, Y. Xiao et al., "Ultrasound-mediated augmented exosome release from astrocytes alleviates amyloid-β-induced neurotoxicity," *Theranostics*, vol. 11, no. 9, pp. 4351–4362, 2021.

[52] Y. Qi, L. Guo, Y. Jiang, Y. Shi, H. Sui, and L. Zhao, "Brain delivery of quercetin-loaded exosomes improved cognitive function in AD mice by inhibiting phosphorylated tau-mediated neurofibrillary tangles," *Drug Delivery*, vol. 27, no. 1, pp. 745–755, 2020.

[53] I. O. Sun, A. Santelli, A. Abumoawad et al., "Loss of renal peritubular capillaries in hypertensive patients is detectable by urinary endothelial microparticle levels," *Hypertension*, vol. 72, no. 5, pp. 1180–1188, 2018.

[54] A. Santelli, I. O. Sun, A. Eirin et al., "Senescent kidney cells in hypertensive patients release urinary extracellular vesicles," *Journal of the American Heart Association*, vol. 8, no. 11, article e012584, 2019.

[55] A. Tapia-Castillo, D. Guanzon, C. Palma et al., "Downregulation of exosomal miR-192-5p and miR-204-5p in subjects with nonclassic apparent mineralocorticoid excess," *Journal of Translational Medicine*, vol. 17, no. 1, p. 392, 2019.

[56] L. N. Masi, L. N. Masi, P. A. Lotufo et al., "Profiling plasma-extracellular vesicle proteins and microRNAs in diabetes onset in middle-aged male participants in the ELSA-Brasil study," *Physiological Reports*, vol. 9, no. 3, article e14731, 2021.

[57] Y. Zhao, A. Shen, F. Guo et al., "Urinary exosomal miRNA-4534 as a novel diagnostic biomarker for diabetic kidney disease," *Frontiers in Endocrinology*, vol. 11, p. 590, 2020.

[58] B. Yu, M. Xiao, F. Yang et al., "MicroRNA-431-5p encapsulated in serum extracellular vesicles as a biomarker for proliferative diabetic retinopathy," *The International Journal of Biochemistry & Cell Biology*, vol. 135, p. 105975, 2021.

[59] A. Mazzeo, T. Lopatina, C. Gai, M. Trento, M. Porta, and E. Beltramo, "Functional analysis of miR-21-3p, miR-30b-5p and miR-150-5p shuttled by extracellular vesicles from diabetic subjects reveals their association with diabetic retinopathy," *Experimental Eye Research*, vol. 184, pp. 56–63, 2019.

[60] A. Mazzeo, E. Beltramo, T. Lopatina, C. Gai, M. Trento, and M. Porta, "Molecular and functional characterization of circulating extracellular vesicles from diabetic patients with and without retinopathy and healthy subjects," *Experimental Eye Research*, vol. 176, pp. 69–77, 2018.

[61] J. Xiao, H. Zhang, F. Yang et al., "Proteomic analysis of plasma sEVs reveals that TNFAIP8 is a new biomarker of cell proliferation in diabetic retinopathy," *Journal of Proteome Research*, vol. 20, no. 3, pp. 1770–1782, 2021.

[62] M. Muraca and A. Cappariello, "The role of extracellular vesicles (EVs) in the epigenetic regulation of bone metabolism and osteoporosis," *International Journal of Molecular Sciences*, vol. 21, no. 22, article ijms21228682, p. 8682, 2020.

[63] X. Zhang, W. Wang, Y. Wang et al., "Extracellular vesicle-encapsulated miR-29b-3p released from bone marrow-derived mesenchymal stem cells underpins osteogenic differentiation," *Frontiers in Cell and Development Biology*, vol. 8, p. 581545, 2020.

[64] K. Chen, Y. Jiao, L. Liu et al., "Communications between bone marrow macrophages and bone cells in bone remodeling," *Frontiers in Cell and Development Biology*, vol. 8, p. 598263, 2020.

[65] Z. Yang, W. Zhang, X. Ren, C. Tu, and Z. Li, "Exosomes: a friend or foe for osteoporotic fracture?," *Front Endocrinol (Lausanne)*, vol. 12, p. 679914, 2021.

[66] Z. Teng, Y. Zhu, X. Zhang, Y. Teng, and S. Lu, "Osteoporosis is characterized by altered expression of exosomal long non-coding RNAs," *Frontiers in Genetics*, vol. 11, p. 566959, 2020.

[67] J. Y. Noh, Y. Yang, and H. Jung, "Molecular mechanisms and emerging therapeutics for osteoporosis," *International Journal of Molecular Sciences*, vol. 21, no. 20, article ijms21207623, p. 7623, 2020.

[68] A. Qadir, S. Liang, Z. Wu, Z. Chen, L. Hu, and A. Qian, "Senile osteoporosis: the involvement of differentiation and senescence of bone marrow stromal cells," *International Journal of Molecular Sciences*, vol. 21, no. 1, p. 349, 2020.

[69] A. Chandra and J. Rajawat, "Skeletal aging and osteoporosis: mechanisms and therapeutics," *International Journal of Molecular Sciences*, vol. 22, no. 7, p. 3553, 2021.

[70] S. Fulzele, B. Mendhe, A. Khayrullin et al., "Muscle-derived miR-34a increases with age in circulating extracellular vesicles and induces senescence of bone marrow stem cells," *Aging*, vol. 11, no. 6, pp. 1791–1803, 2019.

[71] Q. Lu, H. Qin, H. Tan et al., "Senescence osteoblast-derived exosome-mediated miR-139-5p regulates endothelial cell functions," *BioMed Research International*, vol. 2021, Article ID 5576023, 12 pages, 2021.

[72] M. Furmanik, R. van Gorp, M. Whitehead et al., "Endoplasmic reticulum stress mediates vascular smooth muscle cell calcification via increased release of Grp78 (glucose-regulated protein, 78 kDa)-loaded extracellular vesicles," *Arteriosclerosis, Thrombosis, and Vascular Biology*, vol. 41, no. 2, pp. 898–914, 2021.

[73] L. A. Pescatore, L. F. Gamarra, and M. Liberman, "Multifaceted mechanisms of vascular calcification in aging," *Arteriosclerosis, Thrombosis, and Vascular Biology*, vol. 39, no. 7, pp. 1307–1316, 2019.

[74] Z. X. Wang, Z. W. Luo, F. X. Z. Li et al., "Aged bone matrix-derived extracellular vesicles as a messenger for calcification paradox," *Nature Communications*, vol. 13, no. 1, p. 1453, 2022.

[75] W. Wei, X. Guo, L. Gu et al., "Bone marrow mesenchymal stem cell exosomes suppress phosphate-induced aortic calcification via SIRT6-HMGB1 deacetylation," *Stem Cell Research & Therapy*, vol. 12, no. 1, p. 235, 2021.

[76] Y. Guo, S. Bao, W. Guo et al., "Bone marrow mesenchymal stem cell-derived exosomes alleviate high phosphorus-induced vascular smooth muscle cells calcification by modifying microRNA profiles," *Functional & Integrative Genomics*, vol. 19, no. 4, pp. 633–643, 2019.

[77] Z. W. Luo, F. X. Z. Li, Y. W. Liu et al., "Aptamer-functionalized exosomes from bone marrow stromal cells target bone to promote bone regeneration," *Nanoscale*, vol. 11, no. 43, pp. 20884–20892, 2019.

[78] J. Xun, C. Li, M. Liu et al., "Serum exosomes from young rats improve the reduced osteogenic differentiation of BMSCs in aged rats with osteoporosis after fatigue loading in vivo," *Stem Cell Research & Therapy*, vol. 12, no. 1, p. 424, 2021.

[79] X. Wang, X. Li, J. Li et al., "Mechanical loading stimulates bone angiogenesis through enhancing type H vessel formation and downregulating exosomal miR-214-3p from bone marrow-derived mesenchymal stem cells," *The FASEB Journal*, vol. 35, no. 1, article e21150, 2021.

[80] K. F. Eichholz, I. Woods, M. Riffault et al., "Human bone marrow stem/stromal cell osteogenesis is regulated via mechanically activated osteocyte-derived extracellular vesicles," *Stem Cells Translational Medicine*, vol. 9, no. 11, pp. 1431–1447, 2020.

[81] Y. Hu, Y. Zhang, C. Y. Ni et al., "Human umbilical cord mesenchymal stromal cells-derived extracellular vesicles exert potent bone protective effects by CLEC11A-mediated regulation of bone metabolism," *Theranostics*, vol. 10, no. 5, pp. 2293–2308, 2020.

[82] X. Yang, J. Yang, P. Lei, and T. Wen, "LncRNA MALAT1 shuttled by bone marrow-derived mesenchymal stem cells-secreted exosomes alleviates osteoporosis through mediating microRNA-34c/SATB2 axis," *Aging*, vol. 11, no. 20, article 102264, pp. 8777–8791, 2019.

[83] S. Sonoda, S. Murata, K. Nishida et al., "Extracellular vesicles from deciduous pulp stem cells recover bone loss by regulating telomerase activity in an osteoporosis mouse model," *Stem Cell Research & Therapy*, vol. 11, no. 1, p. 296, 2020.

[84] Y. Wei, C. Tang, J. Zhang et al., "Extracellular vesicles derived from the mid-to-late stage of osteoblast differentiation markedly enhance osteogenesis *in vitro* and *in vivo*," *Biochemical and Biophysical Research Communications*, vol. 514, no. 1, pp. 252–258, 2019.

[85] M. Qiu, S. Zhai, Q. Fu, and D. Liu, "Bone marrow mesenchymal stem cells-derived exosomal microRNA-150-3p promotes osteoblast proliferation and differentiation in osteoporosis," *Human Gene Therapy*, vol. 32, no. 13-14, pp. 717–729, 2021.

[86] G. D. Lu, P. Cheng, T. Liu, and Z. Wang, "BMSC-derived exosomal miR-29a promotes angiogenesis and osteogenesis," *Frontiers in Cell and Development Biology*, vol. 8, p. 608521, 2020.

[87] X. Zhang, Y. Wang, H. Zhao et al., "Extracellular vesicle-encapsulated miR-22-3p from bone marrow mesenchymal stem cell promotes osteogenic differentiation via FTO inhibition," *Stem Cell Research & Therapy*, vol. 11, no. 1, p. 227, 2020.

[88] H. Song, X. Li, Z. Zhao et al., "Reversal of osteoporotic activity by endothelial cell-secreted bone targeting and biocompatible exosomes," *Nano Letters*, vol. 19, no. 5, pp. 3040–3048, 2019.

[89] Y. Wang, J. Yao, L. Cai et al., "Bone-targeted extracellular vesicles from mesenchymal stem cells for osteoporosis therapy," *International Journal of Nanomedicine*, vol. 15, pp. 7967–7977, 2020.

[90] M. C. Oliveira, B. C. H. Pieters, P. B. Guimarães et al., "Bovine milk extracellular vesicles are osteoprotective by increasing osteocyte numbers and targeting RANKL/OPG system in experimental models of bone loss," *Frontiers in Bioengineering and Biotechnology*, vol. 8, p. 891, 2020.

[91] B. Yun, B. E. Maburutse, M. Kang et al., "*Short communication:* Dietary bovine milk -derived exosomes improve bone health in an osteoporosis-induced mouse model," *Journal of Dairy Science*, vol. 103, no. 9, pp. 7752–7760, 2020.

[92] M. Gatti, F. Beretti, M. Zavatti et al., "Amniotic fluid stem cell-derived extracellular vesicles counteract steroid-induced osteoporosis in vitro," *International Journal of Molecular Sciences*, vol. 22, no. 1, p. 38, 2020.

[93] Y. Hu, R. Xu, C. Y. Chen et al., "Extracellular vesicles from human umbilical cord blood ameliorate bone loss in senile osteoporotic mice," *Metabolism*, vol. 95, pp. 93–101, 2019.

[94] K. Otani, M. Yokoya, T. Kodama et al., "Plasma exosomes regulate systemic blood pressure in rats," *Biochemical and Biophysical Research Communications*, vol. 503, no. 2, pp. 776–783, 2018.

[95] L. Cambier, J. F. Giani, W. Liu et al., "Angiotensin II-induced end-organ damage in mice is attenuated by human exosomes and by an exosomal Y RNA fragment," *Hypertension*, vol. 72, no. 2, pp. 370–380, 2018.

[96] R. Feng, M. Ullah, K. Chen, Q. Ali, Y. Lin, and Z. Sun, "Stem cell-derived extracellular vesicles mitigate ageing-associated arterial stiffness and hypertension," *Journal of Extracellular Vesicles*, vol. 9, no. 1, p. 1783869, 2020.

[97] R. Xue, W. Tan, Y. Wu et al., "Role of exosomal miRNAs in heart failure," *Frontiers in Cardiovascular Medicine*, vol. 7, p. 592412, 2020.

[98] X. S. Ren, Y. Tong, Y. Qiu et al., "miR155-5p in adventitial fibroblasts-derived extracellular vesicles inhibits vascular smooth muscle cell proliferation via suppressing angiotensin-converting enzyme expression," *Journal of Extracellular Vesicles*, vol. 9, no. 1, p. 1698795, 2020.

[99] Y. Nakamura, S. Kita, Y. Tanaka et al., "Adiponectin stimulates exosome release to enhance mesenchymal stem-cell-driven therapy of heart failure in mice," *Molecular Therapy*, vol. 28, no. 10, pp. 2203–2219, 2020.

[100] L. Qiao, S. Hu, S. Liu et al., "MicroRNA-21-5p dysregulation in exosomes derived from heart failure patients impairs regenerative potential," *The Journal of Clinical Investigation*, vol. 129, no. 6, pp. 2237–2250, 2019.

[101] N. El Harane, A. Kervadec, V. Bellamy et al., "Acellular therapeutic approach for heart failure: in vitro production of extracellular vesicles from human cardiovascular progenitors," *European Heart Journal*, vol. 39, no. 20, pp. 1835–1847, 2018.

[102] M. T. Chen, Y. T. Zhao, L. Y. Zhou et al., "Exosomes derived from human umbilical cord mesenchymal stem cells enhance insulin sensitivity in insulin resistant human adipocytes," *Current Medical Science*, vol. 41, no. 1, pp. 87–93, 2021.

[103] Y. Sun, Y. Zhou, Y. Shi et al., "Expression of *miRNA-29* in Pancreatic β Cells Promotes Inflammation and Diabetes via TRAF3," *Cell Reports*, vol. 34, no. 1, p. 108576, 2021.

[104] D. Corella and J. M. Ordovás, "Aging and cardiovascular diseases: the role of gene-diet interactions," *Ageing Research Reviews*, vol. 18, pp. 53–73, 2014.

[105] C. D. Mathers and D. Loncar, "Projections of global mortality and burden of disease from 2002 to 2030," *PLoS Medicine*, vol. 3, no. 11, article e442, 2006.

[106] S. Du, H. Ling, Z. Guo, Q. Cao, and C. Song, "Roles of exosomal miRNA in vascular aging," *Pharmacological Research*, vol. 165, p. 105278, 2021.

[107] Y. Q. Ni, X. Lin, J. K. Zhan, and Y. S. Liu, "Roles and functions of exosomal non-coding RNAs in vascular aging," *Aging and Disease*, vol. 11, no. 1, pp. 164–178, 2020.

[108] F. Triposkiadis, A. Xanthopoulos, and J. Butler, "Cardiovascular Aging and Heart Failure:," *Journal of the American College of Cardiology*, vol. 74, no. 6, pp. 804–813, 2019.

[109] A. Sheydina, D. R. Riordon, and K. R. Boheler, "Molecular mechanisms of cardiomyocyte aging," *Clinical Science (London, England)*, vol. 121, no. 8, pp. 315–329, 2011.

[110] K. Tepp, M. Puurand, N. Timohhina et al., "Changes in the mitochondrial function and in the efficiency of energy transfer pathways during cardiomyocyte aging," *Molecular and Cellular Biochemistry*, vol. 432, no. 1-2, article 3005, pp. 141–158, 2017.

[111] Y. Zhang, C. Wang, J. Zhou et al., "Complex inhibition of autophagy by mitochondrial aldehyde dehydrogenase shortens lifespan and exacerbates cardiac aging," *Biochimica et Biophysica Acta - Molecular Basis of Disease*, vol. 1863, no. 8, article S0925443917301035, pp. 1919–1932, 2017.

[112] O. Martinez-Arroyo, A. Ortega, J. Redon, and R. Cortes, "Therapeutic potential of extracellular vesicles in hypertension-associated kidney disease," *Hypertension*, vol. 77, no. 1, pp. 28–38, 2021.

[113] J. R. Zhang and H. J. Sun, "Extracellular vesicle-mediated vascular cell communications in Hypertension: mechanism insights and therapeutic potential of ncRNAs," *Cardiovascular Drugs and Therapy*, vol. 36, no. 1, pp. 157–172, 2022.

[114] P. Pittayapruek, J. Meephansan, O. Prapapan, M. Komine, and M. Ohtsuki, "Role of matrix metalloproteinases in photoaging and photocarcinogenesis," *International Journal of Molecular Sciences*, vol. 17, no. 6, p. 868, 2016.

[115] A. Mukherjee and S. Swarnakar, "Implication of matrix metalloproteinases in regulating neuronal disorder," *Molecular Biology Reports*, vol. 42, no. 1, pp. 1–11, 2015.

[116] C. Yu and J. H. Xiao, "The Keap1-Nrf2 system: a mediator between oxidative stress and aging," *Oxidative Medicine and Cellular Longevity*, vol. 2021, Article ID 6635460, 16 pages, 2021.

[117] B. Uyar, D. Palmer, A. Kowald et al., "Single-cell analyses of aging, inflammation and senescence," *Ageing Research Reviews*, vol. 64, p. 101156, 2020.

[118] M. E. Good, L. Musante, S. la Salvia et al., "Circulating extracellular vesicles in normotension restrain vasodilation in resistance arteries," *Hypertension*, vol. 75, no. 1, pp. 218–228, 2020.

[119] E. R. Barros and C. A. Carvajal, "Urinary exosomes and their cargo: potential biomarkers for mineralocorticoid arterial hypertension?," *Frontiers in Endocrinology*, vol. 8, p. 230, 2017.

[120] H. B. Muss, A. Smitherman, W. A. Wood et al., "p16 a biomarker of aging and tolerance for cancer therapy," *Translational Cancer Research*, vol. 9, no. 9, pp. 5732–5742, 2020.

[121] Q. Wu, X. Yuan, B. Li et al., "Differential miRNA expression analysis of extracellular vesicles from brain microvascular pericytes in spontaneous hypertensive rats," *Biotechnology Letters*, vol. 42, no. 3, pp. 389–401, 2020.

[122] D. Zheng, M. Huo, B. Li et al., "The role of exosomes and exosomal microRNA in cardiovascular disease," *Frontiers in Cell and Development Biology*, vol. 8, p. 616161, 2020.

[123] A. E. Berezin and A. A. Berezin, "Extracellular endothelial cell-derived vesicles: emerging role in cardiac and vascular remodeling in heart failure," *Frontiers in Cardiovascular Medicine*, vol. 7, p. 47, 2020.

[124] C. Tian, L. Gao, M. C. Zimmerman, and I. H. Zucker, "Myocardial infarction-induced microRNA-enriched exosomes contribute to cardiac Nrf2 dysregulation in chronic heart failure," *American Journal of Physiology. Heart and Circulatory Physiology*, vol. 314, no. 5, pp. H928–H939, 2018.

[125] C. Tian, L. Gao, and I. H. Zucker, "Regulation of Nrf2 signaling pathway in heart failure: role of extracellular vesicles and non-coding RNAs," *Free Radical Biology & Medicine*, vol. 167, pp. 218–231, 2021.

[126] E. Kurtzwald-Josefson, N. Zeevi-Levin, V. Rubchevsky et al., "Cardiac fibroblast-induced pluripotent stem cell-derived exosomes as a potential therapeutic mean for heart failure," *International Journal of Molecular Sciences*, vol. 21, no. 19, p. 7215, 2020.

[127] J. G. Oh, P. Lee, R. E. Gordon, S. Sahoo, C. Kho, and D. Jeong, "Analysis of extracellular vesicle miRNA profiles in heart failure," *Journal of Cellular and Molecular Medicine*, vol. 24, no. 13, pp. 7214–7227, 2020.

[128] S. Kumar, M. Vijayan, J. S. Bhatti, and P. H. Reddy, "MicroRNAs as peripheral biomarkers in aging and age-related diseases," *Progress in Molecular Biology and Translational Science*, vol. 146, pp. 47–94, 2017.

[129] J. M. Forbes and M. E. Cooper, "Mechanisms of diabetic complications," *Physiological Reviews*, vol. 93, no. 1, pp. 137–188, 2013.

[130] J. Guo, H. J. Zheng, W. Zhang et al., "Accelerated kidney aging in diabetes mellitus," *Oxidative Medicine and Cellular Longevity*, vol. 2020, Article ID 1234059, 24 pages, 2020.

[131] A. Vaiserman and O. Lushchak, "Developmental origins of type 2 diabetes: focus on epigenetics," *Ageing Research Reviews*, vol. 55, p. 100957, 2019.

[132] F. Prattichizzo, G. Matacchione, A. Giuliani et al., "Extracellular vesicle-shuttled miRNAs: a critical appraisal of their potential as nano-diagnostics and nano-therapeutics in type 2 diabetes mellitus and its cardiovascular complications," *Theranostics*, vol. 11, no. 3, pp. 1031–1045, 2021.

[133] A. Kumar, K. Sundaram, J. Mu et al., "High-fat diet-induced upregulation of exosomal phosphatidylcholine contributes to insulin resistance," *Nature Communications*, vol. 12, no. 1, p. 213, 2021.

[134] D. Li, H. Song, L. Shuo et al., "Gonadal white adipose tissue-derived exosomal miR-222 promotes obesity-associated insulin resistance," *Aging (Albany NY)*, vol. 12, no. 22, pp. 22719–22743, 2020.

[135] A. J. M. Bailey, H. Li, A. Kirkham et al., "MSC-derived extracellular vesicles to heal diabetic wounds: a systematic review and meta-analysis of preclinical animal studies," *Stem Cell Reviews and Reports*, vol. 27, no. 3, pp. S191–S192, 2021.

[136] M. Pomatto, C. Gai, F. Negro et al., "Differential therapeutic effect of extracellular vesicles derived by bone marrow and adipose mesenchymal stem cells on wound healing of diabetic ulcers and correlation to their cargoes," *International Journal of Molecular Sciences*, vol. 22, no. 8, p. 3851, 2021.

[137] M. Yu, W. Liu, J. Li et al., "Exosomes derived from atorvastatin-pretreated MSC accelerate diabetic wound repair by enhancing angiogenesis via AKT/eNOS pathway," *Stem Cell Research & Therapy*, vol. 11, no. 1, p. 350, 2020.

[138] J. Yang, Z. Chen, D. Pan, H. Li, and J. Shen, "Umbilical cord-derived mesenchymal stem cell-derived exosomes combined pluronic F127 hydrogel promote chronic diabetic wound healing and complete skin regeneration," *International Journal of Nanomedicine*, vol. 15, pp. 5911–5926, 2020.

[139] K. Chen, T. Yu, and X. Wang, "Inhibition of circulating exosomal miRNA-20b-5p accelerates diabetic wound repair," *International Journal of Nanomedicine*, vol. 16, pp. 371–381, 2021.

[140] Y. Xu, L. Ouyang, L. He, Y. Qu, Y. Han, and D. Duan, "Inhibition of exosomal miR-24-3p in diabetes restores angiogenesis and facilitates wound repair via targeting PIK3R3," *Journal of Cellular and Molecular Medicine*, vol. 24, no. 23, pp. 13789–13803, 2020.

[141] Y. Wang, S. K. Shan, B. Guo et al., "The multi-therapeutic role of MSCs in diabetic nephropathy," *Frontiers in Endocrinology*, vol. 12, p. 671566, 2021.

[142] K. Barreiro, O. P. Dwivedi, G. Leparc et al., "Comparison of urinary extracellular vesicle isolation methods for transcriptomic biomarker research in diabetic kidney disease," *Journal of Extracellular Vesicles*, vol. 10, no. 2, article e12038, 2020.

[143] J. Chen, Q. Zhang, D. Liu, and Z. Liu, "Exosomes: advances, development and potential therapeutic strategies in diabetic nephropathy," *Metabolism*, vol. 122, p. 154834, 2021.

[144] Y. Lu, D. Liu, Q. Feng, and Z. Liu, "Diabetic nephropathy: perspective on extracellular vesicles," *Frontiers in Immunology*, vol. 11, p. 943, 2020.

[145] E. Xiang, B. Han, Q. Zhang et al., "Human umbilical cord-derived mesenchymal stem cells prevent the progression of early diabetic nephropathy through inhibiting inflammation and fibrosis," *Stem Cell Research & Therapy*, vol. 11, no. 1, p. 336, 2020.

[146] J. Jin, Y. Shi, J. Gong et al., "Exosome secreted from adipose-derived stem cells attenuates diabetic nephropathy by promoting autophagy flux and inhibiting apoptosis in podocyte," *Stem Cell Research & Therapy*, vol. 10, no. 1, p. 95, 2019.

[147] Z. Z. Jiang, Y. M. Liu, X. Niu et al., "Exosomes secreted by human urine-derived stem cells could prevent kidney complications from type I diabetes in rats," *Stem Cell Research & Therapy*, vol. 7, no. 1, p. 24, 2016.

[148] S. Vujosevic, S. J. Aldington, P. Silva et al., "Screening for diabetic retinopathy: new perspectives and challenges," *The Lancet Diabetes & Endocrinology*, vol. 8, no. 4, pp. 337–347, 2020.

[149] C. Gu, H. Zhang, and Y. Gao, "Adipose mesenchymal stem cells-secreted extracellular vesicles containing microRNA-192 delays diabetic retinopathy by targeting ITGA1," *Journal of Cellular Physiology*, vol. 236, no. 7, pp. 5036–5051, 2021.

[150] Z. Xu, N. Tian, S. Li et al., "Extracellular vesicles secreted from mesenchymal stem cells exert anti- apoptotic and anti-inflammatory effects via transmitting microRNA-18b in rats with diabetic retinopathy," *International Immunopharmacology*, vol. 101, Part B, p. 108234, 2021.

[151] P. Venkat, C. Cui, Z. Chen et al., "CD133+exosome treatment improves cardiac function after stroke in type 2 diabetic mice," *Translational Stroke Research*, vol. 12, no. 1, pp. 112–124, 2021.

[152] J. Wang, S. Chen, W. Zhang, Y. Chen, and J. C. Bihl, "Exosomes from miRNA-126-modified endothelial progenitor cells alleviate brain injury and promote functional recovery after stroke," *CNS Neuroscience & Therapeutics*, vol. 26, no. 12, pp. 1255–1265, 2020.

[153] Y. Liu, J. Xu, R. Gu et al., "Circulating exosomal miR-144-3p inhibits the mobilization of endothelial progenitor cells post myocardial infarction via regulating the MMP9 pathway," *Aging (Albany NY)*, vol. 12, no. 16, pp. 16294–16303, 2020.

[154] L. Eckhart and P. L. J. M. Zeeuwen, "The skin barrier: epidermis vs environment," *Experimental Dermatology*, vol. 27, no. 8, pp. 805-806, 2018.

[155] Y. Gu, J. Han, C. Jiang, and Y. Zhang, "Biomarkers, oxidative stress and autophagy in skin aging," *Ageing Research Reviews*, vol. 59, p. 101036, 2020.

[156] M. Wlaschek, I. Tantcheva-Poór, L. Naderi et al., "Solar UV irradiation and dermal photoaging," *Journal of Photochemistry and Photobiology. B*, vol. 63, no. 1-3, pp. 41–51, 2001.

[157] L. Rittie and G. J. Fisher, "Natural and sun-induced aging of human skin," *Cold Spring Harbor Perspectives in Medicine*, vol. 5, no. 1, article a015370, 2015.

[158] Y. Zhang, X. Zhang, X. Jin et al., "Adipose collagen fragment: a novel adipose-derived extracellular matrix concentrate for skin filling," *Aesthetic Surgery Journal*, vol. 42, no. 5, pp. -NP337–NP350, 2022.

[159] U. T. T. Than, D. I. Leavesley, and T. J. Parker, "Characteristics and roles of extracellular vesicles released by epidermal keratinocytes," *Journal of the European Academy of Dermatology and Venereology*, vol. 33, no. 12, pp. 2264–2272, 2019.

[160] J. S. Choi, W. L. Cho, Y. J. Choi et al., "Functional recovery in photo-damaged human dermal fibroblasts by human adipose-derived stem cell extracellular vesicles," *Journal of Extracellular Vesicles*, vol. 8, no. 1, p. 1565885, 2019.

[161] H. Dumbuya, S. Y. Hafez, and E. Oancea, "Cross talk between calcium and ROS regulate the UVA-induced melanin response in human melanocytes," *The FASEB Journal*, vol. 34, no. 9, pp. 11605–11623, 2020.

[162] P. Wu, B. Zhang, X. Han et al., "hucMSC exosome-delivered 14-3-3ζ alleviates ultraviolet radiation-induced photodamage via SIRT1 pathway modulation," *Aging (Albany NY)*, vol. 13, no. 8, pp. 11542–11563, 2021.

[163] S. Hu, Z. Li, J. Cores et al., "Needle-free injection of exosomes derived from human dermal fibroblast spheroids ameliorates skin photoaging," *ACS Nano*, vol. 13, no. 10, pp. 11273–11282, 2019.

[164] J. M. van Deursen, "The role of senescent cells in ageing," *Nature*, vol. 509, no. 7501, article BFnature13193, pp. 439–446, 2014.

[165] M. Chaudhary, A. Khan, and M. Gupta, "Skin ageing: pathophysiology and current market treatment approaches," *Current Aging Science*, vol. 13, no. 1, pp. 22–30, 2020.

[166] X. Li, K. Yang, S. Gao et al., "Carnosine stimulates macrophage-mediated clearance of senescent skin cells through activation of the AKT2 signaling pathway by CD36 and RAGE," *Frontiers in Pharmacology*, vol. 11, p. 593832, 2020.

[167] Z. Cao, S. Jin, P. Wang et al., "Microneedle based adipose derived stem cells-derived extracellular vesicles therapy ameliorates UV-induced photoaging in SKH-1 mice," *Journal of Biomedical Materials Research. Part A*, vol. 109, no. 10, pp. 1849–1857, 2021.

[168] S. Liu, V. Mahairaki, H. Bai et al., "Highly purified human extracellular vesicles produced by stem cells alleviate aging cellular phenotypes of senescent human cells," *Stem Cells*, vol. 37, no. 6, pp. 779–790, 2019.

Hindawi
Oxidative Medicine and Cellular Longevity
Volume 2022, Article ID 9325973, 11 pages
https://doi.org/10.1155/2022/9325973

Research Article

Rosin Derivative IDOAMP Inhibits Prostate Cancer Growth via Activating RIPK1/RIPK3/MLKL Signaling Pathway

Hong Xu,[1] Xingkai Zeng,[2] Xuecheng Wei,[1] Zhongfeng Xue,[2] Naiwen Chen,[1] Wei Zhu,[1] Wenhua Xie,[1] and Yi He[1]

[1]*Department of Urology, The Affiliated Hospital of Jiaxing University, Jiaxing, China*
[2]*College of Pharmacy, Guangxi University of Chinese Medicine, Nanning, China*

Correspondence should be addressed to Yi He; heyi@zjxu.edu.cn

Received 3 June 2022; Accepted 25 July 2022; Published 4 August 2022

Academic Editor: En Yin Lai

Rosin derivatives such as dehydroabietic acid and dehydroabietic amine belonging to diterpenoids have similar structure with androgen that inhibited the occurrence and development of prostate cancer. In this study, the effects and possible mechanism of the rosin derivative IDOAMP on prostate cancer were investigated. Our results showed that IDOAMP effectively inhibited cell viabilities of LNCaP, PC3, and DU145 prostate cells. After the treatment with IDOAMP, the levels of cleaved-PARP, LC3BII/I, and HMGB1 were increased, whereas the expression of GPX4 was decreased. Interestingly, cell viability was reversed by the supplements of necrostatin-1 and necrosulfonamide. Meanwhile, the IDOAMP downregulated the expression of human Aurora kinase A that was overexpressed in prostate cancer. In addition, co-IP results showed that IDOAMP inhibited the binding of Aurora kinase A to the receptor-interacting serine/threonine kinase 1 (RIPK1) and RIPK3. However, the binding of RIPK1 to FADD, RIPK3, or MLKL was significantly promoted. Further studies showed that the phosphorylation levels of RIPK1, RIPK, and MLKL were increased in a concentration-dependent manner. In in vivo model, IDOAMP reduced the tumor volumes and weights. In conclusion, IDOAMP directly inhibited Aurora kinase A and promoted the RIPK1/RIPK3/MLKL necrosome activation to inhibit the prostate cancer.

1. Introduction

Prostate cancer (PCa), a malignant tumor of the male genitourinary system, is the 2nd most prevalent cancer affecting males [1], the 4th most frequently diagnosed cancer, and the 5th leading cause of death worldwide, comprising 14.1% of total new cancer cases and 6.8% of the total cancer-associated deaths in 2020 among males [2, 3]. Among all therapies for PCa, endocrine therapy is the most effective option [4], and three most commonly used endocrine drugs including goserelin, leuprorelin, and triptorelin are usually combined with bicalutamide or flutamide for the clinical treatment. Although these three endocrine drugs have shown the powerful anticancer properties owing to the structural similarity to luteinizing hormone-releasing hormone (LHRH), the resistance and other side effects of endocrine therapy would be unavoidable but appear eventually [5]. Therefore, developing effective therapies for PCa with less adverse effects is urgent.

Terpenoids are an important class of natural drugs or drug precursors for treating or preventing cancers and other diseases [6]. A previous study showed that *Ganoderma* triterpenoids significantly suppressed cell proliferation of two human PCa cell lines, LNCaP and PC3 [7]. Similarly, diterpenoids have been reported to possess biological activities against tumors particularly for PCa [8–10]. Moreover, numerous studies have shown that rosin derivatives extracted from plants exhibit antitumor effects [11–15]. Rosin derivatives such as dehydroabietic acid and dehydroabietic amine make up a large group of diterpenes. Dehydroabietic acid and dehydroabietic amine, which are two kinds of rosin derivatives, are typical diterpenes compounds. The

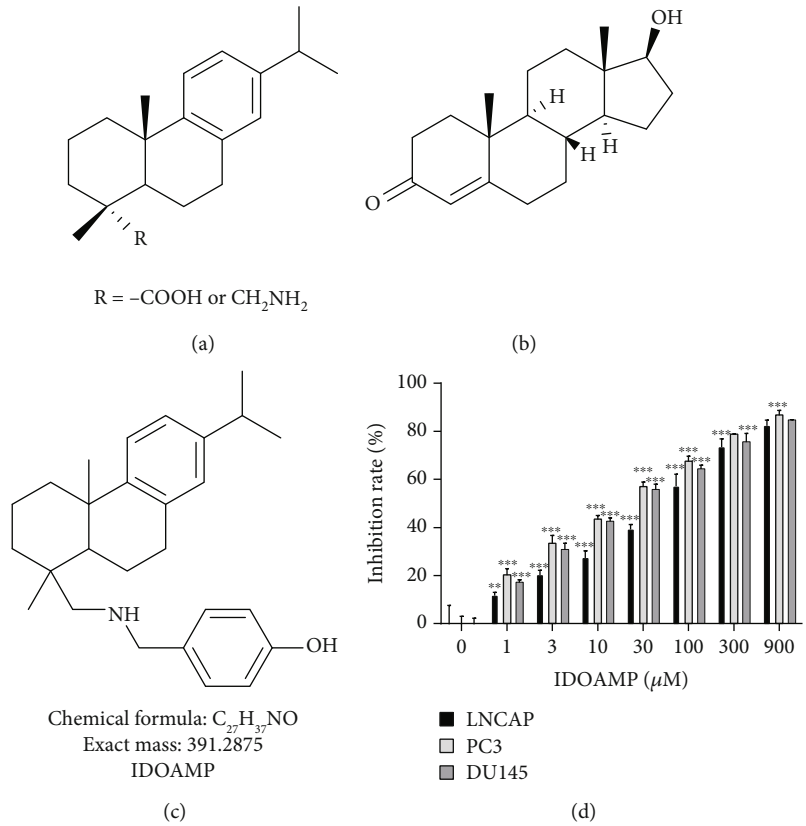

Figure 1: Structures of rosin derivative dehydroabietic acid and dehydroabietic amine (a), androgen (b), and IDOAMP (c). Growth inhibition of LNCaP, PC3, and DU145 cells in the presence of IDOAMP after 24 h treatment (d). (IDOAMP exhibited an inhibitory effect on LNCaP, PC3, and DU145 cells for drug groups at different concentrations compared with control group.) Data are presented as mean ± SD ($n = 3$). $^{**}p < 0.01$ and $^{***}p < 0.001$ vs. the control group.

rosin derivatives hydroabietic acid and dehydroabietic amine show similarities to androgen in their chemical structure, suggesting they may be active against PCa cells. Thus, we synthesized the rosin derivative 4-((((7-isopropyl-1,4a-dimethyl-1,2,3,4,4a,9,10,10a-octahydrophenanthren-1-yl)methyl)amino)methyl)phenol whose structure is similar to androgen. It is termed as IDOAMP because of its chemical structure, and we investigate that this IDOAMP has the potential to suppress PCa.

Previous studies showed that Aurora kinase A usually overexpressed in PCa is a direct negative regulator of necrosome activation, with its kinase activity necessary for binding to RIPK1/3 necrosome during necroptosis [16, 17]. Regulation of necrosis occurs through the programmed necrosis or necroptosis, which is emerging as an important target for cancer treatment [18–20]. Previous research reported that mediators including the receptor-interacting serine/threonine kinase 1 or 3 (RIPK1 or RIPK3) and mixed lineage kinase domain-like (MLKL) played a key role in necroptosis [21]. Based on the above, we have a conjecture that whether the IDOAMP can induce necroptosis via activating RIPK1/RIPK3/MLKL signaling pathway in PC3 cells. In this study, we have carried out the experiments and verified our conjecture. We propose that the IDOAMP emerged as a potential drug for the therapy of PCa.

2. Materials and Methods

2.1. Experimental Drugs and Reagents. Compound IDOAMP (Patent number: 2018101855645) was provided by Prof. Chunxin Lv from the College of Biological, Chemical Sciences and Engineering, Jiaxing University (Zhejiang, China). Anti-cleaved-poly (ADP-ribose) polymerase (PARP) antibody (cat_no.5625), anti-high-mobility group protein B1 (HMGB1) antibody (cat_no.6893), anti-phos-RIPK1 (Ser166) antibody (cat_no.44590), anti-RIPK1 antibody (cat_no.3493), and anti-MLKL antibody (cat_no.14993) were obtained from Cell Signaling Technology (Danvers, MA, USA). Antilipidation of microtubule-associated protein 1 light chain 3 (LC3B) antibody (ab192890), anti-phos-RIPK3 (Ser227) antibody (ab209384), anti-RIPK3 antibody (ab226297), anti-glutathione peroxidase 4 (GPX4) antibody (ab125066), anti-phos-MLKL (Ser358) antibody (ab187091), anti-Aurora kinase A antibody (ab52973), anti-FADD antibody (ab108601), goat anti-rabbit IgG H&L (horseradish peroxidase) (ab205718), and goat anti-mouse IgG H&L (horseradish peroxidase) (ab205719) were obtained from Abcam (Cambridge, UK). Anti-MLKL antibody (sc-293201) and anti-FADD antibody (sc-271520) were procured from Santa Cruz Biotechnology (Dallas, TX, USA). The Aurora A/Aurora B kinase enzyme system was procured from Promega (Madison, WI, USA). Necrostatin-

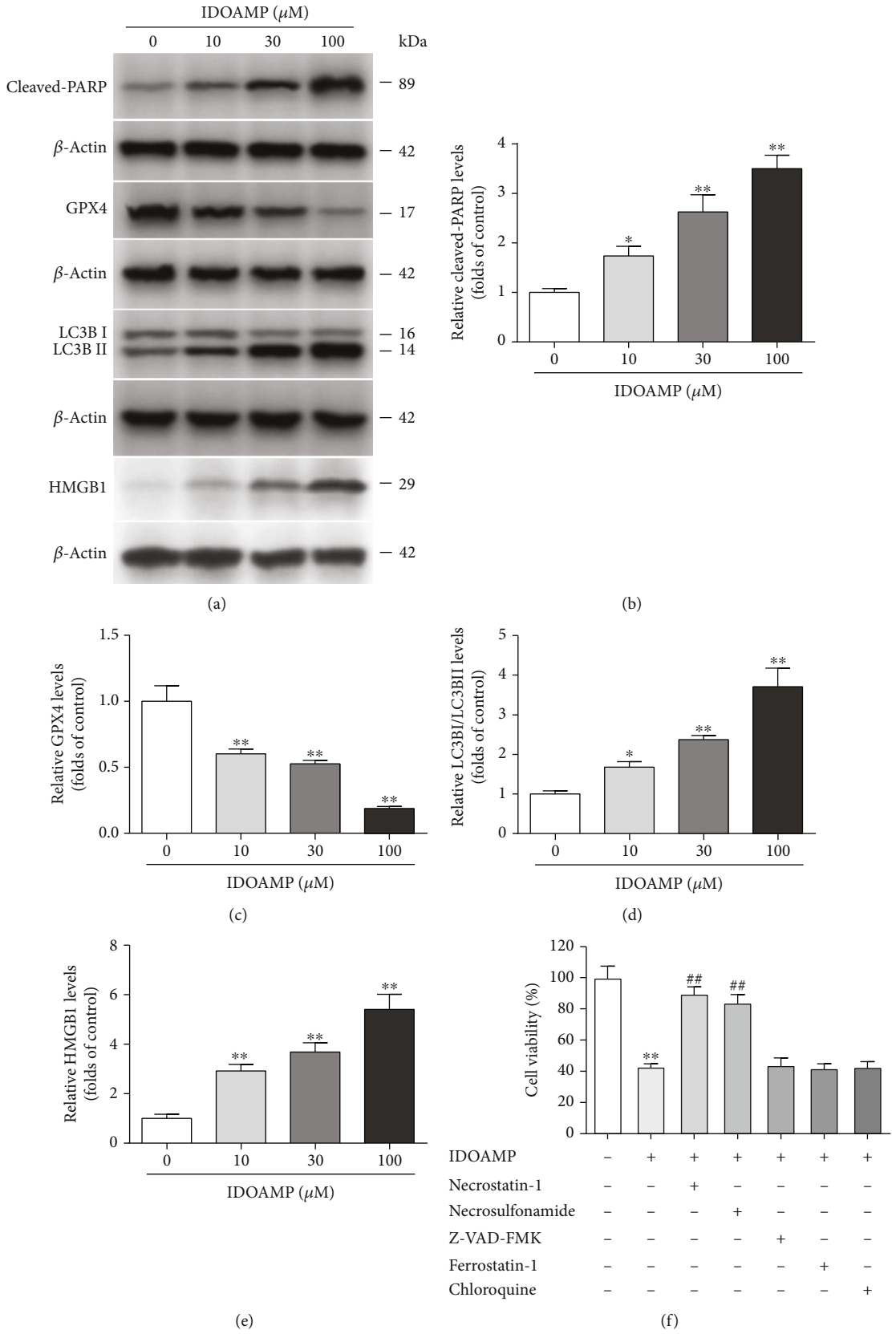

Figure 2: The protein expression level of cleaved-PARP, GPX4, LC3B, and HMGB1 in PC3 cells. (a) Representative bands. The protein expression levels of cleaved-PARP (b), GPX4 (c), LC3B (d), and HMGB1 (e) were normalized to those in the control-treated conditions. (f) PC3 cells were treated with IDOAMP in the absence or presence of the indicated inhibitors for 24 h, and then, cell viability was determined. The results are presented as mean ± SD ($n = 3$). $^{\#\#}p < 0.01$, $^{**}p < 0.01$, and $^{*}p < 0.05$ vs. the control group.

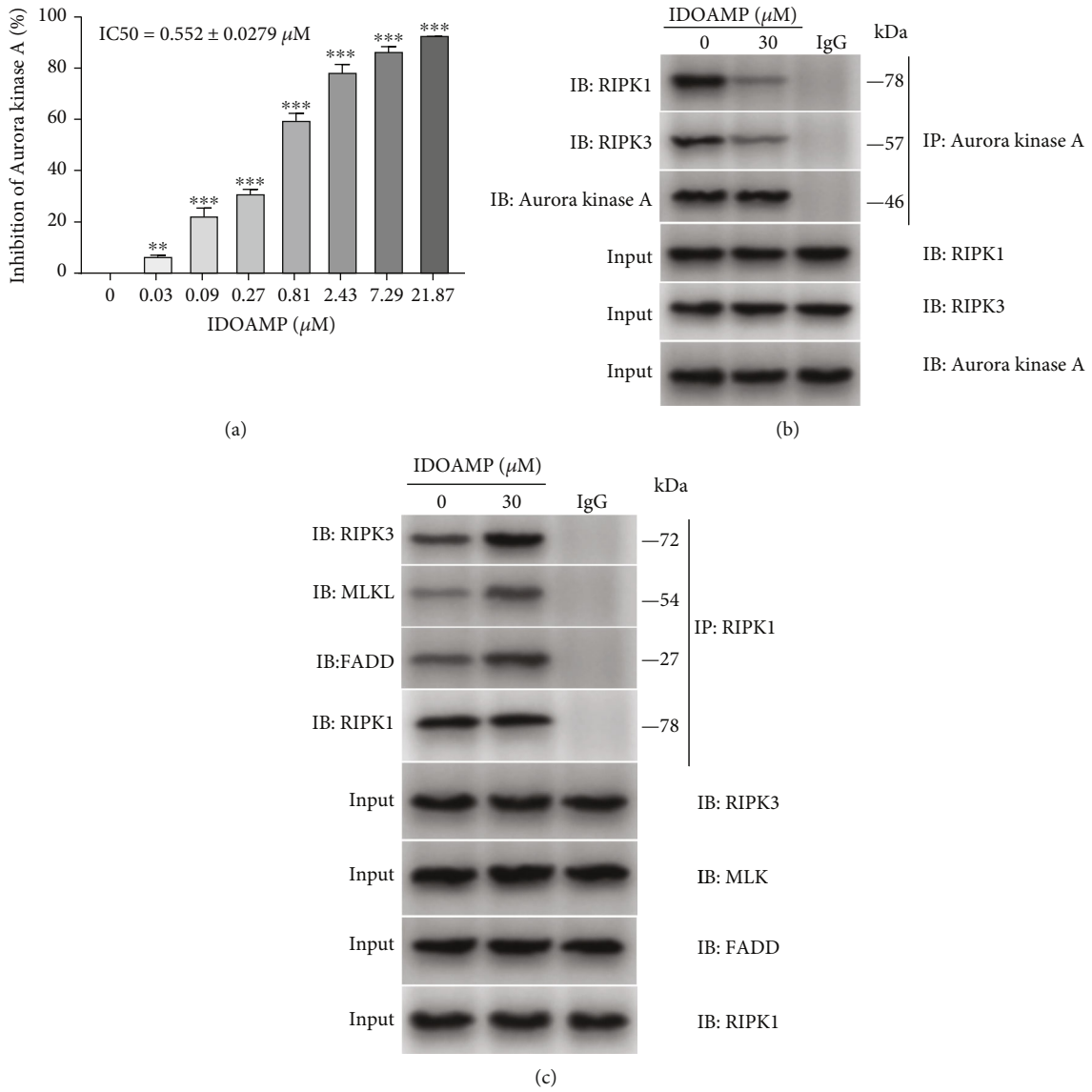

Figure 3: IDOAMP inhibits Aurora kinase A and promotes RIPK1/RIPK3/MLKL necrosome activation. (a) Inhibition of Aurora kinase A in the presence of IDOAMP after 24 h of incubation. (b) Co-IP analysis of the level of RIPK1 binding to FADD, RIPK3, and MLKL in PC3 cells. (c) Co-IP analysis of the levels of Aurora kinase A binding to RIPK1 and RIPK3 in PC3 cells following treatment with IDOAMP for 24 h. Data are presented as mean ± SD ($n = 3$). $^{*}p < 0.05$, $^{**}p < 0.01$, and $^{***}p < 0.001$ vs. the control group.

1, necrosulfonamide, Z-VAD-FMK, ferrostatin-1, and chloroquine were obtained from MedChemExpress (Monmouth Junction, NJ, USA). Fetal bovine serum and F-12K were purchased from Gibco Thermo Fisher Scientific (Grand Island, NY, USA). Penicillin-streptomycin solution was procured from Sigma-Aldrich (St Louis, MO, USA). The hematoxylin-eosin (HE) staining kit was obtained from Beyotime Biotechnology (Shanghai, China).

2.2. Cell Viability. Cell viability of log-phase cells was detected by using the CCK8 assay kit. Briefly, the cells were seeded in 96-well plates (5,000 cells/well) followed by 24 h incubation at 37°C in a 5% CO_2-humidified environment. When the cells reached approximately 90% confluence, three cell lines (LNCAP, PC3, and DU145) were separately transferred to serum-free media and cultured for 2 h. The supernatants were then discarded, and the cells were treated using established protocols for another 24 h. Finally, the CCK-8 solution (10 μL) was added to each well and incubated for 4 h, and the absorbance at 450 nm was measured using a fluorescent microplate reader (Bio-Rad, USA). Cell proliferative ability was determined as follows: cell growth inhibition rate = 1 − (experimental group OD value/control group OD value) × 100%.

2.3. Western Blot. The cells were washed for three times in PBS and then lysed using the RIPA lysis buffer at 4°C. Protein samples were denatured by boiling for 10 min, and protein concentrations were assessed using BCA kits (Pierce BCA; Thermo Scientific). Proteins were subjected to 8%

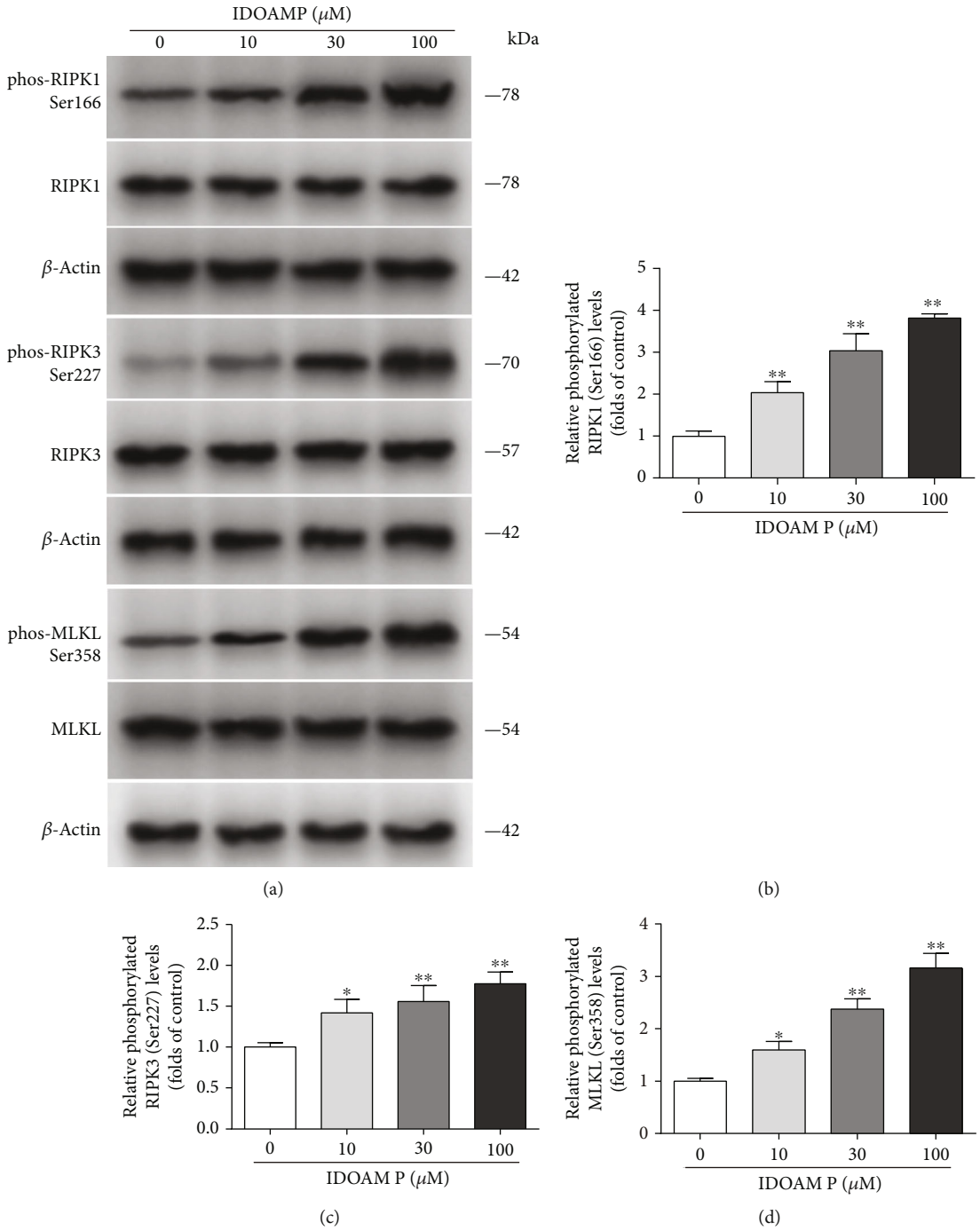

Figure 4: Effect of IDOAMP on RIPK1/RIPK3/MLKL signaling pathways in PC3 cells. (a) The phosphorylation levels of RIPK1, RIPK3, and MLKL in PC3 cells from different groups were detected by western blotting, and the representative bands are shown. Levels of RIPK1 (b), RIPK3 (c), and MLKL (d) were normalized to those in the control-treated conditions. The results are presented as mean ± SD ($n = 3$). $^{*}p < 0.05$ and $^{**}p < 0.01$ vs. the control group.

sodium dodecyl sulfate-polyacrylamide gel electrophoresis and transferred to polyvinylidene fluoride (PVDF) membranes. Membranes were blocked using 5% (m/v) fat-free milk dissolved in Tris-buffered saline with 5% (v/v) Tween-20 (TBS-T) for 1 h. Then, the membranes were incubated with primary antibodies diluted to the appropriate concentrations in TBS-T at 4°C overnight. After washing with TBS, secondary antibodies were diluted to 1 : 5000 in TBS-T and applied to the blots at room temperature for 1 h. Finally, the ECL reagent was used for blot imaging using a Tanon™ 6600 Luminescent Imaging Workstation (Tanon, China). Densitometric evaluation was conducted using the Image Pro Plus 6.0 software (Media Cybernetics Inc., Rockville, MD, USA). The β-actin was used as control, for determination of relative protein expression and phosphorylation levels.

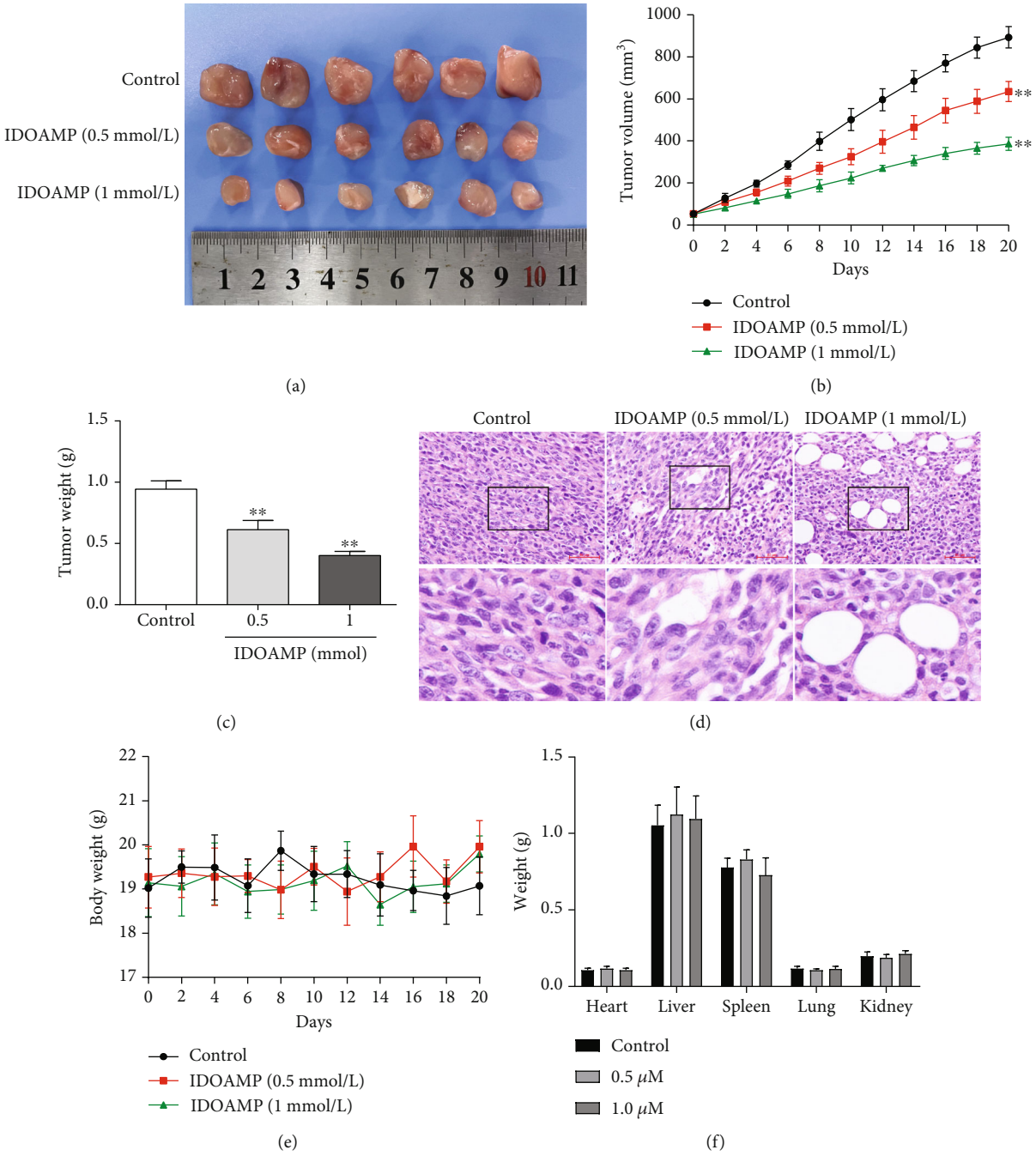

Figure 5: Tumor growth of PC3 xenograft-bearing nude mice. (a) Representative tumor morphology. (b) Tumor volume of the PC3 xenograft in the mice. (c) Effects on tumor weight. (d) HE staining of the tumor in nude mice ($n = 6$). (e) Graph shows the change in weight of the mice during the treatment period. (f) Organ weight of the mice. Weights of the heart, liver, spleen, lung, and kidney of the mice were shown as mean ± SD ($n = 6$). $^{**}p < 0.01$ vs. the control group.

2.4. Human Aurora Kinase A Activity Assay. Human Aurora kinase A activity assay was conducted at room temperature. In brief, 1 μL of IDOAMP, 2 μL of substrate/ATP mix, and 2 μL enzyme were added into each well. The reaction proceeded for 60 min, until the ADP-Glo reagent (5 μL) was then added to each well. Thereafter, the reaction proceeded for 40 min, followed by the addition of 10 μL of kinase detection reagent. Finally, the reaction lasted for 30 min, and the luminescence signal was measured afterwards.

2.5. Co-Immunoprecipitation Assay. The cells were lysed with precooled RIPA lysis buffer. Total cellular proteins were extracted from PC3 cells and incubated with 5 μL of primary antibodies (Aurora kinase A 1 : 50, RIPK1 1 : 100, IgG for the control group) at 4°C on a rocker overnight. Protein-A/G-agarose beads were added to capture antibody-antigen complexes. The antibody-antigen mixture was shaken slowly at 4°C overnight or for 1 h at RT. Immunocomplexes were obtained with protein-A/G-agarose beads and centrifugated

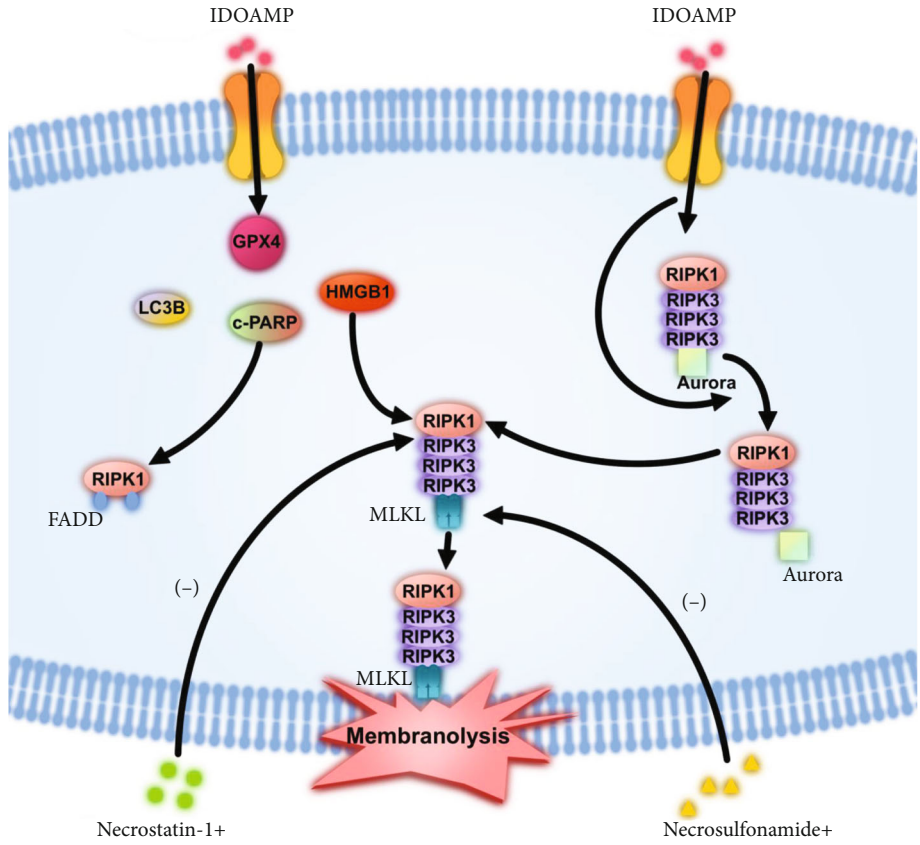

Figure 6: The mechanism of IDOAMP-induced inhibition of prostate cancer cell growth.

at 14,000 × g for 5 s. Sediments were washed thrice in precooled PBS and resuspended in an appropriate volume of loading buffer, followed by 5 min of boiling. Detachments of eluted proteins were analyzed by western blot with appropriate antibodies.

2.6. Animal Procedures. Six-week-old BALB/c nude mice ($n = 18$, male, weight 18–20 g) were supplied by the Model Animal Research Center of Nanjing University (Nanjing, China). All mice were kept in a Laboratory Animal Center SPF grade animal room (23 ± 2°C, natural lighting, free diet). The mice were adaptively bred for 3 days and then xenografted with 3×10^6 PC3 cells/mouse (subcutaneous injection). The mice were randomly divided into low-dose group (0.5 mmol/L IDOAMP), high-dose group (1 mmol/L IDOAMP), and control group (saline) after the tumor reached approximately 50 mm^3. The mice were treated once a day for 20 consecutive days (intraperitoneal injection). Thereafter, the tumors, heart, liver, spleen, lungs, and kidneys were harvested, and tumor weight and volume were measured. Tumor dimensions were measured with calipers, and tumor volume was calculated as $(D \times d^2)/2$, where D and d represent the longest and shortest diameters, respectively.

2.7. HE Staining. Tumors were cut to 4 μm thick sections and dried for 1 h in an oven at 60°C. The paraffin sections were dewaxed with xylene, and a gradient ethanol hydration was performed. Then, the sections were washed with distilled water, stained with hematoxylin, and rinsed under running water. The sections were then placed in 1% (v/v) hydrochloric acid ethanol until they appeared red and rinsed under tap water for blue color recovery. Subsequently, the sections were stained with eosin for 1 min and washed with tap water. Dehydration, hyalinization, and sealing were carried out with gradient ethanol, dimethylbenzene, and neutral gum, respectively. The sections were observed and photographed by inverted phase-contrast microscopy.

2.8. Statistical Analysis. Statistical evaluation was conducted using the GraphPad Prism 9.0 (GraphPad Company, USA). Groups of western blot data were compared by one-way ANOVA and Tukey's post hoc test. All data are expressed as means ± SD. $p < 0.05$ was the cut-off value for significance.

3. Results

3.1. IDOAMP Reduces the Viability of LNCaP, PC3, and DU145 Cells. Dehydroabietic acid and dehydroabietic amine are typical diterpenes compounds (Figure 1(a)). The rosin derivatives hydroabietic acid and dehydroabietic amine have similarities to androgen (Figure 1(b)) in their chemical structure, suggesting that they may be active against PCa cells. Therefore, we synthesized the IDOAMP (Figure 1(c)) whose structure is similar to androgen. Then, CCK-8 cell

viability assays were conducted to assess the efficacy of IDOAMP against PCa cells. IDOAMP exhibited an inhibitory effect on LNCaP, PC3, and DU145 cells (Figure 1(d)). The IC_{50} values for IDOAMP against these cell lines were 53.34 ± 6.21, 16.53 ± 2.01, and $20.89 \pm 0.82\,\mu$M, respectively. These data indicate that the IDOAMP has an inhibitory effect on these three PCa cell lines.

3.2. RIPK1/MLKL May Be Involved in the Inhibitory Effect of IDOAMP on PC3 Cells. Since IDOAMP showed a pronounced inhibitory effect on PCa, we then planned to study the involved mechanism of this inhibition on prostate cancers In this experiment, after treatment of PC3 cells with IDOAMP for 24 h, we tested the protein expression of biomarkers for apoptosis (cleaved-PARP), autophagy (LC3B-I/II), necroptosis/necrosis (HMBG1), and ferroptosis (GPX4) [17]. The results showed that the expression levels of cleaved-PARP, LC3B-II, and HMGB1 significantly increased, but the expression of GPX4 decreased (Figures 2(a)–2(e)). To explore which pathway is involved, we further used necrostatin-1 (inhibitor of RIPK1) [22], necrosulfonamide (an inhibitor of MLKL) [23], Z-VAD-FMK (caspase inhibitor) [24], ferrostatin-1 (inhibitor of ferroptosis) [25], and chloroquine (inhibitor of autophagy) [26]. Remarkably, cell viability in the necrostatin-1- and necrosulfonamide-treated groups was significantly restored, whereas Z-VAD-FMK, ferrostatin-1, and chloroquine had no significant effects on cell viability (Figure 2(f)), indicating RIPK1/MLKL may be involved.

3.3. IDOAMP Inhibits Aurora Kinase A and Promotes RIPK1/RIPK3/MLKL Necrosome Activation. Aurora kinase A is vital for centrosome maturation, meiotic maturation, spindle assembly, and metaphase I spindle orientation [27]. As described previously, Aurora kinase A was overexpressed in PCa [16]. The inhibitory effect of IDOAMP against human Aurora kinase A was determined using an ADP-Glo Kinase Assay Kit (tozasertib was elected as the positive control). Aurora kinase A was inhibited by IDOAMP (Figure 3(a)). These findings imply that human Aurora kinase A may be involved, and Aurora kinase A is crucial for necrosome activation, and its kinase activity is of importance in its binding to RIPK1/3 necrosome during necroptosis [17]. Thus, to investigate whether the IDOAMP affects the relationship between the Aurora kinase A and RIPK1 or RIPK3, we performed the co-IP assay. Our results showed that the IDOAMP inhibited the binding of Aurora kinase A to RIPK1 and RIPK3 in PC3 cells; meanwhile, the binding of RIPK1 to FADD, RIPK3 or MLKL, was significantly increased (Figures 3(b) and 3(c)). Collectively, IDOAMP may inhibit the binding of Aurora kinase A to RIPK1/RIPK3 but may promote RIPK1-RIPK3-MLKL necrosome formation.

3.4. IDOAMP Regulates RIPK1/RIPK3/MLKL Pathway. Necroptosis depends on the activation of a necrosome, a protein complex which is comprised of three core components: RIPK1, MLKL, and RIPK3 [28, 29]. After the supplementation with 10, 30, or 100 μM of IDOAMP for 24 h, the phosphorylation levels of RIPK1, RIPK3, and MLKL in PC3 cells were significantly increased (Figure 4). This result suggests that IDOAMP may regulate the RIPK1/RIPK3/MLKL pathway.

3.5. IDOAMP Can Inhibit PC3 Xenograft Tumor Growth. To investigate the effect of IDOAMP on tumor growth in vivo, IDOAMP was subcutaneously implanted into nude mice. Tumor volumes and tumor weights were significantly lower in the groups with IDOAMP than the control group (Figures 5(a)–5(c)). Moreover, the histopathological analysis revealed vacuolation in PC3 cells, representing steatosis, and the degree of vacuolation was correlated with IDOAMP (Figure 5(d)). These results demonstrated that the IDOAMP inhibits the tumor growth. In addition, there were no significant differences in body weight among the groups in 20 days (Figure 5(e)). The weight of heart, liver, spleen, lung, and kidney of mice from each group showed no significant differences (Figure 5(f)).

4. Discussion

Several studies have shown that rosin derivatives have considerable multifaceted bioactivity, ranging from antibacterial and antianxiety effects to antiviral and anticancer actions [12, 13, 30]. In the present study, we found that a newly developed rosin derivative, which we termed as IDOAMP, exerted inhibitory effect on PC3 cell lines and inhibited the binding of Aurora kinase A to RIPK1 and RIPK3 as well as promoted RIPK1–RIPK3–MLKL necrosome formation to induce necroptosis. The mechanism of IDOAMP-induced inhibition of prostate cancer cell growth is summarized in Figure 6.

Recently, many approaches for inducing tumor cell death which are different from apoptosis, namely, autophagy, necroptosis, ferroptosis, and pyroptosis, have been developed. A previous study indicated that promoting apoptosis with androgen deprivation therapy (ADT) may be a cure for PCa [31]. However, ADT is associated with apoptosis resistance, leading to treatment-resistant PCa [32]. Moreover, upregulation of autophagy-related proteins promotes resistance to ADT [33, 34], suggesting that the autophagy machinery controls the transformations of cell death patterns between necroptosis and apoptosis [35]. Autophagic inhibition enhances the efficacy of abiraterone, a drug commonly used in PCa treatment [36]. In prostate cells with defective autophagy, toxic substances induce necroptosis rather than apoptosis [37]. Thus, suppressing autophagy and/or inducing necroptosis may increase the effectiveness of ADT [31]. Here, we demonstrated that IDOAMP induced PCa cell death with phenotypic features of autophagy, apoptosis, and necroptosis. As previously shown, the expression levels of cleaved-PARP, LC3B-II, and HMGB1 significantly increased, but only cell viability in the necrostatin-1- and necrosulfonamide-treated groups was significantly restored. This may result from the fact that Aurora kinase A is a direct negative regulator of necrosome activation that attaches importance to necroptosis. Meanwhile, our results showed that the IDOAMP inhibited the Aurora kinase A activity. Therefore, we concluded that the IDOAMP induces

necroptosis rather than other forms of cell death in PCa. Nevertheless, necroptotic signaling played a vital role in mediating the anticancer activities of IDOAMP in PCa cells. Pharmacologic necroptosis inhibition considerably blocked IDOAMP-mediated PCa cell death.

Aurora kinase A is a constituent of the necrosome that can impede necroptosis by binding to RIPK1 and RIPK3 [17]. This is consistent with our results that IDOAMP showed obvious inhibitory effects against Aurora kinase A and reduced the binding of Aurora kinase A to RIPK1 and RIPK3. Thereafter, IDOAMP induced the necroptosis. At the same time, the IDOAMP increased the binding of RIPK1 to FADD, RIPK3, and MLKL. Thus, we speculate that IDOAMP inhibited Aurora kinase A and promoted necrosome activation of RIPK1/RIPK3/MLKL to induce necroptosis. However, necroptosis differs from apoptosis. The effect of necroptosis circumvents the development of multidrug resistance that results from the widespread use of chemotherapy drugs [17]. As apoptosis resistance may be a hallmark of cancer cells [38]. Our results showed that IDOAMP effectively activates necroptosis in PCa, and this may contribute to the avoidance of apoptosis resistance. Thus, IDOAMP has the potential for cancer treatments.

RIPK1/RIPK3/MLKL pathway-mediated necroptosis has been a research hotspot in recent years [39–41]. Necroptosis is modulated by RIPK1 that is a critical regulator [42]. When necroptosis is induced, RIPK1 can bind to RIPK3 via RHIM domains to phosphorylate RIPK1. Under the action of stimulating factors, RIPK3 is also phosphorylated. Next, p-RIPK3 forms a necrosome complex with p-RIPK1 to regulate necroptosis [40]. In our study, the results showed that IDOAMP directly inhibited the Aurora kinase A and reduced its binding to RIPK1 and RIPK3. A previous study has shown that the interaction between RIPK1 and RIPK3 is increased by the inhibition of Aurora kinase A, which is related to the enhanced RIPK-3-mediated phosphorylation of MLKL [17]. Phosphorylated MLKL is translocated to the plasma membrane and induces membrane rupture to precipitate the lethal step of necroptosis [43]. Our results showed that the IDOAMP induces necroptosis in PCa cells via activating RIPK1/RIPK3/MLKL signaling pathway, consistent with the findings of the above studies.

Our study showed that IDOAMP has anticancer effects both in vitro and in vivo. However, the specific mechanism of IDOAMP in vivo is in need of careful exploration. As we noted that these effects in humans have not been evaluated, further studies are necessary to determine the mechanism in vivo and potential for applying to clinic practice.

In summary, our results demonstrated that IDOAMP inhibited Aurora kinase A, promoting the RIPK1/RIPK3/MLKL necrosome activation to antiprostate cancer. Since IDOAMP has significant antitumor activities in vivo and in vitro, therefore, it possesses visible potential as drug candidate for prostate cancer treatment.

Data Availability

The data used to support the finding of this study are included within the article.

Conflicts of Interest

The authors declare no conflicts of interest.

Authors' Contributions

Hong Xu and Xingkai Zeng contributed equally to this work.

Acknowledgments

This work was supported by grants to Yi He from the Medical Scientific Research Foundation of Zhejiang Province, China (2019KY694), Prostate Cancer-Specific Cohort Study (SQ2017YFSF090096), Jiaxing Medical Key Subject Funding of Zhejiang Province (2019-ZC-07), and Jiaxing Key Laboratory of Precise Diagnosis and Treatment of Urological Tumor (2020-MNZDSYS) and to Zhongfeng Xue from the Guangxi Natural Science Foundation (2020GXNSFBA238008) and the Doctoral Research Startup Fund Project of Guangxi University of Chinese Medicine (2017BS026).

References

[1] S. Liu, W. Wang, Y. Zhao, K. Liang, and Y. Huang, "Identification of potential key genes for pathogenesis and prognosis in prostate cancer by integrated analysis of gene expression profiles and the Cancer Genome Atlas," *Frontiers in oncology*, vol. 10, p. 809, 2020.

[2] H. Sung, J. Ferlay, R. L. Siegel et al., "Global Cancer Statistics 2020: GLOBOCAN Estimates of Incidence and Mortality Worldwide for 36 Cancers in 185 Countries," *CA: a cancer journal for clinicians*, vol. 71, no. 3, pp. 209–249, 2021.

[3] W. Cao, H. D. Chen, Y. W. Yu, N. Li, and W. Q. Chen, "Changing profiles of cancer burden worldwide and in China: a secondary analysis of the global cancer statistics 2020," *Chinese Medical Journal*, vol. 134, no. 7, pp. 783–791, 2021.

[4] X. Gong, J. S. Wang, X. D. Yu et al., "Assessment of the efficacy of Chinese patent medicine on treating pain caused by prostate cancer: a protocol for systematic review and meta analysis," *Medicine (Baltimore)*, vol. 98, no. 51, article e17820, 2019.

[5] X. Liu, X. Guo, and Z. Zhang, "Preoperative serum hypersensitive-c-reactive-protein (Hs-CRP) to albumin ratio predicts survival in patients with luminal B subtype breast cancer," *OncoTargets and therapy*, vol. Volume 14, pp. 4137–4148, 2021.

[6] S. Tarhouni-Jabberi, O. Zakraoui, E. Ioannou et al., "Mertensene, a halogenated monoterpene, induces G2/M cell cycle arrest and caspase dependent apoptosis of human colon adenocarcinoma HT29 cell line through the modulation of ERK-1/-2, AKT and NF-κB signaling," *Marine drugs*, vol. 15, no. 7, p. 221, 2017.

[7] T. Wang, Z. P. Xie, Z. S. Huang et al., "Total triterpenoids from Ganoderma lucidum suppresses prostate cancer cell growth by inducing growth arrest and apoptosis," *Journal of Huazhong University of Science and Technology. Medical Sciences*, vol. 35, no. 5, pp. 736–741, 2015.

[8] J. Xu, J. Yang, Q. Ran et al., "Synthesis and biological evaluation of novel 1-O- and 14-O-derivatives of oridonin as potential anticancer drug candidates," *Bioorganic & Medicinal Chemistry Letters*, vol. 18, no. 16, pp. 4741–4744, 2008.

[9] J. Nateewattana, S. Dutta, S. Reabroi et al., "Induction of apoptosis in cholangiocarcinoma by an andrographolide analogue is mediated through topoisomerase II alpha inhibition," *European Journal of Pharmacology*, vol. 723, pp. 148–155, 2014.

[10] J. J. Johnson, D. N. Syed, C. R. Heren, Y. Suh, V. M. Adhami, and H. Mukhtar, "Carnosol, a dietary diterpene, displays growth inhibitory effects in human prostate cancer PC3 cells leading to G2-phase cell cycle arrest and targets the 5'-AMP-activated protein kinase (AMPK) pathway," *Pharmaceutical research*, vol. 25, no. 9, pp. 2125–2134, 2008.

[11] Y. Xing, W. Zhang, J. Song, Y. Zhang, X. Jiang, and R. Wang, "Anticancer effects of a novel class rosin-derivatives with different mechanisms," *Bioorganic & Medicinal Chemistry Letters*, vol. 23, no. 13, pp. 3868–3872, 2013.

[12] C. Wasowski and M. Marder, "Central nervous system activities of two diterpenes isolated from Aloysia virgata," *Phytomedicine*, vol. 18, no. 5, pp. 393–401, 2011.

[13] M. A. Gonzalez, D. Perez-Guaita, J. Correa-Royero et al., "Synthesis and biological evaluation of dehydroabietic acid derivatives," *European Journal of Medicinal Chemistry*, vol. 45, no. 2, pp. 811–816, 2010.

[14] Y. Chen, Z. X. Lin, and A. M. Zhou, "Synthesis and antitumour activities of a novel class of dehydroabietylamine derivatives," *Natural Product Research*, vol. 26, no. 23, pp. 2188–2195, 2012.

[15] H. Luo, C. T. Vong, H. Chen et al., "Naturally occurring anticancer compounds: shining from Chinese herbal medicine," *Chinese medicine*, vol. 14, no. 1, p. 48, 2019.

[16] K. Nikhil, A. Raza, H. S. Haymour, B. V. Flueckiger, J. Chu, and K. Shah, "Aurora kinase A-YBX1 synergy fuels aggressive oncogenic phenotypes and chemoresistance in castration-resistant prostate cancer," *Cancers*, vol. 12, no. 3, p. 660, 2020.

[17] Y. Xie, S. Zhu, M. Zhong et al., "Inhibition of aurora kinase A induces necroptosis in pancreatic carcinoma," *Gastroenterology*, vol. 153, no. 5, pp. 1429–1443.e5, 2017.

[18] P. Vandenabeele, L. Galluzzi, T. Vanden Berghe, and G. Kroemer, "Molecular mechanisms of necroptosis: an ordered cellular explosion," *Nature reviews Molecular cell biology*, vol. 11, no. 10, pp. 700–714, 2010.

[19] X. Liu, Y. Li, S. Peng et al., "Epstein-Barr virus encoded latent membrane protein 1 suppresses necroptosis through targeting RIPK1/3 ubiquitination," *Cell death & disease*, vol. 9, no. 2, p. 53, 2018.

[20] X. Xie, Y. Zhao, C. Y. Ma et al., "Dimethyl fumarate induces necroptosis in colon cancer cells through GSH depletion/ROS increase/MAPKs activation pathway," *British Journal of Pharmacology*, vol. 172, no. 15, pp. 3929–3943, 2015.

[21] M. Pasparakis and P. Vandenabeele, "Necroptosis and its role in inflammation," *Nature*, vol. 517, no. 7534, pp. 311–320, 2015.

[22] A. Linkermann, J. H. Bräsen, F. De Zen et al., "Dichotomy between RIP1- and RIP3-mediated necroptosis in tumor necrosis Factor-α-Induced shock," *Molecular medicine*, vol. 18, no. 4, pp. 577–586, 2012.

[23] L. Sun, H. Wang, Z. Wang et al., "Mixed lineage kinase domain-like protein mediates necrosis signaling downstream of RIP3 kinase," *Cell*, vol. 148, no. 1-2, pp. 213–227, 2012.

[24] U. Ros, A. Peña-Blanco, K. Hänggi et al., "Necroptosis execution is mediated by plasma membrane nanopores independent of calcium," *Cell reports*, vol. 19, no. 1, pp. 175–187, 2017.

[25] B. Yu, B. Choi, W. Li, and D. H. Kim, "Magnetic field boosted ferroptosis-like cell death and responsive MRI using hybrid vesicles for cancer immunotherapy," *Nature communications*, vol. 11, no. 1, 2020.

[26] L. Turcios, E. Chacon, C. Garcia et al., "Autophagic flux modulation by Wnt/β-catenin pathway inhibition in hepatocellular carcinoma," *PLoS One*, vol. 14, no. 2, p. e0212538, 2019.

[27] V. Bavetsias and S. Linardopoulos, "Aurora kinase inhibitors: current status and outlook," *Frontiers in oncology*, vol. 5, p. 278, 2015.

[28] R. Weinlich, A. Oberst, H. M. Beere, and D. R. Green, "Necroptosis in development, inflammation and disease," *Nature reviews Molecular cell biology*, vol. 18, no. 2, pp. 127–136, 2017.

[29] L. Galluzzi, O. Kepp, F. K.-M. Chan, and G. Kroemer, "Necroptosis: mechanisms and relevance to disease," *Annual Review of Pathology: Mechanisms of Disease*, vol. 12, pp. 103–130, 2017.

[30] C. L. Lee, L. C. Chiang, L. H. Cheng et al., "Influenza A (H_1N_1) antiviral and cytotoxic agents from Ferula assa-foetida," *Journal of Natural Products*, vol. 72, no. 9, pp. 1568–1572, 2009.

[31] K.-X. Zhang, J. Firus, B. Prieur, W. Jia, and P. S. Rennie, "To die or to survive, a fatal question for the destiny of prostate cancer cells after androgen deprivation therapy," *Cancers*, vol. 3, no. 2, pp. 1498–1512, 2011.

[32] M. V. Fiandalo, W. Wu, and J. L. Mohler, "The role of intracrine androgen metabolism, androgen receptor and apoptosis in the survival and recurrence of prostate cancer during androgen deprivation therapy," *Current Drug Targets*, vol. 14, no. 4, pp. 420–440, 2013.

[33] H.-Y. Zhang, Y.-D. Ma, Y. Zhang, J. Cui, and Z.-M. Wang, "Elevated levels of autophagy-related marker ULK1 and mitochondrion- associated autophagy inhibitor LRPPRC are associated with biochemical progression and overall survival after androgen deprivation therapy in patients with metastatic prostate cancer," *Journal of Clinical Pathology*, vol. 70, no. 5, pp. 383–389, 2017.

[34] G. J. Berchem, M. Bosseler, L. Y. Sugars, H. J. Voeller, S. Zeitlin, and E. P. Gelmann, "Androgens induce resistance to bcl-2-mediated apoptosis in LNCaP prostate cancer cells," *Cancer Research*, vol. 55, no. 4, pp. 735–738, 1995.

[35] M. L. Goodall, B. E. Fitzwalter, S. Zahedi et al., "The autophagy machinery controls cell death switching between apoptosis and necroptosis," *Developmental Cell*, vol. 37, no. 4, pp. 337–349, 2016.

[36] X. Ma, L. Zou, X. Li, Z. Chen, Z. Lin, and X. Wu, "Inhibition of autophagy improves the efficacy of abiraterone for the treatment of prostate cancer," *Cancer Biotherapy and Radiopharmaceuticals*, vol. 34, no. 3, pp. 181–188, 2019.

[37] P. Kharaziha, D. Chioureas, G. Baltatzis et al., "Sorafenib-induced defective autophagy promotes cell death by necroptosis," *Oncotarget*, vol. 6, no. 35, pp. 37066–37082, 2015.

[38] N. Seko, N. Oue, T. Noguchi et al., "Olfactomedin 4 (GW112, hGC-1) is an independent prognostic marker for survival in patients with colorectal cancer," *Experimental and Therapeutic Medicine*, vol. 1, no. 1, pp. 73–78, 2010.

[39] A. Linkermann and D. R. Green, "Necroptosis," *The New England Journal of Medicine*, vol. 370, no. 5, pp. 455–465, 2014.

[40] F. Humphries, S. Yang, B. Wang, and P. N. Moynagh, "RIP kinases: key decision makers in cell death and innate immunity," *Cell Death & Differentiation*, vol. 22, no. 2, pp. 225–236, 2015.

[41] J. Li, T. McQuade, A. B. Siemer et al., "The RIP1/RIP3 necrosome forms a functional amyloid signaling complex required for programmed necrosis," *Cell*, vol. 150, no. 2, pp. 339–350, 2012.

[42] K. Newton, K. E. Wickliffe, D. L. Dugger et al., "Cleavage of RIPK1 by caspase-8 is crucial for limiting apoptosis and necroptosis," *Nature*, vol. 574, no. 7778, pp. 428–431, 2019.

[43] Y. Dondelinger, W. Declercq, S. Montessuit et al., "MLKL compromises plasma membrane integrity by binding to phosphatidylinositol phosphates," *Cell Reports*, vol. 7, no. 4, pp. 971–981, 2014.